

**MECHANISTIC STUDIES OF  
NATURAL RIBOZYMES AND A SYNTHETIC DNAZYME**

by

JASON M. THOMAS

B.Sc. (Honours), University of British Columbia, 2002

A THESIS SUBMITTED IN PARTIAL FULFILLMENT OF THE  
REQUIREMENTS FOR THE DEGREE OF

DOCTOR OF PHILOSOPHY

in

THE FACULTY OF GRADUATE STUDIES

(Chemistry)

THE UNIVERSITY OF BRITISH COLUMBIA

(Vancouver)

August 2009

© Jason M. Thomas, 2009

## ABSTRACT

This thesis reports the results of experiments designed to help elucidate the catalytic mechanisms of three RNA cleaving nucleic acid catalysts (the 9<sub>25</sub>-11 DNAzyme, and the hammerhead and hairpin ribozymes). A number of enzymological and chemical probing experiments were employed in this regard, which were inspired by antecedent studies of RNA cleaving protein enzymes. First, a novel affinity labeling technique for nucleic acid catalysts was developed to probe general base catalysis. The affinity labeling substrate analogues bear a 2'-bromoacetamide modification at their cleavage sites. The second mechanistic probe employed was 5'-bridging phosphorothioate (S-link) substrate analogues, in which sulphur replaces the native oxygen leaving group. Investigation of S-link substrate cleavage in the context of active site mutations provided insight into general acid catalysis. A novel, simplified method for synthesizing S-link substrates is also presented. Several other experiments provided further mechanistic insight including pH-rate profiling, p*K*<sub>a</sub> perturbation, and the use of nonbridging phosphorothioate substrates.

Using many of the aforementioned experiments, the catalytic mechanism 9<sub>25</sub>-11 DNAzyme (a synthetically modified DNAzyme that contains unnatural protein-like functional groups) was investigated in detail. The data suggest that 9<sub>25</sub>-11 uses its synthetic functional groups to mimic the active site mechanism of the protein enzyme RNaseA.

Affinity labeling, p*K*<sub>a</sub> perturbation, and S-link cleavage experiments were also applied to the hammerhead ribozyme. The affinity labeling data suggest that the deprotonated N1 position of G12 acts as a general base catalyst. The results of p*K*<sub>a</sub> perturbation and S-link cleavage experiments provide strong evidence for a unique

general acid mechanism in the hammerhead ribozyme. Therein, metal coordination is used to acidify a 2'-hydroxyl and thereby improve its ability to act as general acid.

Finally, affinity labeling was used to characterize the role of hairpin ribozyme G8 residue, which occupies a similar structural position to the hammerhead G12 residue. Affinity labeling indeed identified G8 as a potential general base in the hairpin ribozyme. The properties of the hairpin and hammerhead affinity labeling reactions are compared and the mechanistic implications are discussed.

# TABLE OF CONTENTS

ABSTRACT.....	ii
TABLE OF CONTENTS .....	iv
LIST OF TABLES .....	vii
LIST OF FIGURES .....	ix
LIST OF EQUATIONS.....	xxiv
LIST OF ABBREVIATIONS .....	xxvi
ACKNOWLEDGEMENTS .....	xxix
<b>CHAPTER 1: GENERAL INTRODUCTION TO THE CHEMISTRY AND CATALYSIS OF RNA CLEAVAGE.....</b>	<b>1</b>
1.1 PREFACE .....	1
1.2 THE CHEMISTRY OF RNA CLEAVAGE .....	1
1.3 NON-ENZYMATIC CATALYSIS OF RNA CLEAVAGE.....	4
1.3.1 Specific Acid/Base Catalysis .....	4
1.3.2 General Acid/Base Catalysis .....	10
1.3.3 Metal Cation Catalysis .....	14
1.4 ENZYMATIC CATALYSIS OF RNA CLEAVAGE.....	15
1.4.1 Ribonuclease A: Metal Cation Independent Catalysis .....	15
1.4.2 Ribonuclease H: Metal Cation Dependent Catalysis .....	17
1.5 CATALYTIC NUCLEIC ACIDS .....	18
1.5.1 Ribozymes.....	18
1.5.2 DNazymes .....	24
<b>CHAPTER 2: CHEMICAL PROBES FOR GENERAL ACID/BASE CATALYSIS OF RNA CLEAVAGE.....</b>	<b>27</b>
2.1 INTRODUCTION .....	27
2.1.1 Probing General Base Catalysis with Affinity Labeling.....	27
2.1.2 Probing General Acid Catalysis with Bridging Phosphorothioate Substrate Analogues .....	31
2.1.3 pH-Rate Profiling, $pK_a$ Perturbation, and Kinetic Ambiguity .....	42

<b>2.2 MATERIALS AND METHODS</b> .....	<b>49</b>
2.2.1 pH-rate Profile Simulations .....	49
2.2.2 Chemicals and Biochemicals .....	50
2.2.3 Preparation of Oligonucleotide-based Affinity Labels .....	50
2.2.4 Quantification of Bromoacetylation by Gel Mobility Shift Assay .....	51
2.2.5 Synthesis of Bridging 5'-Thiophosphorylated Oligonucleotides .....	51
2.2.6 MALDI-TOF Mass Spectrometric Analysis .....	53
2.2.7 Synthesis of Bridging 5'-Phosphorothioate Substrate Analogues .....	54
2.2.8 Characterization of Bridging 5'-Phosphorothioate Substrate Analogues .....	55
<b>2.3 RESULTS AND DISCUSSION</b> .....	<b>56</b>
2.3.1 Preparation and Characterization of Oligonucleotide-based Affinity Labels .....	56
2.3.2 A Novel Method for Synthesizing Bridging 5'-Thiophosphorylated DNA Oligonucleotides .....	63
2.3.3 A Novel Method for Synthesizing Bridging 5'-Phosphorothioate Substrate Analogues .....	72

**CHAPTER 3: MECHANISTIC INVESTIGATION OF THE 9<sub>25</sub>-11 DNAZYME:  
A RIBONUCLEASE A MIMIC? ..... 79**

<b>3.1 INTRODUCTION</b> .....	<b>79</b>
3.1.1 RNaseA Mimicry .....	79
3.1.2 The 9 <sub>25</sub> -11 DNAzyme .....	82
3.1.3 Mechanistic Characterization of 9 <sub>25</sub> -11 Catalysis .....	85
3.1.4 Metal Cation Binding Properties of 9 <sub>25</sub> -11 .....	86
<b>3.2 MATERIALS AND METHODS</b> .....	<b>88</b>
3.2.1 Chemicals and Biochemicals .....	88
3.2.2 Oligonucleotide Sequences .....	89
3.2.3 Metal Cation Inhibition of <i>Cis</i> -cleaving 9 <sub>25</sub> -11 .....	91
3.2.4 Kinetic Experiments with <i>Trans</i> -cleaving 9 <sub>25</sub> -11 .....	93
3.2.5 2'-Bromoacetamide Affinity Labeling Experiments .....	95
<b>3.3 RESULTS AND DISCUSSION</b> .....	<b>97</b>
3.3.1 Metal Cation Binding and Inhibition of 9 <sub>25</sub> -11 Self-Cleavage .....	97
3.3.2 General Properties of 9 <sub>25</sub> -11 Catalysis .....	103
3.3.3 Probing General Base Catalysis .....	111
3.3.4 Probing General Acid Catalysis .....	123
3.3.5 Probing DNAzyme-Scissile Phosphate Interactions .....	128
<b>3.4 CONCLUSIONS</b> .....	<b>139</b>

**CHAPTER 4: PROBING GENERAL ACID/BASE CATALYSIS IN THE  
HAMMERHEAD RIBOZYME..... 1422**

<b>4.1 INTRODUCTION</b> .....	<b>1422</b>
4.1.1 "Minimal" Hammerheads: A Structure and Function Dilemma .....	1422
4.1.2 "Extended" Hammerheads: Reconciliation of the Structure-Function Dilemma? .....	1477
<b>4.2 MATERIALS AND METHODS</b> .....	<b>15050</b>
4.2.1 Chemicals and Biochemicals .....	15050
4.2.2 Oligonucleotide Sequences .....	15050
4.2.3 Oligonucleotide Preparation .....	1511

4.2.4 Ribozyme Affinity Labeling Reactions .....	1522
4.2.5 Alkaline Footprinting of the Alkylation Sites .....	1533
4.2.6 Aniline Footprinting of the Alkylation Sites .....	1555
4.2.7 Ribozyme Kinetic Experiments .....	1555
<b>4.3 PROBING GENERAL BASE CATALYSIS IN THE HAMMERHEAD RIBOZYME .....</b>	<b>1577</b>
4.3.1 Results .....	1577
4.3.1.1 Hammerhead Ribozyme Affinity Labeling .....	1577
4.3.1.2 Footprinting the Alkylation Site: 5'-Labeled Ribozyme .....	1588
4.3.1.3 Footprinting the Alkylation Site: 3'-Labeled Ribozyme .....	1633
4.3.1.4 Assignment of an Unidentified 5'-Labeled Cleavage Fragment .....	1722
4.3.1.5 Properties of the Affinity Labeling Reactions .....	18080
4.3.2 Discussion .....	1866
4.3.2.1 Structural Implications of the Affinity Labeling Data .....	1866
4.3.2.2 Mechanistic Implications of the Affinity Labeling Data .....	1888
4.3.3 Conclusions .....	19090
<b>4.4 PROBING GENERAL ACID CATALYSIS IN THE HAMMERHEAD RIBOZYME.....</b>	<b>1911</b>
4.4.1 Results .....	1911
4.4.1.1 S-link Substrate Cleavage and Ribozyme Mutation .....	1911
4.4.1.2 pH-Rate Profiles .....	1988
4.4.2 Discussion .....	2011
4.4.2.1 S-link Substrate Cleavage and Ribozyme Mutation .....	2011
4.4.2.2 pH-Rate Profiles .....	2055
4.4.3 Conclusions .....	2099
<b>CHAPTER 5: PROBING GENERAL BASE CATALYSIS IN THE HAIRPIN</b>	
<b>RIBOZYME .....</b>	<b>21010</b>
<b>5.1 INTRODUCTION .....</b>	<b>21010</b>
5.1.1 Hairpin Ribozyme Structure and Function .....	21010
5.1.2 The Role of G8 in Hairpin Catalysis .....	21414
<b>5.2 MATERIALS AND METHODS .....</b>	<b>2199</b>
5.2.1 Chemicals and Biochemicals .....	2199
5.2.2 Oligonucleotide Preparation .....	2199
5.2.3 Ribozyme Affinity Labeling Reactions .....	22020
5.2.4 Reverse Transcription Footprinting of the Alkylation Site.....	22120
5.2.5 Alkaline Footprinting of the Alkylation Site .....	2211
5.2.6 Nuclease Digestion/MALDI-TOF Mass Spectrometry .....	2233
<b>5.3 RESULTS.....</b>	<b>2244</b>
5.3.1 Hairpin Ribozyme Affinity Labeling .....	2244
5.3.2 Reverse Transcription Footprinting of the Alkylation Site.....	2266
5.3.3 Alkaline Footprinting of the Alkylation Site .....	2299
5.3.4 Enzymatic Digestion/MALDI-TOF Mass Spectrometric Analysis of the Alkylation Site ..	2311
5.3.5 Properties of the Alkylation Reaction .....	2344
<b>5.4 DISCUSSION AND CONCLUSIONS .....</b>	<b>2411</b>
<b>REFERENCES.....</b>	<b>2456</b>

## LIST OF TABLES

<b>Table 2.1:</b> Assignments and predicted and observed m/z values for the [M-H] <sup>-</sup> molecular ions observed in the MALDI-TOF spectra shown in Figure 2.14. ....	59
<b>Table 2.2:</b> Assignments and predicted and observed m/z values for the [M-H] <sup>-</sup> molecular ions observed in the MALDI-TOF spectra in Figure 2.20.....	67
<b>Table 3.1:</b> Assignments and predicted and observed m/z values for peaks observed in the MALDI-TOF spectrum shown in Figure 3.10.....	105
<b>Table 3.2:</b> The effects on 9 <sub>25</sub> -11 catalysis of changing the unpaired substrate nucleotides. The changes made to the native substrate sequence are highlighted in red. Note that these measurements were made at 24 °C.....	106
<b>Table 3.3:</b> The effects of individual synthetic functional group deletion on the observed rate constants for 9 <sub>25</sub> -11 catalyzed cleavage of the native (O-link) substrate in standard buffer (pH 7.5). ....	108
<b>Table 3.4:</b> Assignments and predicted and observed m/z values for the peaks observed in the MALDI-TOF spectra shown in Figures 3.15 and 3.16. Residues which originate from the DNAzyme and substrate analogue strands are coloured blue and black, respectively.....	119
<b>Table 3.5:</b> The effects of individual synthetic functional group deletion on the observed rate constants for 9 <sub>25</sub> -11 catalyzed cleavage of the bridging 5'-phosphorothioate (S-link) substrate in standard buffer (pH 7.5). The data for native substrate cleavage from Table 3.3 is included for comparison. ....	126
<b>Table 3.6:</b> $R^2$ values for the fits of the kinetic data in Figure 3.21. Clearly, native substrate cleavage fits very well to a monophasic model for wildtype and all mutants tested. Cleavage of the nonbridging phosphorothioate mixture fits well to a monophasic model only for the T21 mutant; notably, this is the only case in which the biphasic fit offers no improvement in the $R^2$ value. In all other cases, the biphasic fits returned much improved $R^2$ values relative to the monophasic fits. ....	134
<b>Table 3.7:</b> First order rate constants for nonbridging phosphorothioate cleavage by 9 <sub>25</sub> -11 and variants (determined by fitting the data in Figure 3.21). $k_{S \text{ fast}}$ and $k_{S \text{ slow}}$ describe the fast and slow phases, respectively, for biphasic cleavage of the nonbridging phosphorothioate substrate mixture.....	135

**Table 3.8:** Comparison of the kinetic parameters determined for native and nonbridging phosphorothioate substrate cleavage by 9<sub>25-11</sub> and variants.  $k_O$  is the observed rate constant for native substrate cleavage (see Table 3.3) and  $k_{S \text{ fast}}$  and  $k_{S \text{ slow}}$  are the observed rate constants for the fast and slow phases, respectively, of nonbridging phosphorothioate substrate cleavage (see Table 3.7). The endpoints ( $P_\infty$ ) for each of the phosphorothioate cleavage phases and those for native substrate are also compared. ....136

**Table 4.1:** Initial rate constants determined for the formation of Bands I and II for the wild type and various mutant *S. mansoni* hammerhead ribozymes. All reactions contained 50 mM MgCl<sub>2</sub>, 100 mM NaCl, 50 mM Tris-HCl pH 8, except for the reaction which lacked Mg<sup>2+</sup>, which contained 50 mM Tris-HCl pH 8, 100 mM NaCl, 5 mM EDTA. ....182

**Table 4.2:** First order rate constants determined for single turnover cleavage of O-link and S-link substrates by the wildtype and mutant *S. mansoni* hammerhead ribozymes. All reactions were carried out in 2 mM MgCl<sub>2</sub>, 100 mM NaCl, 50 mM Na-PIPES pH 7. ....195

**Table 4.3:** First order rate constants determined for single turnover cleavage of O-link and S-link substrates by the wildtype, 2'-deoxy-G8, and 2'-O-methyl-G8 *S. mansoni* hammerhead ribozymes in the presence of various metal cations. All reactions were carried out in 50 mM Na-PIPES pH 7. ....197

**Table 4.4:** The  $pK_a$  values determined from the pH-rate profile data (Figure 4.22) for O-link substrate cleavage by the wildtype, 2'-deoxy-G8, and 2'-O-methyl-G8 *S. mansoni* hammerhead ribozymes. All reactions contained 1 mM M<sup>2+</sup>, 100 mM NaCl, 50 mM Buffer. Standard error limits generated by fitting the pH-rate profile data are given. The  $pK_a$  values reported as “ >9 ” could not be fit reliably because the titrations occur outside the observable pH range. ....200

**Table 5.1:** Predicted and observed m/z values and sequence assignments for the digestion fragments observed in the MALDI-TOF spectra shown in Figure 5.8. ....233

**Table 5.2:** Rate constants and extents of reaction for the hairpin ribozyme affinity labeling in 50 mM Na-Cacodylate pH 7.5, 50 mM MgCl<sub>2</sub>. ....239

## LIST OF FIGURES

**Figure 1.1:** RNA cleavage by 2'-transphosphorylation yields 5'-hydroxy and 2',3'-cyclic phosphodiester terminated products, the latter of which is subsequently hydrolyzed irreversibly to yield 2'- and 3'-phosphate terminated products. The ribose 2', 3', and 5'-carbons are indicated in blue. ....3

**Figure 1.2:** Simplified representation of the specific acid, specific base, and uncatalyzed reaction channels for RNA cleavage. Combinations of specific acid/base catalysis are also possible for less populated protonation states (not shown).<sup>12</sup> Kinetically insignificant proton transfers involving H<sub>2</sub>O are omitted.<sup>13</sup> .....6

**Figure 1.3:** (A) Idealized pH-rate profile for specific acid/base catalyzed RNA cleavage at 37 °C based on:  $pK_{a1} = 13.7$ ,  $pK_{a2} = 1$ ,  $pK_{a3} = -3.5$ ,  $k_{max\ 1} = 0.02\ \text{min}^{-1}$ ,  $k_{max\ 2} = 1 \cdot 10^{-8}\ \text{min}^{-1}$ ,  $k_{max\ 3} = 2 \cdot 10^{-4}\ \text{min}^{-1}$ , and  $k_{uncat} = 2 \cdot 10^{-13}\ \text{min}^{-1}$ .<sup>12</sup> The approximate slope of the plot is indicated for each grey coloured pH-range; white coloured pH-ranges indicate slope transitions. (B) Plots of the logarithm of the fold rate enhancement (over the uncatalyzed rate) attributed to each of 2'-hydroxyl deprotonation (blue), nonbridging oxygen protonation (green), and 5'-oxygen protonation (red). ....9

**Figure 1.4:** General strategies for catalyzing RNA cleavage,<sup>12</sup> (colour coded as in Figure 1.3; purple indicates the rate enhancement gained by enforcing the in-line attack geometry, as can be achieved by enzyme binding). ....10

**Figure 1.5:** Idealized general acid/base catalyzed mechanism, where it is assumed that substrate cleavage proceeds via a single reaction channel in which buffer molecules are positioned in the correct protonation states for general acid and base catalysis, respectively, as shown in the kinetic scheme at left. S = RNA substrate. ....12

**Figure 1.6:** Idealized pH-rate profile (black) for the non-enzymatic general acid/base catalysis, given by Equation 1.7, for the mechanism shown in Figure 1.5. The buffer  $pK_a$  was set to 7, and  $k_{max}$  was set to  $0.5\ \text{min}^{-1}$ . The titrations describing the fraction of buffer in the correct protonation state for general base (blue) and general acid (red) are given by Equations 1.5 & 1.6, respectively. ....14

**Figure 1.7:** Potential mechanisms of divalent metal cation mediated Lewis-acid catalysis of RNA cleavage<sup>29</sup> (combinations of these are also possible<sup>30</sup>); chelation of one metal cation by two functional groups is also plausible. Metal aqua or hydroxide species can also mediate proton transfer in Brønsted general acid/base catalysis (for example, see Figure 1.12 – *vide infra*). ....15

**Figure 1.8:** The metal independent RNA cleavage mechanism at the active site of RNaseA.<sup>31, 35, 36</sup> .....17

**Figure 1.9:** (A) The two-metal-cation catalytic mechanism of RNA hydrolysis at the active site of RNaseH.<sup>43</sup> (B) A related, hypothetical two-metal-cation catalytic mechanism for 2'-transphosphorylation.....18

**Figure 1.10:** Tobacco Ring Spot Virus satellite RNA is replicated via a symmetric rolling circle mechanism.<sup>54</sup> Upon co-inoculation with the virus, the linear, monomeric satellite RNA (+)-strand is circularized by RNA ligase enzymes in the host cells. The circularized RNA is then used as an indefinitely repeating template from which concatemeric (-)-strand RNA is transcribed by the viral RNA polymerase. Hairpin ribozyme self-cleavage of the concatemeric (-)-strand RNA yields linear, monomeric (-)-strand RNA; the reverse reaction (hairpin self-ligation) yields circular (-)-strand RNA, which serves as a rolling circle template for transcription of concatemeric (+)-strand RNA. Hammerhead ribozyme self-cleavage, followed by host mediated ligation<sup>63</sup> completes the replication cycle by regenerating circular (+)-strand RNA. Infectious satellite virions are formed by commandeering viral coat proteins to encapsulate the linear, monomeric (+)-strand RNA. ....21

**Figure 1.11:** (A) Secondary structure representation and (B) cartoon depiction of an HDV ribozyme crystal structure (post-cleavage).<sup>65</sup> The cleavage site is marked with a red arrow. An unnatural hairpin loop sequence (indicated by the red box) was inserted into the ribozyme to provide a recognition site for the U1A protein (yellow ribbon), the binding of which facilitated crystalization.<sup>66</sup> The image in panel (B) was generated using PyMol.<sup>67</sup> .....23

**Figure 1.12:** Proposed active site mechanism by which the HDV ribozyme catalyzes RNA cleavage.<sup>64, 68</sup> .....24

**Figure 1.13:** Secondary structure representations of (A) the 8-17 and (B) 10-23 DNazymes.<sup>72</sup> Only the nucleotides essential for catalytic activity are shown; sequence variation is well tolerated in the guide sequences (bold black lines) which bind substrate via Watson-Crick pairing. Semi-conserved nucleotides are indicated as follows: R = A or G, Y = U or C. ....25

**Figure 2.1:** (A) General base catalysis by His12 in RNaseA compared to (B) His12 alkylation by 2'-deoxy-2'-bromoacetamido-uridine.<sup>96</sup> .....29

**Figure 2.2:** Illustration of a transition state for enzyme catalyzed cleavage of a bridging 5'-phosphorothioate RNA substrate. The reaction is subject to general base catalysis, but not general acid catalysis. ....32

**Figure 2.3:** (A) Illustration of the contribution of leaving group protonation to rate enhancement for S-link and O-link cleavage. Rate enhancements due to 2'-hydroxyl protonation and nonbridging oxygen protonation are assumed to be the same for S-link as for O-link cleavage (shown as in Figure 1.3). (B) Comparison of the predicted pH-rate profiles for the specific acid/base catalyzed S-link and O-link cleavage. The pH-range over which leaving group protonation is expected to contribute to rate enhancement over the background rate is shown by the red arrows.  $pK_{a1}$  and  $pK_{a2}$  are set to 13.7 and 1, respectively, for both the O-link and S-link substrates.  $pK_{a3}$  is set to -3.5 for the O-link, and -8 for the S-link substrate. ....34

**Figure 2.4:** Phosphatidyl-inositol substrates used to probe general acid in phospholipase catalyzed phosphodiester cleavage. X = O: native substrate; X = S: S-link substrate.....37

**Figure 2.5:** A mononucleotide substrate analogue with a *para*-nitro-phenolate leaving group was used to probe general acid catalysis in RNaseA.....38

**Figure 2.6:** Specific activation of S-link cleavage in the presence of soft metal cations provides strong evidence for metal cation stabilization of the leaving group in the *Tetrahymena* ribozyme.<sup>103</sup> .....40

**Figure 2.7:** Retrosynthetic disconnection of Das and Piccirilli's photo-caged S-link substrate; the modified nucleoside phosphoramidite precursors required for the automated solid phase synthesis are shown at left.<sup>68</sup> .....41

**Figure 2.8:** Illustration of the ambiguity inherent in the interpretation of pH-rate profiles and  $pK_a$  perturbation.<sup>23, 68</sup> pH-rate profiles based on distinct (A) and overlapping (B) general acid (red) and base (blue) titrations are shown (solid lines). In each case, the effect of lowering the  $pK_a$  of the more acidic titration is also illustrated (dashed lines). For clarity,  $k_{max}$  is arbitrarily set to 0.5 in all cases. Simulations were generated as described in Section 2.2.1. ....43

**Figure 2.9:** Perturbation of the general acid and base  $pK_a$ 's at the active site of RNaseA by 4F-His substitution for His12 and/or His 119.<sup>121</sup> .....45

**Figure 2.10:** Idealized simulation of the effects of 4-fluorohistidine (4F-His) substitution on pH-rate profile (black) for RNaseA catalyzed RNA cleavage: (A) 4F-His12 and 4F-His119; (B) 4F-His12 and His119 (C) His 12 and 4F-His119.  $pK_a$  values for His12 and His119 were set to 6.5;  $pK_a$  values for 4F-His12 and 4F-His 119 were set to 3.5. For clarity,  $k_{max}$  is arbitrarily set to 0.5 in all cases. Solid lines indicate the wildtype titrations and pH-rate profile; dashed lines indicate titrations and pH-rate profiles altered by mutation. Simulations were generated as described in Section 2.2.1. ....45

**Figure 2.11:** The general acid  $pK_a$  in the HDV ribozyme was perturbed downward by substitution of 6-aza-cytidine for C76.<sup>68</sup> The contribution of the general base titration to the pH-rate profile was eliminated altogether in the absence of divalent metal cations.<sup>64</sup> .....46

**Figure 2.12:** Idealized simulation of the effects upon the HDV ribozyme pH-rate profile (black) caused by: (A) general acid  $pK_a$  perturbation, where 6-aza-cytidine (or adenosine) is substituted for the native C76 general acid; and (B) the lack of general base catalysis in the absence of divalent metal cations. For general base titrations (blue),  $pK_{a\text{HB}}$  was set to 9. For general acid titrations (red),  $pK_{a\text{HA}}$  was set to 6.3 for cytidine and 6.0 for 6-aza-cytidine. For clarity,  $k_{\text{max}}$  is set to 0.5 in all cases except in the absence of  $\text{Mg}^{2+}$ , where  $k_{\text{max}}$  is set to 0.00005. Solid lines indicate wildtype titrations and pH-rate profile; dashed lines indicate titrations and pH-rate profiles for C76 mutation or the absence of  $\text{Mg}^{2+}$ . Simulations were generated as described in Section 2.2.1. ....47

**Figure 2.13:** Bromoacetylation of an internal 2'-deoxy-2'-amino-nucleotide using *N*-hydroxy-succinimidyl-bromoacetate. ....57

**Figure 2.14:** MALDI-TOF analysis of the products of the 2'-amine bromoacetylation reaction for (A) a 14-mer RNA 2'-amino-oligonucleotide and (B) a 17-mer DNA 2'-amino-oligonucleotide. Bromoacetylation adds 121 m/z units (average of <sup>79</sup>Br and <sup>81</sup>Br masses) for each 2'-amino-oligonucleotide.  $\text{Na}^+$  adducts (at increments of +22 m/z units) are prominent for both the bromoacetylated products and the unreacted 2'-amino-oligonucleotides. ....59

**Figure 2.15:** Analysis by gel shift assay of 2'-amino bromoacetylation of 5'-<sup>32</sup>P-labeled 2'-amino substrate analogue for 9<sub>25-11</sub>. Lane 1: no reaction; Lane 2: treatment with 1:1 mixture of 250 mM BrAcNHS (in DMF) and 400 mM Na-Borate (pH 8); Lane 3: treatment with 1:1 mixture of 250 mM BrAcNHS (in 1:1 formamide/DMF) and 400 mM Na-Borate (pH 8); Lane 4: sample from Lane 2 treated with 200 mM 2-aminoethanethiol; Lane 5: sample from Lane 3 treated with 200 mM 2-aminoethanethiol. Samples were analyzed by high resolution 20% d-PAGE. ....61

**Figure 2.16:** Analysis by gel shift assay of 2'-amino bromoacetylation of 5'-<sup>32</sup>P-labeled 2'-amino substrate analogue for the hairpin ribozyme. Lane 1: no reaction; Lane 2: treatment with 1:1 mixture of 250 mM BrAcNHS (in DMF) and 400 mM Na-Borate (pH 8); Lane 3: sample from Lane 2 treated with 200 mM 2-aminoethanethiol. Samples were analyzed by high resolution 20% d-PAGE. ....62

**Figure 2.17:** Structures assigned to Bands I, II, and III observed in Figures 2.15 and 2.16. ....62

**Figure 2.18:** Summary of the oligonucleotide 5'-thiophosphorylation methodology developed in this work. Rapid dephosphorylation at pH 5 to yield the 5'-thiol-oligonucleotide is diagnostic for the presence of the desired bridging 5'-thiophosphate linkage where sulphur is bonded to the 5'-carbon. ....64

**Figure 2.19:** Schematic representation of the UV-shadowing image observed after d-PAGE separation of the products of the 5'-iodination and 5'-thiophosphorylation reactions for the 9<sub>25</sub>-11 3'-product oligonucleotide. Lane A: Oligonucleotide treated with conc. NH<sub>4</sub>OH and desalted. Lane B: Oligonucleotide treated with conc. NH<sub>4</sub>OH, desalted, and treated with PNK and ATP. This lane provides an authentic standard of the 5'-O-phosphorylated 3'-product. Lane C: Oligonucleotide treated with [(PhO)<sub>3</sub>PCH<sub>3</sub>][I] in DMF, then NH<sub>4</sub>OH. Lane D: Oligonucleotide treated with [(PhO)<sub>3</sub>PCH<sub>3</sub>][I] in DMF, then Na<sub>3</sub>SPO<sub>3</sub>, then NH<sub>4</sub>OH. BΦB = bromophenol blue.....65

**Figure 2.20:** MALDI-TOF analysis of the oligonucleotides identified by d-PAGE purification in Figure 2.18. (A) d-PAGE purified Band 1. (B) Unpurified products of the 5'-iodination reaction obtained after NH<sub>4</sub>OH deprotection, Bands 1, 2, 3, and 6. (C) d-PAGE purified Band 6. (D) d-PAGE purified Band 6 treated with 25 mM NH<sub>4</sub>OAc (pH 5) at 37 °C for 1 hour. Note that only the peaks corresponding to the 5'-thiol-oligonucleotide are observed following dephosphorylation in (D); no peak corresponding to the 5'-hydroxy-oligonucleotide is visible, which indicates that the thiophosphate is bonded to the 5'-carbon exclusively via sulphur, not oxygen. The peak assignments, with their predicted and observed m/z values are summarized in Table 2.2. ....66

**Figure 2.21:** Possible mechanisms of side product formation during oligonucleotide 5'-iodination/NH<sub>4</sub>OH deprotection (based on m/z values for [M-H]<sup>-</sup> molecular ions in Figure 2.20B and Table 2.2). ....69

**Figure 2.22:** MALDI-TOF analysis of (A) the d-PAGE purified, 5'-thiophosphorylated 3'-product of the *S. mansoni* hammerhead ([M-H]<sup>-</sup> predicted m/z: 4885.8; observed m/z: 4885.9) and (B) the 5'-thiol-oligonucleotide produced by treatment with pH 5 NH<sub>4</sub>OAc buffer ([M-H]<sup>-</sup> predicted mass: 4805.8; observed mass: 4803.7). ....70

**Figure 2.23:** Ligation based synthesis of the bridging 5'-phosphorothioate (S-link) substrate developed in this work. ....73

**Figure 2.24:** Analysis by 20% TAE d-PAGE of radiolabeled oligonucleotides released upon decanting, washing, and eluting the solid phase-bound S-link ligation products. Lane 1: material decanted following binding of ligation products to solid phase; Lane 2: material washed from the solid phase with 100mM NaCl, 25 mM Na-PIPES, 10 mM EDTA; Lane 3: material washed from the solid phase with 5 mM Na-PIPES; Lanes 4 & 5: material eluted with two successive portions of aqueous 10% formamide (37 °C); Lane 6: authentic 5'-<sup>32</sup>P-labeled O-link substrate. ....74

**Figure 2.25:** Comparison of the properties of the O-link and S-link substrates for the *S. mansoni* hammerhead ribozyme. Lanes 1 & 2: no treatment. Lanes 3 & 4: 1 μM wildtype ribozyme, 2 mM MgCl<sub>2</sub>, 50 mM Na-PIPES pH 7 for 10 minutes. Lanes 5 & 6: 1 unit RNaseA, 50 mM Na-PIPES pH 7 for 10 minutes. Lanes 7 & 8: 50 mM NaOH at 60 °C for 10 minutes. Lanes 9 & 10: 5 mM Cd(NO<sub>3</sub>)<sub>2</sub> for 10 minutes. Lanes 11 & 12: 5 mM AgNO<sub>3</sub> for 10 minutes. Samples were analyzed by 20% TAE d-PAGE.....76

**Figure 2.26:** Comparison of the properties of the S-link and O-link substrates for the 9<sub>25</sub>-11 DNAzyme. Lanes 1 & 2: no treatment. Lanes 3 & 4: 5 μM 9<sub>25</sub>-11 in 200 mM NaCl, 50 mM Tris-HCl pH 8, 1 mM EDTA for 2 hours. Lanes 5 & 6: 1 unit RNaseA in 10 mM Tris-HCl pH 8 for 10 minutes. Lanes 8 to 10: (S-link) 5 mM Cd(NO<sub>3</sub>)<sub>2</sub> for 1, 3, and 10 minutes. Lane 11: (O-link) 5 mM Ag(NO<sub>3</sub>) for 10 minutes. Samples were analyzed by 20% TAE d-PAGE. ....76

**Figure 3.1:** Examples of synthetic, sequence specific RNaseA mimics that contain cationic amine and/or imidazole (or related) functionality.<sup>147, 153</sup> .....81

**Figure 3.2:** (A) The *cis*-cleaving 9<sub>25</sub>-11 DNAzyme and (B) the *trans*-cleaving 9<sub>25</sub>-11 DNAzyme in complex with its substrate. The embedded ribo-C cleavage site (red) is indicated by the arrow; the catalytic stem loop of 9<sub>25</sub>-11 (blue) is numbered from the 5'-terminus of the DNAzyme strand; cP denotes a 2',3'-cyclic phosphate. (C) Structures of the modified nucleotides incorporated into 9<sub>25</sub>-11: 8-histaminy-2'-deoxy-adenosine (<sup>his</sup>dA) and 5-(amino-allyl)-2'-deoxy-uridine (<sup>aa</sup>dU). These modified nucleotides are indicated in panel (A) as bold text **A** and **U**, respectively.....84

**Figure 3.3:** Substitutions made at the scissile ribonucleotide in the substrate analogues used in this study.....86

**Figure 3.4:** Kinetic scheme for M<sup>2+</sup> inhibition of 9<sub>25</sub>-11 self cleavage. A very low, steady state concentration of free 9<sub>25</sub>-11 is assumed. It is further assumed that the M<sup>2+</sup>-bound 9<sub>25</sub>-11 is catalytically inactive.....92

**Figure 3.5:** Qualitative survey of the effects of various metal cations on 9<sub>25</sub>-11 self cleavage activity. ....98

**Figure 3.6:** Autoradiogram which exemplifies  $\text{Hg}^{2+}$ -dependent inhibition of 9<sub>25</sub>-11 self-cleavage activity. ....98

**Figure 3.7:** Graphical analysis of  $\text{Hg}^{2+}$  (black) and  $\text{Cu}^{2+}$  (blue) inhibition of 9<sub>25</sub>-11 self-cleavage. (A) Plot of relative rate constant as a function of  $\text{Hg}^{2+}$  or  $\text{Cu}^{2+}$  concentration ( $k_{\text{cat}}$  = rate constant in the absence of any  $\text{M}^{2+}$ ). (B) Plot of  $k_{\text{obs}}^{-1}$  as a function of  $\text{Hg}^{2+}$  or  $\text{Cu}^{2+}$  concentration.  $K_d$  was determined to be  $110 \pm 9$  nM for  $\text{Hg}^{2+}$  and  $2.5 \pm 0.1$   $\mu\text{M}$  for  $\text{Cu}^{2+}$  from slope of these plots, using Equation 3.6. ....100

**Figure 3.8:** Hill plot analysis of  $\text{Hg}^{2+}$  inhibition of 9<sub>25</sub>-11 self cleavage. According to Equation 3.7, the Hill coefficient ( $n$ ) of  $\sim 1.3$  was determined from the slope of this plot.....101

**Figure 3.9:** Restoration of  $\text{Hg}^{2+}$ -inhibited 9<sub>25</sub>-11 self-cleavage activity upon the addition of  $\text{Hg}^{2+}$  chelators. For all lanes, samples were preincubated in 30  $\mu\text{M}$   $\text{Hg}^{2+}$ , 25 mM cacodylate (pH 7.5), 200 mM NaCl. Lanes 3 & 4 were rescued with 1/10<sup>th</sup> volume of 100 mM DTT, Lanes 5 & 6 rescued with 1/10<sup>th</sup> volume of 250 mM EDTA. ....102

**Figure 3.10:** MALDI-TOF analysis of the products of 9<sub>25</sub>-11 catalyzed substrate cleavage. The reaction was run to completion under multiple turnover conditions with 1 nmol of substrate and 100 pmol 9<sub>25</sub>-11. Prior to MALDI-TOF analysis, the reaction mixture was desalted, but not d-PAGE purified. The [M-H]<sup>+</sup> molecular ion assignments are detailed in Table 3.1. Peaks observed at intervals of +22 m/z units are attributed to  $\text{Na}^+$  adducts. The inset shows the spectrum obtained for an authentic sample of 2',3'-cyclic phosphate terminated 5'-product (see Section 3.2.2).....104

**Figure 3.11:** The nucleotide substitutions used in the functional group deletion variants of 9<sub>25</sub>-11 used in this study. (A) 8-histaminyl-dA (<sup>his</sup>dA) was replaced with 8-methylamino-dA or (B) 5-(amino-allyl)-dU (<sup>aa</sup>dU) was replaced with natural dT. ....107

**Figure 3.12:** pH-rate ( $\circ$ ) and pD-rate ( $\square$ ) profiles for 9<sub>25</sub>-11 catalyzed cleavage of native (O-link) substrate in standard buffer. The data were fit to a general acid/base catalysis model:  $\log k_{\text{obs}} = \log \left( k_{\text{max}} / (1 + 10^{\text{p}K_{\text{a}1} - \text{pH}} + 10^{\text{pH} - \text{p}K_{\text{a}2}} + 10^{\text{p}K_{\text{a}1} - \text{p}K_{\text{a}2}}) \right)$ .<sup>23</sup> The kinetic  $\text{p}K_{\text{a}}$  values determined were:  $7.6 \pm 0.1$  and  $8.4 \pm 0.1$  in  $\text{H}_2\text{O}$  buffers, and  $8.4 \pm 0.8$  and  $8.9 \pm 1.3$  in  $\text{D}_2\text{O}$  buffers The magnitude of the solvent kinetic isotope effect is measured by the difference in rates at the plateaus of the pH- and pD-rate profiles ( $k_{\text{H}_2\text{O}}/k_{\text{D}_2\text{O}} \sim 2$ ). The magnitude of solvent equilibrium isotope is approximated by the shift in optimum pH (+0.7 pH units on going from  $\text{H}_2\text{O}$  to  $\text{D}_2\text{O}$  solvent. ....110

**Figure 3.13:** Autoradiogram showing the d-PAGE separation of a higher molecular weight, crosslinked species following reaction of  $^{32}\text{P}$ -labeled 9<sub>25</sub>-11 with the 2'-bromoacetamide affinity label. Lane 1:  $^{32}\text{P}$ -labeled 9<sub>25</sub>-11 (no reaction). Lane 2 to 5: Reaction of  $^{32}\text{P}$ -labeled 9<sub>25</sub>-11 with substrate analogue at pH 7 for 0.5, 1, 2, 4 hours. Lane 6: Reaction for 4 hrs at pH 6. Lane 7: An aliquot of the reaction (at 4 hours) was treated with hot piperidine (15 min at 95 °C).....112

**Figure 3.14:** Effects of reaction conditions on the 9<sub>25</sub>-11 affinity labeling reaction. (A) Alkylation reactions were carried out under standard conditions (pH 7.5), in the absence of NaCl, in the presence of 0.5 mM Hg<sup>2+</sup>, and in the presence of 10 μM 2'-amino substrate analogue. All reactions were carried out in standard buffer (pH 7.5) with the noted changes. (B) Kinetic plots of 9<sub>25</sub>-11 alkylation at: pH 8.5, pH 8, pH 7.5, pH 7, pH 6.5, pH 6. (C) Alkylation reaction pH-rate profile (based on initial rates). The data were fit to  $\log k_{\text{obs}} = \log(k_{\text{max}} / (1 + 10^{\text{p}K_{\text{a}} - \text{pH}}))$ , which yielded  $\text{p}K_{\text{a}} = 7.7 \pm 0.1$  (data for pH 6 were not included in the fit, as explained in the text). ....113

**Figure 3.15:** (A) 20% d-PAGE analysis following 5'- $^{32}\text{P}$ -labeling of fragments resulting from exhaustive nuclease digestion of: unreacted 9<sub>25</sub>-11 and 2'-amino substrate analogue (Lane 1) and purified alkylated 9<sub>25</sub>-11 (Lane 2). An RNA cleavage ladder is labeled at left to help gauge the digestion fragment sizes. (B) MALDI-TOF spectrum obtained for the alkylated catalyst digestion sample analyzed in panel A. The peak assignments are given in Table 3.4 and Figure 3.17. ....116

**Figure 3.16:** MALDI-TOF spectra for two less extensively digested samples of alkylated 9<sub>25</sub>-11. Alkaline phosphatase was included in the digestion mixture for the sample in panel (B); therefore, the m/z values for these fragments reflect the absence of a 3'-phosphate. The peak assignments are given in Table 3.4 and Figure 3.17.....117

**Figure 3.17:** Structures assigned to digestion fragments that contain the alkylation linkage (based on MALDI-TOF spectra in Figures 3.15 and 3.16). Residues which originate from the DNAzyme and substrate analogue strands are coloured blue and black, respectively.....120

**Figure 3.18:** Alkylation of 9<sub>25</sub>-11 imidazole deletion variants in standard buffer at pH 7.5. (A) Autoradiogram showing d-PAGE separated products resulting from the alkylation of the indicated 9<sub>25</sub>-11 variants. (B) The fraction of DNAzyme alkylated is plotted as a function of time for wildtype 9<sub>25</sub>-11 and the A13, A19, A23, and A24 imidazole deletion variants. ....122

**Figure 3.19:** Representative data for 9<sub>25</sub>-11 catalyzed S-link substrate cleavage. (A) Autoradiogram showing time dependent S-link cleavage for wildtype 9<sub>25</sub>-11 (time points taken from 0.17 to 28 minutes). (B) Plots of showing the progress of S-link substrate cleavage for wildtype, A24, A19 and A23. ....125

**Figure 3.20:** Monophasic cleavage of the nonbridging phosphorothioate substrate in 0.5% K<sub>2</sub>CO<sub>3</sub> at 92 °C under mineral oil. The data were fit to the single exponential rate Equation 3.8, yielding the following parameters:  $P_0 = 9.4 \times 10^{-11}$ ,  $P_\infty = 0.995$ ,  $k_{\text{obs}} = 0.0107 \text{ min}^{-1}$ ,  $R^2 = 0.9983$ .....130

**Figure 3.21:** Comparison of native substrate and phosphorothioate substrate (diastereomeric mixture) cleavage kinetics for wildtype 9<sub>25</sub>-11 and variants in which individual <sup>aa</sup>dU residues are replaced with dT. All native substrate cleavage data were fit to monophasic Equation 3.8; phosphorothioate substrate cleavage data were fit to both Equation 3.8 (red), and biphasic Equation 3.9 (black). The constituent cleavage phases are shown as dashed lines for wildtype cleavage of the phosphorothioate substrate mixture.  $R^2$  values for all fits are given in Table 3.6, and kinetic parameters are given in Table 3.7. All reactions were performed in standard buffer at pH 7.5. ....131

**Figure 3.22:** Possible enzymatic mechanisms for acid/base catalyzed cleavage of phosphoester linkages by 2'-transphosphorylation. (A) Phosphotriester cleavage, (B) phosphodiester cleavage via a “triest-er-like” mechanism,<sup>228</sup> and (C) and phosphodiester cleavage via a “classical” dianionic mechanism.<sup>229</sup> .....138

**Figure 3.23:** Catalytic mechanism for 9<sub>25</sub>-11 proposed based upon the data presented in this chapter. The role depicted for A13 is highly speculative. ....140

**Figure 4.1:** Secondary structure diagrams of the *trans*-cleaving (A) HH16 (minimal)<sup>211</sup> and (B) *S. mansoni* (extended)<sup>268</sup> hammerhead ribozymes that were used in this study. The nucleotides in the conserved catalytic core are numbered according to convention.<sup>269</sup> The substrate cleavage sites are indicated with red arrows. The unpaired loops involved in tertiary interactions (unique to extended hammerheads) are indicated by the red box. ....144

**Figure 4.2:** Crystal structures of (A) the *S. mansoni*<sup>270</sup> and (B) a minimal hammerhead<sup>249</sup> ribozyme. The ribozyme and substrate strands are coloured orange and teal respectively; the nucleotides of interest in this study are colour coded as indicated; the scissile substrate nucleotide is coloured white. Close up images are focused on the nucleotides of interest in this study for (C) the *S. mansoni* and (D) the minimal hammerheads ribozymes. Images were generated using PyMol.<sup>67</sup> .....145

**Figure 4.3:** Catalytic mechanism for hammerhead ribozymes which has been proposed based on the *S. mansoni* crystal structure and subsequent computational studies.<sup>270, 284-287</sup> .....149

**Figure 4.4:** Alkylation of the HH16 (minimal) and the *S. mansoni* (extended) hammerhead ribozymes (5'-<sup>32</sup>P labeled) with both RNA and DNA 2'-bromoacetamide substrate analogues in 50 mM MgCl<sub>2</sub>, 100 mM NaCl, 50 mM Tris-HCl pH 7.5 for 24 hrs. The alkylation bands characterized in this study (I and II) are indicated. Lane 1: HH16 ribozyme + DNA substrate analogue. Lane 2: HH16 ribozyme + RNA substrate analogue. Lane 3: Co-spot of unreacted HH16 and *S. mansoni* ribozymes. Lane 4: *S. mansoni* ribozyme + DNA substrate analogue. Lane 5: *S. mansoni* ribozyme + RNA substrate analogue. Samples were analyzed by 10% d-PAGE. Rz = ribozyme.....158

**Figure 4.5:** Illustration explaining the interpretation of alkaline footprinting patterns with 5'-<sup>32</sup>P-labeled ribozyme. RNA cleavage sites and the corresponding bands they produce in d-PAGE analysis are numbered as indicated.....160

**Figure 4.6:** (A) Alkaline footprinting analysis with 5'-labeled *S. mansoni* hammerhead. Lane 1: Ribozyme treated with 0.5% K<sub>2</sub>CO<sub>3</sub>; Lane 2: Ribozyme treated with RNase T1; Lane 3: Band II treated with 0.5% K<sub>2</sub>CO<sub>3</sub>; Lane 4: Band I treated with 0.5% K<sub>2</sub>CO<sub>3</sub>. (B) Quantitative analysis of autoradiography data in panel (A). .....162

**Figure 4.7:** Illustration explaining the interpretation of alkaline footprinting patterns with 3'-<sup>32</sup>P-labeled ribozyme. RNA cleavage sites and the corresponding bands they produce in d-PAGE analysis are numbered as indicated.....164

**Figure 4.8:** Secondary structure compression near G10 prevents clear sequence assignment in standard d-PAGE analysis (B) of footprinting experiments with 3'-labeled ribozyme. The application of higher power (100 W) during electrophoresis (C) prevents formation of the hairpin loop responsible for the compression observed in panel (B). The sequence region of interest is shown in panel (A) where the RNase T1 cleavage sites are indicated by dashed red lines. ....165

**Figure 4.9:** (A) Alkaline footprinting analysis with 3'-labeled *S. mansoni* hammerhead. Lane 1: Band II treated with 0.5% K<sub>2</sub>CO<sub>3</sub>; Lane 2: Ribozyme treated with 0.5% K<sub>2</sub>CO<sub>3</sub>; Lane 3: Ribozyme treated with RNase T1; Lane 4: Band I (wildtype ribozyme) treated with 0.5% K<sub>2</sub>CO<sub>3</sub>; Lane 5: Band I (A6U ribozyme) treated with 0.5% K<sub>2</sub>CO<sub>3</sub>. (B) Quantitative analysis of autoradiography data in panel (A). .....167

**Figure 4.10:** Aniline catalyzed cleavage at abasic sites produces 5'-phosphorylated 3'-<sup>32</sup>P-labeled fragments, whereas RNase T1 or alkaline cleavage produces 5'-hydroxy 3'-<sup>32</sup>P-labeled fragments. Subsequent treatment of both samples with polynucleotide kinase and unlabeled ATP synchronizes the phosphorylation states of all fragments. ....170

**Figure 4.11:** Comparison of aniline and alkaline footprinting patterns for Bands I and II (3'-labeled wildtype ribozyme). Lane 1: Band I treated with 0.5 M anilinium acetate; Lane 2: Band I treated with 0.5% K<sub>2</sub>CO<sub>3</sub>; Lane 3: Ribozyme treated with RNase T1; Lane 4: Ribozyme treated with K<sub>2</sub>CO<sub>3</sub>; Lane 5: Band II treated with K<sub>2</sub>CO<sub>3</sub>; Lane 6: Band II treated with 0.5 M anilinium acetate. To facilitate direct comparison of electrophoretic mobilities, all samples were treated with polynucleotide kinase and ATP to synchronize the 3'- and 5'-phosphorylation states before d-PAGE analysis.....171

**Figure 4.12:** Close up view of anilinium acetate footprinting patterns of Band I for the indicated 3'-labeled mutant ribozymes.....172

**Figure 4.13:** Reactions observed by Küpfer and Leumann upon alkaline treatment of abasic sites in RNA.<sup>295</sup> .....173

**Figure 4.14:** (A) Alkaline footprinting analysis of Band I (5'-labeled wildtype ribozyme) with and without subsequent polynucleotide kinase catalyzed 3'-dephosphorylation of all fragments. The red asterisk marks the anomalous cleavage band. (B) Quantitative analysis of autoradiography data in panel (A). .....175

**Figure 4.15:** Candidate structures considered for the unidentified cleavage band in footprinting patterns of Band I. Black coloured structures are those which result from alkaline cleavage of the ribozyme (at right without PNK treatment, at left with PNK treatment). The red structures are ruled out based on their predicted electrophoretic mobility and/or the results of mutation experiments (see text). The green structure is assigned to the unidentified cleavage band. Fragment structures are arranged according to their predicted electrophoretic mobilities.....177

**Figure 4.16:** (A) Closeup view of the alkaline footprinting pattern of Band I for the indicated mutant ribozymes (5'-labeled). The red asterisk marks the unidentified cleavage band. (B) Quantitative analysis of autoradiography data in panel (A). .....179

**Figure 4.17:** Alkylation reaction time courses for the indicated 5'-<sup>32</sup>P-labeled *S. mansoni* hammerhead ribozymes in 50 mM Tris-HCl pH 8, 100 mM NaCl, 50 mM MgCl<sub>2</sub>. “WT + 2'-NH<sub>2</sub>” indicates that the reaction contained 10 μM 2'-amino substrate analogue, in addition to the 2'-bromoacetamide affinity label. Time points were taken to 43 hours in each case.....181

**Figure 4.18:** (A) Autoradiograms showing time dependent hammerhead alkylation in 50 mM Tris-HCl pH 8.2, 100 mM NaCl, at various  $[Mg^{2+}]$ . The same time points were taken in each reaction out to 3.8 hours. Plots of time dependent alkylation for (B) Band I and (C) Band II at  $[Mg^{2+}] = 0$  mM, 0.5 mM, 1 mM, 5 mM, 10 mM, and 25 mM. (D) Plot of the  $[Mg^{2+}]$ -dependence of the initial rate constants for Band I and Band II formation in the wildtype hammerhead. The 0 mM  $Mg^{2+}$  reaction contained 5 mM EDTA, and all reactions contained. The data for Band II (G12 alkylation) were fit to Equation 4.1, which returned  $k_{max} = 0.049$  hr<sup>-1</sup>,  $[Mg^{2+}]_{1/2} = 47$  mM, and a Hill-type coefficient  $n = 1.05$ . .....183

**Figure 4.19:** Autoradiograms showing time dependent alkylation of the (A) wildtype, and (B) G12A hammerhead ribozymes in 50 mM buffer (at the indicated pH values), 100 mM NaCl, 50 mM  $MgCl_2$ . For each ribozyme the same time points were taken for all reactions (out to 50 hours for wildtype and 43 hours for G12A). (C) Plots of time dependent alkylation for Band II at pH = 6.5, 7, 7.5, 8, 8.5, and 9. The pH-rate profiles are shown for alkylation of the (D) wildtype and (E) G12A hammerhead ribozymes. The logarithm of the initial rate constants (hr<sup>-1</sup>) for the formation of Band I and Band II are plotted as a function of pH. The idealized pH-rate profile for alkylation of anionic N1 of G12 is simulated according to  $k_{obs} = k_{max}/(1+10^{pK_a-pH})$ , where  $\log(k_{max} WT) = \log(k_{max} G12A) = -1.1$  and  $pK_a = 8.4$  for N1 of G12. ....185

**Figure 4.20:** An example of biphasic kinetics encountered for S-link cleavage by the *S. mansoni* hammerhead ribozyme and mutants. Data for single turnover cleavage of the S-link substrate by wildtype ribozyme are shown (reaction conditions: 2 mM  $MgCl_2$ , 100 mM NaCl, 50 mM Na-PIPES pH 7). (A) The full data set clearly does not fit well ( $R^2 = 0.980$ ) to a monophasic model (Equation 4.2). (B) A truncated data set fit adequately to a monophasic model ( $R^2 = 0.996$ ) (the longest time points are removed while still preserving enough data to accurately fit the parameters). (C) The autoradiography data used to generate the plots in (A) and (B). Time points (in minutes) analyzed were: 0, 0.22, 0.33, 0.47, 0.58, 0.71, 0.85, 1.12, 1.28, 1.50, 1.75, 2.00, 2.50, 3.00, 3.75, 4.50. ....193

**Figure 4.21:** The “base paired” (BP) hammerhead ribozyme referred to in Table 4.2. The altered sequence is highlighted by the red box, and permits continuous base pairing with the substrate (more like a minimal hammerhead). .....196

**Figure 4.22:** pH-rate profiles for O-link substrate cleavage by the wildtype, 2'-deoxy-G8, and 2'-OMe-G8 *S. mansoni* hammerhead ribozymes in the presence of (A) 1 mM  $Mg^{2+}$  or (B) 1 mM  $Cd^{2+}$ . All reactions contained 100 mM NaCl and 50 mM Buffer. Data were fit to a general acid/base catalysis model according to  $k_{obs} = k_{max} / (1 + 10^{pK_{a1}-pH} + 10^{pH-pK_{a2}} + 10^{pK_{a1}-pK_{a2}})$ .<sup>50</sup> For  $Cd^{2+}$  containing reactions, data for pH >8 were omitted from the fits as 1 mM  $Cd^{2+}$  is prone to precipitation above pH ~8. Error bars indicated standard deviations of the data points. ....199

**Figure 4.23:** Possible mechanisms of general acid catalysis involving both the G8 2'-hydroxyl and a  $Mg^{2+}$  cofactor. ....203

**Figure 4.24:** Simulation of the effects on the pH-rate profile for O-link substrate cleavage caused by perturbation of the general acid  $pK_a$ . The general base titration is coloured blue, the general acid titration is coloured red, and the observed rate constant is coloured black. (A) Substitution of  $Cd^{2+}$  for  $Mg^{2+}$  dramatically lowers the  $pK_a$  of the general acid. (B) Presumed substitution of a  $Mg^{2+}$ -bound water ligand for the G8 2'-hydroxyl slightly increases the  $pK_a$  of the general acid in the dG8 mutant relative to wildtype. (C) The dG8 mutation similarly raises the general acid  $pK_a$  relative to wildtype in the presence of  $Cd^{2+}$ . The general base titration is invariant in all cases ( $pK_a$  set to 8). For clarity,  $f_{max}$  was set to 0.1 for wildtype and 0.001 for dG8. Simulations were generated as described in Section 2.2.1.....207

**Figure 4.25:** Possible general acid catalysis mechanisms for (A) wildtype and (B) dG8 hammerhead ribozymes. ....208

**Figure 5.1:** Secondary structure representation of the *trans*-cleaving EH4 hairpin ribozyme in complex with substrate.<sup>315</sup> The ribozyme strand (black) is numbered from 5' to 3' starting from A<sub>1</sub>; ribozyme residues particularly crucial for catalytic activity are numbered. In the substrate strand (blue), the cleavage site is indicated by the red arrow. Canonical Watson-Crick base pairs are indicated by the black bars; non-canonical base pairs are indicated by black dots. The reverse transcription primer binding site corresponds to the ribozyme sequence inside the dashed green box (see Section 5.2.4).....211

**Figure 5.2:** Crystal structure of a hairpin ribozyme bound to a vanadate-triester transition state analogue.<sup>319</sup> The ribozyme and substrate strands are coloured teal and orange, respectively; the U1A RNA binding protein is coloured green; the scissile substrate nucleotide is coloured white; and the G8 and A38 ribozyme residues are colour coded as indicated. The full structure (A) is depicted along with a cartoon stick and ribbon model (B). A close up view of the active site is also shown (C). Images were generated from protein data bank (pdb) files using PyMol.<sup>67</sup> .....213

**Figure 5.3:** Hydrogen bond interactions (dashed red lines) involving G8 and A38, which were identified in the crystal structure of the hairpin ribozyme bound to a vanadate transition state analogue.<sup>319</sup> .....214

**Figure 5.4:** Either of two kinetically ambiguous mechanisms can account for the change in pH-rate profile caused substitution of 2,6-diaminopurine for G8 in the hairpin ribozyme. (A) Mechanism requiring protonated G8 and A38, and specific base catalysis.<sup>324-326</sup> (B) Mechanism requiring deprotonated G8 and protonated A38.<sup>23</sup> pH-rate profiles are shown in black; solid lines correspond to wildtype and dashed lines to the G8(2,6-diaminopurine) mutant. Titrations are colour green for G8 and diaminopurine, orange for A38, and blue for the 2'-hydroxyl. The following  $pK_a$  values were used: 9 for G8, 6 for 2,6-diaminopurine, 5 for A38, and 13 for the substrate 2'-hydroxyl. For clarity,  $k_{max}$  was arbitrarily set to  $0.5 \text{ min}^{-1}$  in all cases. Simulations were generated as described in Section 2.2.1. ....216

**Figure 5.5:** Observation of higher molecular weight, crosslinked species upon reaction of <sup>32</sup>P-labeled hairpin ribozymes with the 2'-bromoacetamido affinity label. The time point and fraction alkylated are indicated for each lane for alkylation of (A) wildtype, (B) G8A, and (C) 7-deaza-dG8 ribozymes, each in 50 mM MgCl<sub>2</sub>, 50 mM Na-cacodylate pH 7.5.....225

**Figure 5.6:** Reverse transcription footprinting assay (using 5'-<sup>32</sup>P-labeled primer) to locate the alkylation linkage on the hairpin ribozyme. Lanes 1-4: sequencing by dideoxy termination of (non-alkylated) hairpin ribozyme template. The dideoxy nucleotide (ddX) triphosphate included in each reaction is indicated, along with the complementary nucleotide in the RNA template sequence. Lanes 5 & 6: Reverse transcription of alkylated G8A and wildtype ribozymes respectively.....228

**Figure 5.7:** (A) Alkaline footprinting analysis with 5'-labeled hairpin ribozyme. Lane 1: Untreated alkylated ribozyme; Lane 2: Untreated ribozyme; Lane 3: Alkylated ribozyme treated with 0.5% K<sub>2</sub>CO<sub>3</sub>; Lane 4: Ribozyme treated with 0.5% K<sub>2</sub>CO<sub>3</sub>; Lane 5: Ribozyme treated with RNase T1. (B) Quantitative analysis of autoradiography data in panel (A).. ....230

**Figure 5.8:** MALDI-TOF spectrum obtained for nuclease digested samples of alkylated hairpin ribozyme. The region of the spectrum from  $m/z = 930$  to  $1110$  is magnified in the inset.....232

**Figure 5.9:** Structures assigned to the digestion fragments observed by MALDI-TOF analysis in Figure 5.8 whose  $m/z$  values are consistent with the presence of the alkylation linkage.....234

**Figure 5.10:** Kinetic plots of hairpin ribozyme alkylation under various conditions and or for ribozyme mutants. Unless otherwise stated, reactions were in 50 mM Na-Cacodylate pH 7.5, 50 mM MgCl<sub>2</sub>, for wildtype, dG8c<sup>7</sup>, G8A, C25A, Wildtype in the presence of unreactive 2'-NH<sub>2</sub> substrate analogue, and Wildtype in the absence of Mg<sup>2+</sup>. ....237

**Figure 5.11:** (A) Plots of the progress of wildtype hairpin ribozyme alkylation in 50 mM MgCl<sub>2</sub> and 50 mM buffer pH 7.5, pH 8.0, pH 8.5, and pH 9.0. (B) Logarithmic plot of the pH-dependence of the reaction endpoint ( $P_{\infty}$ ), the first order alkylation rate constant determined by fitting the data in Panel A, and the initial rate constant, estimated as described in the Table 5.1 footnotes. For comparison, a log-linear plot with slope of 1 is included (dashed line). .....240

**Figure 5.12:** The two limiting cases proposed in the literature<sup>23, 158, 324</sup> for the role hairpin G8 (see Figure 5.4A & B) could be rapidly interconverting with the aid of a specific or general base prior to nucleophilic attack by the 2'-oxygen. The pK<sub>a</sub>'s for the protonation sites of interest are indicated in blue text. ....244

## LIST OF EQUATIONS

Equation 1.1: Fraction present in basic form .....	7
Equation 1.2: Fraction present in acidic form.....	7
Equation 1.3: Definition of the rate enhancement factor (“enh”).....	7
Equation 1.4: Calculation of $k_{\text{obs}}$ for specific acid/base catalysis .....	8
Equation 1.5: Fraction of general base present in deprotonated form .....	12
Equation 1.6: Fraction of general acid present in protonated form .....	13
Equation 1.7: Calculation of $k_{\text{obs}}$ for general acid/base catalysis.....	13
Equation 2.1: Calculation of $k_{\text{obs}}$ for general acid/base catalysis.....	49
Equation 2.2: Fraction of general acid present in protonated form .....	49
Equation 2.3: Fraction of general base present in deprotonated form .....	49
Equation 2.4: Dependence of $k_{\text{obs}}$ on one basic and two acidic titrations.....	50
Equation 3.1: Integrated first order rate equation .....	91
Equation 3.2: Steady state approximation for 9 <sub>25</sub> -11 inhibition .....	92
Equation 3.3: Mass balance for 9 <sub>25</sub> -11 inhibition .....	92
Equation 3.4: Expression for total uncleaved 9 <sub>25</sub> -11 .....	92
Equation 3.5: Rate equation for 9 <sub>25</sub> -11 inhibition.....	93
Equation 3.6: Reciprocal rate equation used in Figure 3.7 .....	93
Equation 3.7: Hill plot equation used in Figure 3.8.....	93
Equation 3.8: Monophasic integrated first order rate equation.....	94

Equation 3.9: Biphasic integrated first order rate equation .....	94
Equation 4.1: $Mg^{2+}$ dependence equation used in Figure 4.18D .....	152
Equation 4.2: Integrated first order rate equation .....	155

## LIST OF ABBREVIATIONS

$^{32}\text{P}$	Phosphate containing phosphorus-32
4F-His	4-Fluoro-histidine
$^{\circ}\text{C}$	Degrees celsius
$[\text{Mg}^{2+}]_{1/2}$	$\text{Mg}^{2+}$ concentration at which the rate is half-maximal
$[\text{M-H}]^{-}$	Singly deprotonated molecular ion
Å	Angstrom ( $1 \cdot 10^{-10}$ metre)
$\mu\text{Ci}$	Microcurie
$\mu\text{L}$	Microlitre ( $1 \cdot 10^{-6}$ litre)
$\mu\text{M}$	Micromolar ( $1 \cdot 10^{-6}$ mole/litre)
A	Adenosine
AcOPh	Phenoxyacetyl-
AH	A general acid catalyst in its functional form
Alk	Alkylated ribozyme
AnAc	Anilinium acetate
Arg	Arginine
ATP	Adenosine-5'-triphosphate
$^{aa}\text{dU}$	5-(Amino-allyl)-2'-deoxy-uridine
$^{aa}\text{dUTP}$	5-(Amino-allyl)-2'-deoxy-uridine-5'-triphosphate
B:	A general base catalyst in its functional form
BΦB	Bromophenol blue
BP	Base paired hammerhead ribozyme mutant
BrAcNHS	<i>N</i> -hydroxy-succinimidyl-bromoacetate
C	Cytidine
$c^7$	<i>N</i> 7-deaza
cDNA	Complementary DNA produced by reverse transcription
cP	2',3'-Cyclic phosphodiester
cpm	Counts per minute
d	2'-Deoxy-
d-PAGE	Denaturing polyacrylamide gel electrophoresis (7M Urea)
dATP	2'-Deoxy-adenosine-5'-triphosphate
dCTP	2'-Deoxy-cytidine-5'-triphosphate
ddATP	2',3'-Dideoxy-adenosine-5'-triphosphate
ddCTP	2',3'-Dideoxy-cytidine-5'-triphosphate
ddGTP	2',3'-Dideoxy-guanosine-5'-triphosphate
ddTTP	2',3'-Dideoxy-thymidine-5'-triphosphate
dGTP	2'-Deoxy-guanosine-5'-triphosphate
dTTP	Thymidine-5'-triphosphate
DMF	Dimethylformamide
DMT	Dimethoxytrityl-
DNA	Deoxyribonucleic acid
DTT	Dithiothreitol
dTTP	2'-Deoxy-thymidine-5'-triphosphate
EDTA	Ethylenediamine-tetra-acetic acid
ESR	Electron spin resonance

<i>f</i>	Fraction
G	Guanosine
$H_0$	Hammett acidity function
HDV	Hepatitis delta virus
HEPES	<i>N</i> -2-hydroxyethyl-piperazine- <i>N'</i> -2-ethane-sulphonic acid
His	Histidine
<sup>his</sup> dA	8-Histaminyl-2'-deoxy-adenosine
<sup>his</sup> dATP	8-Histaminyl-2'-deoxy-adenosine-5'-triphosphate
hr <sup>-1</sup>	Per hour
$K_a$	Thermodynamic acid dissociation constant
kcal	Kilocalorie
$k_{cat}$	First order rate constant for the rate-limiting step
$K_d$	Thermodynamic dissociation constant
$K_m$	Michaelis constant
$k_{max}$	Maximum rate constant
$k_O$	Observed first order rate constant for native substrate cleavage
$k_{obs}$	Observed first order rate constant
$k_{off}$	Dissociation rate constant
$k_{on}$	Association rate constant
$k_S$	Observed first order rate constant for phosphorothioate (bridging or nonbridging) substrate cleavage
$K_{sp}$	Solubility product constant
$k_{uncat}$	Rate constant for uncatalyzed reaction
log	Logarithm (base 10)
Lys	Lysine
m/z	Mass to charge ratio
M	Molar (mole/litre)
M <sup>-1</sup>	Per molar
M <sup>2+</sup>	Divalent metal cation
MALDI	Matrix assisted laser desorption of ions
MES	2-( <i>N</i> -morpholino)-ethane-sulphonic acid
min <sup>-1</sup>	Per minute
mL	Millilitre
mM	Millimolar ( $1 \cdot 10^{-3}$ mole/litre)
MOPS	3-( <i>N</i> -morpholino)-propane-sulphonic acid
mRNA	Messenger RNA
<i>n</i>	Hill coefficient
NaOMe	Sodium methoxide
NHAcBr	Bromoacetamido-
nmol	Nanomole
nM	Nanomolar ( $1 \cdot 10^{-9}$ mole/litre)
NMR	Nuclear magnetic resonance
O-link	Native ribophosphodiester substrate
OMe	Methoxy-
P	Phosphate
<i>P</i>	Fraction converted to product at time <i>t</i>

$P_0$	Fraction converted to product at time zero
$P_\infty$	Fraction converted to product at the reaction endpoint
pCp	Cytidine-3',5'-bisphosphate
pD	$-\log [D_3O^+]$
pH	$-\log [H_3O^+]$
PIPES	Piperazine- <i>N,N'</i> -bis(2-ethane-sulphonic acid)
$pK_a$	$-\log K_a$
pmol	Picomole
PNA	Peptide nucleic acid
PNK	Polynucleotide kinase
r	Ribo-
RNA	Ribonucleic acid
RNase	Ribonuclease
RT	Reverse transcription
Rz	Ribozyme
S-link	Bridging 5'-phosphorothioate
SELEX	Systematic evolution of ligands by exponential enrichment
T	Thymidine
$t$	Time
TAE	Tris-acetate/EDTA buffer (40 mM Tris-acetate and 1 mM EDTA pH 6.7)
TBDMS	Tertiary-butyl-dimethyl-silyl-
TBE	Tris-borate/EDTA buffer (89 mM Tris-borate and 2 mM EDTA, pH 8.3)
Tr	Trityl-
Tris	Tris(hydroxymethyl)-amino-methane
tRNA	Transfer RNA
TOF	Time of flight
U	Uridine
UTR	Untranslated region in an mRNA transcript
UV	Ultraviolet
W	Watt
WT	Wildtype
X	Ribocytidine
X(sP)	Ribocytidine with 3'-nonbridging phosphorothioate (mixture of diastereomers)
$Y_1$	2',5'-Dideoxy-5'-mercapto-guanosine
$Y_2$	2',5'-Dideoxy-5'-mercapto-cytidine
Z	2'-Deoxy-2'-amino-cytidine

## ACKNOWLEDGEMENTS

I would like to first thank my family for their love and support through this long process. Their support has made it possible for me to follow a path in scientific education chosen not for its tangible benefits (financial or otherwise), but because it is my way of contributing to human endeavour, and simply the right thing for a hopelessly curious, analytical mind to do. My love and thanks go to: my parents Mrs. Joan Thomas and Mr. Kevin Thomas; my grandparents Mrs. Beryl Henderson, Mr. Bill Henderson, and Mrs. Ellen Thomas; and my sisters Ms. Megan Thomas and Ms. Brittany Thomas.

I would like to express my gratitude to my supervisor, Prof David M. Perrin, for his hard work and sacrifice to provide a well funded, stimulating research environment. I also thank Prof. Perrin for his especially keen interest in helping to decipher a complex kinetic mechanism. This was an important, early learning experience for me. Prof. Perrin deserves special recognition for then allowing me to pursue projects suited to my own scientific interests, despite the fact that these diverged from his own core research interests, and were not specifically funded. By allowing me to develop projects on my own, and see them through to fruition, Prof. Perrin has given me an extraordinary opportunity to develop the skills necessary to continue independently in research. Finally, I thank Prof. Perrin for his openness and understanding, which helped me in times of personal difficulty.

I also acknowledge my undergraduate research supervisor Prof. Michael C.L. Gerry for taking a sincere interest in my success and well-being. In my formative research experience as an undergraduate, Prof. Gerry set an exceptional example as both a meticulous, respectful scientist and a revered teacher. This example has served as the basis for my scientific and ethical values. Most importantly, from my experience working with Prof. Gerry, I learned to appreciate the beauty and importance of a rigorous understanding of “how things work” at their most fundamental level.

I am also grateful to many life-long friends such as Mr. Ryan Schopman and his family, Mr. Brent Marley, Mr. Kevin Roberge, Ms. Stacy McLennan, and Mr. Tony Chico Stogiannos, and many others (too many to thank individually here – you know

who you are). These kind souls have always been there to make me feel better and to help me balance a life in science with the simple pleasures that truly make life sweet: riding waist-deep pow on the gnarl factor (after an appropriate safety discussion, of course), going to see Mad Caddies or The Slackers for the 12<sup>th</sup> time, or playing a round at Hackers' Haven, to name a few. I am also grateful to several coworkers with whom I have become close friends: Prof. Stephen A. Cooke, Dr. Marcel Hollenstein, Ms. Alison Palmer, Mr. Jonathan Pellicelli, and Mr. Béchara Saab. I also thank members of the Perrin Lab for kindness, understanding, and good times, especially Dr. Ali Asadi (Chief), Mr. Antoine Blanc, Mr. David Deitrich (Deetch), Mr. Benjamin Haffemayer, Dr. Curtis Harwig (Activator), Mr. Chris Hipolito (Hippo), Mr. Curtis Lam (Clam), Dr. Leonard Lermer, Ms. Ying Li (Yingster), and Dr. Jon May (Minty).

Several UBC faculty members deserve recognition for kindly taking the time to provide useful scientific advice and discussion over the years: Prof. Derek Gates, Prof. George Mackie, and Prof. Glen Sammis. In particular, I would like to thank Prof. Pierre Kennepohl for carefully reading my thesis prior to submission, and Prof. Stephen G. Withers for taking time to share his enzymology expertise. I also acknowledge Prof. Subha R. Das (Carnegie Mellon University) and Prof. Andrew J. Bennett (Simon Fraser University) for helpful discussions. Prof. Chris Orvig also deserves to be acknowledged for his help as graduate advisor. I feel that Prof. Orvig deserves credit for performing this duty with the utmost professionalism, fairness, and care.

I also acknowledge the help of numerous chemistry department staff members who have all made life easier for me as a graduate student. In particular, I acknowledge Mr. Marshal Lapawa and Ms. Suzanne Perry for great help with mass spectrometry experiments, Ms. Sheri Harbour for help with administrative issues, and the talented staff of the mechanical and electronics shops for always having a solution for a broken instrument. I would also like to make special mention of Mr. Jon Ellis: it is rare that one has the pleasure of dealing with someone who is not only good natured, but who does their job with such stunning efficiency, precision, and professionalism.

**Co-authorship statement:** Prof. David M. Perrin is acknowledged for the design of the research program involving the 9<sub>25</sub>-11 DNAzyme described in Sections 3.3.1, 3.3.2, & 3.3.3. Prof. Perrin deserves particular credit for forwarding the idea for the 9<sub>25</sub>-

11 affinity labeling experiments and for significant contribution to data analysis and interpretation in the study of 9<sub>25</sub>-11 kinetics and inhibition. Prof. Perrin also wrote the manuscript describing Hg<sup>2+</sup>-inhibition of 9<sub>25</sub>-11 (Thomas, Ting, Perrin, *OBC* **2004**, 2, 307-312). Dr. Leonard Lermer and Dr. Yoanne Roupioz are acknowledged for synthesizing the monomer phosphoramidites used in the preparation of 9<sub>25</sub>-11. Mr. Jungki Yoon is acknowledged for assisting with some of the mechanistic characterization of 9<sub>25</sub>-11. Mr. Christopher Hipolito is acknowledged for synthesizing <sup>his</sup>dATP. Dr. Richard Ting is acknowledged for performing kinetic experiments and data analysis, and helping to write the manuscript describing 9<sub>25</sub>-11 kinetics, in collaboration with Prof. Perrin and me (Ting, Thomas, Lermer, Perrin *NAR* **2004**, 32, 6660-6672).

I performed and analyzed the experiments described in this thesis (an exception is noted for the first entry of Table 3.2, which was determined by Dr. Ting). I also wrote first drafts and worked on the final drafts of the manuscripts describing my studies of general acid/base catalysis in the 9<sub>25</sub>-11 DNAzyme and the hairpin and hammerhead ribozymes (Thomas & Perrin, *JACS* **2006**, 128, 16540-16545; Thomas & Perrin, *JACS* **2008**, 130, 15467-15475; Thomas & Perrin, *JACS* **2009**, 131, 1135-1143; Thomas, Yoon, Perrin, *JACS* **2009**, 131, 5648-5658). Prof. Perrin is acknowledged as co-author of these works, and made important intellectual contributions to experimental design, analysis, and manuscript writing.

# **CHAPTER 1: GENERAL INTRODUCTION TO THE CHEMISTRY AND CATALYSIS OF RNA CLEAVAGE**

## **1.1 PREFACE**

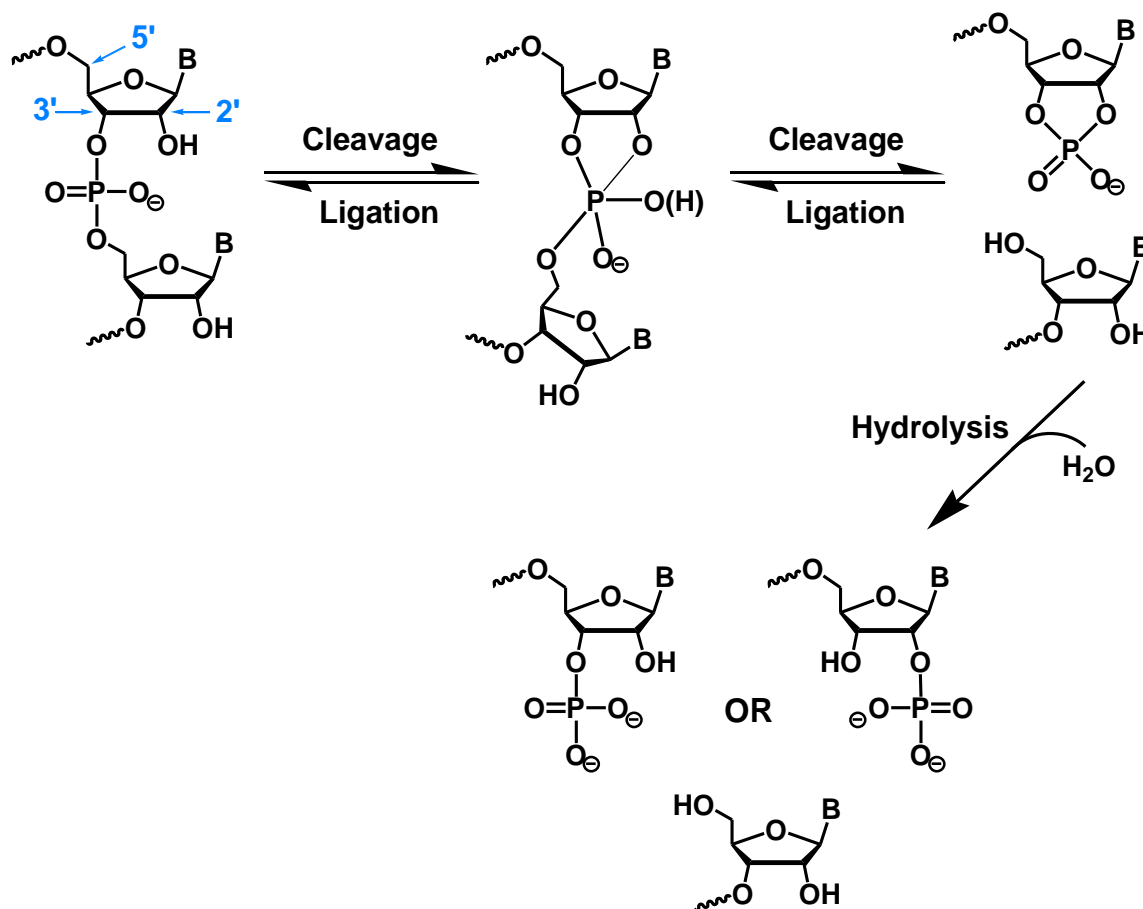
The unifying theme of the experiments reported in this thesis concerns the use of chemical probes to investigate the catalytic mechanisms of RNA cleaving ribozymes and DNAzymes. This chapter offers a general introduction, beginning with a brief discussion of the basic chemistry of RNA cleavage and hydrolysis. A discussion of non-enzymatic catalysis follows, which exposes the mechanistic strategies available to RNA cleavage catalysts in general. Next, a brief discussion of two well understood RNA cleaving enzymes illustrates the implementation of these catalytic strategies in two chemically distinct active site mechanisms. This chapter closes with a general introduction to RNA cleaving ribozymes and DNAzymes. Section 2.1 offers an introduction to the specific chemical probes that are used in this thesis to investigate the catalytic mechanisms of three nucleic acid catalysts (in Chapters 3, 4, and 5).

## **1.2 THE CHEMISTRY OF RNA CLEAVAGE**

In all known forms of life, ribonucleic acid (RNA) is the central intermediary in decoding genetic information, which is stored permanently in the sequence of deoxyribonucleic acid (DNA).<sup>1</sup> The *in vivo* stability and processing of nucleic acids depends upon the chemistry of the phosphodiester linkages that join the monomer nucleotides in RNA and DNA polymers. The presence of the 2'-hydroxyl group

drastically alters the cleavage chemistry (and stability) of RNA relative to DNA. That is, RNA cleavage can proceed via facile intramolecular nucleophilic attack of a 2'-oxygen on an adjoining phosphodiester linkage (Figure 1.1), whereas DNA cleavage must proceed hydrolytically via intermolecular nucleophilic attack of hydroxide or water. In the case of RNA cleavage, a short-lived penta-coordinate phosphorane intermediate forms,<sup>2,3</sup> and then collapses by expelling the 5'-hydroxyl leaving group to yield a 2',3'-cyclic phosphodiester terminated product. Under physiological conditions, the half-lives for non-enzymatic (background) phosphodiester cleavage in RNA and DNA are estimated to be on the order of ~1 year<sup>4</sup> and ~100000 years,<sup>5</sup> respectively. These cleavage properties appear to have provided the basis for the evolutionary differentiation of the biological roles of RNA and DNA: given its remarkable kinetic stability, DNA is more suitable for long-term information storage, whereas the predisposition of RNA toward cleavage makes it more suitable for the temporary storage and transfer of information.

**Figure 1.1:** RNA cleavage by 2'-transphosphorylation yields 5'-hydroxy and 2',3'-cyclic phosphodiester terminated products, the latter of which is subsequently hydrolyzed irreversibly to yield 2'- and 3'-phosphate terminated products. The ribose 2', 3', and 5'-carbons are indicated in blue.



RNA cleavage by 2'-transphosphorylation is relatively thermoneutral (in terms of free energy) as one phosphoester bond is formed and one is broken. The production of the ring strained 2',3'-cyclic phosphodiester is enthalpically disfavoured (by ~5 kcal/mole), but the production of two products from one reactant is entropically favoured, especially at high dilution.<sup>6</sup> RNA cleavage is therefore reversible in principle, especially where reactant and products remain bound in a folded ribozyme structure (in this case,

the reaction thermodynamics become coupled with conformational thermodynamics, which could favour the uncleaved form).<sup>7</sup> However, once the 2',3'-cyclic phosphate is hydrolyzed to the more thermodynamically and kinetically stable 2'- or 3'-phosphate, RNA cleavage is rendered essentially irreversible (ligation in this case would require phosphate activation at the expense of an ATP equivalent). Note that non-enzymatic hydrolysis rates for 2',3'-cyclic phosphodiester are up to  $\sim 10^7$ -fold faster than for simple acyclic phosphodiester;<sup>6</sup> this discrepancy reflects both the relief of ring strain<sup>2</sup> and favourable stereo-electronic effects<sup>8</sup> in the transition state. Because the RNA cleaving ribozymes and DNAzyme investigated in this thesis do not catalyze 2',3'-cyclic phosphodiester hydrolysis, further discussion of RNA cleavage chemistry is limited to the initial 2'-transphosphorylation reaction.

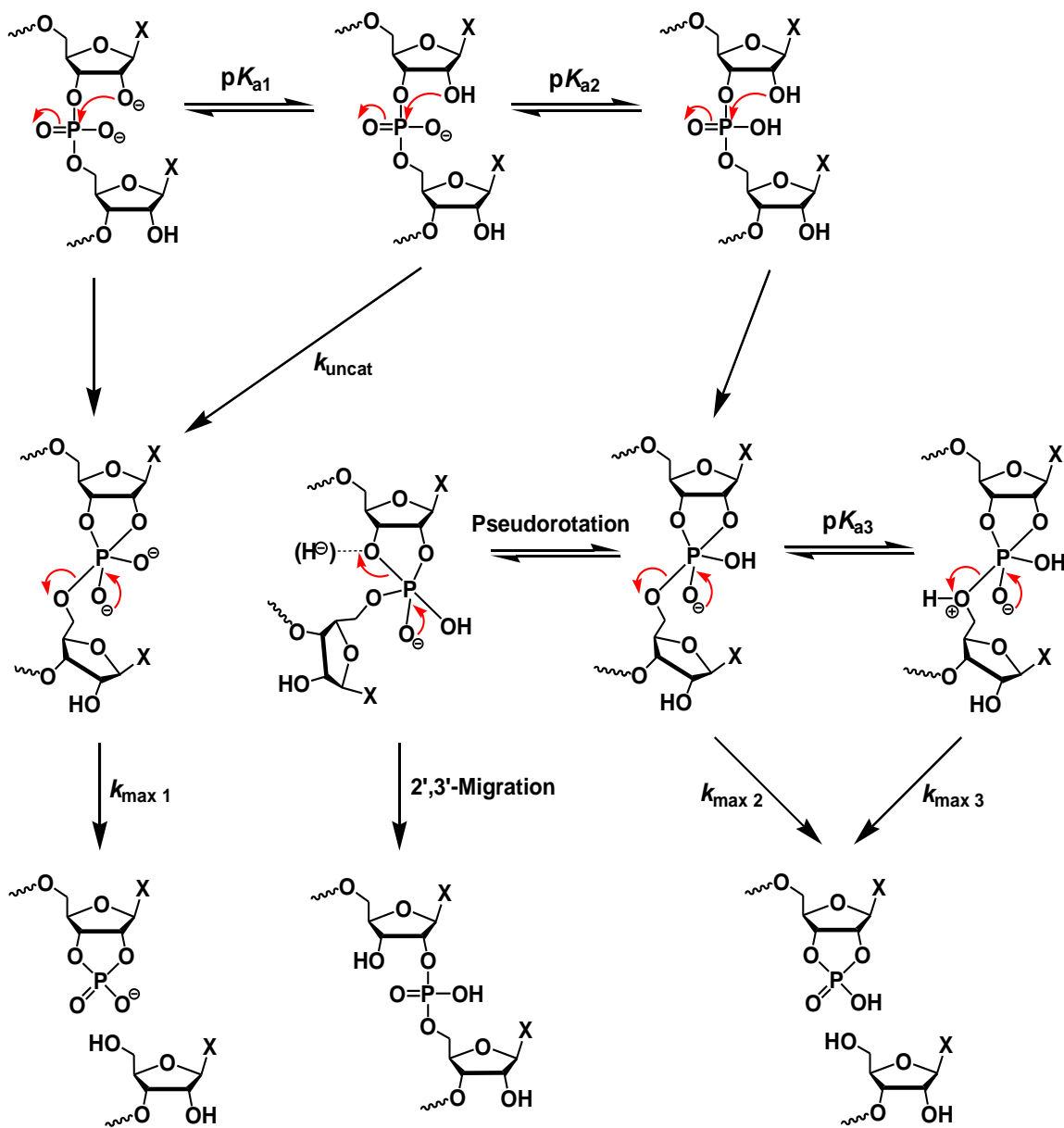
## **1.3 NON-ENZYMATIC CATALYSIS OF RNA CLEAVAGE**

### **1.3.1 Specific Acid/Base Catalysis**

In order to illustrate the most general mechanistic strategies available to RNA cleavage catalysts, this section presents a discussion of the non-enzymatic mechanisms of RNA cleavage catalysis. The rate of spontaneous 2'-transphosphorylation depends upon the protonation states of multiple reactive functional groups and is strongly accelerated at low and high pH.<sup>9, 10</sup> The reaction is therefore susceptible to both specific acid and base catalysis, which can be viewed as fast, equilibrium proton transfer steps that precede the rate limiting step(s). Accordingly, the specific acid/base catalyzed pH-rate profile will reflect the titration of the reactive substrate functional groups.<sup>11</sup>

Although the detailed mechanism(s) of specific acid/base catalyzed RNA cleavage are still not thoroughly understood, Breaker and coworkers have presented a very useful analysis that clearly illustrates the general strategies that can be exploited to catalyze RNA cleavage.<sup>12</sup> In their interpretation, the pH-dependence of the RNA cleavage rate can be rationalized based on the rate enhancements that result from specific base catalyzed 2'-hydroxyl deprotonation (nucleophile activation) and specific acid catalyzed nonbridging oxygen and 5'-oxygen protonation (electrophile and leaving group activation, respectively). These rate enhancement mechanisms are illustrated in Figure 1.2 in separate reaction channels for specific acid and base catalysis (other reaction channels involving simultaneous specific acid and base catalysis are also possible). As illustrated in Figure 1.2, 5'-oxygen protonation is believed to occur only in the intermediate or transition state, whereas 2'-hydroxyl deprotonation and nonbridging oxygen protonation apply to the reactants.<sup>12</sup> The reaction channel involving the RNA protonation state that predominates from pH ~1-13 proceeds at the slowest rate, and is therefore fixed as the minimum “uncatalyzed” rate (denoted by  $k_{\text{uncat}}$  in Figure 1.2).

**Figure 1.2:** Simplified representation of the specific acid, specific base, and uncatalyzed reaction channels for RNA cleavage. Combinations of specific acid/base catalysis are also possible for less populated protonation states (not shown).<sup>12</sup> Kinetically insignificant proton transfers involving H<sub>2</sub>O have been omitted.<sup>13</sup>



Rate enhancement by specific acid and/or base catalysis depends upon the fraction of RNA substrate present in the reactive protonation state(s). Based on the thermodynamic definition of the acid dissociation constant ( $K_a$ ),<sup>14</sup> the pH-dependence of the fraction ( $f_i$ ) of a given functional group in its deprotonated and protonated forms are given by Equations 1.1 and 1.2, respectively.

$$f_{X^-} = \frac{[X^-]}{[X^-] + [XH]} = \frac{1}{1 + 10^{pK_{a,XH} - pH}} \quad (1.1)$$

$$f_{XH} = \frac{[XH]}{[X^-] + [XH]} = \frac{1}{1 + 10^{pH - pK_{a,XH}}} \quad (1.2)$$

The logarithm of the rate enhancement factor, “enh<sub>i</sub>”, that is attributed to each of 2'-hydroxyl deprotonation and nonbridging oxygen and leaving group protonation is then calculated using Equation 1.3. (The values of  $k_{max\ i}$  and  $k_{uncat}$  have been estimated by Breaker based on data for model reactions).<sup>12</sup> In the numerator in Equation 1.3, the uncatalyzed rate constant is added to the catalyzed rate constant to ensure that  $k_{uncat}$  is fixed as the minimum rate constant (at any pH). In this way, only rate enhancement over the uncatalyzed rate is reflected in enh<sub>i</sub> (that is, enh<sub>i</sub> is never less than zero, so that the overall rate constant calculated in Equation 1.4 never falls below  $k_{uncat}$ ).

$$\text{enh}_i = \log \frac{f_i k_{max_i} + k_{uncat}}{k_{uncat}} \quad (1.3)$$

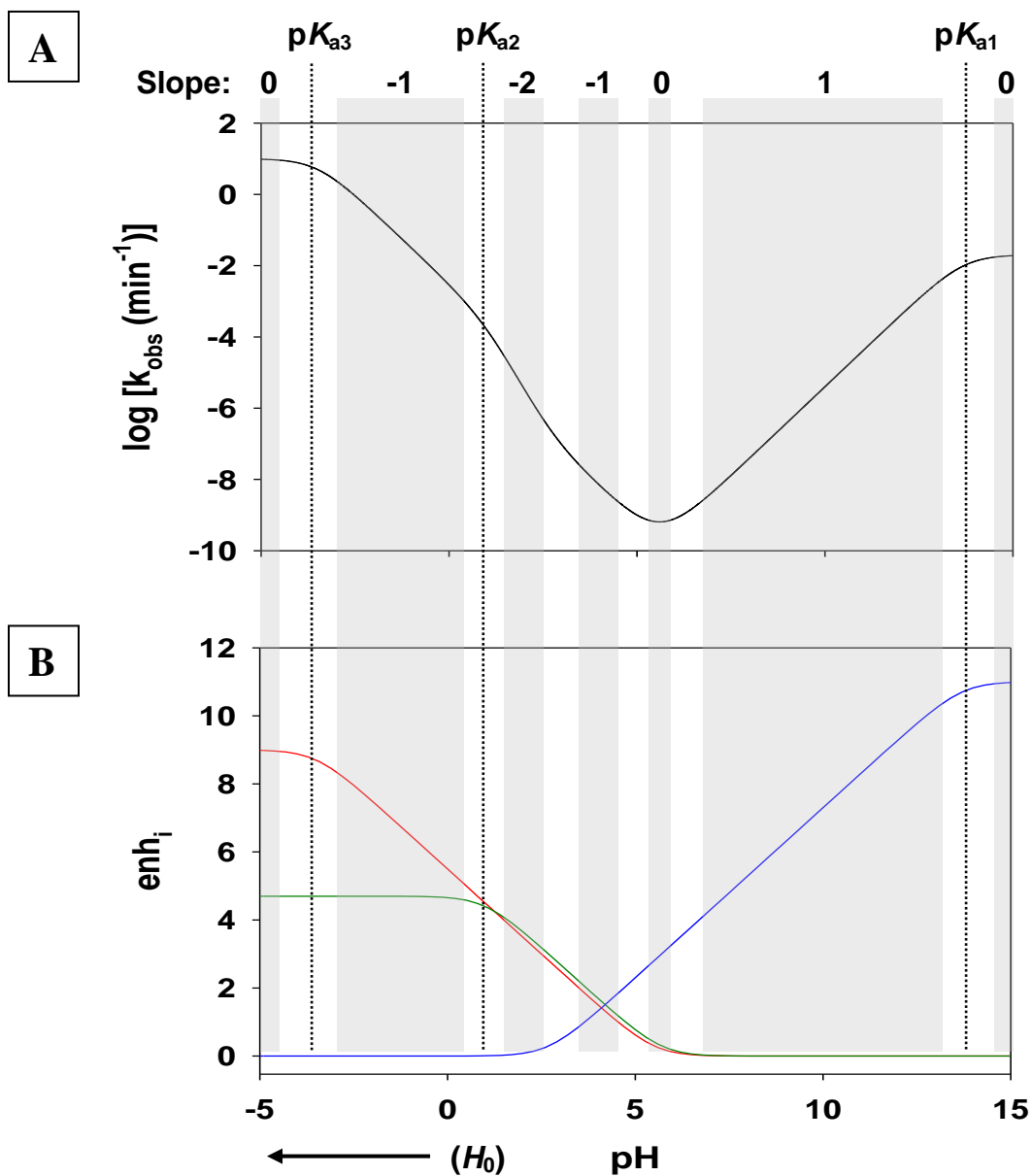
Finally, the pH-dependence of the observed rate constant is given by applying the rate enhancement factors calculated in Equation 1.3 to the uncatalyzed rate:

$$\log(k_{\text{obs}}) = \log(k_{\text{uncat}}) + \sum_i \text{enh}_i \quad (1.4)$$

According to Breaker's analysis, the shape of the pH-rate profile (Figure 1.3A) can be rationalized by considering each of the three rate enhancement mechanisms separately (Figure 1.3B). Above pH ~6, the slope of 1 indicates that the rate is enhanced only by specific base catalyzed 2'-hydroxyl deprotonation. Above pH ~14, the slope is zero because the 2'-hydroxyl is completely titrated, and present only as the active alkoxide nucleophile. Under acidic conditions, the observation of a slope of -2 indicates that specific acid catalysis by protonation of both 5'- and nonbridging oxygens is operative (specific base catalysis is not). The slope changes to 1 below pH ~1 as the nonbridging oxygen become fully protonated, and then changes to zero near  $H_0 = -4$  as the leaving group becomes fully protonated. The slope reversal that is observed between pH ~3 and pH ~6 reflects the change in mechanism from specific acid to specific base catalysis; inspection of Figure 1.3B reveals that all three mechanisms of rate enhancement are operative over this pH range.

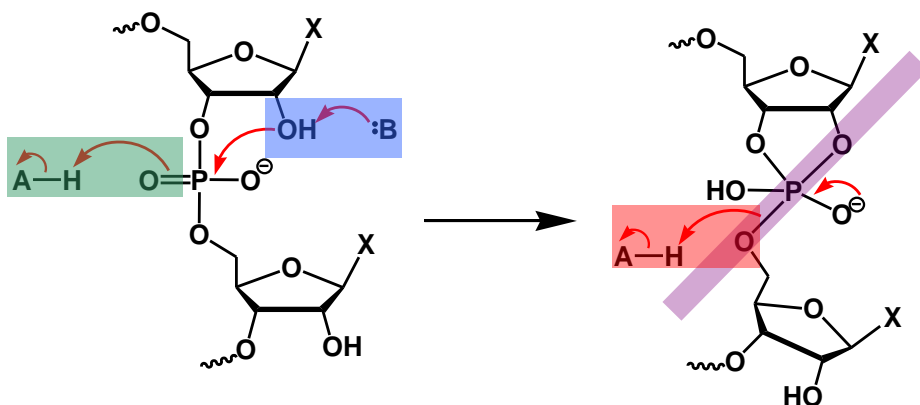
Note that the protonation state of the phosphorane intermediate also affects the outcome of the reaction. In the specific acid catalyzed reaction channel, the monoanionic phosphorane intermediate exists long enough to undergo pseudorotation,<sup>3</sup> which leads to expulsion of the 3'-oxygen leaving group to yield a migration product (with a 2',5'-phosphodiester linkage). Although a dianionic intermediate is believed to exist in the specific base catalyzed reaction channel,<sup>15</sup> it is too short-lived to undergo pseudorotation; accordingly, no migration product has ever been observed above pH ~6.<sup>3, 9, 10, 12</sup>

**Figure 1.3:** (A) Idealized pH-rate profile for specific acid/base catalyzed RNA cleavage at 37 °C based on:  $pK_{a1} = 13.7$ ,  $pK_{a2} = 1$ ,  $pK_{a3} = -3.5$ ,  $k_{max 1} = 0.02 \text{ min}^{-1}$ ,  $k_{max 2} = 1 \cdot 10^{-8} \text{ min}^{-1}$ ,  $k_{max 3} = 2 \cdot 10^{-4} \text{ min}^{-1}$ , and  $k_{uncat} = 2 \cdot 10^{-13} \text{ min}^{-1}$ .<sup>12</sup> The approximate slope of the plot is indicated for each grey coloured pH-range; white coloured pH-ranges indicate slope transitions. (B) Plots of the logarithm of the rate enhancement factor attributed to each of 2'-hydroxyl deprotonation (blue), nonbridging oxygen protonation (green), and 5'-oxygen protonation (red).



In summary, analysis of the specific acid/base catalyzed RNA cleavage mechanism exposes three potential strategies for acid/base catalysis available to RNA cleaving enzymes/catalysts (Figure 1.4). Additionally, RNA cleavage can be accelerated where RNA binding in an enzyme active site enforces the reactive “in-line attack geometry” in which the nucleophile and leaving group are oriented at an angle of 180° degrees relative to one another.<sup>12</sup>

**Figure 1.4:** General strategies for catalyzing RNA cleavage,<sup>12</sup> (colour coded as in Figure 1.3; purple indicates the rate enhancement gained by enforcing the in-line attack geometry, as can be achieved by enzyme binding).



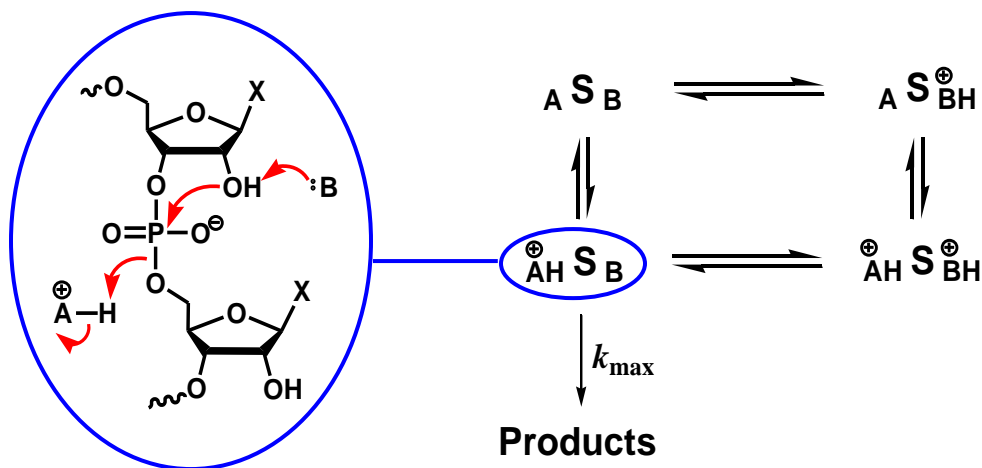
### 1.3.2 General Acid/Base Catalysis

General acid/base catalysis differs from specific acid/base catalysis in that proton transfer to and from the reactive RNA substrate functional groups is mediated directly by buffer molecules (or enzyme functional groups), not  $\text{H}_3\text{O}^+$  or  $\text{OH}^-$ . The overall general acid/base catalyzed rate therefore depends on the concentration of buffer in its catalytically active protonation states, which depends on both the pH and the total buffer concentration. As a result, the pH-rate profiles for general acid/base catalyzed reactions

are governed by titration of the buffer, not the reactive substrate functional groups (at least in the pH range ~3-10 where buffer catalysis is usually studied, which lies between the  $pK_a$ 's of the reactive RNA functional groups).

A great deal of effort has been devoted to characterizing the mechanism buffer catalyzed RNA cleavage as a model system for enzymatic RNA cleavage. Although general acid and base catalysis have been invoked to rationalize the kinetic data,<sup>16, 17</sup> the mechanism remains highly controversial.<sup>18-20</sup> Interpretation of the kinetic data is complicated by factors such as buffer and pH dependent medium effects<sup>21, 22</sup> and the existence of additional specific acid and/or base catalyzed reaction channels. Also, the buffer catalyzed mechanism does not necessarily follow that which occurs in a particular enzyme active site. Therefore, for illustrative purposes, the discussion here is simplified by considering a mechanism involving only general base catalyzed 2'-hydroxyl deprotonation and general acid catalyzed 5'-oxygen protonation (this mechanism is relevant to many RNA cleaving enzymes).

**Figure 1.5:** Idealized general acid/base catalyzed mechanism, where it is assumed that substrate cleavage proceeds via a single reaction channel in which buffer molecules are positioned in the correct protonation states for general acid and base catalysis, respectively, as shown in the kinetic scheme at left. S = RNA substrate.



In analyzing the pH-dependence of this reaction it is assumed that: (1) the rate determining step does not change with pH, and (2) the reaction proceeds only via the general acid and base catalyzed reaction channel (see kinetic scheme in Figure 1.5), not via specific acid and/or base catalyzed reaction channels. According to assumption (2), both the general acid and base must be present in their catalytically active protonation states. Therefore, the observed rate constant ( $k_{\text{obs}}$ ), at a given buffer concentration, is obtained from Equation 1.7 by multiplying the intrinsic rate constant ( $k_{\text{max}}$ ) for the catalyzed reaction by the fractions of buffer molecule in the basic and acidic protonation states ( $f_{\text{B}}$  and  $f_{\text{AH}^+}$ , which are given by Equations 1.5 & 1.6, respectively):<sup>23</sup>

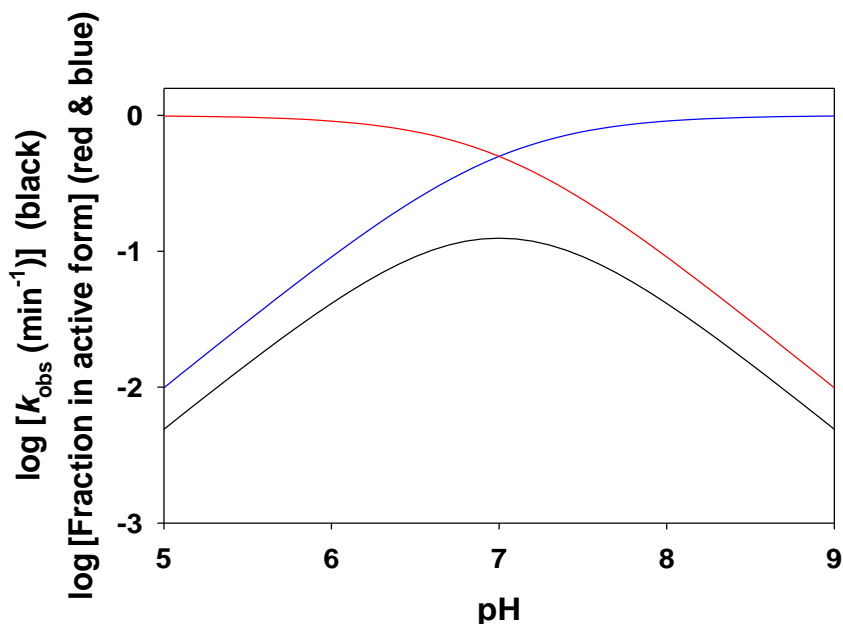
$$f_{\text{B}} = \frac{[\text{B}]}{[\text{B}] + [\text{BH}^+]} = \frac{1}{1 + 10^{\text{p}K_{\text{a}}^{\text{BH}^+} - \text{pH}}} \quad (1.5)$$

$$f_{\text{HA}} = \frac{[\text{AH}^+]}{[\text{A}] + [\text{AH}^+]} = \frac{1}{1 + 10^{\text{pH} - \text{p}K_{\text{aAH}^+}}} \quad (1.6)$$

$$k_{\text{obs}} = k_{\text{max}} f_{\text{AH}^+} f_{\text{B}} = \frac{k_{\text{max}}}{1 + 10^{\text{pH} - \text{p}K_{\text{aAH}^+}} + 10^{\text{p}K_{\text{aBH}^+} - \text{pH}} + 10^{\text{p}K_{\text{aBH}^+} - \text{p}K_{\text{aAH}^+}}} \quad (1.7)$$

According to Equation 1.7, the pH-rate profile for the catalytic mechanism shown in Figure 1.5 reflects titration of both the general acid and base (Figure 1.6). In the case of a buffer catalyzed reaction (where  $A = B$  and  $\text{p}K_{\text{aAH}^+} = \text{p}K_{\text{aBH}^+}$ ), the maximum reaction rate is observed at the pH where the buffer is hemi-protonated. pH-rate profiles for enzymatic catalysis (where A and B may be different residues with different  $\text{p}K_{\text{a}}$  values) are discussed in detail in Section 2.1.3 following the model developed here.

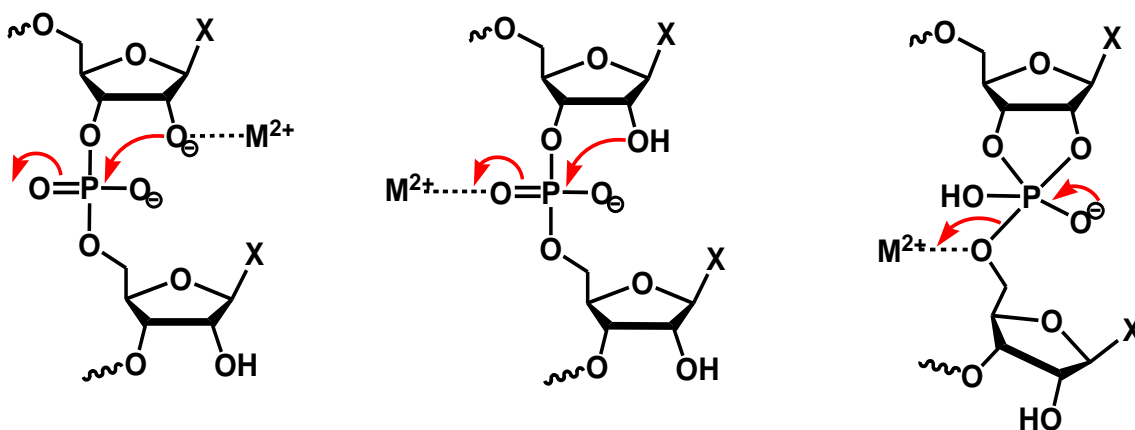
**Figure 1.6:** Idealized pH-rate profile (black), given by Equation 1.7, for the non-enzymatic general acid/base catalyzed mechanism shown in Figure 1.5. The buffer  $pK_a$  was set to 7, and  $k_{max}$  was set to  $0.5 \text{ min}^{-1}$ . The titrations describing the fraction of buffer in the correct protonation state for general base (blue) and general acid (red) are given by Equations 1.5 & 1.6, respectively.



### 1.3.3 Metal Cation Catalysis

The presence of various metal cations is also known to accelerate RNA cleavage.<sup>24-27</sup> Metal cation coordinated water or hydroxide ligands can engage in proton transfer, like any other general acid or base (as in Figure 1.12 – *vide infra*). Alternatively, metal cations can act as Lewis-acids to stabilize the build-up of negative charge on any of the activated 2'-hydroxyl, the nonbridging oxygen(s), or the leaving group (Figure 1.7). Because metal cations can play multiple roles in transition state stabilization, the detailed interpretation of kinetic data for (non-enzymatic) metal cation catalyzed RNA cleavage is very complex.<sup>28</sup>

**Figure 1.7:** Potential mechanisms of divalent metal cation mediated Lewis-acid catalysis of RNA cleavage<sup>29</sup> (combinations of these are also possible<sup>30</sup>); chelation of one metal cation by two functional groups is also plausible (for example, see Figure 1.9 – *vide infra*). Metal cation-bound water or hydroxide ligands can also mediate proton transfer in Brønsted general acid/base catalysis (for example, see Figure 1.12 – *vide infra*).



## 1.4 ENZYMATIC CATALYSIS OF RNA CLEAVAGE

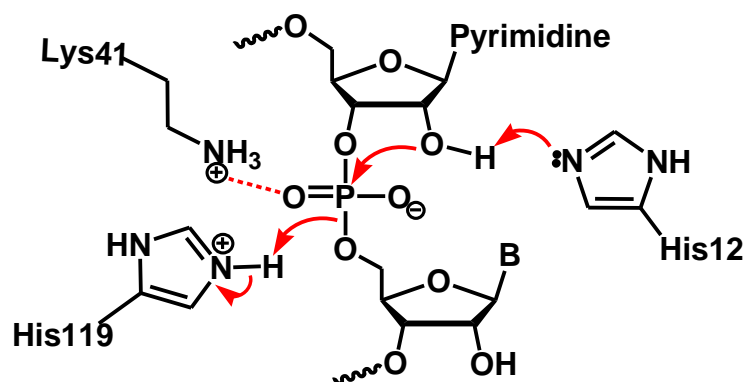
### 1.4.1 Ribonuclease A: Metal Cation Independent Catalysis

Ribonuclease A (RNaseA) is one of the most heavily studied protein enzymes of the twentieth century. RNaseA therefore serves as a prototypical system in the study of the enzymatic catalysis of RNA cleavage and is discussed extensively throughout this thesis. RNaseA catalyzed RNA cleavage proceeds via the same 2'-transphosphorylation mechanism as the non-enzymatic reaction, to yield 2',3'-cyclic phosphodiester and 5'-hydroxyl terminated products.<sup>31</sup> Although not discussed further here, RNaseA subsequently catalyzes the hydrolysis of the 2',3'-cyclic phosphodiester using the same active site, to yield a 3'-phosphate terminated product.<sup>31</sup>

RNaseA has achieved catalytic perfection<sup>32,33</sup> in that (under appropriate conditions) diffusion controlled substrate association has been shown to be the rate limiting step in catalysis.<sup>34</sup> The active site which delivers this remarkable degree of transition state stabilization is depicted in Figure 1.8; therein, the imidazole side chains of His119 and His12 act as general acid and base catalysts, respectively.<sup>31, 35</sup> The cationic amine side chain of Lys41 is also believed to provide electrostatic/hydrogen bond stabilization of the developing negative charge on the nonbridging scissile phosphate oxygens in the transition state.<sup>36</sup> Because this mechanism invokes general acid and base catalysis by residues with very similar  $pK_a$ 's, a characteristic “bell-shaped” pH-rate profile is observed, which is very similar to that shown in Figure 1.6.

It is particularly noteworthy that RNaseA catalyzes RNA cleavage so efficiently without the involvement of a divalent metal cation ( $M^{2+}$ ) cofactor. In contrast,  $M^{2+}$ -mediated catalysis is a common mechanistic strategy in many other phosphodiester transfer or hydrolysis catalysts, be they protein enzymes, catalytic nucleic acids, or synthetic catalysts.<sup>30, 37-42</sup> Thus, the active site mechanism of RNaseA represents a venerable example of the power of organo-catalysis at the enzymatic level, and sets a benchmark against which other  $M^{2+}$ -independent RNA cleavage catalysts are compared.

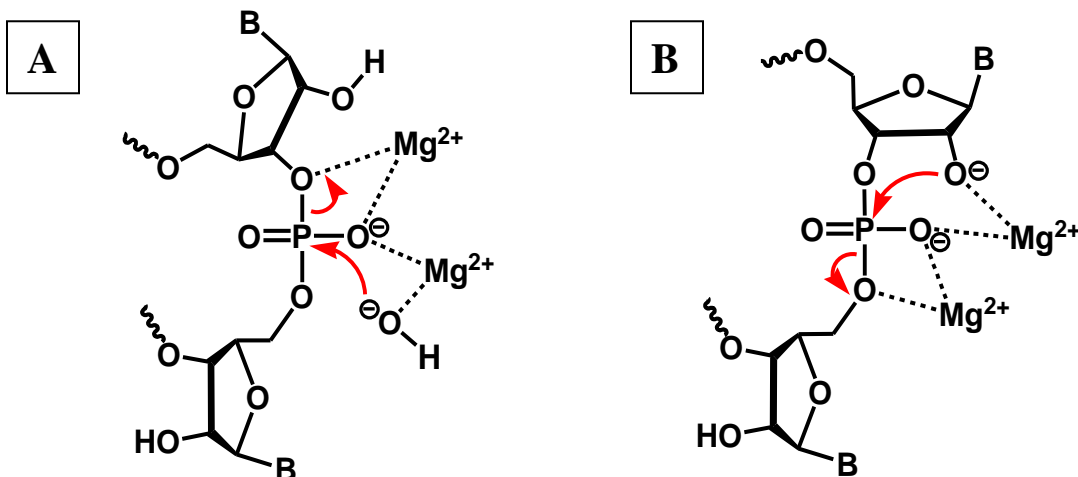
**Figure 1.8:** The metal independent RNA cleavage mechanism at the active site of RNaseA.<sup>31, 35, 36</sup>



### 1.4.2 Ribonuclease H: Metal Cation Dependent Catalysis

Ribonuclease H (RNaseH), which degrades the RNA strand in RNA-DNA heteroduplexes, provides a useful example of a divalent metal cation dependent RNA cleavage mechanism. The chemistry of RNaseH catalyzed RNA cleavage differs from the common 2'-transphosphorylation mechanism in that the nucleophile is  $Mg^{2+}$ -bound hydroxide rather than a 2'-hydroxyl, and the leaving group is a 3'-hydroxyl rather than a 5'-hydroxyl; nevertheless, the same principles of catalysis apply.<sup>43</sup> As shown in Figure 1.9A, two divalent metal cations act as Lewis-acid cofactors to (1) promote the deprotonation of  $M^{2+}$ -coordinated water to form an active hydroxide nucleophile, (2) stabilize negative charge buildup on the nonbridging oxygen, and (3) stabilize negative charge buildup on the leaving group.<sup>43</sup> As shown in Figure 1.9B, an analogous catalytic mechanism for 2'-transphosphorylation can be envisioned in which the  $M^{2+}$  cofactors play the same catalytic roles in the context of a different nucleophile and leaving group.

**Figure 1.9:** (A) The two-metal-cation catalytic mechanism of RNA hydrolysis at the active site of RNaseH.<sup>43</sup> (B) A related, hypothetical two-metal-cation catalytic mechanism for 2'-transphosphorylation.



## 1.5 CATALYTIC NUCLEIC ACIDS

### 1.5.1 Ribozymes

In its original formulation, the central dogma of molecular biology held that DNA permanently stores genetic information (genotype) and RNA mediates the decoding of this information into protein sequences, which express a corresponding functional effect (phenotype). Proteins were therefore believed to be responsible for catalyzing all of the chemical reactions necessary for life, including those involved in the replication and manipulation of nucleic acids. Nucleic acids were believed to function only as a supramolecular system for encoding protein sequence and templating protein synthesis. Although this dogma appeared to be satisfactory in explaining contemporary molecular biology,<sup>44</sup> it presented a conundrum with regard to the origin of life: if protein is

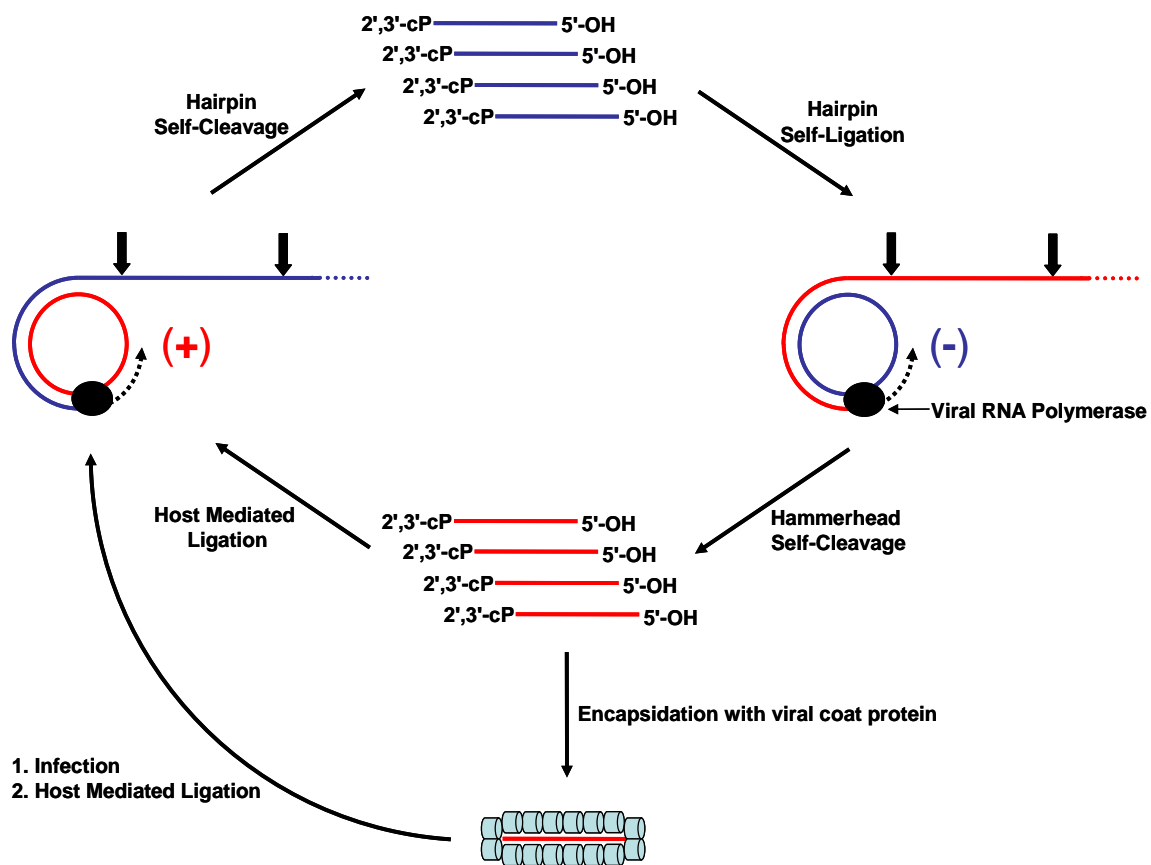
synthesized based on DNA sequence, and DNA is replicated by the action of protein catalysts, neither could have preceded the other!

A solution to this conundrum came with discovery that naturally occurring single stranded RNA molecules could catalyze RNA cleavage and splicing reactions.<sup>45, 46</sup> RNA can therefore embody both genotype (in its primary sequence) and phenotype (by folding into catalytically active tertiary structures) within one molecule. This realization is the foundation for the so-called “RNA world hypothesis”,<sup>47, 48</sup> which posits that RNA was the first of the three main players in modern molecular biology to emerge in early life forms. Proteins and DNA are believed to have evolved later to enhance biological catalysis and information storage, respectively. In support of this hypothesis, ribozymes have been selected *in vitro* that catalyze a myriad of biologically relevant chemical reactions other than RNA cleavage (not least of which templated RNA polymerization<sup>49</sup>). Many other apparent relics of an earlier RNA world can be found in modern biology, such as RNA catalyzed protein synthesis in the ribosome<sup>50, 51</sup> and the ubiquitous appearance of adenosine nucleotides in enzyme cofactors.<sup>52</sup>

The first natural ribozymes to be discovered were the *Tetrahymena* Group I intron<sup>46</sup> and the RNaseP<sup>45</sup>, which catalyze RNA splicing and RNA hydrolysis, respectively. Shortly thereafter, several other smaller catalytic RNAs were discovered, which mediate replication of the circular viral satellite RNAs. These so-called “small nucleolytic ribozymes” catalyze RNA cleavage via 2'-transphosphorylation, and also catalyze the reverse ligation reaction in some cases. As exemplified in Figure 1.10, ribozyme cleavage divides the concatemeric products of rolling circle replication into monomeric genome units (in some cases, these are recircularized by ribozyme ligation).

Until recently, only four distinct small nucleolytic ribozymes had been discovered in Nature. The hammerhead<sup>53-55</sup> and hairpin<sup>56</sup> ribozymes, which are investigated in this thesis, were first identified in viral satellite RNAs. A ribozyme also facilitates rolling circle replication in the Hepatitis Delta Virus (HDV) satellite RNA,<sup>57-59</sup> a human pathogen; a very similar ribozyme sequence has recently been identified in the human genome.<sup>60</sup> The *Varkud* satellite (VS) ribozyme processes concatemeric mRNAs produced by rolling circle transcription of a mitochondrial satellite DNA in the *Neurospora* fungus.<sup>61</sup> Very recently, a fifth, RNA cleaving ribozyme has been discovered in mRNA 5'-UTR sequences in some prokaryotic organisms.<sup>62</sup> This *GlmS* ribozyme appears to be unique in that its activity is activated by metabolite binding.

**Figure 1.10:** Tobacco Ring Spot Virus satellite RNA is replicated via a symmetric rolling circle mechanism.<sup>54</sup> Upon co-inoculation with the virus, the linear, monomeric satellite RNA (+)-strand (—) is circularized by RNA ligase enzymes in the host cells. The circularized RNA is then used as an indefinitely repeating template from which concatemeric (-)-strand RNA (—) is transcribed by a viral RNA polymerase. Hairpin ribozyme self-cleavage of the concatemeric (-)-strand RNA yields linear, monomeric (-)-strand RNA; the reverse reaction (hairpin self-ligation) then produces circular (-)-strand RNA, which serves as a rolling circle template for transcription of concatemeric (+)-strand RNA. Hammerhead ribozyme self-cleavage, followed by host mediated ligation<sup>63</sup> completes the replication cycle by regenerating circular (+)-strand RNA. Infectious satellite virions are formed by commandeering viral coat proteins to encapsulate the linear, monomeric (+)-strand RNA.

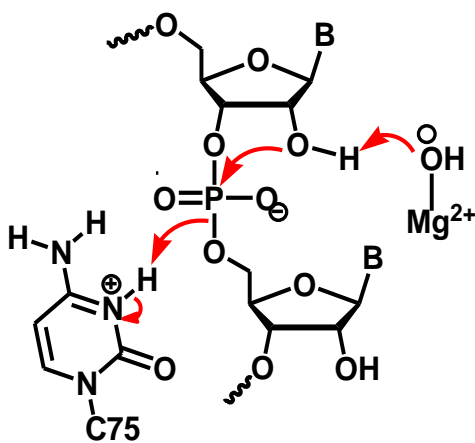


From a chemical perspective, nucleic acid catalysis is particularly intriguing because nucleic acids lack the diverse array of catalytically useful functional groups available to protein catalysts (in their 20+ different amino acid side chains). Consequently, nucleic acid catalyzed RNA cleavage was originally thought to rely on the contribution of metal cation cofactors (usually  $Mg^{2+}$ ). More recent structural and mechanistic data appear to refute this assumption, as RNA functional groups have been implicated in active site chemistry in all of the small nucleolytic ribozymes.<sup>165</sup> The issue of the role of  $M^{2+}$  cofactors in ribozyme catalysis is discussed in detail in Sections 4.1 & 5.1, for the hairpin and hammerhead ribozymes, respectively. One of the principal goals of the work presented in this thesis is to help clarify the contribution of RNA functional groups to catalysis in these two ribozymes.

The HDV ribozyme provides a particularly well characterized example of a small nucleolytic ribozyme (the secondary and tertiary structures are depicted in Figures 1.11A & B, respectively). Based on extensive structural and biophysical studies (see Sections 2.1.2 & 2.1.3), a mechanism has been proposed involving general acid catalysis by protonated C75 and general base catalysis by  $Mg^{2+}$ -bound hydroxide (Figure 1.12).<sup>64, 68</sup> This mechanism is discussed further both to introduce mechanistic probes in Chapter 2, and to provide a point of comparison for the results presented in Chapters 3 & 4.



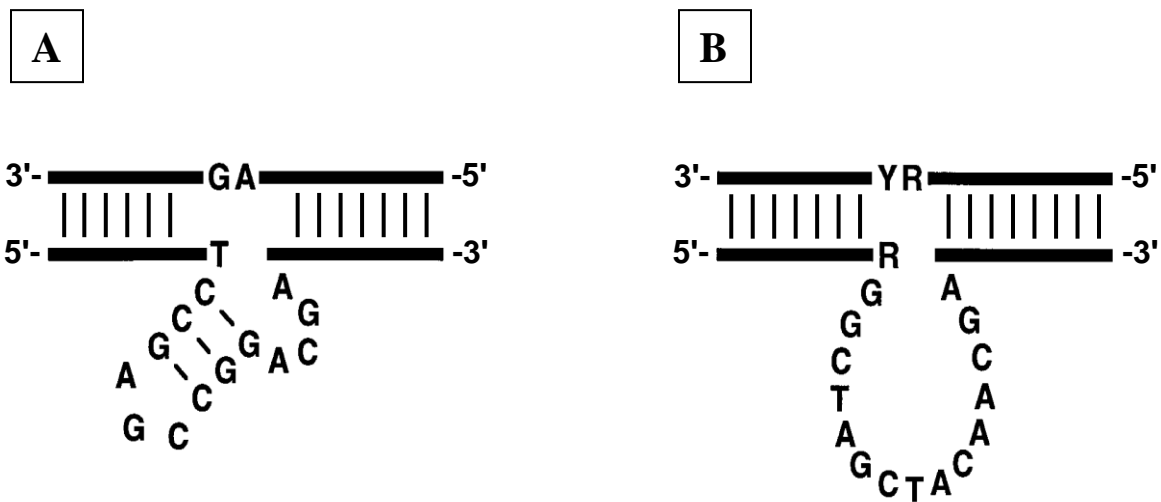
**Figure 1.12:** Proposed active site mechanism by which the HDV ribozyme catalyzes RNA cleavage.<sup>64, 68</sup>



### 1.5.2 DNAzymes

Catalytic DNA sequences (DNAzymes) have not been observed in Nature, which is consistent with the view that DNA emerged as an evolutionary afterthought to improve the long term stability of genetic information. DNAzymes can be produced via *in vitro* (“SELEX”) experiments,<sup>69-71</sup> wherein catalytically active sequences are isolated from large pools of random sequences based on their ability to catalyze self-modification reactions. RNA cleaving DNAzymes are therefore selected based on their ability to cleave a substrate to which they are covalently tethered. By severing the link to their substrate strand, active DNAzymes can be converted to true catalysts capable of multiple turnovers. Two well known divalent-metal cation dependent DNAzymes are shown in Figure 1.13.<sup>72</sup>

**Figure 1.13:** Secondary structure representations of (A) the 8-17 and (B) 10-23 DNAzymes.<sup>72</sup> Only the nucleotides essential for catalytic activity are shown; sequence variation is well tolerated in the guide sequences (bold black lines) which bind substrate via Watson-Crick pairing. Semi-conserved nucleotides are indicated as follows: R = A or G, Y = U or C.



RNA cleaving DNAzymes have potential for use *in vivo* as anti-sense therapeutic agents<sup>73-78</sup> in that they can be engineered to cleave RNA sequences associated with a disease state. For example, by targeting viral RNAs, DNAzymes could help prevent virus replication. Also, by targeting appropriate mRNA sequences *in vivo*, the expression of proteins associated with disease could also be controlled. Some progress has been made toward these goals in recent years;<sup>79-84</sup> however, the utility of current DNAzymes can be complicated by factors such as poor drug delivery across cell membranes and poor accessibility of binding sites in highly structured target RNAs.<sup>85, 86</sup>

With respect to therapeutic use, the Achilles heel of current DNAzyme technologies is the fact that for efficient catalytic activity, most DNAzymes require the

presence of  $M^{2+}$  cofactors at concentrations that far exceed those *in vivo*.<sup>71, 72, 87-89</sup> Two notable studies showed that *in vitro* selections conducted in the absence of  $M^{2+}$  cofactors yield DNAzymes with catalytic rates (at physiological pH and ionic strength) that fall short of the maximum rates observed for  $M^{2+}$ -dependent DNAzymes by 4 to 5 orders of magnitude.<sup>90, 91</sup> More recently, synthetic modification of DNAzymes with protein-like functional groups has been explored in an effort to alleviate the  $M^{2+}$ -dependence of DNAzyme catalysis. In two notable cases, modified DNAzymes have been selected which exhibit modestly improved  $M^{2+}$ -independent RNA cleavage catalysis relative to unmodified DNAzymes.<sup>87, 92, 93</sup> In both these cases, the DNAzymes were appended with the same imidazole and cationic amine functional groups that make possible efficient,  $M^{2+}$ -independent RNA cleavage in the active site of RNaseA. The catalytic mechanism and the basis for the  $M^{2+}$ -independence of one of these modified DNAzymes (9<sub>25-11</sub>) are investigated in Chapter 3 of this thesis.

# CHAPTER 2: CHEMICAL PROBES FOR GENERAL ACID/BASE CATALYSIS OF RNA CLEAVAGE

## 2.1 INTRODUCTION

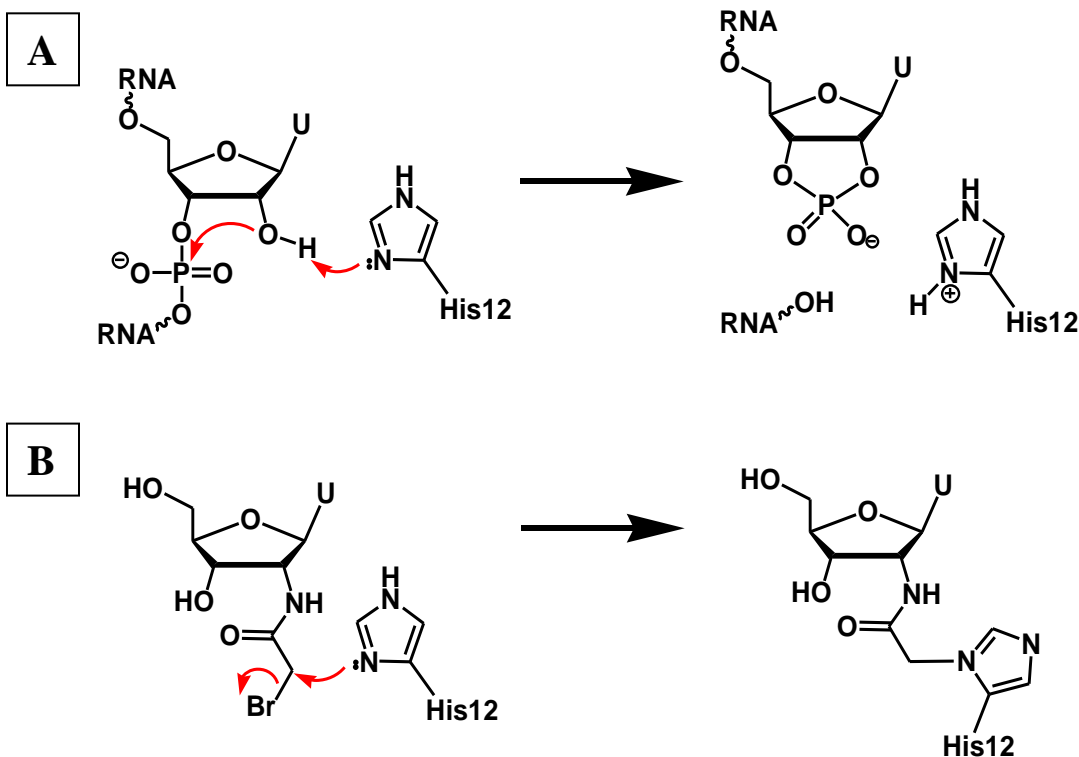
This chapter introduces three general techniques that are used in this thesis to probe the mechanisms of general acid/base catalysis in RNA cleaving nucleic acid catalyts. The techniques to be introduced are: affinity labeling, 5'-bridging phosphorothioate substitution in the substrate, and pH-rate profiling in conjunction with general acid/base  $pK_a$  perturbation. This chapter also details the novel synthetic methodologies used to prepare the affinity labeling and 5'-bridging phosphorothioate substrate analogues; characterization data for these products is also presented. Chapters 3, 4, and 5 report the results of the application of these mechanistic probes to three different nucleic acid catalyts.

### 2.1.1 Probing General Base Catalysis with Affinity Labeling

An affinity label is a substrate analogue that bears an unnatural, reactive functional group (an electrophile), but retains sufficient structural similarity to the native substrate so that it retains high affinity for the enzyme active site.<sup>33</sup> Nucleophilic amino acid side chains present in a protein enzyme active site can then be identified if they react to form covalent adducts with the affinity label. With regard to RNA cleavage catalyts, affinity labeling of RNaseA has been successful using both 2'- and 3'-bromoacetamido-ribonucleosides.<sup>94-96</sup> In the case of the 2'-bromoacetamido-ribonucleosides, the reactive

electrophile is incorporated in place of the nucleophilic 2'-hydroxyl at the scissile ribose, which is commonly deprotonated by a general base during enzymatic RNA cleavage. Therefore, the 2'-bromoacetamide is well positioned to alkylate active site residues that play the role of general base catalyst. Accordingly, RNaseA is alkylated by 2'-bromoacetamido-uridine with absolute regio-specificity for the N-3 position of the His12 imidazole side chain (Figure 2.1).<sup>96</sup> The results of this experiment uniquely identify, by covalent modification, the general base catalyst in RNaseA catalyzed RNA cleavage.

**Figure 2.1:** (A) General base catalysis by His12 in RNaseA compared to (B) His12 alkylation by a 2'-deoxy-2'-bromoacetamido-uridine affinity label.<sup>96</sup>



The distinction between an affinity label and a mechanism based inhibitor (or suicide substrate) should be emphasized: both are irreversible inhibitors which covalently modify the active site, but mechanism based inhibitors are distinguished by the fact that their reactive functional groups are produced as a consequence of the normal catalytic action of the enzyme.<sup>33</sup> Because affinity labels generally contain highly reactive and rather indiscriminant electrophiles, alkylation by an affinity label could simply reflect structural proximity of a nucleophilic active site residue that has no role in catalytic chemistry. It should be further cautioned that affinity labeling could occur within an inactive conformation (either naturally occurring or the result of misfolding induced by

the binding of the unnatural affinity label structure). In the case of the 2'-bromoacetamide affinity labels, the electrophilic site is shifted from the site of native 2'-hydroxyl deprotonation by not less than  $\sim 2 \text{ \AA}$ ; therefore, it is certainly plausible that nucleophilic active site residues, which are not involved in general base catalysis, could be alkylated adventitiously. Although the specific alkylation of His12 in RNaseA<sup>96</sup> is an encouraging sign that 2'-bromoacetamide affinity labeling can offer relevant mechanistic insight, the high reactivity and altered structure of the 2'-bromoacetamide probe demands caution in drawing mechanistic conclusions from novel affinity labeling of other catalysts.

Comparison of the properties of the catalytic and affinity labeling reactions can provide some indication of whether the latter occurs within a catalytically active enzyme conformation, and whether it offers any mechanistic insight. For example, if affinity labeling indeed reflects the mechanism of general base catalysis in RNA cleavage, the two reactions should be expected to share similar sensitivity to inhibitors, conditions, and cofactors, as well as similar titration of general base/nucleophile activity in pH-rate profiles (as has been observed for the reaction of RNaseA with bromoacetate<sup>97</sup>).

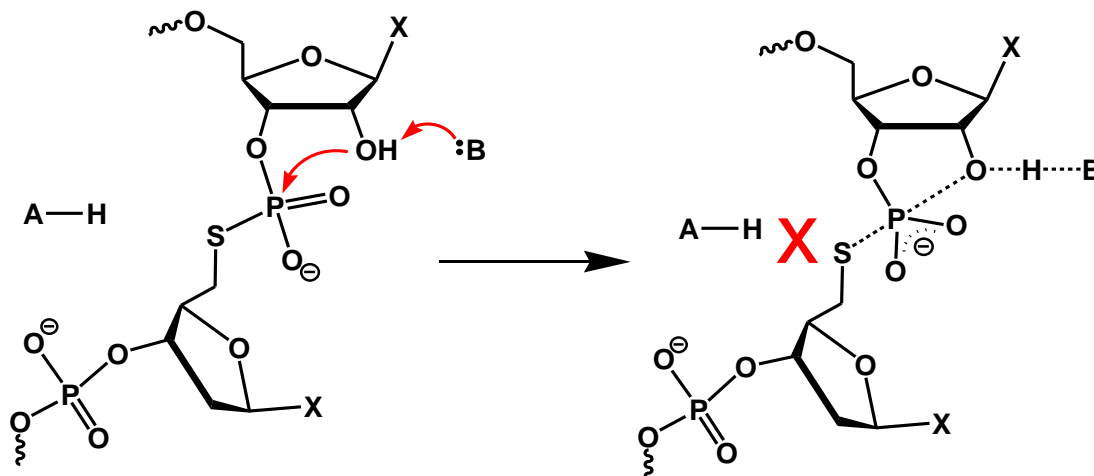
Encouraged by the success of 2'-bromoacetamide affinity labeling in RNaseA, we have exploited this approach in order to probe for general base catalysis in nucleic acid catalyzed RNA cleavage (bearing in mind the aforementioned caveats). Unlike RNaseA, RNA cleaving ribozymes and DNAzymes do not bind mononucleotide substrate analogues (such as that shown in Figure 2.1B); therefore, the preparation of novel oligonucleotide affinity labels was required. This chapter details the synthesis of the required oligonucleotide affinity labels by selective bromoacetylation of an internal 2'-

deoxy-2'-amino-nucleotide (incorporated into the substrate sequence in place of the scissile ribo-nucleotide). Characterization of the products of this reaction by MALDI-TOF mass spectrometry and electrophoretic mobility shift analysis demonstrates that the desired product is produced in reasonably high yields (~80-85%). Affinity labeling substrates have been prepared for, and reacted with each of the 9<sub>25</sub>-11 DNAzyme, the hammerhead ribozyme, and the hairpin ribozyme, as described in Chapters 3, 4, and 5, respectively.

### **2.1.2 Probing General Acid Catalysis with Bridging Phosphorothioate Substrate Analogues**

In bridging phosphorothioate (S-link) substrate analogues, the native oxygen leaving group in the scissile phosphodiester linkage is replaced with sulphur (Figure 2.2). S-link substrates have been used recently to probe for Brønsted acid or Lewis acid catalysis in phosphodiester transfer and hydrolysis reactions catalyzed by both proteins and ribozymes. Depending on the course of the catalytic reaction under investigation, 5'- or 3'-bridging phosphorothioate substituted DNA or RNA has been applied successfully to RNA cleaving<sup>68, 98-102</sup> and splicing ribozymes<sup>103</sup> as well as DNA cleaving enzymes.<sup>104-106</sup> All of the nucleic acid catalysts investigated in this study cleave RNA by 2'-transphosphorylation, with expulsion of a 5'-alkoxide leaving group; therefore, 5'-bridging phosphorothioate substrate analogues (Figure 2.2) are required in this work.

**Figure 2.2:** Illustration of a transition state for enzyme catalyzed cleavage of a 5'-bridging phosphorothioate RNA substrate. The reaction is subject to general base catalysis, but not general acid catalysis.



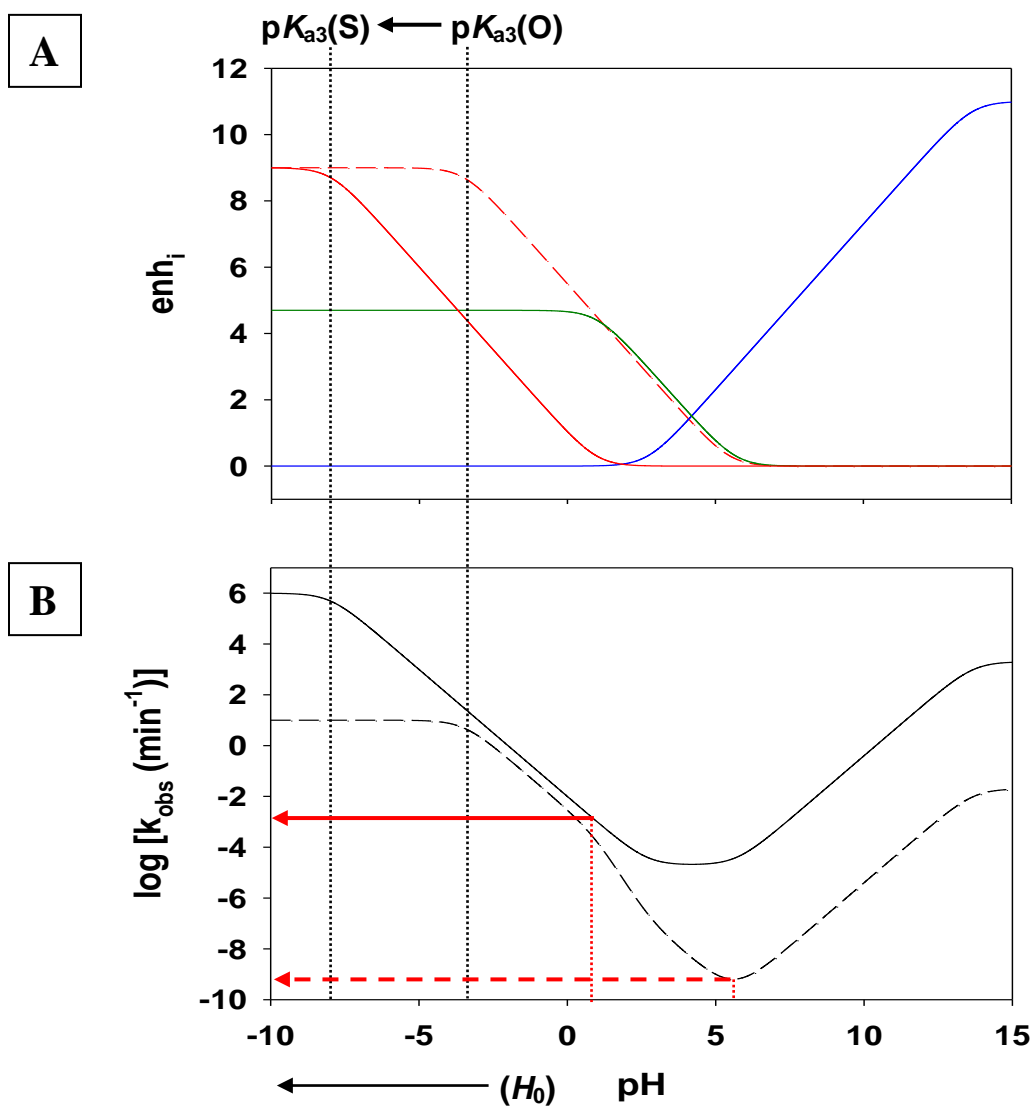
S-link substrates are intrinsically more labile toward cleavage than phosphodiester (O-link) substrates, considering the much lower dissociation energy of the P-S bond versus P-O bond ( $\sim 50$  kcal/mol and  $\sim 90$  kcal/mol respectively<sup>28</sup>). In addition, the lower  $pK_a$  thiolate is both a better leaving group (kinetically) and a more stable product (thermodynamically) than the native alkoxide. Because the thiolate is more polarizable and better able to stabilize negative charge buildup in the transition state, leaving group protonation is not expected to enhance S-link cleavage.<sup>28, 68, 107</sup>

In order to illustrate this point quantitatively, I have simulated the pH-dependence of S-link cleavage (Figure 2.3) using a rate enhancement model, as was described by Breaker and coworkers for native (O-link) RNA cleavage (Figure 1.3).<sup>12</sup> Note that this analysis assumes that S-link cleavage follows the same reaction mechanism as O-link cleavage and that the  $pK_a$ 's and rate enhancements associated with 2'-hydroxyl

deprotonation and nonbridging oxygen protonation are the same for S-link and O-link substrates. Considering that Breaker *et al.* have estimated a  $pK_a$  of  $\sim 3.5$  for protonated 5'-oxygen atom in the phosphorane transition state,<sup>12</sup> the  $pK_a$  difference between the 5'-thiol and 5'-hydroxyl ( $pK_a$ 's of  $\sim 11$  and  $\sim 16$  respectively<sup>28</sup>) suggests that the  $pK_a$  of 5'-sulphur at the transition state is  $\sim 8$  or lower. It is also worth noting that the estimated 5'-oxygen  $pK_a$  is similar to that for protonated dimethyl-ether (both  $\sim 3.5$ ).<sup>12</sup> By the same reasoning, the  $pK_a$  of  $\sim 7$  for protonated dimethyl sulphide<sup>108</sup> should likewise provide some guidance in estimating the 5'-sulphur  $pK_a$ . Also, considering that specific base catalyzed cleavage proceeds  $\sim 10^5$ -fold faster for S-link versus O-link substrates,<sup>28, 68</sup> I estimated the value of  $k_{\text{uncat}}$  for S-link cleavage to be  $2 \cdot 10^{-8} \text{ min}^{-1}$  by multiplying the value of  $k_{\text{uncat}}$  for O-link cleavage<sup>4</sup> by  $10^5$ . To my knowledge no kinetic data for S-link cleavage at acid pH exist for comparison with the pH-rate simulation in Figure 1.3B.

The contributions of specific acid/base catalysis to rate enhancement in O-link and S-link substrate cleavage are simulated in Figure 2.3A. The onset of rate enhancement by specific acid catalyzed leaving group protonation is shifted below pH 1 for S-link cleavage, whereas the analogous onset occurs near pH 6 for O-link cleavage. That is, leaving group protonation is  $>10^5$ -fold less effective in enhancing S-link cleavage, compared to O-link cleavage (this estimate should also apply roughly in the case of enzymatic general acid catalysis as well). Moreover, biological general acids (with  $pK_a$ 's  $> \sim 4$ ) are far better adapted to serve as general acids for a 5'-oxygen leaving group. Overall, neither specific nor general acid catalysis is expected to enhance the rate of S-link cleavage.

**Figure 2.3:** (A) Illustration of the contribution of leaving group protonation to rate enhancement for S-link (—) and O-link cleavage (---). Rate enhancements due to 2'-hydroxyl protonation (—) and nonbridging oxygen protonation (—) are assumed to be the same for S-link as for O-link cleavage (as shown in Figure 1.3). (B) Comparison of the predicted pH-rate profiles for the specific acid/base catalyzed S-link (—) and O-link (---) cleavage. The pH-range over which leaving group protonation is expected to contribute to rate enhancement is shown by the red arrows.  $pK_{a1}$  and  $pK_{a2}$  are set to 13.7 and 1, respectively, for both the O-link and S-link substrates.  $pK_{a3}$  is set to -3.5 for the O-link, and -8 for the S-link substrate.



The preceding discussion, following Breaker's analysis,<sup>12</sup> is certainly useful in illustrating that it is highly unlikely that 5'-sulphur protonation contributes to rate enhancement in S-link cleavage (at least in the physiological pH-range). However, the assumption that S-link cleavage proceeds through a transition state very similar to O-link cleavage is not likely valid. A more rigorous discussion should consider the nature of the S-link cleavage transition state, relative to that for O-link cleavage. The results of computational studies<sup>98, 109, 110</sup> predict a clear difference in the respective reaction coordinate diagrams for base catalyzed S-link and O-link cleavage. For O-link cleavage, two successive transition states are predicted, which are separated by an unstable, fleeting intermediate.<sup>15</sup> Base catalyzed nucleophilic attack of the 2'-alkoxide occurs in the first transition state, followed by departure of the 5'-alkoxide leaving group in the second, decidedly rate-limiting transition state.<sup>98, 109, 110</sup> In contrast, for S-link cleavage, a single, early transition state is predicted, which features a high degree of bond formation to the incoming nucleophile, but little fission of the bond to the leaving group. This prediction is in accord with the Hammond postulate:<sup>111</sup> the much more stable thiolate product causes S-link cleavage to be more exothermic overall, which shifts the transition state reaction coordinate towards reactants (that is, the transition state structure more closely resembles the reactant, rather than the product structure).<sup>109, 110</sup> Little negative charge build up on the sulphur leaving group is predicted in the early, base catalyzed transition state; therefore, protonation of the 5'-sulphur leaving group S-link cleavage would not be expected to stabilize this transition state. In contrast, under the same conditions, O-link cleavage is readily accelerated by acid catalysis because 5'-oxygen protonation lowers the energy of the rate limiting transition state by stabilizing the considerable build up of

negative charge on the leaving group. Unfortunately, Brønsted analysis has not been reported for S-link cleavage to my knowledge, so neither  $\beta_{lg}$  nor  $\alpha$  coefficient values are known. These values would help to characterize the nature of the transition state by quantifying the degree of negative charge accumulation on sulphur, and the degree of proton transfer to sulphur, respectively. Ye *et al.* have reported  $\beta_{lg}$  values which indicate a highly dissociative transition state (with considerable negative charge on the leaving group) for low  $pK_a$  phenolate and thiophenolate leaving groups in model phosphodiester compounds, but these conclusions do not necessarily apply to the case of RNA cleavage.<sup>112</sup>

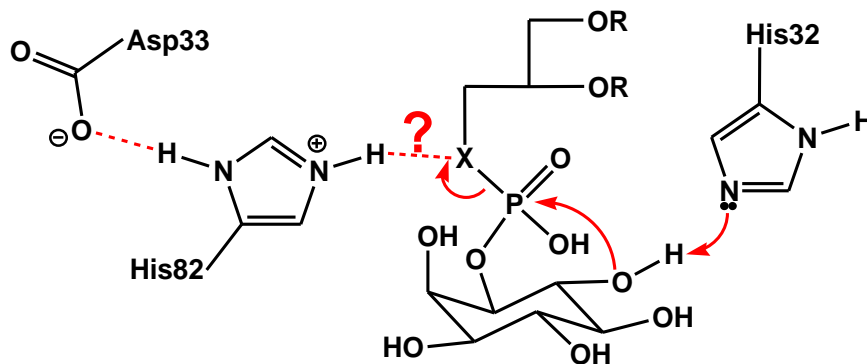
Because O-link cleavage is strongly accelerated by leaving group protonation, whereas S-link cleavage is not, catalyst mutations that impair general acid catalysis should severely inhibit O-link cleavage, but should have little effect on S-link substrate cleavage rates. Conversely, mutations which impair aspects of catalysis unrelated to general acid catalysis should affect catalyst activity against O-link and S-link substrates to a similar degree. Thus, if a given catalyst modification elicits a conspicuously large ratio of rate constants for S-link and O-link substrate cleavage ( $k_S/k_O$ ), it is likely that the modified functional group is involved in general acid catalysis.<sup>68, 107</sup>

Three relevant examples of the application of S-link (or related) substrates to probe general acid catalysis in phosphodiester transfer catalysts are cited for comparison with the results reported in this work. First, Das and Piccirilli used a 5'-bridging phosphorothioate RNA substrate to provide very convincing evidence that the N-3 of C76 transfers its proton to the native alkoxide leaving group in the antigenomic HDV ribozyme (Figure 1.12).<sup>68</sup> Their results were particularly clear cut, in that only mutations

which disrupted proton transfer from N-3 of C76 elicited very large  $k_S/k_O$  values. As expected, mutation of other residues not involved in general acid catalysis elicited similar  $k_S/k_O$  values to those observed for the wildtype ribozyme.

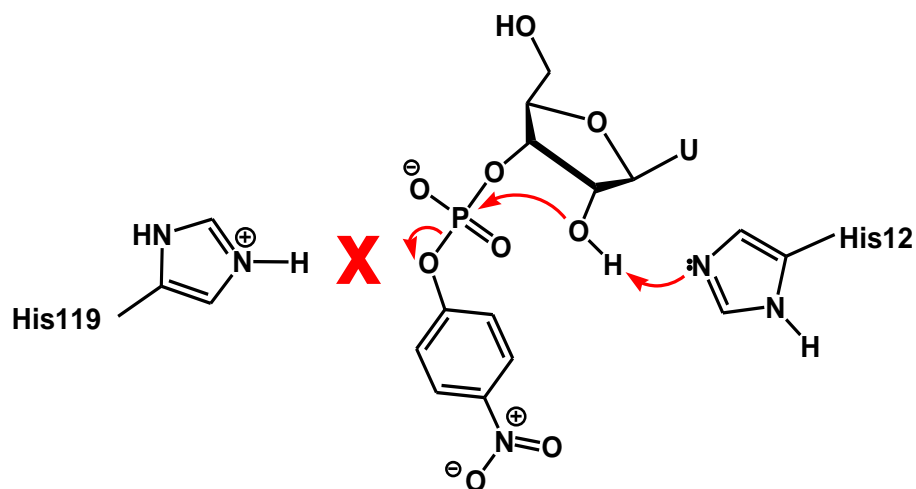
In a second relevant example, Tsai and coworkers employed bridging phosphorothioate substrates to probe general acid catalysis in a phospholipase enzyme.<sup>107, 113, 114</sup> This enzyme catalyzes the cleavage of phosphatidyl-inositol to yield diacylglycerol and inositol-1,2-cyclic phosphate via intramolecular transphosphorylation (Figure 2.4) that is reminiscent of RNA cleavage by 2'-transphosphorylation. In this case, conspicuously large  $k_S/k_O$  values were observed upon mutation of either of two active site residues (Asp33 or His82). In light of these data, and with support from crystal structures,<sup>115</sup> the authors interpreted these data to indicate that phospholipase general acid catalysis is delivered by a catalytic dyad comprised of these two residues. Specifically, the His82 imidazole side chain is proposed to transfer a proton to the leaving group, while the carboxylate side chain of Asp33 assists by forming a crucial hydrogen bond which orients His82 productively for catalysis (Figure 2.4).

**Figure 2.4:** Phosphatidyl-inositol substrates used to probe general acid in phospholipase catalyzed phosphodiester cleavage. X = O: native substrate; X = S: S-link substrate.



In a third relevant example, Thompson and Raines have investigated the cleavage of a substrate analogue with a *para*-nitro-phenolate leaving group to probe the role of His119 in RNaseA catalysis (Figure 2.5).<sup>35</sup> With a  $pK_a$  of 7.1 (lower still than the 5'-thiolate), the *para*-nitro-phenolate is an excellent leaving group, the departure of which most certainly does not require acid catalysis. Not surprisingly, mutation of either of His12 and His119 drastically impaired RNaseA activity against a native RNA substrate. Most importantly, cleavage activity was dramatically restored, to near wildtype levels, against the nitro-phenolate substrate only in the case of the His119 mutant. These data provided strong evidence that His119 acts as a general acid to protonate the native 5'-oxygen leaving group in RNaseA catalysis.

**Figure 2.5:** A mononucleotide substrate analogue with a *para*-nitro-phenolate leaving group was used to probe general acid catalysis in RNaseA.

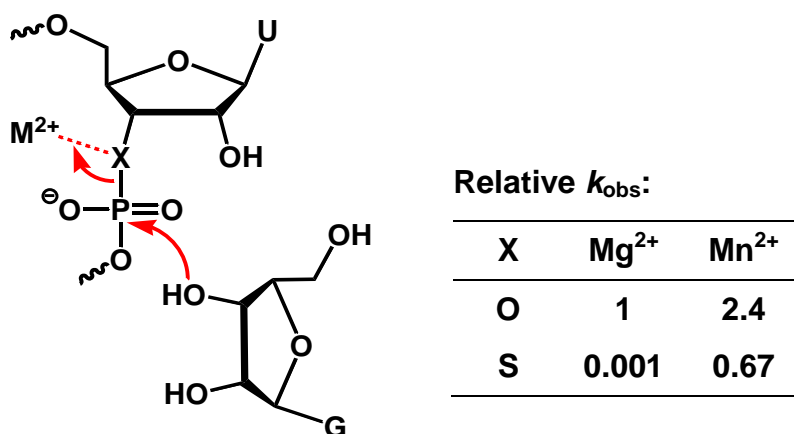


S-link substrates are also useful for identifying Lewis-acid catalysis of phosphodiester cleavage where the leaving group is stabilized by metal cation coordination (Figure 2.6). It is well established that phosphorothioates coordinate with much higher affinity to softer metal cations (such as  $\text{Mn}^{2+}$ ) relative to hard cations (such as  $\text{Mg}^{2+}$ ). Phosphate oxygens, on the other hand, coordinate effectively to both  $\text{Mn}^{2+}$  and  $\text{Mg}^{2+}$ .<sup>116, 117</sup> Therefore, in cases where phosphodiester cleavage is catalyzed by metal cation coordination of the leaving group, S-link, but not O-link, substrate cleavage is expected to be dramatically enhanced in the presence of soft metal cations. In the case of non-enzymatic cleavage of S-link ribozyme substrates, rate acceleration has been reported to correlate well with the softness of the metal cation present.<sup>68, 118</sup> However, other results for dinucleotide cleavage were less conclusive, and the authors cautioned that the analysis of these results is complicated by the fact that the metal cation may play multiple roles in non-enzymatic catalysis (see Section 1.3.3).<sup>28</sup>

Enhancement of S-link substrate cleavage in the presence soft metal cations has been much more definitively characterized in cases of enzymatic catalysis. Specific and dramatic activation of S-link cleavage is in fact observed for enzymes which are hypothesized to employ Lewis-acid stabilization of the leaving group by metal cation cofactor. For example, in the case of the *Tetrahymena* ribozyme (Figure 2.6), S-link cleavage is 1000-fold slower than O-link cleavage in the presence of  $\text{Mg}^{2+}$ ; however, when  $\text{Mg}^{2+}$  is replaced with  $\text{Mn}^{2+}$ , S-link cleavage is enhanced by 670-fold, whereas O-link cleavage is enhanced by just 2.4-fold.<sup>103</sup> Very similar results have been reported for hydrolytic DNA cleavage via a similar Lewis-acid catalyzed mechanism in the 3'-5' exonuclease domain of DNA Polymerase I.<sup>106</sup> On the other hand, in cases such as the

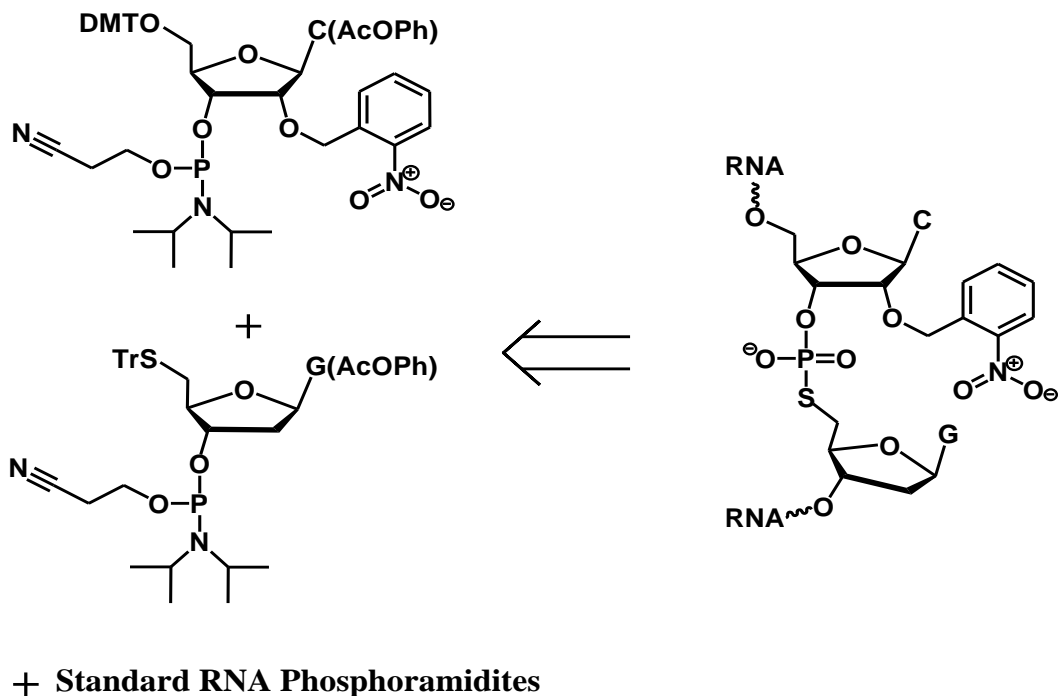
HDV ribozyme, where metal ion coordination of the leaving group is *not* believed to be operative, cleavage of the S-link and O-link substrates is very similar in the presence of  $Mg^{2+}$ , and neither O-link nor S-link cleavage is particularly sensitive to soft metal cation substitution.<sup>68</sup>

**Figure 2.6:** Specific activation of S-link cleavage in the presence of soft metal cations provides strong evidence for metal cation stabilization of the leaving group in the *Tetrahymena* ribozyme.<sup>103</sup>



S-link substrates have been prepared by standard automated solid phase synthesis using a variety of protecting groups for the 2'-hydroxyl at the sensitive phosphorothioate linkage.<sup>98, 118</sup> Most recently, Das and Piccirilli have described an elegant strategy involving a photo-caged S-link substrate for the HDV ribozyme (Figure 2.7).<sup>68</sup> The advantage of this strategy is that the 2'-hydroxyl at the scissile phosphorothioate linkage remains protected throughout standard oligonucleotide deprotection and purification. The scissile 2'-hydroxyl can be subsequently deprotected (quantitatively) by brief exposure to UV-light immediately before use in kinetic experiments.

**Figure 2.7:** Retrosynthetic disconnection of Das and Piccirilli's photo-caged S-link substrate. The modified nucleoside phosphoramidite precursors required for the automated solid phase synthesis are shown at left.<sup>68</sup>



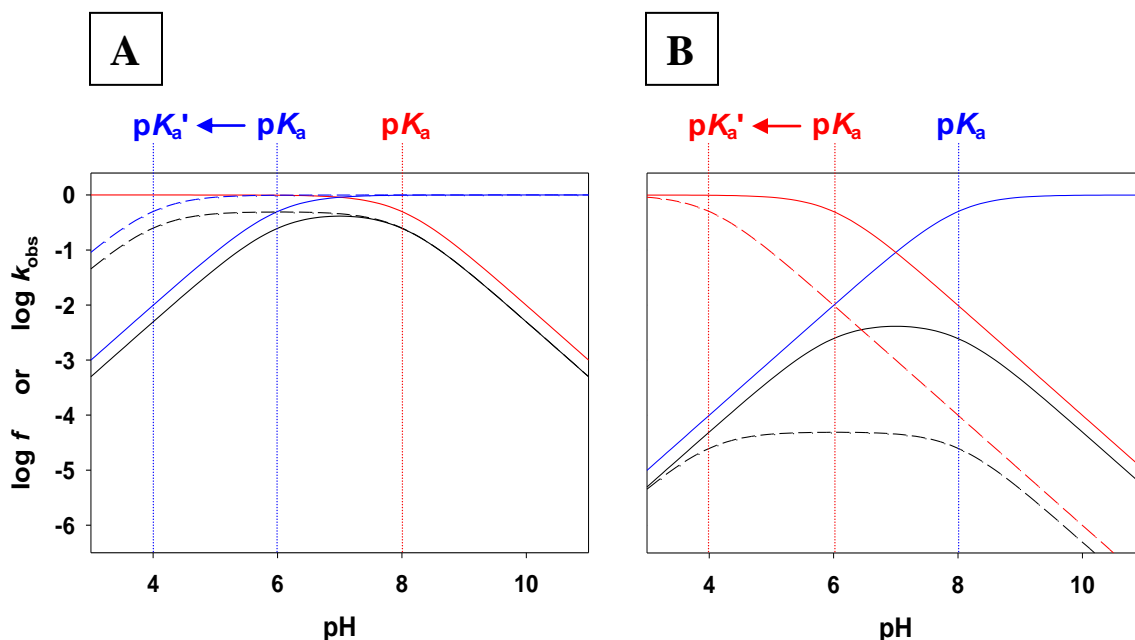
In all cases, previous S-link substrate preparations have necessitated the synthesis of unusual phosphoramidite monomers for use in solid phase oligonucleotide synthesis. In order to avoid the significant cost of synthesizing specialty phosphoramidites, we have developed a simple and inexpensive ligation based strategy (see Figure 2.23) to produce radiochemical quantities of S-link substrate which are suitable for use in single-turnover cleavage reactions. This strategy required 5'-thiophosphorylated oligonucleotide ligation substrates, which we have prepared by a simple solid supported synthesis. The 5'-

thiophosphorylation and S-link synthesis methodologies, along with product characterization data, are discussed in detail in Sections 2.3.2 and 2.3.3.

### **2.1.3 pH-Rate Profiling, $pK_a$ Perturbation, and Kinetic Ambiguity**

In cases where the chemical step of enzyme catalysis is rate limiting, pH-rate profile analysis can provide circumstantial evidence to help identify functional groups involved in general acid/base catalysis. Although the local dielectric constant and other active site properties can lead to sometimes substantial  $pK_a$  shifts,<sup>119</sup> the kinetic  $pK_a$  expressed by the general acid and/or base in the enzyme active site usually correlates roughly (within  $\pm 2$   $pK_a$  units) with the  $pK_a$  of the corresponding free amino acid, nucleotide, or cofactor. This analysis assumes that the rate determining step remains the same at all pH values examined; a change in rate determining step could lead to the determination of a kinetic  $pK_a$  unrelated to the titration of a catalytic residue. It should be further cautioned that the titration of structurally important residues can be reflected in the pH-rate profile. Finally, in cases where both general acid and base catalysis are operative, a further complication arises in that the assignment of kinetic  $pK_a$ 's to either the general acid or base is inherently ambiguous. This "Principle of Kinetic Ambiguity" is illustrated by the fact that the pH-rate profiles for distinct and overlapping titrations (Figure 2.8A and 2.8B respectively) have exactly the same shape.<sup>23, 120</sup> That is, pH-rate profile data can be fit equally well by either model (the only difference is the fitted  $k_{max}$  value, which cannot be predicted *a priori*).

**Figure 2.8:** Illustration of the kinetic ambiguity inherent in the interpretation of pH-rate profiles and  $pK_a$  perturbation.<sup>23, 68</sup> pH-rate profiles (solid black) based on distinct (A) and overlapping (B) general acid (solid red) and base (solid blue) titrations are shown. In each case, the effect of lowering the  $pK_a$  of the more acidic titration by 2 units is also illustrated (dashed lines). For clarity,  $k_{\max}$  is arbitrarily set to 0.5 in all cases. Simulations of the pH-dependence of  $\log k_{\text{obs}}$  and  $\log f$  were generated as described in Section 2.2.1.



More precise evidence to implicate a particular active site functional group in general acid/base catalysis is provided by perturbing its  $pK_a$  through mutation or synthetic modification. If a kinetic  $pK_a$  observed in a pH-rate profile is attributable to the titration of a catalytic functional group, replacement of that functional group with a  $pK_a$  perturbed isostere should lead to a predictable change in the pH-rate profile. That is, the kinetic  $pK_a$  attributed to the perturbed residue should change so as to reflect the  $pK_a$

difference between the freely dissolved model compounds. In principle, distinct and overlapping titrations should be distinguishable based on whether or not  $pK_a$  perturbation diminishes the maximum  $k_{obs}$  (compare Figures 2.8A & B). In practice, however, kinetic ambiguity persists because the effect on  $k_{max}$  cannot be readily predicted for a given active site mutation which is not perfectly isosteric (that is, the degree of structural perturbation of the active site and the consequent effect on catalysis is difficult to predict for an imperfect isostere). Finally, it must be noted that kinetic  $pK_a$ 's attributable to the titration of structurally important protonation sites could also be subject to the effects of  $pK_a$  perturbation.

Jackson et al. provide an exceptional example of the use of  $pK_a$  perturbation to characterize general acid/base catalysis in their study of RNaseA (Figure 2.9).<sup>121</sup> In that study, 4-fluorohistidine (4F-His) was substituted as a low  $pK_a$  analogue for His12 and/or His119 (the  $pK_a$ 's for the protonated imidazole and protonated fluoro-imidazole in the free His and 4F-His amino acids are 6.8 and 3.5, respectively<sup>122</sup>). Simultaneous substitution of His12 and His 119 with 4F-His maintained the bell shaped pH-rate profile, but dramatically lowered the optimum pH for catalysis (Figure 2.10A). This simultaneous lowering of both the general acid and base  $pK_a$ 's provides compelling evidence that the His12/His119 pair is responsible for general acid/base catalysis, but kinetic ambiguity prevents the differentiation of their roles. Individual 4F-His substitution of either His 12 or His 119 broadened the pH-rate profile equally (Figure 2.10B & C), consistent with a lowered  $pK_a$  for either the general acid or base in each case. Remarkably, as predicted for the mechanism shown in Figure 2.9, the distinct and overlapping titrations for the 4F-His12 and 4F-His119 mutants, respectively, are clearly

manifested in their relative catalytic rates.<sup>121</sup> Evidently 4F-His is an excellent isostere for His, as this substitution has only a minor effect on enzyme structure and function.

**Figure 2.9:** Perturbation of the general acid and base  $pK_a$ 's at the active site of RNaseA by 4F-His substitution for His12 and/or His 119.<sup>121</sup>

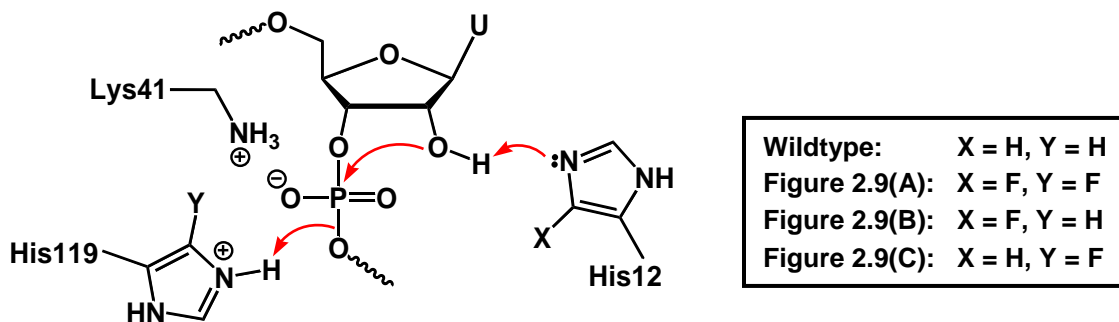
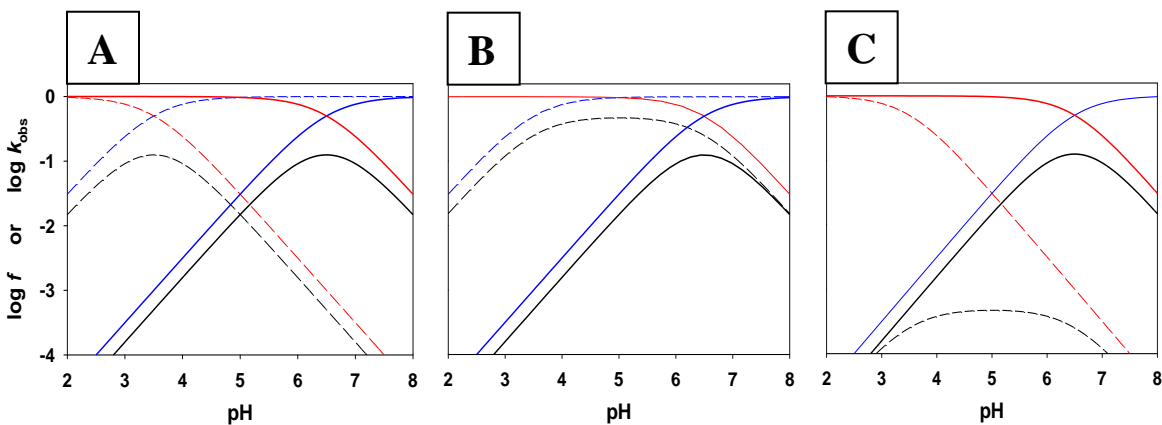


**Figure 2.10:** Idealized simulation of the effects of 4-fluorohistidine (4F-His) substitution on pH-rate profile (black) for RNaseA-catalyzed RNA cleavage: (A) 4F-His12 and 4F-His119; (B) 4F-His12 and His119 (C) His 12 and 4F-His119.  $pK_a$  values for His12 and His119 were set to 6.5;  $pK_a$  values for 4F-His12 and 4F-His 119 were set to 3.5. For clarity,  $k_{max}$  is arbitrarily set to 0.5 in all cases. Solid lines indicate the wildtype titrations and pH-rate profile; dashed lines indicate titrations and pH-rate profiles altered by mutation. Simulations were generated as described in Section 2.2.1.



In the case of the HDV ribozyme, Bevilacqua and coworkers have characterized an abrupt change in the pH-rate profile in the absence of  $\text{Mg}^{2+}$  (Figure 2.11 and 2.12).<sup>64, 123</sup> The pH-rate profile in the presence of  $\text{Mg}^{2+}$  appears to reflect general acid and base catalysis, whereas in the presence of high concentrations of monovalent cations alone, only general acid catalysis is evident. These insightful observations appear to eliminate ambiguity in assigning the general acid and base titrations in the  $\text{Mg}^{2+}$ -dependent pH-rate profile. Specifically, the lower  $\text{p}K_a$  titration observed in the presence of  $\text{Mg}^{2+}$  corresponds well with the lone acidic titration in the absence of  $\text{Mg}^{2+}$ , which suggests that both of these should be attributed to the general acid residue in the HDV ribozyme. Furthermore,  $\text{Mg}^{2+}$  is clearly required for general base catalysis, and the high  $\text{p}K_a$  expressed by the remaining  $\text{Mg}^{2+}$ -dependent basic titration could be consistent with the direct participation of a  $\text{L}_n\text{Mg}(\text{OH})^{m+}$  species ( $\text{p}K_a > 9$ ) in general base catalysis.

**Figure 2.11:** The general acid  $\text{p}K_a$  in the HDV ribozyme was perturbed downward by substitution of 6-aza-cytidine for C76.<sup>68</sup> The contribution of the general base titration to the pH-rate profile was eliminated altogether in the absence of divalent metal cations.<sup>64</sup>

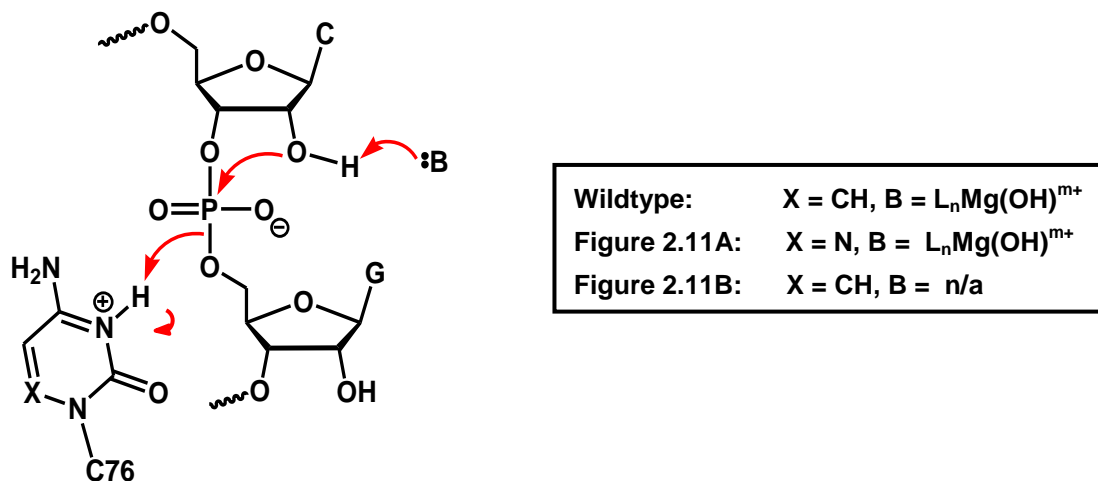
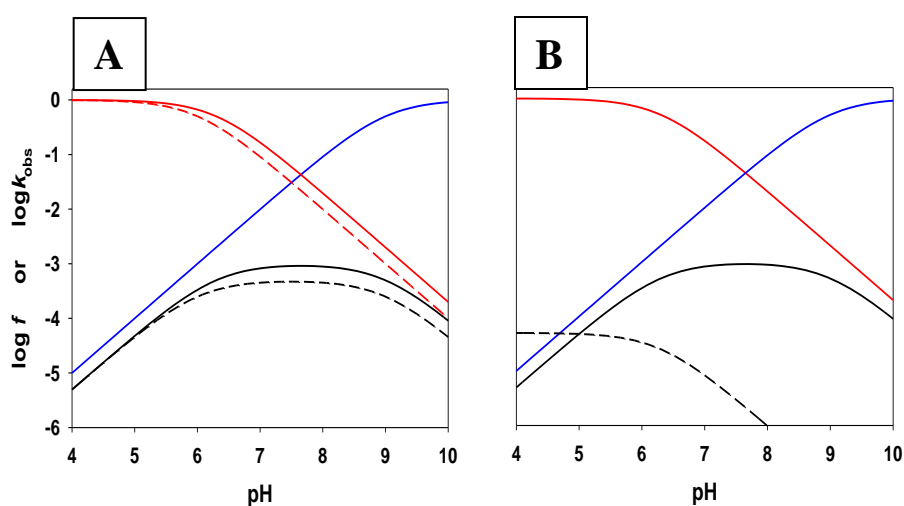


**Figure 2.12:** Idealized simulation of the effects on the HDV ribozyme pH-rate profile (black) caused by: (A) general acid  $pK_a$  perturbation, where 6-aza-cytidine (or adenosine) is substituted for the native C76 general acid; and (B) the lack of general base catalysis in the absence of divalent metal cations. For general base titrations (blue),  $pK_{a\text{HB}}$  was set to 9. For general acid titrations (red),  $pK_{a\text{HA}}$  was set to 6.3 for cytidine and 6.0 for 6-aza-cytidine. For clarity,  $k_{\text{max}}$  is set to 0.5 in all cases except in the absence of  $\text{Mg}^{2+}$ , where  $k_{\text{max}}$  is set to 0.00005. Solid lines indicate the wildtype titrations and pH-rate profile; dashed lines indicate the titrations and pH-rate profiles for C76 mutation or the absence of  $\text{Mg}^{2+}$ . Simulations were generated as described in Section 2.2.1



In light of the crystal structure and S-link cleavage data (*vide supra*), the assignment of C76 as general acid in the antigenomic HDV ribozyme has been confirmed by  $pK_a$  perturbation data (Figure 2.11 and 2.12).<sup>68</sup> Das and Piccirilli observed a slight decrease (0.2  $pK_a$  units) in the general acid  $pK_a$  upon substitution of 6-aza-cytidine for the native C76 residue, although the change was smaller than might be expected considering the difference in the free nucleoside  $pK_a$ 's (the  $pK_a$ 's for N3 protonated 6-aza-cytosine and cytosine are 2.6 and 4.2 for, respectively).<sup>124</sup> An analogous downward shift of  $\sim 0.5$   $pK_a$  units was observed for the C75A and C76A mutants ( $pK_a$  of adenosine N1 is 3.7<sup>125</sup>)

of the genomic<sup>64</sup> and antigenomic<sup>126</sup> ribozymes respectively (C75 and C76 are structurally equivalent residues in the genomic and antigenomic ribozymes, respectively). Furthermore, chemical rescue data for C75 or C76 mutants showed that the  $pK_a$  of the exogenous buffer catalyst was reflected predictably by the general acid titration.<sup>126, 127</sup> Other studies by Been and coworkers in this regard also illustrated the perils inherent in the interpretation of pH-rate profile data, by revealing that titration of a structurally important, protonated cytidine (C41) may complicate the analysis of pH-rate profiles of genomic HDV ribozymes.<sup>127, 128</sup> Detailed biophysical studies by Bevilacqua and coworkers have since confirmed that the general acid titration observed in the absence of  $Mg^{2+}$  is indeed attributable to C75, at least in the wildtype genomic ribozyme.<sup>123</sup>

## 2.2 MATERIALS AND METHODS

### 2.2.1 pH-rate Profile Simulations

In Section 2.1.3 and throughout this thesis, pH-rate profiles for general acid/base catalyzed enzymatic reactions are simulated according to the model developed in Section 1.3.2.<sup>23</sup> The pH-dependence of the observed cleavage rate constant ( $k_{\text{obs}}$ ) for a general acid/base catalyzed reaction is described by:

$$k_{\text{obs}} = k_{\text{max}} / \left( 1 + 10^{\text{p}K_{\text{aHB}} - \text{pH}} + 10^{\text{pH} - \text{p}K_{\text{aHA}}} + 10^{\text{p}K_{\text{aHB}} - \text{p}K_{\text{aHA}}} \right) \quad (2.1)$$

The general acid titrations are given by:

$$f_{\text{HA}} = 1 / \left( 1 + 10^{\text{pH} - \text{p}K_{\text{aAH}}} \right) \quad (2.2)$$

and the general base titrations are given by:

$$f_{\text{B}} = 1 / \left( 1 + 10^{\text{p}K_{\text{aHB}} - \text{pH}} \right) \quad (2.3)$$

where it should be noted that  $\text{p}K_{\text{aHB}}$  refers to dissociation of the conjugate acid form of the general base. Note that in cases where either of acid or base titration (not both) contributes to the pH-rate profile, the expressions for  $k_{\text{obs}}$  are obtained by including the factor  $k_{\text{max}}$  in the numerator of Equation 2.2 or 2.3. In Figure 5.4A, the pH-rate profile reflecting one basic and two acidic titrations was simulated according to:

$$k_{\text{obs}} = k_{\text{max}} / \left( \begin{array}{l} 1 + 10^{\text{p}K_{\text{aHB}} - \text{pH}} + 10^{\text{pH} - \text{p}K_{\text{aHA1}}} + 10^{\text{pH} - \text{p}K_{\text{aHA2}}} + 10^{\text{p}K_{\text{aHB}} - \text{p}K_{\text{aHA1}}} \\ + 10^{\text{p}K_{\text{aHB}} - \text{p}K_{\text{aHA2}}} + 10^{2\text{pH} - \text{p}K_{\text{aHA1}} - \text{p}K_{\text{aHA2}}} + 10^{\text{pH} + \text{p}K_{\text{aHB}} - \text{p}K_{\text{aHA1}} - \text{p}K_{\text{aHA2}}} \end{array} \right) \quad (2.4)$$

The right-hand side of Equation 2.4 is obtained from the product  $k_{\max} \cdot f_{\text{HA1}} \cdot f_{\text{HA2}} \cdot f_{\text{B}}$  so that  $k_{\text{obs}}$  is sensitive to one base and two acid titrations.

## 2.2.2 Chemicals and Biochemicals

All chemicals and buffers were obtained from Sigma-Aldrich (molecular biology or reagent grade purity) and were used as received. Oligonucleotides were synthesized by standard automated solid phase methods by the NAPS unit at UBC, Dharmacon, Trilink Biotech, and the University of Calgary DNA Services Laboratory. *N*-hydroxy-succinimidyl bromoacetate (BrAcNHS) was freshly prepared every week, as previously described,<sup>129</sup> and stored at -20 °C sealed under argon. T4 polynucleotide kinase and T4 DNA ligase were purchased from Invitrogen, RNaseA from Fermentas, Superase-in RNase inhibitor from Ambion,  $\gamma$ -<sup>32</sup>P-ATP from Perkin-Elmer, and streptavidin magnetic particles from Roche. The sequences of the oligonucleotides used in this chapter are detailed in Chapters 3, 4, and 5.

## 2.2.3 Preparation of Oligonucleotide-based Affinity Labels

In a typical bromoacetylation reaction, 10 to 20 nmol of 2'-amino substrate analogue was dissolved in 20  $\mu$ L of 400 mM Na-borate buffer (pH 8) and combined with 20  $\mu$ L of a 250 mM solution of BrAcNHS in DMF. The mixture was allowed to react for 5 minutes at room temperature, after which 40  $\mu$ L more Na-borate buffer was added, followed immediately by 40  $\mu$ L more BrAcNHS solution. The reaction was allowed to continue for 10 minutes at room temperature. The sample was then precipitated with 10 volumes of ethanol and centrifuged; the supernatant was then decanted, and the resulting

pellet was dried under vacuum. This bromoacetylation procedure was repeated once, after which the product was resuspended in water and desalted by G-10 spin column.

#### **2.2.4 Quantification of Bromoacetylation by Gel Mobility Shift Assay**

The extent of substrate analogue bromoacetylation was analyzed by gel mobility shift assay. This analysis was facilitated by further reaction of the bromoacetamide product with 2-amino-ethane-thiol. For these experiments, ~20 pmol of 5'-<sup>32</sup>P-labeled 2'-amino substrate analogue was bromoacetylated as described above. To test if denaturation could improve bromoacetylation yield, a separate sample was bromoacetylated as described in Section 2.2.3, with the exception that the BrAcNHS was dissolved in a 1:1 mixture of DMF and formamide. Following ethanol precipitation, an aliquot of each bromoacetylated sample was further reacted in a solution of 200 mM 2-amino-ethane-thiol dissolved in a 1:1 mixture of 1 M Na-MOPS (pH 8.1) and DMF at room temperature for 90 minutes. These samples were subsequently ethanol precipitated, vacuum dried, and resuspended in 90% formamide/50 mM EDTA/0.01% xylene cyanol/0.01% bromophenol blue. The products were resolved on high resolution sequencing gels (20% d-PAGE) and visualized by autoradiography.

#### **2.2.5 Synthesis of Bridging 5'-Thiophosphorylated Oligonucleotides**

The desired DNA oligonucleotide sequences were synthesized by standard automated solid phase synthesis (1  $\mu$ mol scale). At this point, the samples were not deprotected or cleaved from the solid support by concentrated NH<sub>4</sub>OH treatment, as is normally done in standard oligonucleotide synthesis. The 5'-hydroxyl group of the solid

phase anchored oligonucleotide was converted to the 5'-iodide by treatment with 1 mL of 0.5 M triphenoxy-methyl-phosphonium iodide [(PhO)<sub>3</sub>PCH<sub>3</sub>][I] in DMF for 5 minutes with shaking, at room temp, in the dark<sup>130</sup> (the DMF had been dried over molecular sieves, which had been activated by extended baking in an oven at 120 °C). The solid phase was then washed with 10 × 1 mL CH<sub>2</sub>Cl<sub>2</sub>, followed by 5 × 1 mL CH<sub>3</sub>CN and 5 × 1 mL CH<sub>2</sub>Cl<sub>2</sub>, and vacuum dried. The 5'-iodide was then converted to the 5'-bridging thiophosphate by shaking the solid phase with 1 mL 200 mM sodium thiophosphate (pH ~12, purged with N<sub>2</sub>) for 72 hours, under N<sub>2</sub>, at room temperature, in the dark.<sup>131</sup> Samples were then lyophilized, resuspended in 1 mL concentrated NH<sub>4</sub>OH and deprotected at room temperature for 22 hours. The NH<sub>4</sub>OH was removed and the solid phase washed with ethanol; these solutions were combined and evaporated to dryness under vacuum. The sample was then resuspended in 25 mM Na-borate (pH 9), desalted on a G-10 spin column, and combined with 1 volume 90% formamide/50 mM EDTA. The 5'-thiophosphorylated-oligonucleotides were purified by d-PAGE (TBE) using 5'-phosphorylated-oligonucleotides of the same sequence as mobility standards (the 7-mer and 16-mer oligonucleotides were purified by 20% and 16% d-PAGE, respectively). The desired products were identified by UV-shadowing and excised from the gel. The products were eluted from the crushed gel slice into two portions of 25 mM Na-borate (pH 9)/5 mM EDTA by freezing, followed by shaking at room temp for 2 hours. The eluate was then decanted and concentrated to ~60 µL using butanol, then desalted by G-10 spin column. Na-borate (pH 9) was added to 10 mM for storage at -20 °C.

## 2.2.6 MALDI-TOF Mass Spectrometric Analysis

For MALDI analysis of bromoacetylation, reactions containing ~2 nmol of 2'-amino-oligonucleotide were carried out as described in Section 2.2.3. Following the final ethanol precipitation, the samples were resuspended in water to 200-300  $\mu$ M, desalted on a G-10 spin column, and analyzed immediately.

For MALDI analysis of the 5'-thiophosphorylated oligonucleotides, ~2 nmol samples were dephosphorylated by treatment with 25 mM  $\text{NH}_4\text{OAc}$  (pH 5) at 37 °C for 1 hour and desalted on a G-10 spin column. Untreated samples, along with the  $\text{NH}_4\text{OAc}$  treated samples, were desalted on a G-10 spin column and concentrated to 200-300  $\mu$ M.

Before mixing with the matrix solutions, the samples were further desalted by incubating with a small portion of cation exchange resin (Bio-Rad AG50W-X8 resin,  $\text{NH}_4^+$ -form) for 15-20 minutes. The matrix solutions used were saturated 3-hydroxypicolinic acid in  $\text{CH}_3\text{CN}/\text{H}_2\text{O}$  (1:1) or 0.5 M trihydroxyacetophenone in ethanol, each of which was combined in a 4:1 ratio with 2.4% aqueous ammonium citrate. A 0.5  $\mu$ L portion of the matrix/citrate solution was applied to the MALDI target and allowed to air dry. A 0.5  $\mu$ L solution of sample was then layered onto the dried matrix, and air dried. Finally, another 0.5  $\mu$ L of matrix/citrate solution was layered onto the dried sample. Spectra were recorded on Bruker BiFlex II or Applied Biosystems Voyager instruments in linear-negative ion mode.

### 2.2.7 Synthesis of Bridging 5'-Phosphorothioate Substrate Analogues

20 pmol of d-PAGE purified 5'-product oligonucleotide was 5'-<sup>32</sup>P-labeled using T4 polynucleotide kinase and  $\gamma$ -<sup>32</sup>P-ATP (typically 30-50  $\mu$ Ci). The sample was then phenol/chloroform extracted, precipitated with 10 volumes of 1% LiClO<sub>4</sub> in acetone, resuspended in 10 mM Tris-HCl (pH 7.5) and desalted on a G-10 spin column. 5'-<sup>32</sup>P-labeled-5'-products were then ligated to their respective 5'-thiophosphorylated 3'-products under the following conditions: 50 mM Na-PIPES pH 6.7, 2 mM MgCl<sub>2</sub>, 5 mM DTT, 20 units RNase inhibitor, 10  $\mu$ M 5'-thiophosphorylated-3'-product, 0.5  $\mu$ M 5'- or 3'-biotinylated DNA template, 2 units DNA ligase, in 50  $\mu$ L. The template and 5'-product oligonucleotides were first annealed in buffer alone by heating to 95 °C for 2 minutes, followed by ambient cooling to room temperature over ~10 min. At this point the reaction was placed on ice briefly, then the other reaction components were added, and the sample was incubated at 16 °C for 2 to 3 hours.

Streptavidin magnetic particles (100  $\mu$ L of suspension) were washed with 4 X 100  $\mu$ L 100 mM NaCl/25mM Na-PIPES (pH 6.7)/10 mM EDTA, resuspended in 50  $\mu$ L of the same solution, and added to the ligation mixture to terminate the reaction. The mixture was incubated at 16 °C for 15 minutes with occasional agitation to allow the biotinylated duplex to bind to the solid phase streptavidin. The solid phase was then sequestered by magnetization and the supernatant decanted. The following brief washes were then applied to the solid phase (10 to 15 sec. each): 1 X (100  $\mu$ L 500 mM NaCl/100 mM Na-PIPES/10 mM EDTA), 1 X 100  $\mu$ L (100 mM NaCl/25 mM Na-PIPES/10 mM EDTA), and 5 X 100  $\mu$ L 5 mM Na-PIPES. Finally, incubation in 10% aqueous formamide for 1 min at 37 °C liberated the desired S-link substrate from the solid phase bound duplex.

After magnetization, the S-link substrate was recovered in the supernatant; 10 units RNase inhibitor were then added, and the sample was G-10 spin column desalted, diluted with 5 mM Na-PIPES (pH 6.7) (usually about five volumes), and used directly in kinetic or characterization experiments.

### **2.2.8 Characterization of Bridging 5'-Phosphorothioate Substrate Analogues**

5'-<sup>32</sup>P-labeled S-link substrates were characterized by comparing their electrophoretic mobilities and cleavage properties to the corresponding O-link substrates. Both substrates were subjected to the following treatments: 1) 5mM AgNO<sub>3</sub> for 10 minutes at room temperature. Ag<sup>+</sup> was then precipitated as AgCl upon addition of NaCl to 20 mM to prevent anomalous PAGE mobilities observed in the presence of Ag<sup>+</sup>. The samples were then centrifuged briefly and decanted. 2) 5mM Cd(NO<sub>3</sub>)<sub>2</sub> for 10 minutes at room temperature. 3) 1 unit RNaseA for 10 minutes at 37 °C in 10 mM buffer. 4) 50 mM NaOH for 10 minutes at 60 °C. 5) 1 μM wildtype hammerhead ribozyme in 5 mM MgCl<sub>2</sub>/50 mM Na-PIPES (pH 7) for 10 minutes at room temperature or 5 μM 9<sub>25-11</sub> in 200 mM NaCl, 50 mM Tris-HCl pH 8, 1 mM EDTA for 2 hours at room temperature. All reactions were quenched by the addition of two volumes of 90% formamide/50 mM Na-PIPES (pH 6.4)/25 mM EDTA/0.01% xylene cyanol/0.01% bromophenol blue, prior to analysis by 20% TAE d-PAGE (pH 6.7).

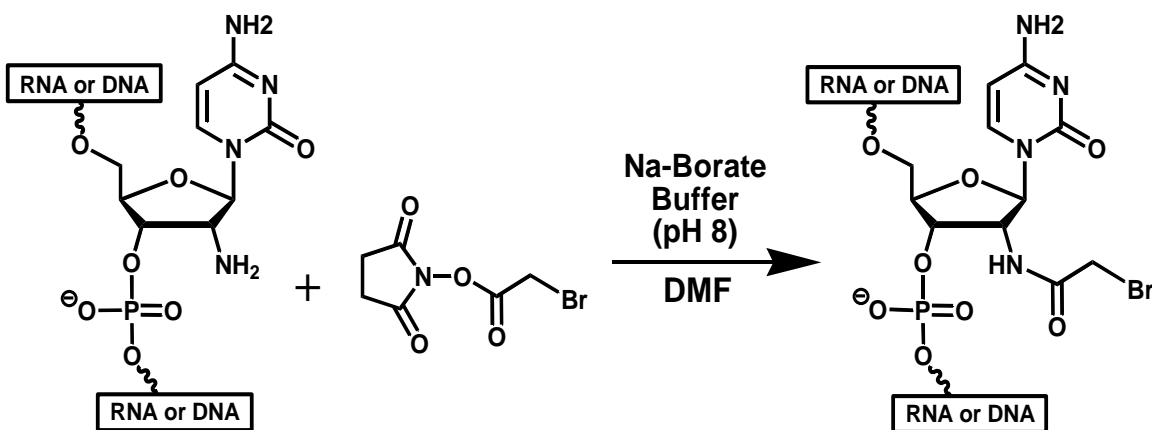
## 2.3 RESULTS AND DISCUSSION

### 2.3.1 Preparation and Characterization of Oligonucleotide-based Affinity Labels

The 2'-bromoacetamide affinity labeling substrate analogues were prepared by selective bromoacetylation, using BrAcNHS, of an internal 2'-deoxy-2'-amino-cytidine residue, incorporated in an otherwise unmodified, fully deprotected RNA or DNA oligonucleotide (Figure 2.13). Weeks and coworkers have demonstrated such chemoselective acylation of internal 2'-amines by reaction with NHS-esters (no undesired acylation of RNA 2'-hydroxyl groups or nucleobase nitrogens could be detected).<sup>132, 133</sup> However, these experiments differed in that they concerned the installation of unreactive acyl groups using NHS-esters which are less electrophilic and more stable to solvolysis than BrAcNHS. We also looked to the work of Povsic and Dervan, who described selective bromoacetylation of a primary alkyl amine tethered to the 5'-terminal residue of a 19-mer oligonucleotide.<sup>129, 134</sup> In this case, bromoacetylation was accomplished by 10 to 15 minute treatment with a 1:1 mixture of 250 mM BrAcNHS and 200 mM Na-Borate buffer pH 8.9 (yield was not reported). We reasoned that this procedure should be transferable to the acylation of the internal 2'-amine. Although more sterically hindered, the 2'-amine has a lower  $pK_a$  compared to an alkylamine ( $pK_a$ 's are  $\sim 6$  and  $\sim 10$ , respectively),<sup>135</sup> and should therefore be present in its nucleophilic, deprotonated form to a greater extent at pH  $\sim 8$  than the primary alkyl amine. Surprisingly, the conditions of Povsic and Dervan did not lead to efficient bromoacetylation as judged by mass spectrometric analysis. Furthermore, we observed that the production of bromoacetic acid by solvolysis of BrAcNHS very quickly overwhelmed the buffer capacity. The

reaction pH dropped to <4 within 2 minutes, as estimated by spotting an aliquot onto pH paper. At this point the 2'-amine would be largely protonated, and hence far less reactive towards bromoacetylation.

**Figure 2.13:** Bromoacetylation of an internal 2'-deoxy-2'-amino-nucleotide using *N*-hydroxy-succinimidyl-bromoacetate (BrAcNHS).



We attempted to improve the yield of the acylation reaction by 1) increasing the buffer concentration to exceed that of BrAcNHS (final concentrations: 200 mM Na-Borate and 125 mM BrAcNHS); 2) adding formamide (to 25%) to try to denature any secondary structures which might cause a steric impediment to 2'-bromoacetylation; and 3) by repeating the bromoacetylation reaction. The increase in buffer concentration appeared to delay the acidification of the reaction mixtures, although all reactions dropped below pH ~4 within 5 minutes. At this point fresh portions of twice the original volumes of buffer and BrAcNHS were added to neutralize the mixture so that the reaction could continue. After proceeding for a further 5 minutes, the reactions were terminated

by ethanol precipitation. In this way, exposure to acidic conditions was minimized, so as to prevent potential damage to the oligonucleotides at low pH (depurination, especially of DNA, as well as cleavage or 2',3'-phosphodiester isomerization of RNA). The addition of formamide was not successful in increasing the bromoacetylation yield, as judged by gel shift assay (*vide infra*), as the yield actually decreased significantly.

Despite efforts to desalt the products of the bromoacetylation reaction, MALDI analysis was hampered by  $\text{Na}^+$  adduct formation. Nevertheless, the singly bromoacetylated product, and  $\text{Na}^+$  adducts thereof, were identified in MALDI spectra (Figure 2.14, Table 2.1), although the estimated yield appeared to be quite low (<45%). MALDI analysis confirmed the production of the singly bromoacetylated oligonucleotide, but it should be stressed that MALDI analysis is not recognized as a reliable technique for quantifying the components of a mixture. We were also concerned that the observation of the bromoacetylated oligonucleotide might be hampered by its reaction with components of the matrix solution. We therefore pursued a gel shift assay in an effort to provide a more reliable quantitative measure of the extent of 2'-amine bromoacetylation.

**Figure 2.14:** MALDI-TOF analysis of the products of the 2'-amine bromoacetylation reaction for (A) a 14-mer RNA 2'-amino-oligonucleotide and (B) a 17-mer DNA 2'-amino-oligonucleotide. Bromoacetylation adds 121 m/z units (average of  $^{79}\text{Br}$  and  $^{81}\text{Br}$  masses) for each 2'-amino-oligonucleotide.  $\text{Na}^+$  adducts (at increments of +22 m/z units) are prominent for both the bromoacetylated products and the unreacted 2'-amino-oligonucleotides.

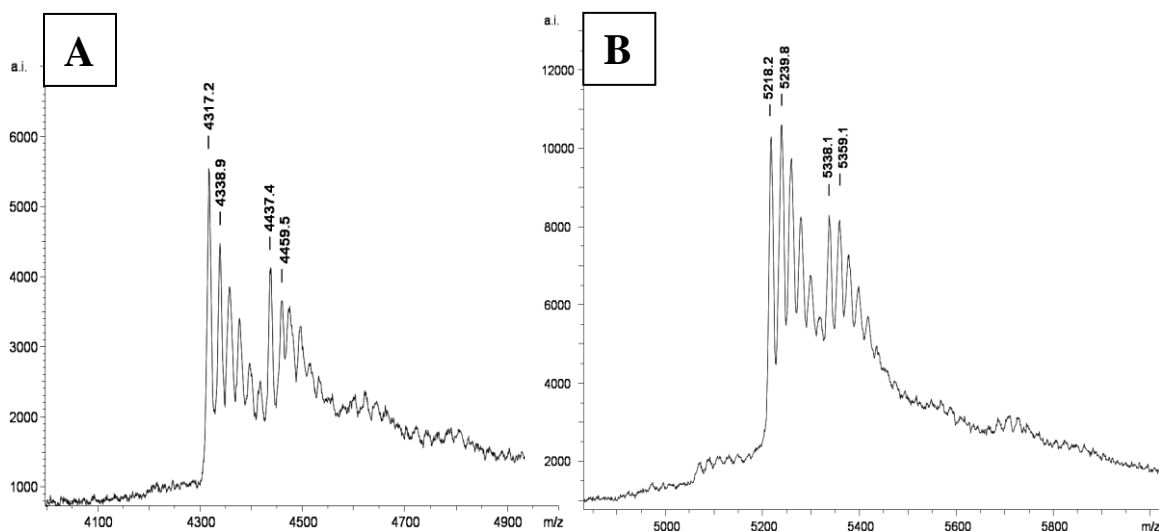


**Table 2.1:** Assignments and predicted and observed m/z values for the  $[\text{M-H}]^-$  molecular ions observed in the MALDI-TOF spectra shown in Figure 2.14.

Oligonucleotide Assignment	$[\text{M-H}]^-$ Predicted	$[\text{M-H}]^-$ Observed
Hairpin 2'-amino substrate analogue <sup>a</sup>	4316.6	4317.2
Bromoacetylated <sup>a</sup>	4437.5 <sup>c</sup>	4437.4
$9_{25-11}$ 2'-amino substrate analogue <sup>b</sup>	5220.9	5218.2
Bromoacetylated <sup>b</sup>	5241.8 <sup>c</sup>	5338.1

<sup>a</sup> UCGC-**Z**-GUCCUAUUU, where **Z** = 2'-deoxy-2'-amino-cytidine

<sup>b</sup> d(GCGTGCC-**Z**-GTCTGTTGG), where **Z** = 2'-deoxy-2'-amino-cytidine

<sup>c</sup> calculated using the average mass of  $^{79}\text{Br}$  and  $^{81}\text{Br}$  isotopes

The 2'-amino- and 2'-bromoacetamido oligonucleotides had very similar electrophoretic mobilities in high resolution d-PAGE analysis, which made direct determination of the bromoacetylation yield difficult, especially for longer substrate analogue sequences such as the 17-mer oligonucleotide (Figure 2.15, Lanes 2 & 3). The separation of the bromoacetylated product was slightly better for the 14-mer oligonucleotide (Figure 2.16, Lane 2). Neither of the 2'-amino- ( $pK_a \sim 6^{135}$ ) or 2'-bromoacetamido-oligonucleotides bears a formal charge during electrophoresis in standard TBE buffer (pH 8.3). Electrophoretic separation of these species is therefore minimal based solely on the relatively small overall increase in size due to bromoacetylation.

In an effort to improve the d-PAGE resolution of the reaction products, bromoacetylation reactions were subsequently treated with 2-amino-ethane-thiol. We hypothesized that the nucleophilic thiol would be quickly and quantitatively alkylated by the electrophilic bromoacetamide, so as to introduce a positive charge into any bromoacetylated oligonucleotides (Figure 2.17) and significantly alter their electrophoretic mobility. Reaction of the 2'-bromoacetamido-oligonucleotide with 2-amino-ethane-thiol appears to be nearly quantitative (Figure 2.15, Lanes 4 & 5; Figure 2.16, Lane 3), and imparts significant retardation of electrophoretic mobility, as predicted. In contrast to the MALDI-TOF data, the gel shift assay data demonstrate conclusively that the bromoacetylation reaction conditions afford ~80-85% conversion to product (based on quantitation of the data in Figures 2.15 and 2.16 by autoradiography). The gel shift data also show that the inclusion of 25% formamide in the reaction mixture lowered the bromoacetylation yield to ~70%.

**Figure 2.15:** Analysis by gel shift assay of 2'-amino bromoacetylation of 5'-<sup>32</sup>P-labeled 2'-amino substrate analogue for 9<sub>25-11</sub>. Lane 1: no reaction; Lane 2: treatment with 1:1 mixture of 250 mM BrAcNHS (in DMF) and 400 mM Na-Borate (pH 8); Lane 3: treatment with 1:1 mixture of 250 mM BrAcNHS (in 1:1 formamide/DMF) and 400 mM Na-Borate (pH 8); Lane 4: sample from Lane 2 treated with 200 mM 2-aminoethanethiol; Lane 5: sample from Lane 3 treated with 200 mM 2-aminoethanethiol. Samples were analyzed by high resolution 20% d-PAGE.

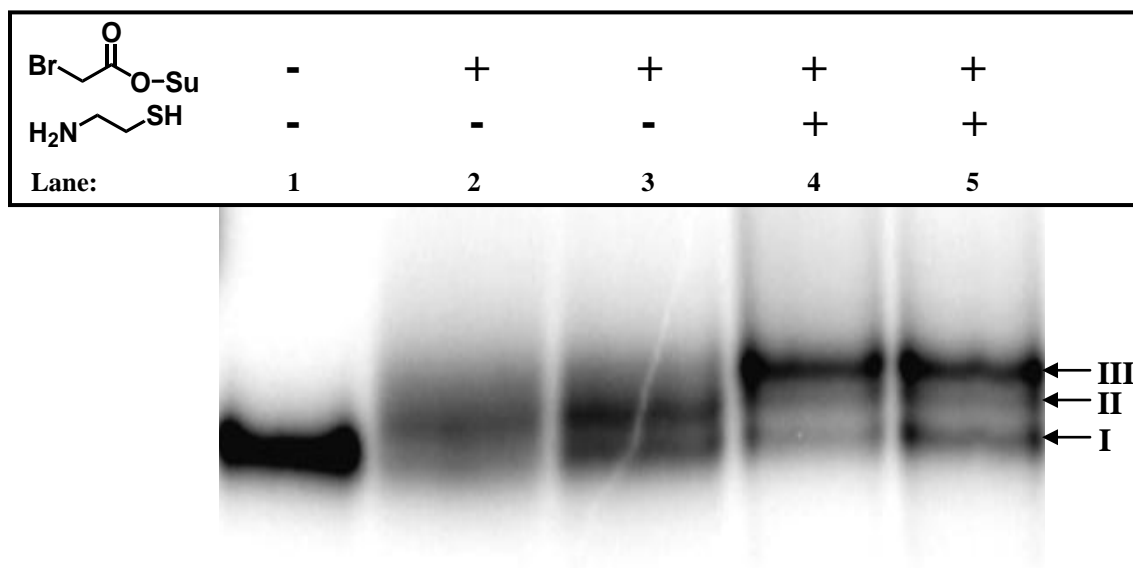


**Figure 2.16:** Analysis by gel shift assay of 2'-amino bromoacetylation of 5'-<sup>32</sup>P-labeled 2'-amino substrate analogue for the hairpin ribozyme. Lane 1: no reaction; Lane 2: treatment with 1:1 mixture of 250 mM BrAcNHS (in DMF) and 400 mM Na-Borate (pH 8); Lane 3: sample from Lane 2 treated with 200 mM 2-aminoethanethiol. Samples were analyzed by high resolution 20% d-PAGE.

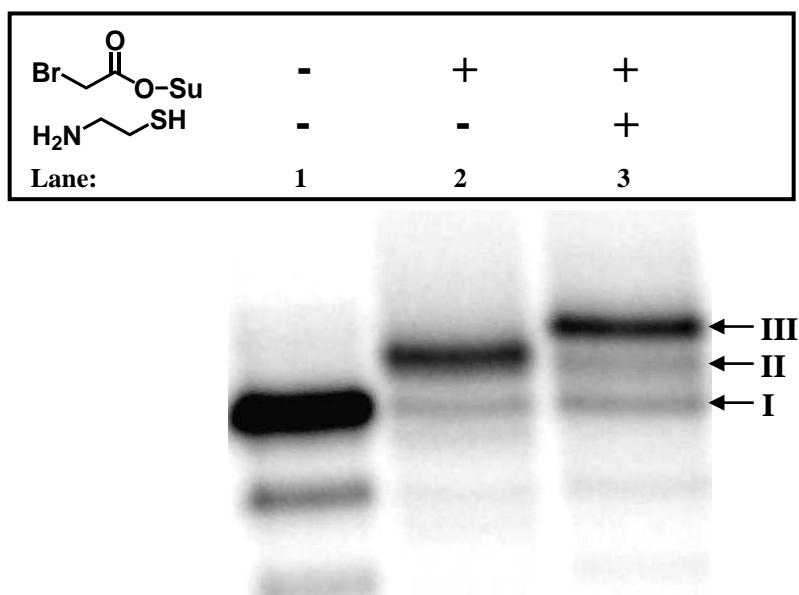
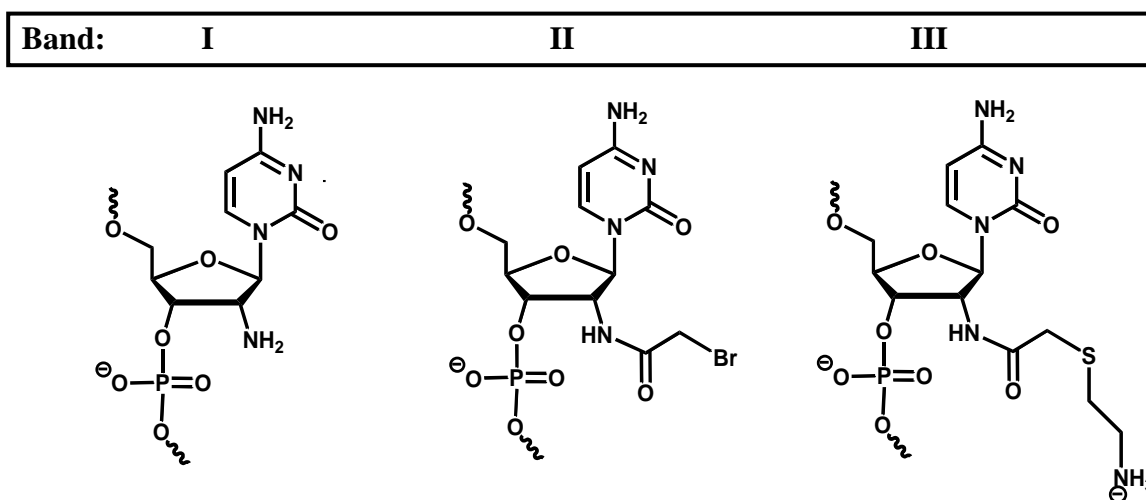


**Figure 2.17:** Structures assigned to Bands I, II, and III observed in Figures 2.15 and 2.16.

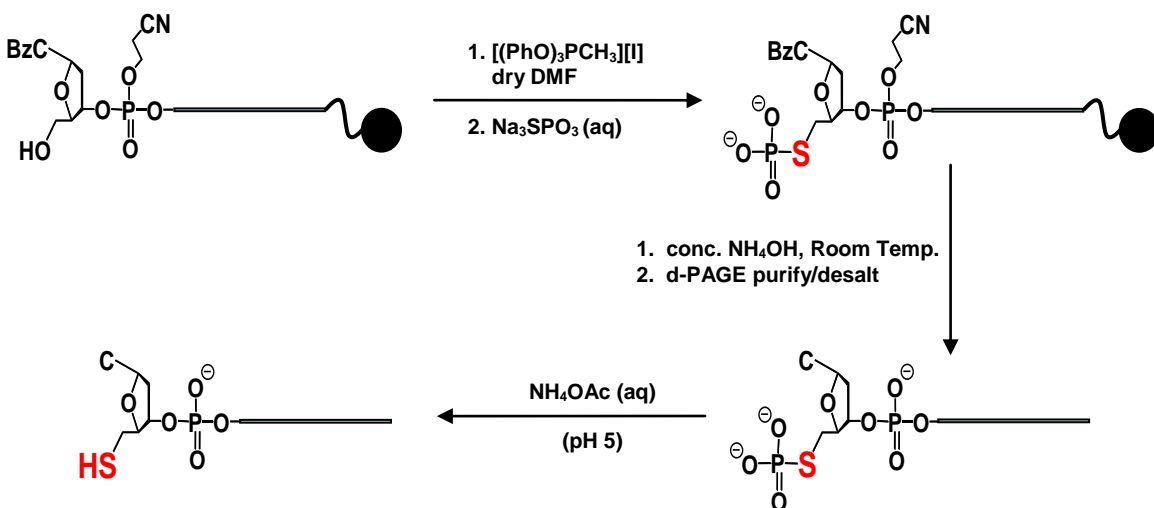


Given the reasonably high yield of the 2'-bromoacetylation reaction and the intractability of separating the reactive bromoacetamide from the 2'-amino-oligonucleotide starting material, the mixture was desalted and used directly in affinity labeling reactions. We were mindful that the contaminating 2'-amino-oligonucleotides might bind preferentially to the ribozyme or DNAzyme and inhibit the affinity labeling reaction. Therefore to minimize this effect, ribozyme or DNAzyme was mixed in a roughly 1:1 ratio with the mixture of affinity label and 2'-amino-oligonucleotide. Application of the affinity labels (synthesized as described above) to the 9<sub>25-11</sub> DNAzyme, the hammerhead ribozyme, and hairpin ribozyme is described in Chapters 3, 4, and 5, respectively.

### **2.3.2 A Novel Method for Synthesizing Bridging 5'-Thiophosphorylated DNA Oligonucleotides**

The ligation-based S-link substrate synthesis we envisioned (see Figure 2.23) first required that we synthesize the appropriate 5'-bridging thiophosphate terminated 3'-product oligonucleotides (Figure 2.18), which are required as ligation substrates. To accomplish this transformation, the 5'-hydroxyls of the protected, solid supported 3'-product oligonucleotides were first converted to the 5'-iodides by brief treatment with [(PhO)<sub>3</sub>PCH<sub>3</sub>]I in DMF.<sup>130</sup> The 5'-bridging thiophosphate moiety was then introduced by nucleophilic displacement of iodide by aqueous Na<sub>3</sub>SPO<sub>3</sub>.<sup>131</sup> Following room temperature NH<sub>4</sub>OH deprotection, the products were resolved by preparative d-PAGE and located by UV-shadowing.

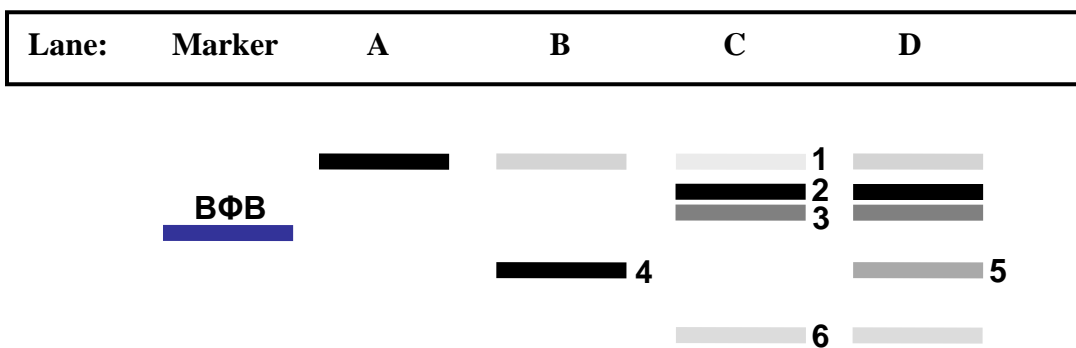
**Figure 2.18:** Summary of the oligonucleotide 5'-thiophosphorylation methodology developed in this work. Rapid dephosphorylation at pH 5 to yield the oligonucleotide-5'-thiol is diagnostic for the presence of the desired bridging 5'-thiophosphate linkage where sulphur is bonded to the 5'-carbon.



As diagrammed in Figure 2.19, bands corresponding to several different  $\text{NH}_4\text{OH}$  deprotected products were identified, in varying yields, following the 5'-iodination and 5'-thiophosphorylation procedures. A standard, deprotected oligonucleotide of the same sequence was 5'-phosphorylated for use as a migration standard (Figure 2.19, Lane B), as we hypothesized that this species would exhibit very similar electrophoretic mobility to the desired 5'-thiophosphorylated oligonucleotide, given their similarity in size and charge. The products of the iodination reaction were analyzed (Figure 2.19, Lane C) so that the products which result uniquely from the thiophosphate treatment would be readily identifiable. A unique product (Figure 2.19, Lane D), which co-migrated with the 5'-phosphorylated oligonucleotide, was observed only following treatment of the 5'-iodinated oligonucleotide with  $\text{NaSPO}_3$  (aq). This product was excised from the gel,

eluted, and desalted on G-10 spin column. The pH was maintained at 9 during product workup, as the rate of hydrolytic decomposition of bridging 5'-thiophosphates becomes problematic below pH ~8.<sup>136</sup>

**Figure 2.19:** Schematic representation of the UV-shadowing image observed after d-PAGE separation of the products of the 5'-iodination and 5'-thiophosphorylation reactions for the 9<sub>25</sub>-11 3'-product oligonucleotide. Lane A: Oligonucleotide treated with NH<sub>4</sub>OH and desalted. Lane B: Oligonucleotide treated with NH<sub>4</sub>OH, desalted, and treated with PNK and ATP. This lane provides an authentic standard of the 5'-O-phosphorylated 3'-product. Lane C: Oligonucleotide treated with [(PhO)<sub>3</sub>PCH<sub>3</sub>][I] in DMF, then NH<sub>4</sub>OH. Lane D: Oligonucleotide treated with [(PhO)<sub>3</sub>PCH<sub>3</sub>][I] in DMF, then Na<sub>3</sub>SPO<sub>3</sub> (aq), then NH<sub>4</sub>OH. BΦB = bromophenol blue (a PAGE mobility standard).



For two different sequences, the molecular formulas of the purified, 5'-thiophosphorylated oligonucleotides were confirmed by MALDI-TOF mass spectrometry (Figures 2.20C and 2.22A, Table 2.2). Importantly, in both cases, the 5'-thiophosphate was quickly and quantitatively hydrolyzed at pH 5 to yield 5'-thiol-oligonucleotides (Figures 2.20D and 2.22B). This unique reactivity proves that the thiophosphates are bonded to the 5'-carbons exclusively via sulphur, and not oxygen.<sup>136</sup>

**Figure 2.20:** MALDI-TOF analysis of the oligonucleotides identified by d-PAGE purification in Figure 2.19. (A) d-PAGE purified Band 1. (B) Unpurified products of the 5'-iodination reaction obtained after  $\text{NH}_4\text{OH}$  deprotection (Bands 1, 2, 3, and 6). (C) d-PAGE purified Band 6. (D) d-PAGE purified Band 6 treated with 25 mM  $\text{NH}_4\text{OAc}$  (pH 5) at 37 °C for 1 hour. Note that only the peaks corresponding to the 5'-thiol-oligonucleotide are observed following dephosphorylation in panel (D) (no peak corresponding to the 5'-hydroxy-oligonucleotide is visible, which indicates that the thiophosphate is bonded to the 5'-carbon exclusively via sulphur, not oxygen). The peak assignments, with their predicted and observed  $m/z$  values are summarized in Table 2.2.

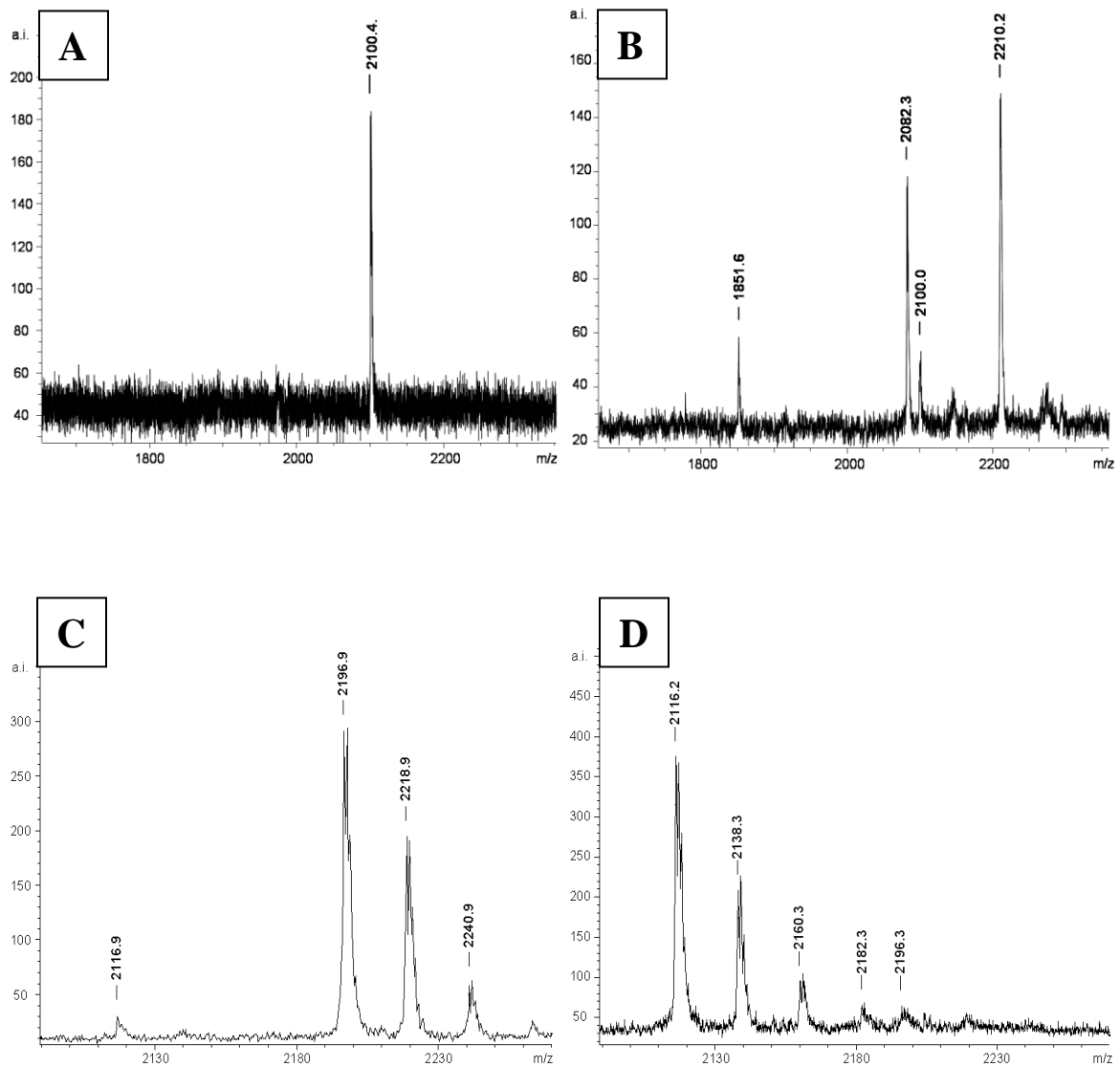


**Table 2.2:** Assignments and predicted and observed  $m/z$  values for the  $[M-H]^-$  molecular ions observed in the MALDI-TOF spectra in Figure 2.20.

Band <sup>a</sup>	Assignment <sup>b</sup>	$[M-H]^-$ Predicted	$[M-H]^-$ Observed	Figure No.
1	Oligo-5'-OH	2100.4	2100.4	2.20A
2	Oligo-5'-I	2210.3	2210.2	2.20B
3	See Figure 2.21	2082.4	2082.3	2.20B
5	Oligo-5'-SPO <sub>3</sub> H <sub>2</sub>	2196.3	2196.9	2.20C
6	See Figure 2.21	1851.3	1851.6	2.20B
n/a <sup>c</sup>	Oligo-5'-SH	2116.4	2116.2	2.20D

<sup>a</sup> The assignments correspond to the bands indicated in Figure 2.19.

<sup>b</sup> Oligo refers to the 9<sub>25</sub>-11 3'-product which has the sequence 5'-d(GTCTGTT).

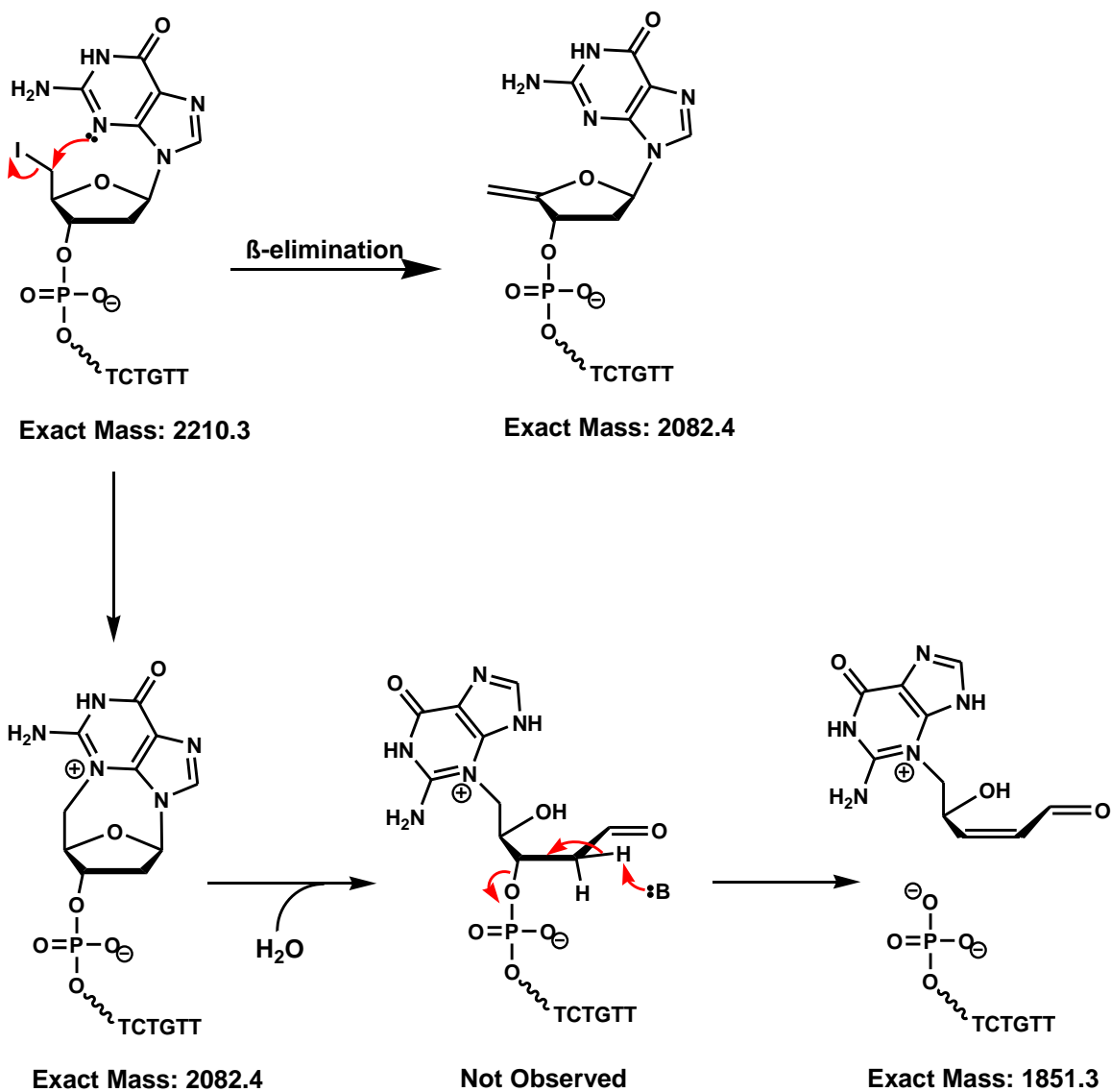
<sup>c</sup> This product was not PAGE purified.

MALDI-TOF spectra were much more difficult to obtain for the 16-mer hammerhead 3'-product (Figure 2.22) than for the 7-mer 9<sub>25</sub>-11 3'-product (Figure 2.20). Much higher laser power was required to obtain reasonable peak intensities. As a result, the mono-isotopic resolution seen in Figure 2.20 was not observed, which diminishes the mass accuracy obtained. We suspect that the application of higher laser power is also the cause of artifactual peaks that were observed (namely  $m/z = 4740.7$  and  $4771.8$  in Figure 2.22A). The peak at  $m/z = 4771.8$  is consistent with fission of the 5'-carbon-sulphur bond, which would decrease the oligonucleotide mass by 133 (predicted  $m/z$ : 4772.8). Following incubation at pH 5, a minor peak was also observed in Figure 2.22B with  $m/z = 4787.5$ , close to that for the 5'-hydroxy-terminated oligonucleotide (predicted  $m/z = 4789.8$ ). This result raises concern that the sample may be contaminated with

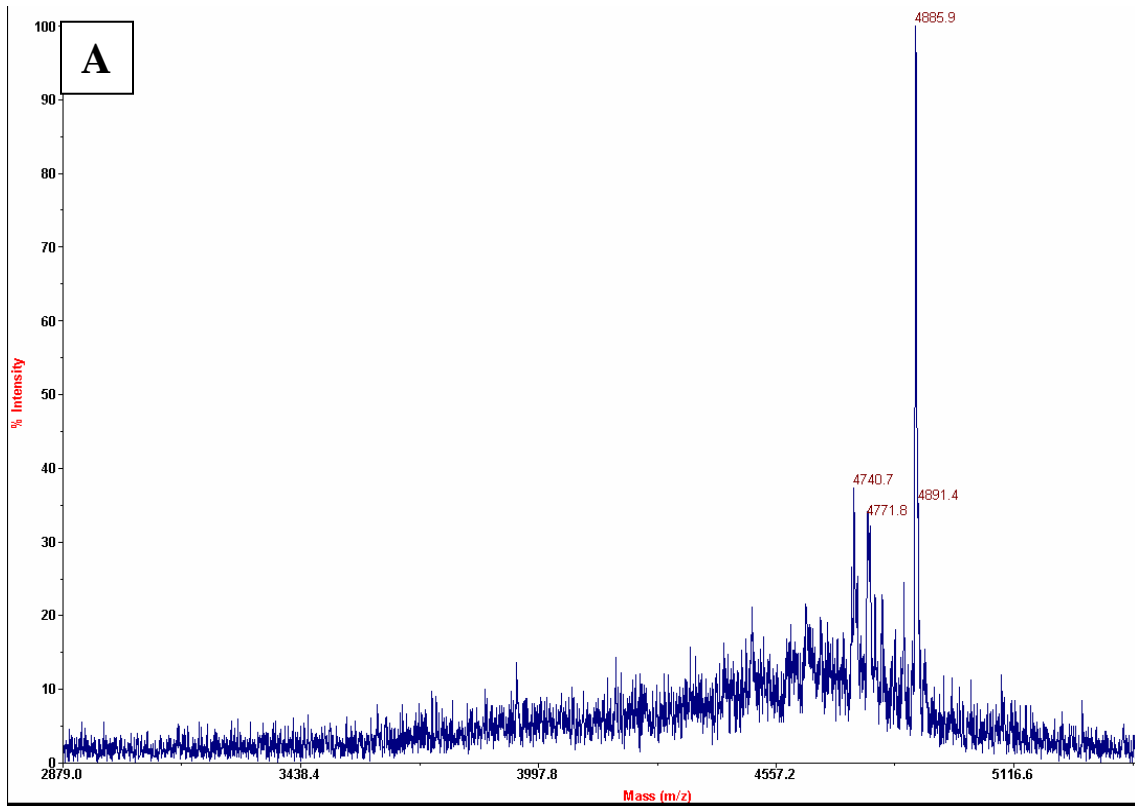
nonbridging (oxygen-linked) 5'-thiophosphorylated oligonucleotide, although this compound would not be expected to undergo rapid 5'-dephosphorylation. This concern is also allayed based on the characterization data for the ligated S-link substrate (Figure 2.25 – *vide infra*), which demonstrate the presence of only the 5'-bridging phosphorothioate linkage.

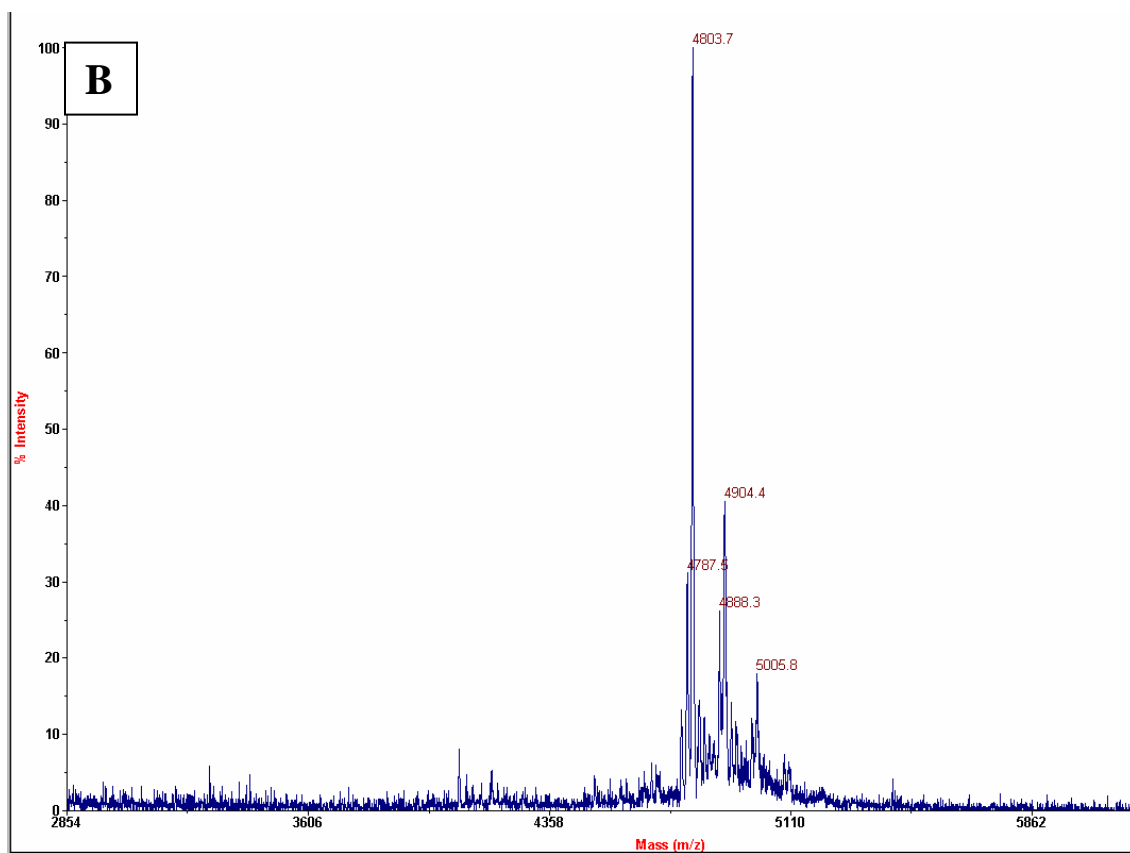
The side products noted in Figure 2.19 (Bands 1, 2, 3, and 6) were also identified mass spectrometrically. For example, these four side products are identified in the MALDI-TOF spectrum obtained for the product mixture obtained following 5'-iodination of the 9<sub>25</sub>-11 3'-product oligonucleotide (Figure 2.20B, Table 2.2). In light of these band assignments, and considering the intensities observed for the assigned bands in Figure 2.19, it is clear that the displacement of the 5'-iodide by thiophosphate is not efficient given the large amount of starting material (Figure 2.19, Band 2) left unreacted. A small amount of 5'-hydroxyl-oligonucleotide is also observed (Band 1), which indicates either incomplete 5'-iodination or alkaline hydrolysis of the 5'-iodide during NH<sub>4</sub>OH deprotection. The molecular weight of Band 3 (Figure 2.20B) is consistent with either 4',5'- $\beta$ -elimination of iodide or thiophosphate, or 5',N3-intramolecular alkylation (Figure 2.21). The formation of either product from the 5'-iodide is well known,<sup>137-139</sup> although 4',5'- $\beta$ -elimination is usually carried out with stronger bases than NH<sub>4</sub>OH, such as NaOMe. The molecular weight of Band 6 is consistent with the 5'-phosphorylated oligonucleotide that would result from  $\beta$ -elimination at the abasic site which could form as a result of guanine N3 alkylation in the 5',N3-intramolecular alkylation product (Figure 2.21).

**Figure 2.21:** Possible mechanisms of side product formation during oligonucleotide 5'-iodination/ $\text{NH}_4\text{OH}$  deprotection (based on  $m/z$  values for  $[\text{M}-\text{H}]^-$  molecular ions in Figure 2.20B and Table 2.2).



**Figure 2.22:** MALDI-TOF analysis of (A) the d-PAGE purified, 5'-thiophosphorylated 3'-product for the *S. mansoni* hammerhead ([M-H]<sup>-</sup> predicted m/z: 4885.8; observed m/z: 4885.9) and (B) the 5'-thiol-oligonucleotide produced by treatment with pH 5 NH<sub>4</sub>OAc buffer ([M-H]<sup>-</sup> predicted mass: 4805.8; observed mass: 4803.7).





Following elution from the gel and desalting, the yield of the desired 5'-thiophosphorylated oligonucleotides was quite low (~10%). However, thiophosphorylation of a standard 1  $\mu\text{mol}$  scale oligonucleotide sample furnished more than ample quantities for our purposes, at low cost, by a simple procedure. The purified 5'-thiophosphorylated-oligonucleotides were stored at  $-20\text{ }^{\circ}\text{C}$  in pH 9 solution, where the 5'-thiophosphate is relatively stable to hydrolysis.<sup>136</sup>

### **2.3.3 A Novel Method for Synthesizing Bridging 5'-Phosphorothioate Substrate Analogues:**

With the 5'-thiophosphorylated 3'-product oligonucleotides in hand, radiochemical quantities of the S-link substrates could be produced by templated ligation to the appropriate 5'-<sup>32</sup>P-labeled-5'-products. Specifically, the 5'-<sup>32</sup>P-labeled-5'-product and 5'-thiophosphorylated-3'-product were annealed to a complementary, biotinylated DNA template, and joined using DNA ligase to yield the full length S-link substrate (Figure 2.23). The resulting biotinylated duplex was bound to streptavidin magnetic particles. Brief washing of the solid phase with low ionic strength buffer (5 mM Na-PIPES) efficiently released unreacted starting materials from the solid phase bound template without significant release of the S-link product (Figure 2.24, Lane 3). This separation is based on the different melting temperatures of the ligation substrates and products (the template forms just 7 base pairs with each of ligation substrates, compared to 14 base pairs with the S-link substrates). The more strongly bound S-link substrate was subsequently liberated from the solid phase under mildly denaturing conditions (10% formamide in water, 37 °C) and desalted (Figure 2.24, Lanes 4 & 5). This procedure very effectively separated the desired S-link substrate and unreacted ligation substrates to yield S-link substrate samples of very high purity (usually >97%). Given the instability of the bridging phosphorothioate linkage, S-link substrates were characterized and used in kinetic experiments within ~2-3 hours of preparation.

**Figure 2.23:** Ligation based synthesis of the bridging 5'-phosphorothioate (S-link) substrate developed in this work.

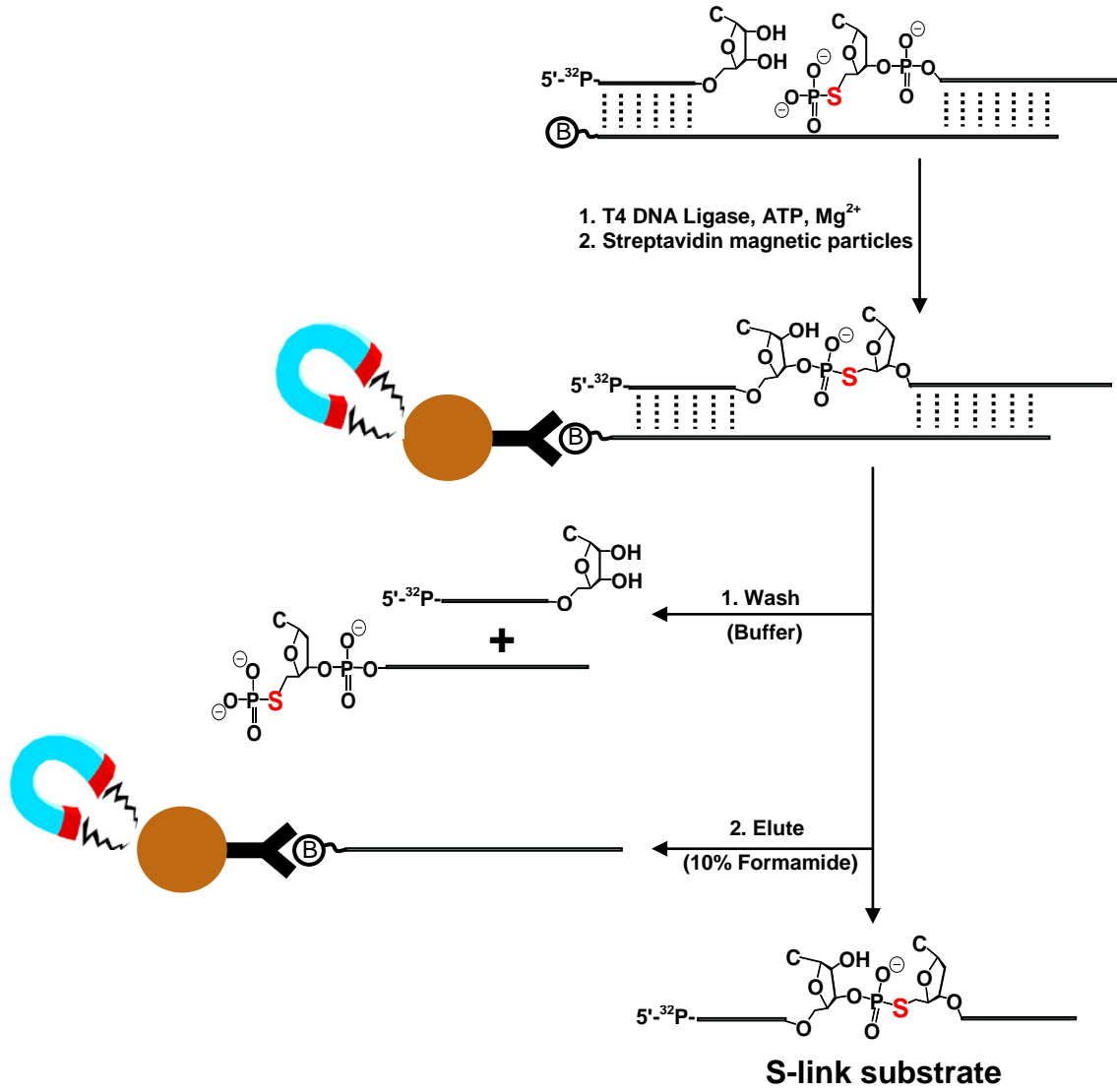
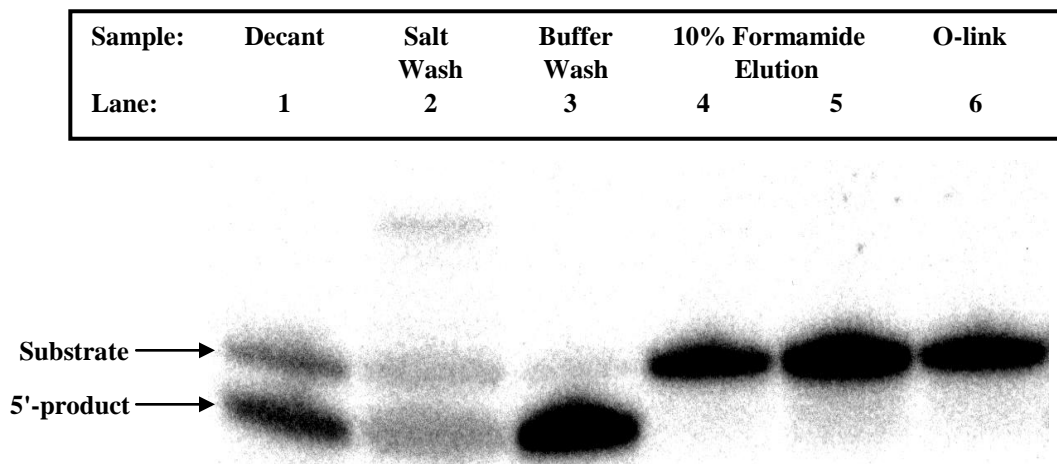


**Figure 2.24:** Analysis by 20% TAE d-PAGE of radiolabeled oligonucleotides released upon decanting and washing the solid phase-bound S-link ligation products. Lane 1: material decanted following binding of ligation products to solid phase; Lane 2: material washed from the solid phase with 100mM NaCl, 25 mM Na-PIPES, 10 mM EDTA; Lane 3: material washed from the solid phase with 5 mM Na-PIPES; Lanes 4 & 5: material eluted with two successive portions of aqueous 10% formamide (37 °C); Lane 6: authentic 5'-<sup>32</sup>P-labeled O-link substrate.



Following the work of Kuimelis and McLaughlin,<sup>100, 101, 118</sup> the S-link substrate was maintained at pH 6.7 (Na-PIPES) in the absence of divalent metal cations whenever possible during preparation and handling (the bridging phosphorothioate linkage is relatively stable under these neutral conditions). Accordingly, in kinetic experiments, ribozyme reactions were quenched in formamide solution containing Na-PIPES pH 6.7, and the samples were analyzed using PAGE gels cast in TAE/urea buffer (pH 6.7), as opposed to the standard TBE/urea buffer (pH 8.3). Note that Mg<sup>2+</sup> is required in the ligation buffer, but was not detrimental given its relatively low concentration and the fact that S-link substrates are particularly stable in the context of a DNA duplex structure.<sup>118</sup>

The constitution and purity of the S-link substrates were verified by comparison of their reactivity with native O-link substrates of the same sequence. The 5'-<sup>32</sup>P-labeled S-link and O-link substrates were indistinguishable by d-PAGE (Lanes 1 & 2 in Figures 2.25 and 2.26), as were their 5'-<sup>32</sup>P-labeled-5'-cleavage products (for example, Lanes 3 and 4 in Figures 2.25 and 2.26). As expected, both S-link substrates were efficiently cleaved by the appropriate nucleic acid catalysts (Lanes 3 & 4 in Figures 2.25 and 2.26) and by RNaseA (Lanes 5 & 6 in Figures 2.25 and 2.26). Cleavage of the 5'-bridging phosphorothioate linkage in RNA is known to be strongly accelerated in the presence of soft metal cations, whereas cleavage of native phosphodiester linkage in RNA is not.<sup>28,100</sup> Accordingly, treatment with Cd<sup>2+</sup> (aq) caused rapid cleavage of the S-link substrates, but not the O-link substrates (Lanes 9 & 10 in Figure 2.25; Lanes 8-11 in Figure 2.26). The results of brief treatment with NaOH (aq) (Lanes 7 & 8 in Figure 2.25) or Ag<sup>+</sup> (aq) (Lanes 11 & 12 in Figures 2.25 and 2.26) provide the most conclusive demonstration of the purity of the S-link substrates: both treatments lead to quantitative cleavage of the S-link substrates,<sup>68</sup> whereas the O-link substrates are completely unaffected by Ag<sup>+</sup> treatment and are cleaved to only a small extent by NaOH treatment. These results demonstrate that the S-link substrate synthesized via our ligation-based method is not detectably contaminated with any native RNA linkage. The S-link substrates, synthesized as described here, are applied to the 9<sub>25-11</sub> DNAzyme in Chapter 3 and to the hammerhead ribozyme in Chapter 4.

**Figure 2.25:** Comparison of the properties of the O-link and S-link substrates for the *S. mansoni* hammerhead ribozyme. Lanes 1 & 2: no treatment. Lanes 3 & 4: 1  $\mu\text{M}$  wildtype ribozyme, 2 mM  $\text{MgCl}_2$ , 50 mM Na-PIPES pH 7 for 10 minutes. Lanes 5 & 6: 1 unit RNaseA, 50 mM Na-PIPES pH 7 for 10 minutes. Lanes 7 & 8: 50 mM NaOH at 60  $^\circ\text{C}$  for 10 minutes. Lanes 9 & 10: 5 mM  $\text{Cd}(\text{NO}_3)_2$  for 10 minutes. Lanes 11 & 12: 5 mM  $\text{AgNO}_3$  for 10 minutes. Samples were analyzed by 20% TAE d-PAGE.

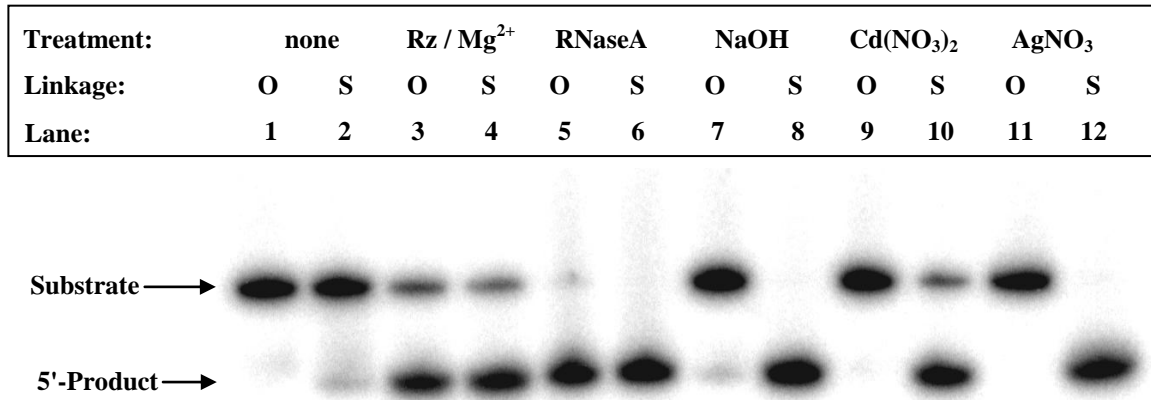
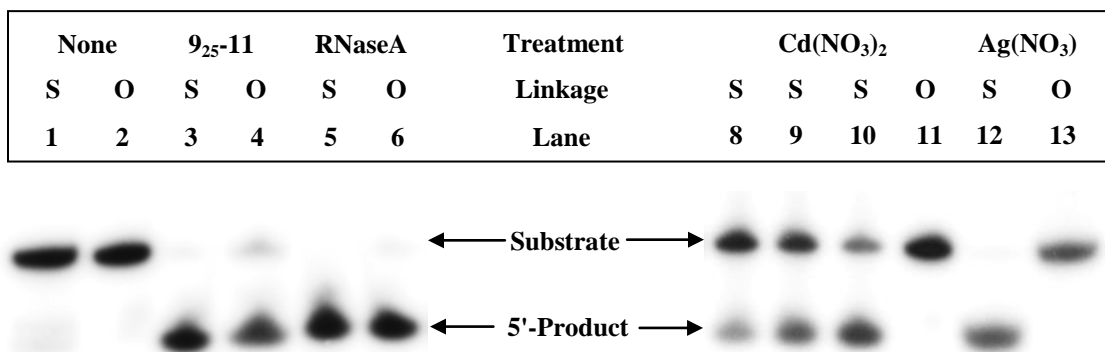


**Figure 2.26:** Comparison of the properties of the S-link and O-link substrates for the 9<sub>25</sub>-11 DNAzyme. Lanes 1 & 2: no treatment. Lanes 3 & 4: 5  $\mu\text{M}$  9<sub>25</sub>-11 in 200 mM NaCl, 50 mM Tris-HCl pH 8, 1 mM EDTA for 2 hours. Lanes 5 & 6: 1 unit RNaseA in 10 mM Tris-HCl pH 8 for 10 minutes. Lanes 8 to 10: (S-link) 5 mM  $\text{Cd}(\text{NO}_3)_2$  for 1, 3, and 10 minutes. Lane 11: (O-link) 5 mM  $\text{Ag}(\text{NO}_3)$  for 10 minutes. Samples were analyzed by 20% TAE d-PAGE.



Our simple, reliable method produced consistently pure S-link substrates in 2-3 hours without the need to synthesize specialty phosphoramidites. This method may be especially advantageous in producing substrates where the phosphorothioate linkage occurs near the 3'-end of longer oligonucleotides. In such cases, yields tend to be lowered because the sensitive phosphorothioate linkage is introduced early in the synthesis and is subjected to many subsequent nucleotide coupling cycles. Our S-link substrate synthesis methodology is limited in practice to radiochemical scale preparations. Scale up of the procedure to nanomole quantities (as required for multiple turnover analysis) is possible in principle, but the cost of, and impracticality in handling the large amount of streptavidin magnetic particles required would likely be prohibitive. It should also be stressed that our methodology has been applied only to the synthesis of chimeric embedded ribose/DNA substrates, as we were concerned that neither standard 2'-*O*-TBDMS protected RNA, nor deprotected RNA would be likely to survive the thiophosphorylation reaction (3 days in 200 mM NaSPO<sub>3</sub> (aq) at pH ~12).

Future work will seek to implement RNA 2'-protection strategies that will withstand the 5'-thiophosphorylation conditions, so that S-link substrates consisting entirely of RNA can be produced by our ligation methodology. We anticipate that thiophosphorylation could be successful using the non-standard, photo-labile 2'-*O*-nitrobenzyl protecting group shown in Figure 2.7.<sup>68</sup> In this case the protected RNA would likely be stable to the thiophosphorylation conditions as well as NH<sub>4</sub>OH deprotection of the nucleobases. Following these procedures, photo-deprotection of the 2'-oxygens would yield the desired 5'-thiophosphorylated-3'-product (composed entirely

of RNA), which could then be annealed to a DNA template and ligated to the appropriate 5'-product (also composed entirely of RNA).

# CHAPTER 3: MECHANISTIC INVESTIGATION OF THE 9<sub>25</sub>-11 DNAZYME: A RIBONUCLEASE A MIMIC?

## 3.1 INTRODUCTION

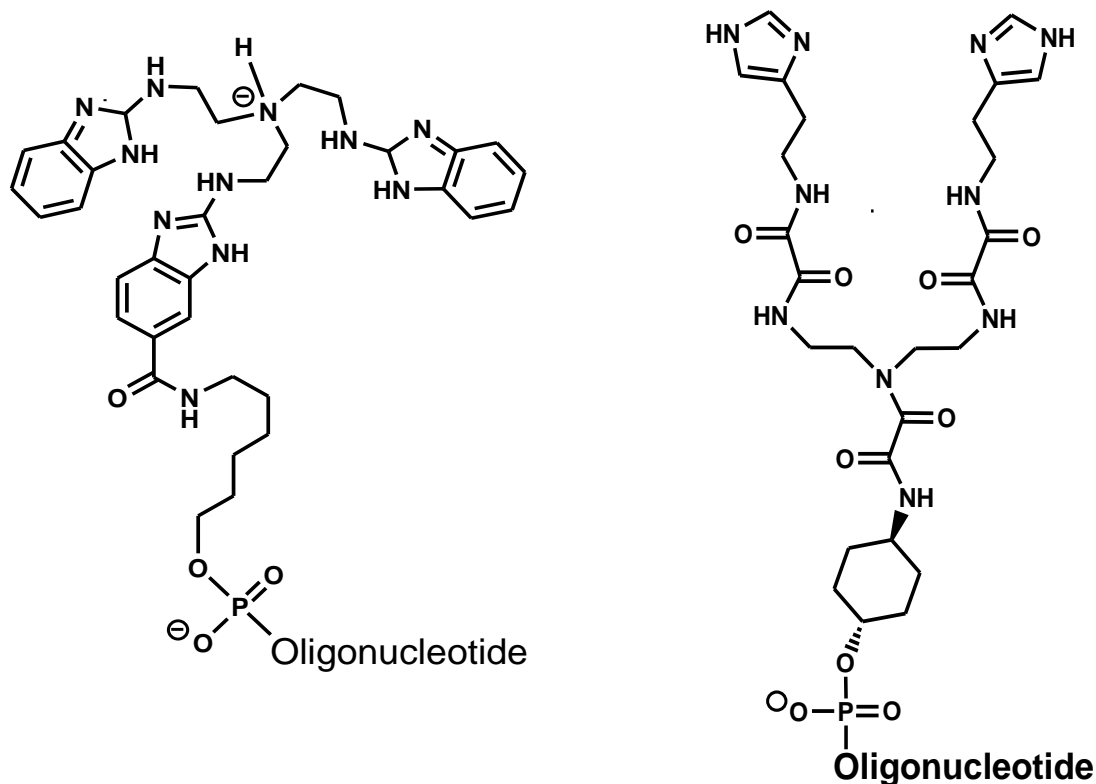
### 3.1.1 RNaseA Mimicry

As discussed in Section 1.4.1, the protein enzyme Ribonuclease A (RNaseA) is particularly noteworthy because it cleaves RNA with catalytic perfection without the assistance of a metal cation cofactor. From the perspective of basic research, the design of synthetic catalysts that imitate this remarkably efficient organo-catalytic reaction mechanism presents a formidable challenge for biomimetic chemists.<sup>16, 140</sup> Furthermore, addressing this challenge serves to test and expand our understanding of the principle underlying the enzymatic mechanism. From a practical point of view, the property of metal cation independence makes RNaseA mimicry an attractive goal in the development of synthetic catalysts for *in vivo* RNA cleavage because the physiological concentrations of appropriate M<sup>2+</sup> cations are often much lower than is required for efficient activity of many M<sup>2+</sup>-dependent RNA cleavage catalysts, such as DNAzymes (see Section 1.5.2).

Efforts toward RNaseA mimicry in synthetic catalysts have generally involved the conjugation of imidazole, amine, guanidine, or related functionalities to a variety of scaffolds; designs have ranged from low molecular weight organic compounds,<sup>141-144</sup> to larger scaffolds such as cyclodextrins and peptides.<sup>16, 140, 145, 146</sup> In some cases, M<sup>2+</sup>-independent cleavage of RNA or model phosphodiester substrates has been demonstrated; however, these types of synthetic constructs generally lack sequence

specificity, which is essential for potential biotechnological/medicinal applications. Sequence specificity can be engineered by covalently linking synthetic RNaseA mimics to oligonucleotides or PNA “guide sequences” (Figure 3.1), so that the catalytic activity is directed specifically to the intended RNA target site through predictable Watson-Crick base-pairing interactions.<sup>147-152, 164</sup> Because small molecule RNaseA mimics are usually attached to the 5'-terminus of the guide sequence, the catalyst as a whole binds to both cleaved and uncleaved target RNA via duplex interactions of similarly high stability. In this situation, product release is likely to be slow, and to the best of our knowledge, multiple turnover has never been demonstrated for such catalysts in the presence of excess substrate.

**Figure 3.1:** Examples of synthetic, sequence specific RNaseA mimics that contain cationic amine and/or imidazole (or related) functionalities.<sup>147, 153</sup>



DNAzymes and ribozymes cleave RNA with both high sequence specificity and reasonably efficient catalytic turnover in some cases, but the catalytic power ( $k_{\text{cat}}/k_{\text{uncat}}$ ) of nucleic acid catalysts generally falls far short of that of RNaseA. Moreover, for optimal activity, nucleic acid catalysts typically require  $M^{2+}$  concentrations (usually 5-25 mM) which exceed physiological levels ( $<1$  mM for  $Mg^{2+}$ ).<sup>154-156</sup> The precise role of  $M^{2+}$  in nucleic acid catalysis has been controversial, and in some cases direct participation of  $M^{2+}$  in active site chemistry appears to be unlikely based on (1) the observation of reasonably efficient RNA cleavage at high (molar) monovalent cation concentrations,<sup>64, 90, 123, 157-163</sup> and (2) recent evidence that suggests RNA functional groups play direct roles

in general acid/base catalysis in many cases (see Sections 4.1 & 5.1, *vide infra*).<sup>165</sup> Nevertheless, the common  $M^{2+}$ -dependence and general catalytic inferiority of nucleic acid catalysts has been attributed in part to the absence of positively charged functional groups, as well as a lack of functionality well suited for general acid/base catalysis at physiological pH.<sup>166</sup> Given these perceived shortcomings in catalytic nucleic acids, the development of synthetic sequence specific RNaseA mimics for potential *in vivo* applications remains an area of active research.

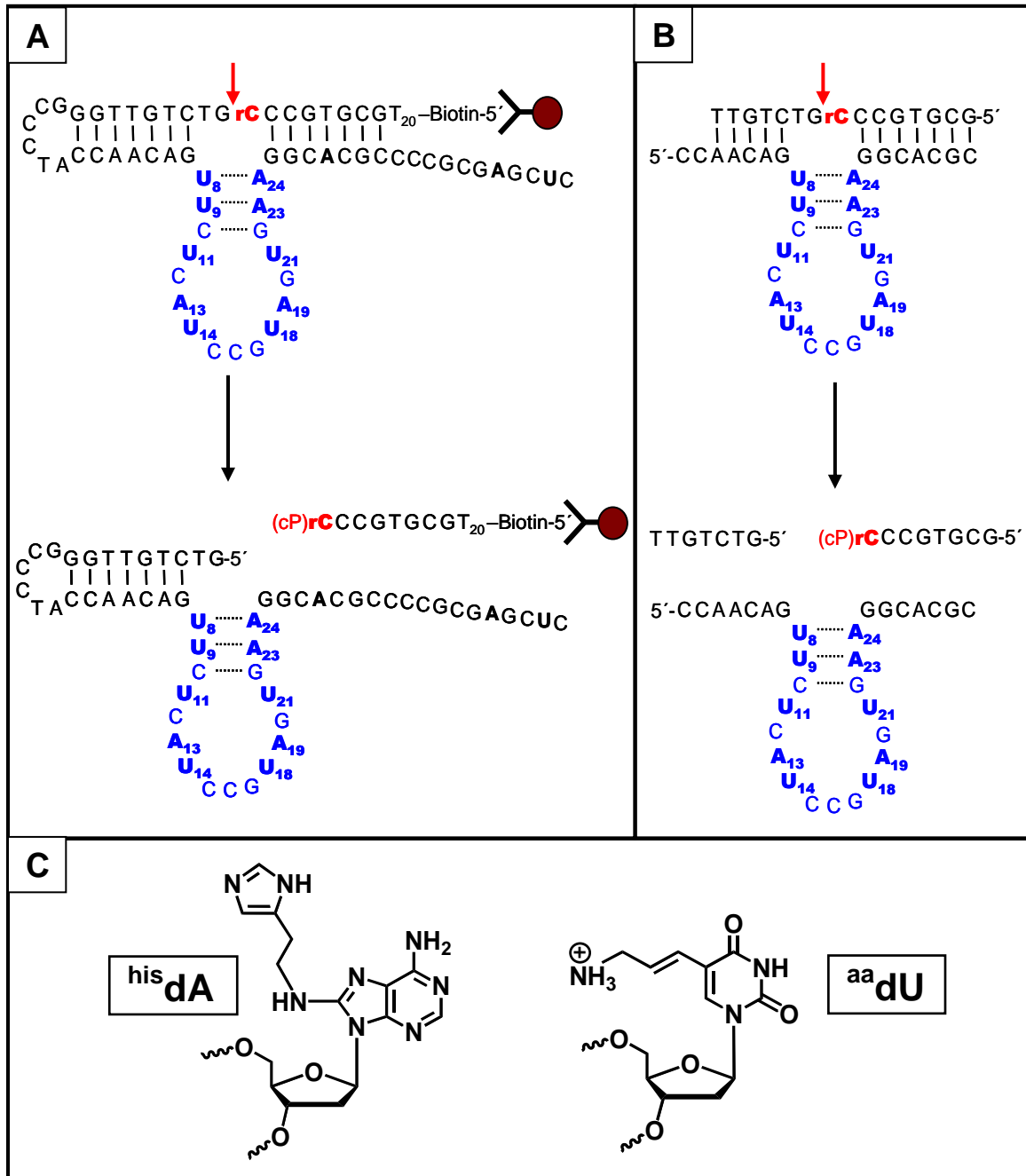
### 3.1.2 The 9<sub>25</sub>-11 DNAzyme

The 9<sub>25</sub>-11 DNAzyme was discovered in an effort to integrate the desirable properties of sequence specificity (characteristic of DNAzymes and ribozymes) and  $M^{2+}$ -independent catalysis (characteristic of RNaseA). The 9<sub>25</sub>-11 DNAzyme was identified through a combinatorial *in vitro* selection (SELEX)<sup>69-71</sup> experiment in which two of the natural deoxy-nucleotide monomers were replaced with analogues bearing imidazoles and cationic amines.<sup>87</sup> This work sought to test the specific hypothesis that the catalytic inferiority of RNA-cleaving DNAzymes in the absence of  $M^{2+}$ -cations (at physiological ionic strength and pH) could be alleviated by endowing them with RNaseA-like functionality. In a more general sense, this experiment sought to address the challenge of RNaseA mimicry through a combinatorial approach, rather than through rational design.

Because phenotype (substrate cleavage) and genotype (catalyst sequence) must be covalently linked in an *in vitro* selection experiment, 9<sub>25</sub>-11 was identified first as the self-cleaving (or *cis*-cleaving) form (Figure 3.2A).<sup>87</sup> Subsequently, the hairpin-loop that joins the catalytic domain to the substrate strand was removed to produce *trans*-cleaving

9<sub>25</sub>-11 (Figure 3.2B), which is a true catalyst capable of intermolecular substrate cleavage with multiple turnover.<sup>93</sup> Although the hypothetical 2D structure of 9<sub>25</sub>-11 is reminiscent of other small ribozymes and DNazymes, 9<sub>25</sub>-11 presents additional chemical functionality owing to its 10 unnatural modified bases: four 8-histaminy-2'-deoxy-adenosine (<sup>his</sup>dA) and six 5-(amino-allyl)-2'-deoxy-uridine (<sup>aa</sup>dU) residues (Figure 3.2C). Therefore, at least with regard to structure, 9<sub>25</sub>-11 integrates characteristics of both DNazymes and synthetic RNaseA mimics. The focus of this work is to establish whether 9<sub>25</sub>-11 actually uses its added functionality to integrate an RNaseA-like catalytic mechanism within a DNzyme scaffold.

**Figure 3.2:** (A) The *cis*-cleaving 9<sub>25-11</sub> DNAzyme and (B) the *trans*-cleaving 9<sub>25-11</sub> DNAzyme in complex with its substrate. The embedded ribo-C cleavage site (red) is indicated by the arrow; the catalytic stem loop of 9<sub>25-11</sub> (blue) is numbered from the 5'-terminus of the DNAzyme strand (cP denotes a 2',3'-cyclic phosphate). (C) Structures of the modified nucleotides incorporated into 9<sub>25-11</sub>: 8-histaminyl-2'-deoxy-adenosine (<sup>his</sup>dA) and 5-(amino-allyl)-2'-deoxyuridine (<sup>aa</sup>dU). These modified nucleotides are indicated in panel (A) as bold text **A** and **U**, respectively.



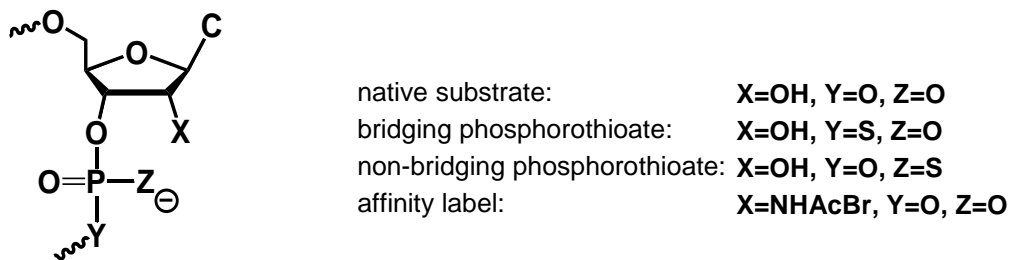
### 3.1.3 Mechanistic Characterization of 9<sub>25</sub>-11 Catalysis

The 9<sub>25</sub>-11 DNAzyme has been shown to cleave a ribophosphodiester embedded within a chimeric DNA substrate oligonucleotide with reasonably efficient turnover in the absence of a M<sup>2+</sup> cofactor;<sup>93</sup> however, the chemical basis for catalysis has not been investigated in detail. Given that the synthetic modifications were incorporated into the *in vitro* selection experiment to make available RNaseA-like functionality, we were particularly curious whether 9<sub>25</sub>-11 represents a functional RNaseA mimic. To address this matter, we have undertaken a detailed enzymological characterization of 9<sub>25</sub>-11 catalysis, in an effort to determine if the synthetic modifications indeed play the intended roles in RNaseA-like catalysis, rather than supporting structural roles. Notably, several other synthetically modified nucleic acid catalysts have been discovered by *in vitro* selection,<sup>92, 167-172</sup> but little subsequent investigation has been reported to characterize the mechanistic roles of the synthetically appended functionalities. Thus, 9<sub>25</sub>-11 presents a useful test case in which to assess the actual contribution to catalysis of synthetic modifications in a nucleic acid catalyst.

We began this study by verifying that the general properties of 9<sub>25</sub>-11 catalysis, such as the structure of the reaction products, the pH-rate profile, and the solvent kinetic isotope effects are consistent with RNA cleavage via rate limiting, general acid/base catalyzed 2'-transphosphorylation. We then probed for specific DNAzyme functional groups involved in active site chemistry using 2'-bromoacetamide affinity labeling and bridging and nonbridging phosphorothioate substrate cleavage experiments (Figure 3.3), each in the context of DNAzyme functional group deletion. The results of these experiments provide strong evidence for imidazole-mediated general acid and base

catalysis, as well as the involvement of a cationic amine in a diastereoselective, transition state-stabilizing interaction with the scissile phosphate. The results presented here for 9<sub>25</sub>-11 strongly parallel those from analogous mechanistic experiments with RNaseA, and provide compelling functional evidence that 9<sub>25</sub>-11 mimics the active site mechanism of RNaseA. Our findings emphasize the value of synthetic modifications for expanding the mechanistic repertoire of nucleic acid catalysts, in this case to improve DNAzyme mediated RNA-cleavage at low ionic strength in the absence of a M<sup>2+</sup> cofactor.

**Figure 3.3:** Substitutions made at the scissile ribonucleotide in the substrate analogues used in this study.



### 3.1.4 Metal Cation Binding Properties of 9<sub>25</sub>-11

In light of recent interest in DNAzymes as metal biosensors,<sup>172-182</sup> we inquired whether the synthetic modifications in 9<sub>25</sub>-11 might impart new or more specific metal cation binding properties, perhaps not otherwise characteristic of nucleic acids. Although no evolutionary pressure for metal cation binding had been applied in the selection of 9<sub>25</sub>-11, we wondered if the dense array of synthetic appendages might form specific metal cation binding sites fortuitously. In particular, we hypothesized that the imidazole

appendages might be useful for binding such metal cations as  $\text{Ni}^{2+}$ ,  $\text{Zn}^{2+}$ ,  $\text{Cu}^{2+}$ , or  $\text{Hg}^{2+}$ , all of which have high affinity for imidazole ligands,<sup>183-185</sup> but are not noted for particularly strong binding to natural nucleic acids (recent work has identified  $\text{Hg}^{2+}$  as an notable exception – *vide infra*).

Given the presence of many potential ligand sites (namely Lewis-basic nucleobase hetero-atoms and phosphate oxygens) many interactions between nucleotide structures and metal cations have been characterized, although modest association constants were usually observed.<sup>186-190</sup> In a biochemical context, the most widely appreciated nucleic acid-metal cation interactions include the ubiquitous binding of alkaline earth metal cations (usually  $\text{Mg}^{2+}$ ) by phosphates in both catalytic and structural contexts.<sup>191, 192</sup> With the exception of metal binding by N7 of guanine<sup>193, 194</sup> (platinum anti-cancer complexes<sup>195-197</sup> are a notable example), nucleic acids do not generally function as particularly high affinity ligands for most transition metal cations.<sup>188</sup> However, since the work described here was published, very strong  $\text{Hg}^{2+}$  binding within  $\text{Hg}^{2+}$ -mediated T-T base pairs<sup>198</sup> in duplex DNA has been characterized and exploited in the context of oligonucleotide<sup>199</sup> and DNAzyme<sup>176</sup>  $\text{Hg}^{2+}$  sensors.

Synthetic modification of nucleic acids has proven fruitful for expanding metal binding properties in nucleic acids. For example, metal-mediated base pairing has been engineered between chelating nucleobase analogues that strongly bind  $\text{Ag}^{+}$ <sup>200, 201</sup> or  $\text{Cu}^{2+}$ <sup>202-205</sup>. With respect to catalysis, unusual metal ion binding properties have been observed for synthetically modified DNAzymes and ribozymes: for example, imidazoles have been introduced for  $\text{Zn}^{2+}$  binding,<sup>170</sup> and pyridyl groups for  $\text{Pd}^0$ <sup>167, 168</sup> or  $\text{Cu}^{2+}$ <sup>169</sup> binding. Phosphorothioate substitution (both bridging and nonbridging) at known  $\text{Mg}^{2+}$

binding sites has also been used in the context of nucleic acid catalysts to engineer specificity for soft metal cations. The sulphur atom in the phosphorothioate provides a soft ligand which has been exploited to produce catalysts whose activities depend specifically upon the presence of  $\text{Hg}^{2+}$ ,<sup>206</sup>  $\text{Cd}^{2+}$ ,<sup>161, 207</sup> or  $\text{Mn}^{2+}$ ,<sup>103</sup> for example.

To characterize metal binding by 9<sub>25</sub>-11, the effect of a wide variety of metal cations on 9<sub>25</sub>-11 self-cleavage was examined. Of those metal cations examined,  $\text{Hg}^{2+}$  and to lesser extent  $\text{Cu}^{2+}$ , showed potent inhibition of 9<sub>25</sub>-11 activity. We therefore quantified the binding of these two metal cations by determining their dissociation constants (110 nM for  $\text{Hg}^{2+}$  and 2.5  $\mu\text{M}$  for  $\text{Cu}^{2+}$ ). We have also shown that  $\text{Hg}^{2+}$  inhibition is readily reversible, as 9<sub>25</sub>-11 activity was readily restored upon addition of  $\text{Hg}^{2+}$  chelators. Overall, our findings suggest that synthetic modification of DNAzymes should be useful for expanding their metal cation binding properties.

## 3.2 MATERIALS AND METHODS

### 3.2.1 Chemicals and Biochemicals

All chemicals and buffers salts were purchased from Sigma-Aldrich (molecular biology or reagent grade purity) and were used as received. Oligonucleotides were synthesized the University of Calgary DNA Services Lab and Trilink Biotech. The preparation of the modified nucleoside phosphoramidites used in the synthesis of *trans*-cleaving 9<sub>25</sub>-11, and the preparation of 5-(amino-allyl)-dUTP (<sup>aa</sup>dUTP) and 8-histaminyl-dATP (<sup>im</sup>dATP) used to produce *cis*-cleaving 9<sub>25</sub>-11, have been described in detail elsewhere.<sup>87, 208, 209</sup> T4 polynucleotide kinase and T4 DNA ligase were purchased from Invitrogen, RNaseA and shrimp alkaline phosphatase from Fermentas, Micrococcal

Nuclease from USB, Superase-in RNase inhibitor from Ambion,  $\gamma$ - $^{32}$ P-ATP and  $\alpha$ - $^{32}$ P-dGTP from Perkin-Elmer, Sequenase 2.0 and pyrophosphatase from Amersham, and streptavidin magnetic particles and unmodified dNTP's from Roche. Deuterated buffer solutions were prepared by dissolving buffer salts in D<sub>2</sub>O (Cambridge Isotopes), adjusting the pH with HCl or NaOH, then lyophilizing the buffer salts to dryness and resuspending in D<sub>2</sub>O four times. The pD was then determined by adding 0.4 to the observed pH-meter reading.<sup>210</sup>

### 3.2.2 Oligonucleotide Sequences

The *trans*-cleaving construct<sup>93</sup> of originally selected 9<sub>25</sub>-11 DNAzyme<sup>87</sup> (Figure 3.2B) is referred to as “wildtype 9<sub>25</sub>-11” in the text: 5'-CCAACAGUUCUC **AUCCGUAGUGAAGGCACGC**, where **A**(bold) is 8-histaminyl-2'-deoxy-adenosine (abbreviated as <sup>his</sup>dA in the text) and **U**(bold) is 5-(amino-allyl)-2'-deoxy-uridine (abbreviated as <sup>aa</sup>dU in the text) (Figure 3.2C). 9<sub>25</sub>-11 functional group deletion variants were synthesized by replacing, one at a time, each <sup>his</sup>dA with 8-methylamino-2'-deoxy-adenosine<sup>209</sup> or each <sup>aa</sup>dU with natural thymidine (see Figure 3.11). These variants are named to reflect the modified nucleotide residue (numbered as in Figure 3.2B) from which the imidazole or cationic amine was deleted (see Table 3.3 footnote). 5'-product: 5'-d(GCGTGCC)**X** where **X** is ribo-cytidine; 3'-product: 5'-d(GTCTGTT); bridging phosphorothioate (S-link) substrate: 5'-d(GCGTGCC-**X**-**Y**<sub>1</sub>-TCTGTT) where **Y**<sub>1</sub> is 2',5'-dideoxy-5'-mercapto-guanosine; native (O-link) substrate: 5'-d(GCGTGCC-**X**-GTCTGTT); ligation template: 5'-biotin-d(AACAGACGGGCACGC); 2'-amino-substrate analogue: 5'-d(GCGTGCC-**Z**-GTCTGTTGG) where **Z** is 2'-deoxy-2'-amino-

cytidine; nonbridging phosphorothioate substrate: 5'-d(GCGTGCC-**X(sP)**-GTCTGTT) where **X(sP)** represents ribo-cytidine with a 3'-nonbridging phosphorothioate linkage (a ~50:50 diastereomeric mixture was used). Except for the S-link substrate, oligonucleotides were prepared by standard solid phase synthesis, purified by 20% TBE d-PAGE, eluted, and desalted on a G-10 spin column.

The 2',3'-cyclic phosphate terminated 5'-product was synthesized by incubating 30 nmol of 3'-phosphate terminated 5'-product (prepared by standard solid phase synthesis) in a solution of 50 mM 1-ethyl-3-(3-dimethylaminopropyl)-carbodiimide hydrochloride and 250 mM Na-MES pH 5.5 and for 2 hours at 37 °C.<sup>211</sup> The product was then ethanol precipitated, purified by 20% TBE d-PAGE, eluted, and desalted by G-10 spin column. MALDI-TOF spectra were recorded as described in Section 2.2.6.

The *cis*-cleaving 9<sub>25</sub>-11 DNAzyme (Figure 3.2A) was prepared enzymatically by primer extension:<sup>87</sup> 20 pMol of primer 5'-biotin-d(T<sub>20</sub>GCGTGCC-**X**-GTCTGTTGGCCC) was annealed to template DNA 5'-d(T<sub>9</sub>GAGCTCGCGGGGCGTGCCTTCACTACGGATGAGAACTGTTGGTAGGGCCCAACAGAGGGCACGCTC GTGTCGT), and enzymatically polymerized at 37 °C using Sequenase 2.0 in the presence of pyrophosphatase, 50 μM <sup>im</sup>dATP, <sup>aa</sup>dUTP, dCTP, dGTP, and trace amounts of α-[<sup>32</sup>P]-dGTP. The reaction was stopped by addition of EDTA (to a final concentration of 25 mM), and the resulting biotinylated duplex product was then desalted on a G-25 spin column.

### 3.2.3 Metal Cation Inhibition of *Cis*-cleaving 9<sub>25</sub>-11

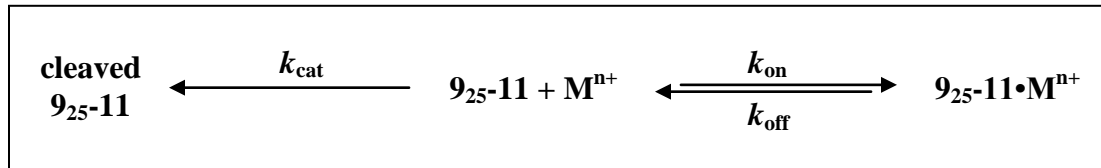
For the kinetic analysis of self-cleavage, ~500,000 cpm, or an estimated 2-5 pmol) of *cis*-cleaving 9<sub>25</sub>-11 were bound (via 5'-biotin) to pre-washed streptavidin magnetic particles in 10 mM Tris-HCl pH 7.5, 100 mM NaCl, 1 mM EDTA. The sample was then decanted, and the template strand was removed by five short washes (~15 seconds each) of 100  $\mu$ L 0.2 M NaOH, followed by a neutralization wash of 100  $\mu$ L 10 mM Na-cacodylate (pH 6.5) and then a 100  $\mu$ L water wash. The streptavidin particles, now bearing single stranded DNAzyme, were resuspended in water and divided into aliquots (~20,000 cpm each). These aliquots were then decanted, resuspended in 100  $\mu$ L of solution containing the appropriate metal cation at the final concentration used in the cleavage reaction, and incubated for 30 minutes. Following this pre-incubation, the streptavidin particles were decanted, whereupon the DNAzyme cleavage reaction was initiated by adding cleavage buffer containing the metal cation of interest (200 mM NaCl, 25 mM cacodylate pH 7.5, and the indicated concentration of metal salt). Reactions were performed at 24 °C and time point aliquots were quenched in an equal volume of 90% formamide/50 mM EDTA/0.01% bromophenol blue/0.01% xylene cyanol. In order to dissociate the uncleaved DNAzymes bound to streptavidin, 1/10<sup>th</sup> volume of 100 mM biotin (in DMF) was added, and the samples were heated to 95 °C for 2 minutes. The samples were then magnetized, decanted, and analyzed by 10% d-PAGE. Autoradiography data were processed using Imagequant v5.2. The first order rate constants ( $k_{obs}$ ) for DNAzyme self-cleavage were determined by fitting the fraction cleaved to Equation 3.1 using Sigma Plot v7.101.

$$P = P_o + P_\infty (1 - e^{-k_{obs}t}) \quad (3.1)$$

where  $P$ ,  $P_0$ , and  $P_\infty$  are the fractions cleaved at time  $t$ , time zero, and the reaction end point, respectively.

Quantitative analysis of  $M^{n+}$  inhibition of 9<sub>25</sub>-11 self-cleavage was based on the kinetic scheme depicted in Figure 3.4.

**Figure 3.4:** Kinetic scheme for  $M^{2+}$  inhibition of 9<sub>25</sub>-11 self cleavage. A very low, steady state concentration of free 9<sub>25</sub>-11 is assumed. It is further assumed that the  $M^{2+}$ -bound 9<sub>25</sub>-11 is catalytically inactive.



Assuming a small, steady state concentration of uninhibited 9<sub>25</sub>-11, the following relationship is obtained:

$$k_{on}[9_{25} - 11][M^{n+}] + k_{cat}[9_{25} - 11] = k_{off}[9_{25} - 11 \bullet M^{n+}] \quad (3.2)$$

where  $[9_{25}-11]$ ,  $[9_{25}-11 \bullet M^{n+}]$ , and  $[M^{n+}]$  are the concentrations of free 9<sub>25</sub>-11, metal cation inhibited 9<sub>25</sub>-11, and metal cation. Solving Equation 3.2 for  $[9_{25}-11 \bullet M^{n+}]$ , and substituting the result into the mass balance Equation 3.3, yields Equation 3.4:

$$[U] = [9_{25} - 11] + [9_{25} - 11 \bullet M^{n+}] \quad (3.3)$$

$$[U] = [9_{25} - 11] \left( 1 + \frac{k_{on}[M^{n+}] + k_{cat}}{k_{off}} \right) \quad (3.4)$$

where [U] denotes the total uncleaved 9<sub>25</sub>-11 remaining. Solving Equation 3.4 for [9<sub>25</sub>-11] and substituting this result into a first order rate expression yields Equation 3.5:

$$\frac{dP}{dt} = -\frac{d[9_{25}-11]}{dt} = k_{\text{cat}} [9_{25}-11] = \left( \frac{k_{\text{cat}} k_{\text{off}}}{k_{\text{off}} + k_{\text{on}}[M^{n+}] + k_{\text{cat}}} \right) [U] = k_{\text{obs}} [U] \quad (3.5)$$

(rate constants are defined in Figure 3.4). By reciprocating the expression for  $k_{\text{obs}}$  in Equation 3.5, the apparent dissociation constant ( $K_d = k_{\text{off}}/k_{\text{on}}$ ) for Hg<sup>2+</sup> can be determined by linear regression from the slope of a plot of  $k_{\text{obs}}^{-1}$  vs. [Hg<sup>2+</sup>], according to:

$$\frac{1}{k_{\text{obs}}} = \frac{k_{\text{off}} + k_{\text{cat}}}{k_{\text{off}} k_{\text{cat}}} + \frac{[Hg^{2+}]}{k_{\text{cat}} K_d} \quad (3.6)$$

where  $k_{\text{cat}}$  is fixed to the value of observed rate constant for the control reaction run in the absence of Hg<sup>2+</sup>. No hill coefficient was included given that Hill plot analysis gave a value of  $n \sim 1$  (see Figure 3.8). Hill-plot analysis was performed as described for a self-cleaving ribozyme,<sup>212</sup> using a logarithmic form of the Hill equation:

$$\log\left(\frac{k_{\text{obs}}}{k_{\text{cat}} - k_{\text{obs}}}\right) = -n \log[Hg^{2+}] + \log K_d \quad (3.7)$$

### 3.2.4 Kinetic Experiments with *Trans*-cleaving 9<sub>25</sub>-11

Single turnover *trans*-cleavage assays were carried out with a saturating excess of 9<sub>25</sub>-11 (2.5 μM, ~35 times greater than  $K_m$ <sup>88</sup>) and a trace of 5'-<sup>32</sup>P-labeled substrate (<10 nM) (either the native, S-link, or nonbridging phosphorothioate substrates). Reactions were performed at 21-22 °C as the rate of 9<sub>25</sub>-11 *trans*-cleavage catalysis is known to

plateau near 24 °C.<sup>88</sup> The standard reaction buffer contained 50 mM Tris-HCl pH 7.5, 200 mM NaCl, 1 mM EDTA. For the pH-rate profile experiments, the buffers used were: Na-MES (6.82-7.11), Na-MOPS (7.12-7.35), Na-HEPES (pH 7.35-7.82), Tris-HCl (pH 7.82-8.67), Na-Borate (8.68-9.0). Buffer specific counter ion effects were minimal, as very similar cleavage rates were observed for different buffers at the pH-range boundaries indicated above (see Figure 3.11-*vide infra*).

Reactions were initiated by the addition of 1/10<sup>th</sup> volume of substrate (in H<sub>2</sub>O or D<sub>2</sub>O) to DNase solutions containing the appropriate buffer salts. At each time point aliquots were quenched in 2 volumes of 90% formamide/50 mM EDTA/0.01% bromophenol blue/0.01% xylene cyanol for O-link and nonbridging phosphorothioate substrate cleavage, or in 90% formamide/50 mM Na-PIPES pH 6.5/25 mM EDTA/0.01% bromophenol blue/0.01% xylene cyanol for S-link cleavage. O-link and nonbridging phosphorothioate samples were analyzed by standard d-PAGE in TBE buffer (pH 8.3) and S-link samples were analyzed by d-PAGE in TAE buffer (40 mM Tris-acetate/1 mM EDTA, pH 6.7).<sup>118</sup> Autoradiographic data were processed using Imagequant v.5.2. Using Sigma Plot v.7.101, the substrate cleavage data were fit to:

$$P = P_o + P_\infty \left(1 - e^{-k_{obs}t}\right) \quad (3.8)$$

where  $k_{obs}$  is the observed first order rate constant, and  $t$  is time, and  $P$ ,  $P_o$ , and  $P_\infty$  are the fractions cleaved at time  $t$ , time zero, and the reaction end point, respectively,. For nonbridging phosphorothioate cleavage experiments, biphasic data were fit to:

$$P = P_o + P_{\infty slow} \left(1 - e^{-k_{slow}t}\right) + P_{\infty fast} \left(1 - e^{-k_{fast}t}\right) \quad (3.9)$$

where a rate constant and endpoint value is determined for each of the two phases (denoted as “fast” and “slow”), which result from the cleavage of the two different cleavage site phosphorothioate diastereomers.

The data reported in Tables 3.3 and 3.5 were obtained by averaging the results for two reactions, run in parallel. In all cases, the results for most duplicate experiments agreed within 10% or better. As much as possible, where kinetic data are compared for a given effect (for example: pH-rate profiling, DNAzyme mutation, phosphorothioate substitution, etc.), reactions were commenced almost simultaneously and run in parallel using the same batches of DNAzymes and labeled substrates. In the case of the S-link cleavage reactions, some reactions were too fast to conduct simultaneously with manual time point quenching; these reactions were conducted consecutively on the same day, with the same batches of reagents.

### **3.2.5 Affinity Labeling Reactions**

The 2'-bromoacetamide substrate analogue was prepared as described in Section 2.2.3. Affinity labeling reaction conditions were: 2.5  $\mu\text{M}$  affinity label oligonucleotide, a trace (<10 nM) of 5'-<sup>32</sup>P-labelled 9<sub>25</sub>-11, in the standard reaction buffer at pH 8, at room temperature in the dark. At each time point aliquots were quenched with 2 volumes of 90% formamide/50 mM EDTA/0.01% bromophenol blue/0.01% xylene cyanol. Reaction products were analyzed by 15% d-PAGE and autoradiography as described above. The pH-rate profile reactions were conducted with 3.0  $\mu\text{M}$  affinity label and 2.5  $\mu\text{M}$  9<sub>25</sub>-11 (including a trace of 5'-<sup>32</sup>P-labelled 9<sub>25</sub>-11) in standard buffer. Initial time points (<15% completion) were analyzed by linear regression for the pH-rate profile to avoid the

complicating effects of variations in the rate of bromoacetamide solvolysis with changing pH. The fraction of alkylated DNAzyme was plotted versus time and rate constants ( $\text{hr}^{-1}$ ) were determined from the slope of a linear regression using Sigma Plot.

Larger scale affinity labeling reactions of 1-2 nmol 9<sub>25</sub>-11 were carried out for digestion/MALDI analysis under the following conditions: 5  $\mu\text{M}$  9<sub>25</sub>-11, 10  $\mu\text{M}$  bromoacetamide substrate analogue, in standard buffer. After ~48 hours, the reactions were terminated by ethanol precipitation. The precipitates were resuspended in 90% formamide/50 mM EDTA/0.01% bromophenol blue/0.01% xylene cyanol. Alkylated 9<sub>25</sub>-11 was resolved by preparative 15% d-PAGE, identified by UV-shadowing, and excised from the gel. The material was eluted from the gel slice into 1%  $\text{LiClO}_4$ /10 mM Tris-HCl at room temperature after freezing on dry ice. The eluate was concentrated to ~100  $\mu\text{L}$ , precipitated with acetone, dried, resuspended in  $\text{H}_2\text{O}$ , and G-25 desalted. Both alkylated and unreacted 9<sub>25</sub>-11 were treated with micrococcal nuclease (typically 10-20 units) in 1 mM  $\text{CaCl}_2$ /10 mM Tris-HCl pH 8 for varying times (up to 72 hrs.) at 37 °C. Some digestion reactions also included 2 units Shrimp Alkaline Phosphatase to remove terminal phosphates; this treatment facilitated the observation of larger digestion fragments in MALDI spectra. Digestion progress was surprisingly slow, perhaps due to the modified nucleotide structures and/or the presence of alkylation linkage between the DNAzyme and substrate strands. Progress was monitored by labeling a few picomoles of material from the digestion mixture with  $\gamma$ -<sup>32</sup>P-ATP and polynucleotide kinase, and then observing the sizes of the labeled fragments resolved by 20% d-PAGE. Digestion samples were precipitated with 1%  $\text{LiClO}_4$ /acetone or vacuum concentrated for MALDI-

TOF analysis. MALDI matrices and sample spots were prepared, and spectra were obtained, as described in Section 2.2.6.

## 3.3 RESULTS AND DISCUSSION

### 3.3.1 Metal Cation Binding and Inhibition of 9<sub>25</sub>-11 Self-Cleavage

Preliminary work has shown that 9<sub>25</sub>-11 activity is strongly inhibited by softer metal cations such as Cu<sup>2+</sup>, Ni<sup>2+</sup>, and Zn<sup>2+</sup> at 500 μM,<sup>87</sup> whereas Mg<sup>2+</sup> (a comparatively hard metal cation) has no significant effect at 1 mM.<sup>88</sup> In this study, we undertook a more comprehensive survey of the effects of various metal cations on 9<sub>25</sub>-11 self-cleavage activity. Metal cation inhibition was surveyed initially by examining the extent of 9<sub>25</sub>-11 cleavage after 10 minutes in the presence of each of the following metal cations, each at concentrations of 10, 30 and 100 μM: Ag<sup>+</sup>, Ba<sup>2+</sup>, Ca<sup>2+</sup>, Cd<sup>2+</sup>, Ce<sup>3+</sup>, Ce<sup>4+</sup>, Co<sup>2+</sup>, Cu<sup>2+</sup>, Eu<sup>3+</sup>, Fe<sup>2+</sup>, Fe<sup>3+</sup>, Hg<sup>2+</sup>, La<sup>3+</sup>, Mn<sup>2+</sup>, Ni<sup>2+</sup>, Pb<sup>2+</sup>, Sm<sup>3+</sup>, Sr<sup>2+</sup>, Y<sup>3+</sup>, Yb<sup>3+</sup>, and Zn<sup>2+</sup>. Self-cleaving 9<sub>25</sub>-11 was pre-incubated with the metal cation of interest for 30 minutes to assure that inhibitory interactions were given ample time to equilibrate. The reactions were then initiated by the addition of buffered NaCl. Within the concentration range 10–100 μM, Ce<sup>3+</sup>, Ce<sup>4+</sup>, Eu<sup>3+</sup>, Fe<sup>3+</sup>, Hg<sup>2+</sup>, La<sup>3+</sup>, Ni<sup>2+</sup>, Sm<sup>3+</sup>, Y<sup>3+</sup>, Yb<sup>3+</sup>, Zn<sup>2+</sup> showed modest inhibition of self-cleavage (Figure 3.5), whereas Cu<sup>2+</sup> and particularly Hg<sup>2+</sup> showed strong inhibitory effects. Hg<sup>2+</sup> is known to have very high affinity for imidazoles (the value of the association constant, logβ<sub>2</sub>, for the *bis*-imidazole Hg<sup>2+</sup> complex ranges from 15 to 21, increasing with pH<sup>185</sup>). It was thus not surprising that, of the metal cations examined, Hg<sup>2+</sup> would be the most effective inhibitor of a DNAzyme where imidazoles

are required for activity.<sup>87, 93</sup>  $\text{Cu}^{2+}$  causes more moderate inhibition of  $9_{25-11}$ , which is consistent with its lower affinity for imidazole ligands, relative to  $\text{Hg}^{2+}$ .<sup>184</sup>

**Figure 3.5:** Qualitative survey of the effects of various metal cations on  $9_{25-11}$  self cleavage activity. The fraction cleaved after 10 min is plotted for three  $\text{M}^{n+}$  concentrations (10, 30, and 100  $\mu\text{M}$ ).

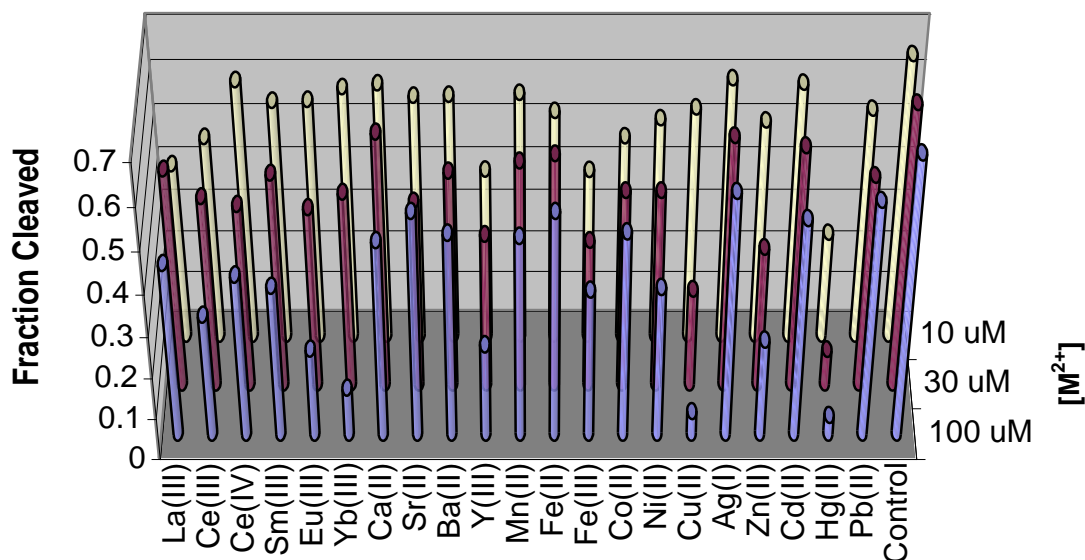
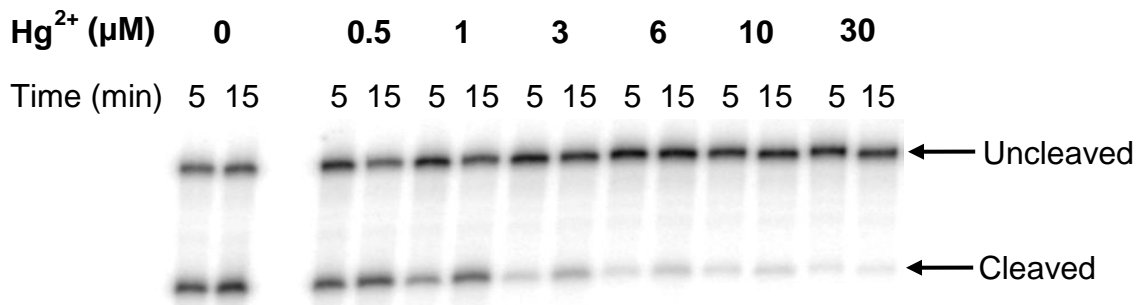


**Figure 3.6:** Autoradiogram which exemplifies  $\text{Hg}^{2+}$ -dependent inhibition of  $9_{25-11}$  self-cleavage activity.



The potent inhibitory properties of  $\text{Cu}^{2+}$  and  $\text{Hg}^{2+}$  were characterized quantitatively (Figure 3.6) by plotting the relative self-cleavage rate constant versus  $[\text{M}^{2+}]$ . These data demonstrate that  $\text{Hg}^{2+}$  is a much stronger inhibitor of 9<sub>25</sub>-11 activity than  $\text{Cu}^{2+}$  (Figure 3.7A). The dissociation constants for each of  $\text{Hg}^{2+}$  and  $\text{Cu}^{2+}$  were determined (Figure 3.7B) based on the assumptions that (1) there exists a steady state concentration of free, catalytically active 9<sub>25</sub>-11, (2) the metal cation bound 9<sub>25</sub>-11 is completely inactive, and (3) that the reverse reaction (ligation) does not occur (see Section 3.2.3 for kinetic scheme and explanation). According to this analysis, the apparent dissociation constant for  $\text{Hg}^{2+}$  binding is  $110 \pm 9$  nM, and that for  $\text{Cu}^{2+}$  binding is  $2.5 \pm 0.1$   $\mu\text{M}$ .  $\text{Hg}^{2+}$  binding was also characterized by Hill plot analysis (Figure 3.8), which yielded a Hill coefficient value of  $\sim 1.3$ . These data suggest that  $\text{Hg}^{2+}$  binds non-cooperatively to 9<sub>25</sub>-11, most likely to a single metal cation binding site.<sup>212</sup>

**Figure 3.7:** Graphical analysis of  $\text{Hg}^{2+}$  (black) and  $\text{Cu}^{2+}$  (blue) inhibition of 9<sub>25</sub>-11 self-cleavage. (A) Plot of relative rate constant as a function of  $\text{Hg}^{2+}$  or  $\text{Cu}^{2+}$  concentration ( $k_{\text{cat}}$  = rate constant in the absence of any  $\text{M}^{2+}$ ). (B) Plot of  $k_{\text{obs}}^{-1}$  as a function of  $\text{Hg}^{2+}$  or  $\text{Cu}^{2+}$  concentration.  $K_d$  was determined to be  $110 \pm 9$  nM for  $\text{Hg}^{2+}$  and  $2.5 \pm 0.1$   $\mu\text{M}$  for  $\text{Cu}^{2+}$  from slope of these plots, using Equation 3.6.

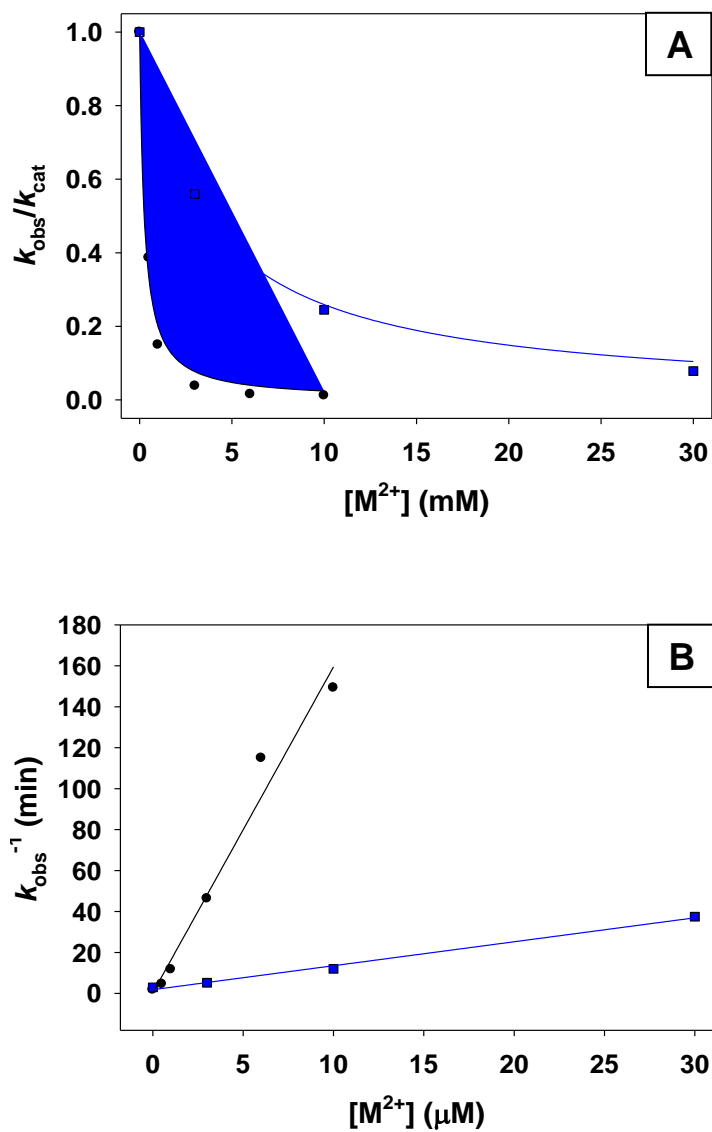
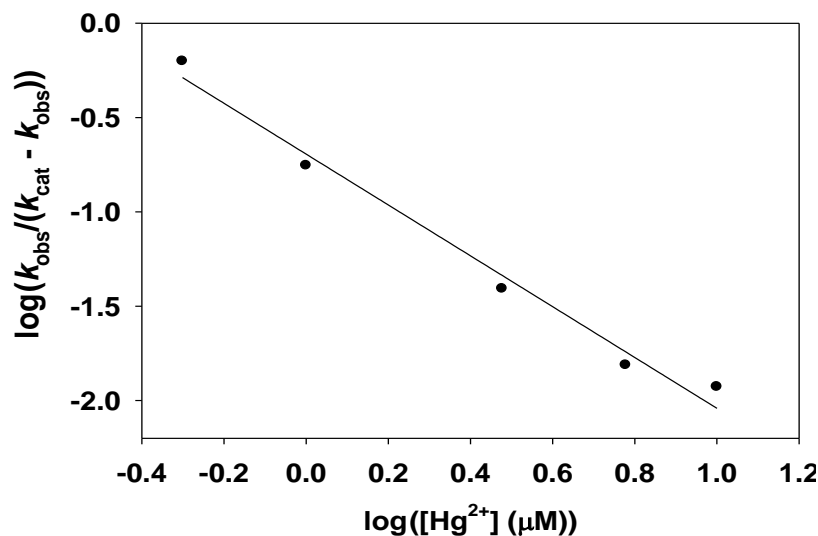
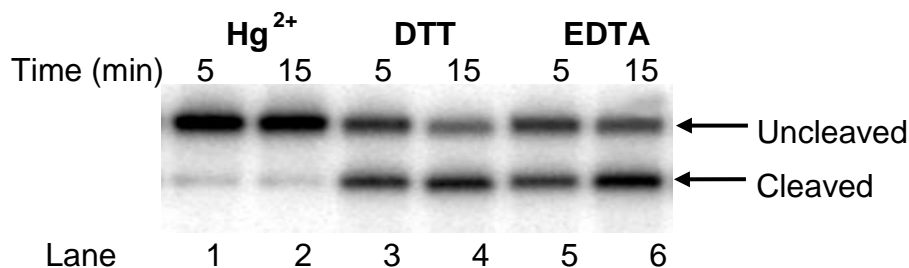


**Figure 3.8:** Hill plot analysis of  $\text{Hg}^{2+}$  inhibition of 9<sub>25</sub>-11 self cleavage. According to Equation 3.7, the Hill coefficient ( $n$ ) of  $\sim 1.3$  was determined from the slope of this plot.



We also questioned the nature of the inhibitory interaction between  $\text{Hg}^{2+}$  and 9<sub>25</sub>-11. Inhibition could result from either a reversible ligand- $\text{Hg}^{2+}$ -type interaction or from an irreversible, covalent modification of 9<sub>25</sub>-11 (for example,  $\text{Hg}^{2+}$  could have mercurated the 5-position of cytosine<sup>213</sup> or reacted with olefins to yield oxy-mercuration products<sup>214</sup>). The  $\text{Hg}^{2+}$  mediated inhibition of 9<sub>25</sub>-11 self-cleavage was readily reversible, which demonstrates that the observed inhibition was likely due to a simple, dissociable  $\text{Hg}^{2+}$ -ligand interaction. In order to demonstrate this, 9<sub>25</sub>-11 self-cleavage activity was first thoroughly poisoned by pre-incubation in the presence of 30  $\mu\text{M}$   $\text{Hg}^{2+}$ , and was subsequently rescued by the addition of  $\text{Hg}^{2+}$  chelators such EDTA or DTT, along with cleavage buffer (Figure 3.9).

**Figure 3.9:** Restoration of Hg<sup>2+</sup>-inhibited 9<sub>25</sub>-11 self-cleavage activity upon the addition of Hg<sup>2+</sup> chelators. For all lanes, samples were preincubated in 30 μM Hg<sup>2+</sup>, 25 mM cacodylate (pH 7.5), 200 mM NaCl. Lanes 3 & 4 were rescued with 1/10<sup>th</sup> volume of 100 mM DTT, Lanes 5 & 6 rescued with 1/10<sup>th</sup> volume of 250 mM EDTA.



It is remarkable that 9<sub>25</sub>-11 would show such strong affinity for Hg<sup>2+</sup>, despite the fact that no evolutionary pressure requiring such metal binding was applied during *in vitro* selection. These results likely reflect both the high affinity of imidazole for Hg<sup>2+</sup>, and the importance of the imidazole modifications for 9<sub>25</sub>-11 catalytic activity. Although the conspicuous specificity for Hg<sup>2+</sup> binding is consistent with the involvement of DNAzyme-based imidazole ligands, we do have any data which can directly rule out Hg<sup>2+</sup> binding by natural DNA functional groups in 9<sub>25</sub>-11. Finally, it should be noted that the current study characterizes DNAzyme inhibition, which provides a negative readout that is not ideal for metal cation bio-sensing applications. It should be possible to select for Hg<sup>2+</sup>-dependent cleavage (a positive readout) which would be more amenable to bio-sensing applications. Recently, Hollenstein *et al.* have described just such a Hg<sup>2+</sup>-activated, imidazole-containing DNAzyme with high affinity for Hg<sup>2+</sup> ( $K_d \sim 1 \mu\text{M}$ ).<sup>172</sup>

### 3.3.2 General Properties of 9<sub>25</sub>-11 Catalysis

Before attempting to characterize the mechanism of 9<sub>25</sub>-11 catalysis using chemical probes, we first established the more general properties of 9<sub>25</sub>-11 catalysis. Specifically, we identified the products of the *trans*-cleavage reaction, located several catalyst and substrate functional groups crucial for activity, and measured pH-rate and solvent isotope effects. Previous kinetics studies have established that single turnover (excess catalyst) cleavage of the native substrate by 9<sub>25</sub>-11 follows well-behaved saturation kinetics under the following conditions: 50 mM Tris-HCl pH 7.5, 200 mM NaCl, 1 mM EDTA at 24 °C.<sup>88</sup> Unless stated otherwise, all experiments reported in this study were performed under similar single turnover conditions (in the same buffer at 21-22 °C), where substrate was saturated with DNAzyme.

We first identified the products resulting from 9<sub>25</sub>-11 catalyzed substrate cleavage by MALDI-TOF analysis (Figure 3.10). These data clearly show that the reaction yields a 2',3'-cyclic phosphate-terminated 5'-product and a 5'-hydroxy-terminated 3'-product; therefore, substrate cleavage must proceed via 2'-transphosphorylation, rather than hydrolysis. Unlike RNaseA, 9<sub>25</sub>-11 does not appear to catalyze the hydrolysis of the 2',3'-cyclic phosphate; we observed only trace amounts of the (open) 2'- or 3'-phosphate products, which likely result from buffer catalyzed hydrolysis. d-PAGE visualization of 2',3'-cyclic phosphate hydrolysis with authentic standards for comparison, would have been ideal, but for the 8-mer product of 9<sub>25</sub>-11 substrate cleavage, the 2',3'-cyclic-phosphate could not be adequately separated from the 2'- or 3'-phosphate.

**Figure 3.10:** MALDI-TOF analysis of the products of 9<sub>25</sub>-11 catalyzed substrate cleavage. The reaction was run to completion under multiple turnover conditions with 1 nmol of substrate and 100 pmol 9<sub>25</sub>-11. Prior to MALDI-TOF analysis, the reaction mixture was desalted, but not d-PAGE purified. The [M-H]<sup>-</sup> molecular ion assignments are detailed in Table 3.1. Peaks observed at intervals of +22 m/z units are attributed to Na<sup>+</sup> adducts. The inset shows the spectrum obtained for an authentic sample of 2',3'-cyclic phosphate terminated 5'-product (see Section 3.2.2).

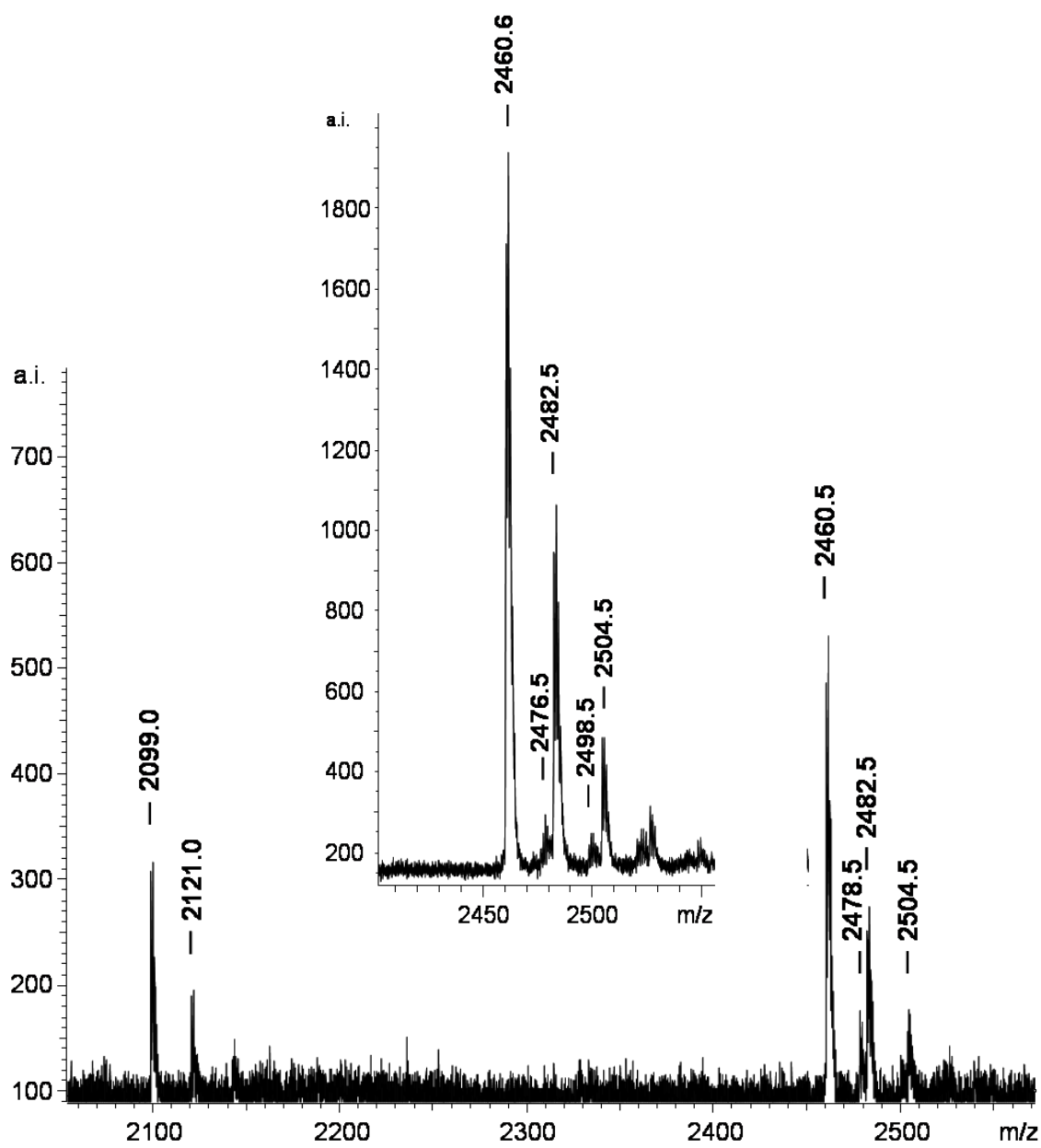


**Table 3.1:** Assignments and predicted and observed m/z values for peaks observed in the MALDI-TOF spectrum shown in Figure 3.10.

Oligonucleotide Assignment	[M-H] <sup>-</sup> Predicted	[M-H] <sup>-</sup> Observed
5'-product (2',3'-cyclic phosphate) <sup>a</sup>	2462.4	2460.5
5'-product (2'- or 3'-phosphate) <sup>a</sup>	2480.4	2478.5
3'-product <sup>b</sup>	2100.4	2099.0

<sup>a</sup> sequence: 5'-d(GCGTGCC)rC

<sup>b</sup> sequence: 5'-d(GTCTGTT)

We also examined the sequence specificity of 9<sub>25-11</sub> with respect to the three unpaired substrate nucleotides (Table 3.2) as previous work had established the requirement for substrate complementarity with the guide sequences<sup>93</sup>. The only sequence variation that was reasonably well tolerated was the substitution of rA for the native rC at the scissile nucleotide (cleavage was slower by less than 4-fold for the rA containing substrate). Similar substitution of rU or rG was more detrimental to catalysis (cleavage was slower by 25- and 50-fold, respectively). Evidently, the catalyst recognizes the hydrogen bonding pattern formed by the *endo*- and *exo*-cyclic (amidine) nitrogens common to the base pairing faces of adenine and cytosine, but not uracil or guanine. The other two unpaired substrate nucleotides (see Figure 3.2) are even more strongly recognized by 9<sub>25-11</sub> than the scissile nucleotide, as substitution of one or both of these residues slowed substrate cleavage by ~250-fold.

**Table 3.2:** The effects 9<sub>25</sub>-11 on catalysis of changing the unpaired substrate nucleotides. The changes made to the native substrate sequence are highlighted in red. Note that these measurements were made at 24 °C.

Substrate Sequence	$k_{\text{cat}}$ (min <sup>-1</sup> )	$k_{\text{rel}}$ <sup>a</sup>
5'-d(GCGTGCC)rCd(GTCTGTT) <sup>b</sup>	0.037	1
5'-d(GCGTGCC)rAd(GTCTGTT)	0.010	0.27
5'-d(GCGTGCC)rGd(GTCTGTT)	0.00066	0.02
5'-d(GCGTGCC)rUd(GTCTGTT)	0.0014	0.04
5'-d(GCGTGCC)rCd(ATCTGTT)	0.00013	0.004
5'-d(GCGTGCC)rCd(ACCTGTT)	0.00015	0.004
5'-d(GCGTGCC)rCd(GCCTGTT)	0.00012	0.003

<sup>a</sup>  $k_{\text{rel}}$  is the relative  $k_{\text{cat}}$ , calculated by dividing  $k_{\text{cat}}$  for the substrate variant by  $k_{\text{cat}}$  for the native substrate.

<sup>b</sup> The kinetic determination for the native substrate was carried out by Richard Ting.

Next, we determined which of the synthetic functional groups in 9<sub>25</sub>-11 are required for efficient catalytic activity. Initial characterization had demonstrated that 9<sub>25</sub>-11 activity is undetectable when all of the <sup>his</sup>dA and <sup>aa</sup>dU residues are simultaneously replaced with natural dA and dT, respectively.<sup>93</sup> In this study we undertook a more precise structure-activity investigation by removing individual imidazole and cationic amine functionalities one at a time (Figure 3.11). Individual <sup>his</sup>dA residues were replaced with 8-methylamino-dA<sup>209</sup> (rather than natural dA) so as to remove the imidazole moiety while still preserving the 8-methylamino group, which could engage in hydrogen bonding or other functions. Individual <sup>aa</sup>dU residues were replaced with natural thymidine residues so as to remove the cationic amine functionality.

Cleavage of the native substrate is significantly impaired by individually deleting three of the four imidazole groups in 9<sub>25-11</sub> (Table 3.3). Notably, the imidazole moiety of the <sup>his</sup>dA24 residue appears to be completely dispensable, as its removal actually leads to slight enhancement of catalytic activity. Individual removal of the cationic amine functionalities caused relatively minor (<10-fold) impairment of activity in all cases except for the T21 variant, which was 50-fold less active than wildtype 9<sub>25-11</sub>. Not surprisingly, it appeared that several of the synthetic appendages, especially imidazole groups, are crucial for proper folding or catalysis in 9<sub>25-11</sub>, but the question remained whether any of the imidazoles, cationic amines, or other functional groups mediated general acid/base catalysis, so as to mimic the mechanism of RNaseA.

**Figure 3.11:** The nucleotide substitutions used in the functional group deletion variants of 9<sub>25-11</sub> used in this study. (A) 8-histaminyl-dA (<sup>his</sup>dA) was replaced with 8-methylamino-dA or (B) 5-(amino-allyl)-dU (<sup>aa</sup>dU) was replaced with natural dT.

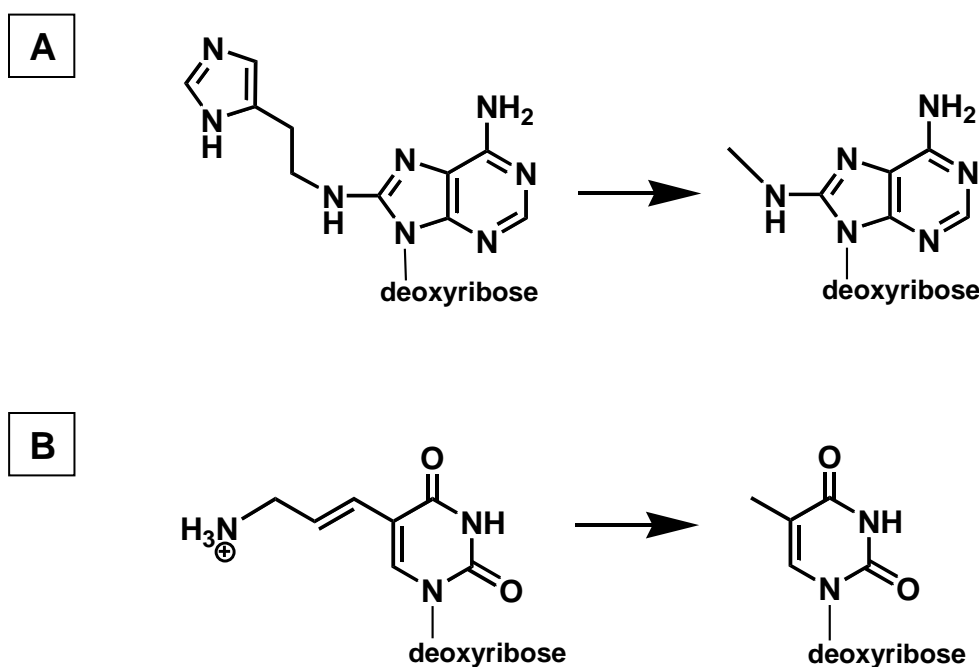


**Table 3.3:** The effects of individual synthetic functional group deletion on the observed rate constants for 9<sub>25</sub>-11 catalyzed cleavage of the native (O-link) substrate in standard buffer (pH 7.5).

DNzyme <sup>a</sup>	$k_O$ (min <sup>-1</sup> ) <sup>b</sup>	$k_{O\text{ rel}}$ <sup>c</sup>
WT	0.020	1
A13	0.00005	0.0025
A19	0.00007	0.0035
A23	<0.00001	<0.00005
A24	0.045	2.3
T8	0.0074	0.37
T9	0.0068	0.34
T11	0.0025	0.13
T14	0.0097	0.49
T18	0.012	0.60
T21	0.0004	0.020

<sup>a</sup> “WT” (wildtype) refers to the originally selected 9<sub>25</sub>-11 DNzyme sequence.<sup>87, 93</sup> 9<sub>25</sub>-11 functional group deletion variants are named to indicate the nucleotide from which the synthetic imidazole or cationic amine functionality was removed. For example, “A13” indicates that 8-methylamino-dA was substituted for the wildtype<sup>his</sup>dA at residue 13, and T8 indicates that thymidine was substituted for<sup>aa</sup>dU at residue 8.

<sup>b</sup>  $k_O$  refers to  $k_{\text{cat}}$  for the native (O-link) substrate.

<sup>c</sup>  $k_{O\text{ rel}}$  is the ratio  $k_O(\text{variant})/k_O(\text{wildtype})$ .

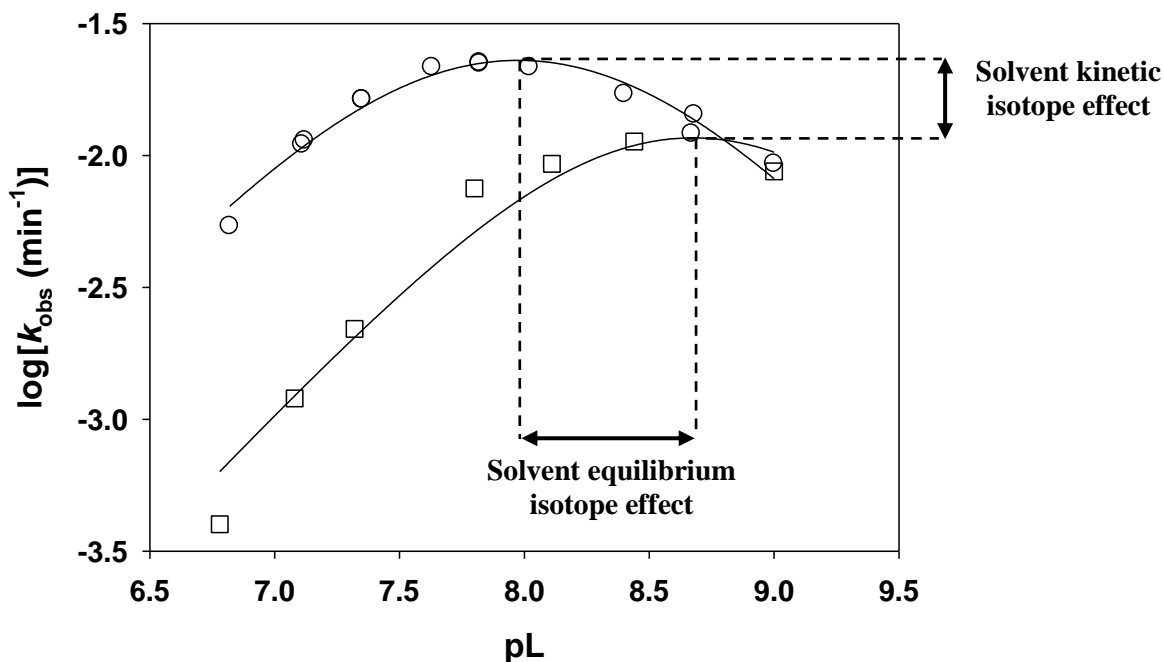
As an important preliminary step in characterizing the mechanism of 9<sub>25</sub>-11 catalysis, we examined the pH-rate profile and solvent isotope effects for indications of general acid/base catalysis. The pH-rate profile for native substrate cleavage by 9<sub>25</sub>-11 (Figure 3.12) exhibited a classic bell shape much like that observed for RNaseA catalysis,<sup>215, 216</sup> which is a hallmark of general acid/base catalysis (Section 1.3.2). As in

the case of RNaseA, the data indicate two titratable catalytic residues with similar  $pK_a$  values ( $7.6 \pm 0.1$  and  $8.4 \pm 0.1$ ). These  $pK_a$  values, however, are significantly higher than those reported for imidazole-mediated general acid/base catalysis in RNaseA (reported as 5.4 and 6.4 based on pH-rate profiling,<sup>216</sup> and 5.8 and 6.2 based on NMR titration<sup>217</sup>). The  $pK_a$  of the conjugate acid of 4-methyl-imidazole (7.45)<sup>218</sup> serves as a useful point of reference for the unperturbed  $pK_a$  of the 4-alkyl-imidazole functionality common to both RNaseA (histidine side chains) and 9<sub>25</sub>-11 (<sup>his</sup>dA side chains). Upward perturbation of imidazole  $pK_a$ 's in the active site of 9<sub>25</sub>-11 would not be surprising in the negatively charged environment of a nucleic acid structure. Conversely, the downward perturbation of the His12 and His119  $pK_a$ 's is consistent with the positive electrostatic potential known to exist in the active site of RNaseA.<sup>219</sup> Therefore, the difference in kinetic  $pK_a$  values observed for RNaseA and 9<sub>25</sub>-11 could be entirely consistent with general acid/base catalysis by a pair of 9<sub>25</sub>-11 imidazole side chains.

In deuterated buffers, the pD-rate profile in D<sub>2</sub>O buffer (Figure 3.12) mirrors the pH-rate profile in H<sub>2</sub>O buffer, except that the entire pD-rate profile is shifted to higher pL by ~0.7 units relative to the pH-rate profile. This shift is due to a solvent equilibrium isotope effect which generally shifts the  $pK_a$ 's of the titratable catalytic residues, and hence the pL-optimum, upward.<sup>210</sup> Upward shifts in  $pK_a$  of ~0.6 units are typical in D<sub>2</sub>O for proton transfer involving nitrogen;<sup>64, 210</sup> therefore, the equilibrium isotope effect observed for 9<sub>25</sub>-11 could be consistent with imidazole mediated general acid catalysis. A solvent kinetic isotope effect is also observed by comparing the rates of 9<sub>25</sub>-11 catalysis in H<sub>2</sub>O versus D<sub>2</sub>O buffer at the respective plateaus (pH-optima) of the pH- and pD-rate profiles (at this point the titratable catalytic residues are protonated to the same

extent, regardless of the solvent). The observed kinetic isotope effect ( $k_{\text{H}_2\text{O}}/k_{\text{D}_2\text{O}} \sim 2$ ) is again generally consistent with a general acid /base catalyzed mechanism.<sup>210</sup> Overall, the pH-rate profile and solvent isotope effect data are consistent with a rate limiting, general acid/base catalyzed chemical step in 9<sub>25</sub>-11 catalysis.<sup>23, 64, 210</sup>

**Figure 3.12:** pH-rate (○) and pD-rate (□) profiles for 9<sub>25</sub>-11 catalyzed cleavage of native (O-link) substrate in standard buffer. The data were fit to a general acid/base catalysis model:  $\log k_{\text{obs}} = \log \left( k_{\text{max}} / (1 + 10^{\text{p}K_{\text{a}1} - \text{pH}} + 10^{\text{pH} - \text{p}K_{\text{a}2}} + 10^{\text{p}K_{\text{a}1} - \text{p}K_{\text{a}2}}) \right)$ .<sup>23</sup> The kinetic  $\text{p}K_{\text{a}}$  values determined were:  $7.6 \pm 0.1$  and  $8.4 \pm 0.1$  in H<sub>2</sub>O buffers, and  $8.4 \pm 0.8$  and  $8.9 \pm 1.3$  in D<sub>2</sub>O buffers. The magnitude of the solvent kinetic isotope effect is measured by the difference in rates at the plateaus of the pH- and pD-rate profiles ( $k_{\text{H}_2\text{O}}/k_{\text{D}_2\text{O}} \sim 2$ ). The magnitude of solvent equilibrium isotope is approximated by the shift in optimum pL (+0.7 pL units) on going from H<sub>2</sub>O to D<sub>2</sub>O solvent.



### 3.3.3 Probing General Base Catalysis

In order to identify DNAzyme functional groups that could be involved in general base catalysis, we employed the affinity labeling approach that was originally used to identify the general base catalyst in RNaseA (Section 2.1.1).<sup>94-96</sup> The highly electrophilic 2'-bromoacetamide probe should likewise be well positioned to alkylate and covalently tag a DNAzyme general base, to facilitate its identification. Reaction of the bromoacetamide probe with 5'-<sup>32</sup>P-labeled 9<sub>25-11</sub> indeed yielded a higher molecular weight covalent adduct of 9<sub>25-11</sub> and the affinity label strand, as revealed by d-PAGE analysis (Figure 3.13). The properties of this alkylation reaction were compared to those of the catalytic reaction (Figure 3.14) in order to gauge whether alkylation occurs within a catalytically competent DNAzyme fold. Like the catalytic reaction,<sup>88</sup> the alkylation reaction is inhibited by the addition of a non-cleavable substrate analogue, which demonstrates that alkylation depends upon normal binding of the affinity label to the DNAzyme in place of the substrate. Also like the catalytic activity, alkylation activity depends upon the presence of NaCl. Finally, Hg<sup>2+</sup> is known to potently inhibit 9<sub>25-11</sub> catalysis (Section 3.3.1), and we observe the same dramatic inhibitory effect upon the alkylation reaction. These observations appear to confirm that the alkylation reaction occurs only within a catalytically competent conformation of the DNAzyme-substrate complex.

**Figure 3.13:** Autoradiogram showing the d-PAGE separation of a higher molecular weight, crosslinked species following reaction of 5'-<sup>32</sup>P-labeled 9<sub>25</sub>-11 with the 2'-bromoacetamide affinity label. Lane 1: 5'-<sup>32</sup>P-labeled 9<sub>25</sub>-11 (no reaction). Lane 2 to 5: Reaction of 5'-<sup>32</sup>P-labeled 9<sub>25</sub>-11 with substrate analogue at pH 7 for 0.5, 1, 2, 4 hours. Lane 6: Reaction for 4 hrs at pH 6. Lane 7: An aliquot of the reaction (at 4 hours) was treated with hot piperidine (15 min at 95 °C).

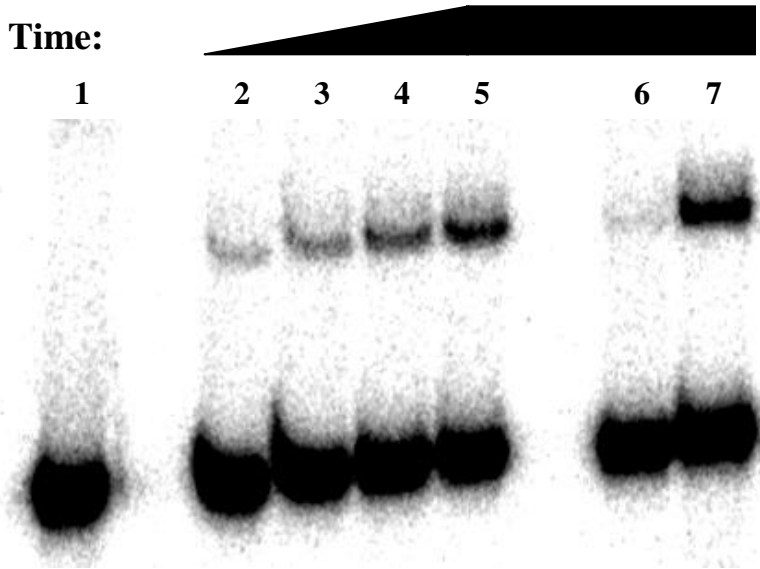
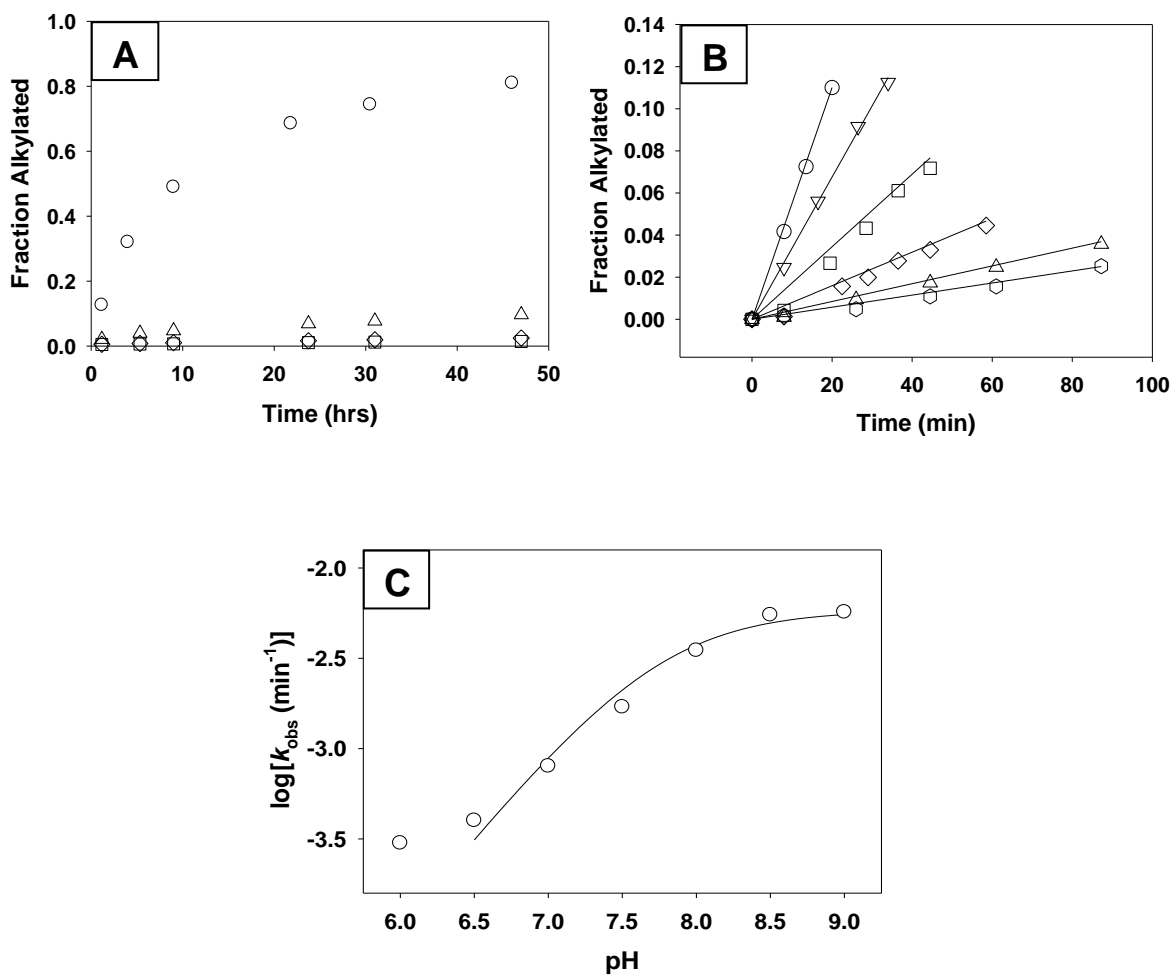


**Figure 3.14:** Effects of reaction conditions on the 9<sub>25</sub>-11 affinity labeling reaction. (A) Alkylation reactions carried out under standard conditions (pH 7.5) (○), in the absence of NaCl (△), in the presence of 0.5 mM Hg<sup>2+</sup> (□), and in the presence of 10 μM 2'-amino substrate analogue (◇). All reactions were carried out in standard buffer (pH 7.5) with the noted changes. (B) Kinetic plots of 9<sub>25</sub>-11 alkylation at: (○) pH 8.5, (▽) pH 8, (□) pH 7.5, (◇) pH 7, (△) pH 6.5, (○) pH 6. (C) Alkylation reaction pH-rate profile (based on initial rates). The data were fit to  $\log k_{\text{obs}} = \log(k_{\text{max}} / (1 + 10^{\text{p}K_{\text{a}} - \text{pH}}))$ , which yielded  $\text{p}K_{\text{a}} = 7.7 \pm 0.1$  (data for pH 6 were not included in the fit, as explained in the text).



The pH dependence of the 9<sub>25</sub>-11 alkylation reaction (Figure 3.14B & C) was also investigated to verify that the alkylated nucleophile is a titratable active site residue, and thus a reasonable candidate for general base catalyst. Above pH ~6.5, the increase in alkylation rate appears to reflect titration of the alkylated nucleophile (in analogy to titration of the general base), as it becomes fully deprotonated by pH ~9. Furthermore, the apparent pK<sub>a</sub> for the alkylated nucleophile closely matches one of the pK<sub>a</sub>'s derived from the catalytic pH-rate profile (7.6 ±0.1 for catalysis versus 7.7 ±0.1 for alkylation). This correspondence suggests that the alkylated nucleophile is the same DNAzyme functional group which acts as the general base in the catalytic reaction.

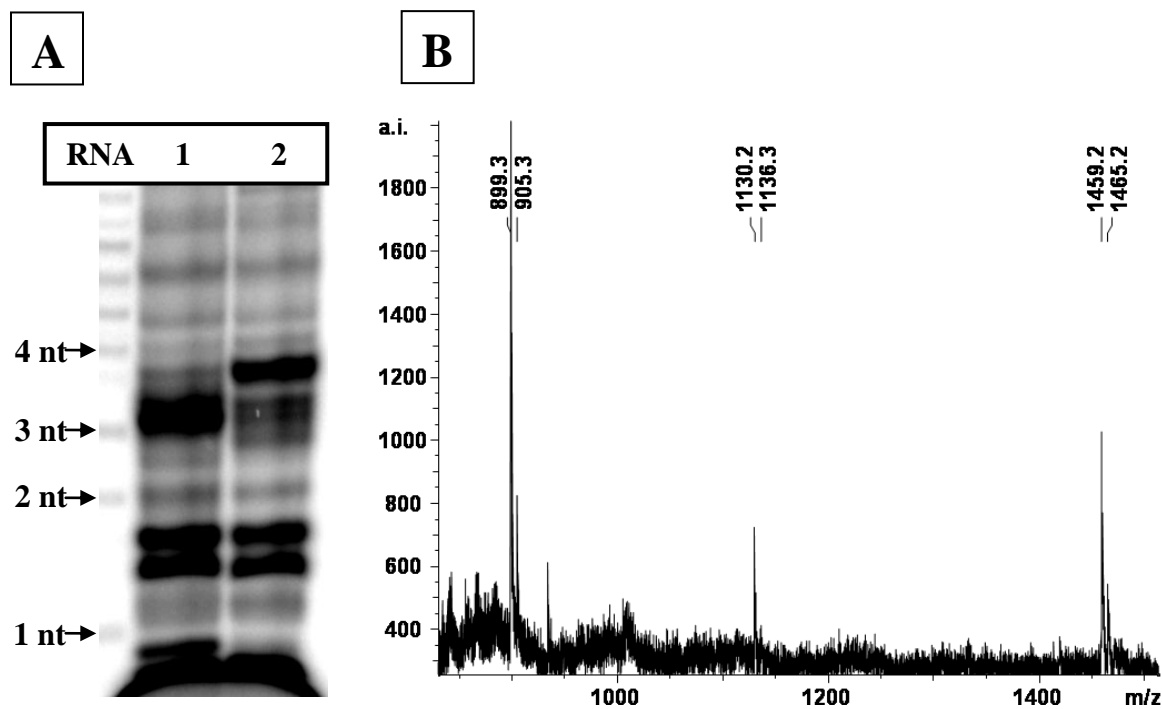
As expected, the alkylation rate does not decrease above pH ~8, as does the catalytic rate, because general acid deprotonation is inconsequential for the general base alkylation reaction, whereas general acid deprotonation inhibits the catalytic reaction. Surprisingly, alkylation activity levels off below pH ~7, which is contrary to the continued titration of the general base expected at lower pH. This unexpected effect is attributed to a basal, pH-independent alkylation mechanism, perhaps akin to an electrophilic aromatic substitution mechanism where alkylation would precede loss of a proton. The rate of this pH-independent alkylation mechanism overwhelms that of the pH-dependent mechanism as the nucleophile becomes largely protonated at below pH ~7. A similar effect is observed with respect to guanine N1 alkylation in the hammerhead ribozyme (*vide infra*). For the most part, the properties of the 9<sub>25</sub>-11 alkylation reaction appear to reflect those of the catalytic reaction, which suggests that 2'-bromoacetamide affinity labeling offers relevant mechanistic insight into general base catalysis.

Next, we sought to locate the site(s) of 9<sub>25</sub>-11 alkylation. Alkylation lesions on RNA are readily located by alkaline footprinting (*vide infra*), but such a simple approach is impossible for a DNAzyme given the relative hydrolytic stability of the DNA, even at high pH and temperature. As an alternative, hydroxyl radical and DNaseI footprinting were attempted, but neither approach yielded clear results. Alkylation of purine N3 or N7 positions can be readily located in DNA as these lesions lead to depurination; the resulting abasic site can be revealed by strand cleavage induced by hot piperidine treatment.<sup>220</sup> Importantly, the 9<sub>25</sub>-11 alkylation linkage was completely stable to hot piperidine treatment (Figure 3.13, Lane 7), thereby ruling out purine N3 or N7 alkylation in the case of 9<sub>25</sub>-11 (purine N1 alkylation cannot be ruled out as these lesions do not cause significant depurination<sup>220</sup>). In order to more precisely identify the alkylated DNAzyme nucleotide, the alkylated DNAzyme was submitted to enzymatic digestion followed by mass spectrometric fragment analysis.

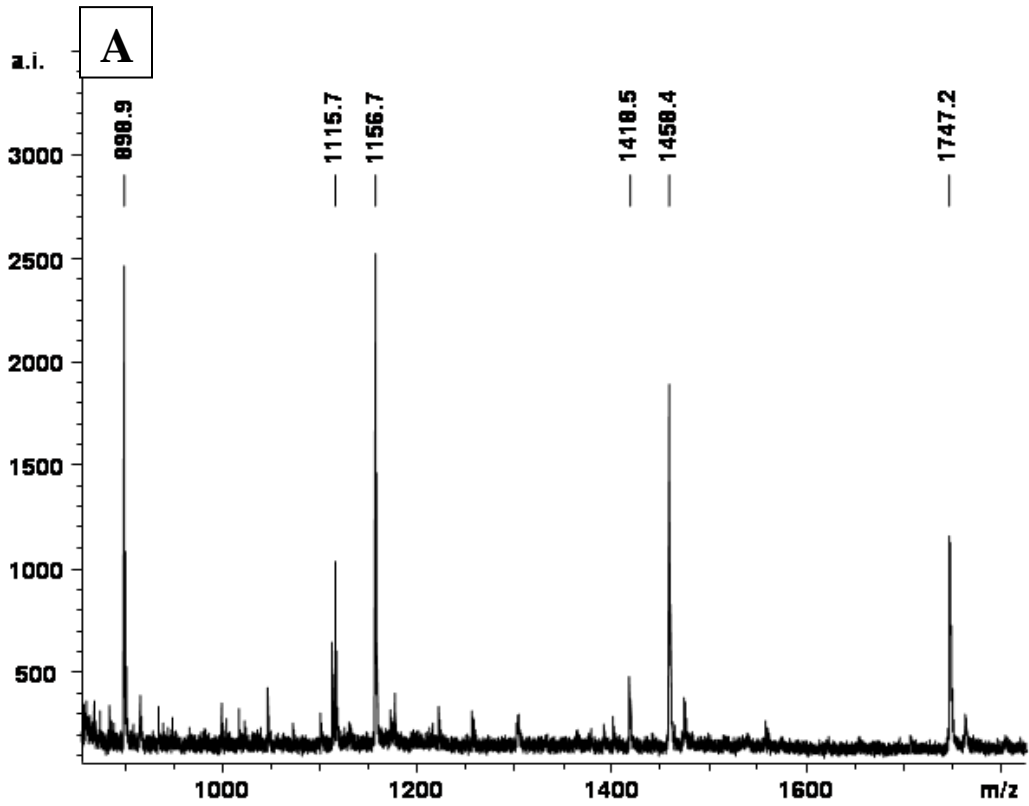
For mass spectrometric analysis, the alkylation reaction was performed on larger scale (1 to 2 nmol 9<sub>25</sub>-11). The alkylated DNAzyme was isolated by preparative d-PAGE, desalted, and subjected to nuclease digestion. The digestion progress could be monitored by 5'-<sup>32</sup>P-labeling the resulting fragments and gauging their size distribution by d-PAGE analysis. For example, Figure 3.15A shows the results of this analysis for a sample of alkylated 9<sub>25</sub>-11 subjected to exhaustive nuclease digestion as compared with a similarly digested mixture of unreacted 9<sub>25</sub>-11 and 2'-amino substrate analogue; clearly, unique fragments appear due to the presence of the alkylation linkage. The assignments of the digestion fragments observed in the MALDI-TOF spectra (Figures 3.15B, and 3.16A & B) that contain the alkylation lesion are summarized in Figure 3.17 and Table

3.4. The sequence assignments of the observed alkylation fragments are consistent with alkylation cross-linking of one, or both, of <sup>his</sup>dA23 and <sup>his</sup>dA24 (these possibilities cannot be distinguished based on mass spectrometric data alone). All alkylation fragments also contain at least one dG residue, which is assigned to the substrate analogue strand. Evidently, the nuclease is unable to remove the nucleotide at the 3'-side of the 2'-acetamide linked substrate nucleotide; this same effect was observed for ribonuclease digestion of alkylated hairpin ribozyme (*vide infra*).

**Figure 3.15:** (A) 20% d-PAGE analysis following 5'-<sup>32</sup>P-labeling of fragments resulting from exhaustive nuclease digestion of: unreacted 9<sub>25</sub>-11 and 2'-amino substrate analogue (Lane 1) and purified alkylated 9<sub>25</sub>-11 (Lane 2). An RNA cleavage ladder is labeled at left to help gauge the digestion fragment sizes. (B) MALDI-TOF spectrum obtained for the alkylated catalyst digestion sample analyzed in panel A. The peak assignments are given in Table 3.4 and Figure 3.17.



**Figure 3.16:** MALDI-TOF spectra for two (A & B) less extensively digested samples of alkylated 9<sub>25</sub>-11. Alkaline phosphatase was included in the digestion mixture for the sample in panel (B); therefore, the m/z values for these fragments reflect the absence of a 3'-phosphate. The peak assignments are given in Table 3.4 and Figure 3.17.



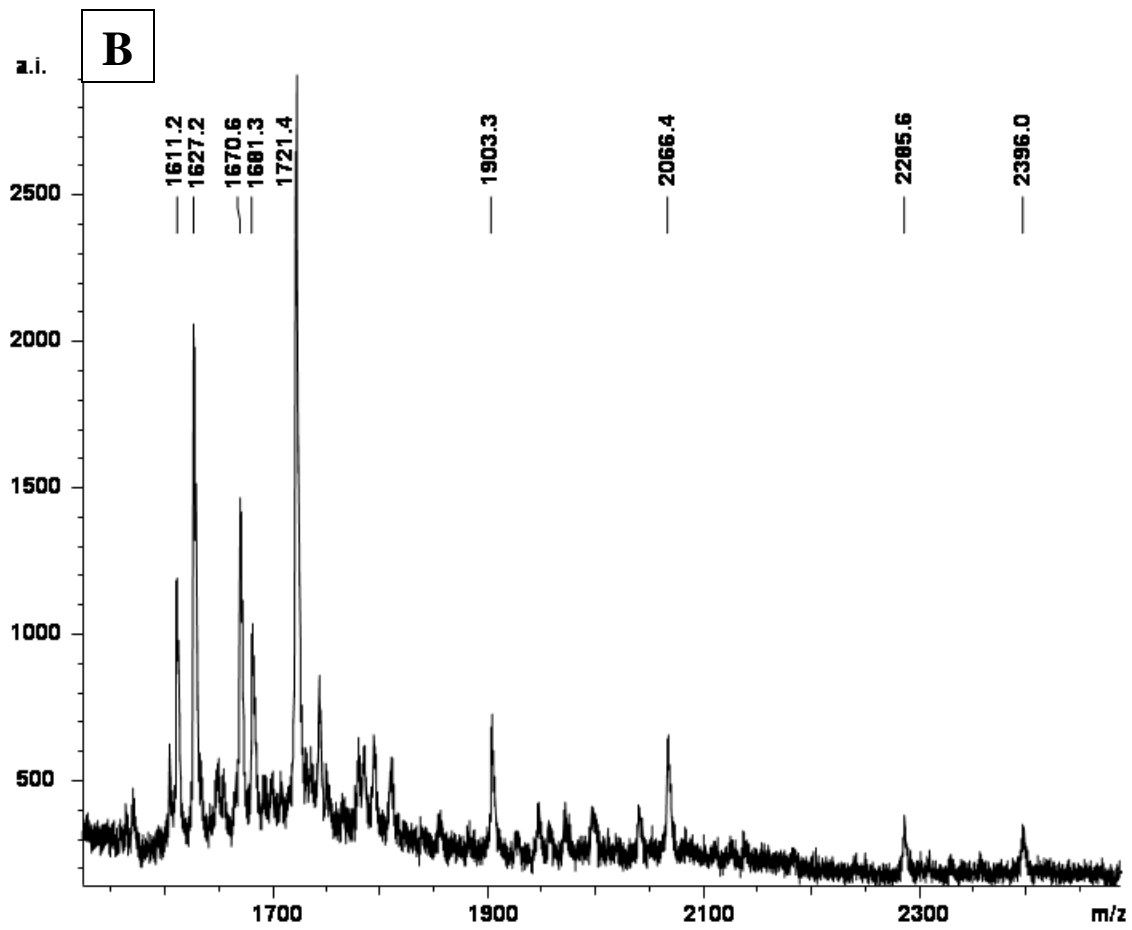
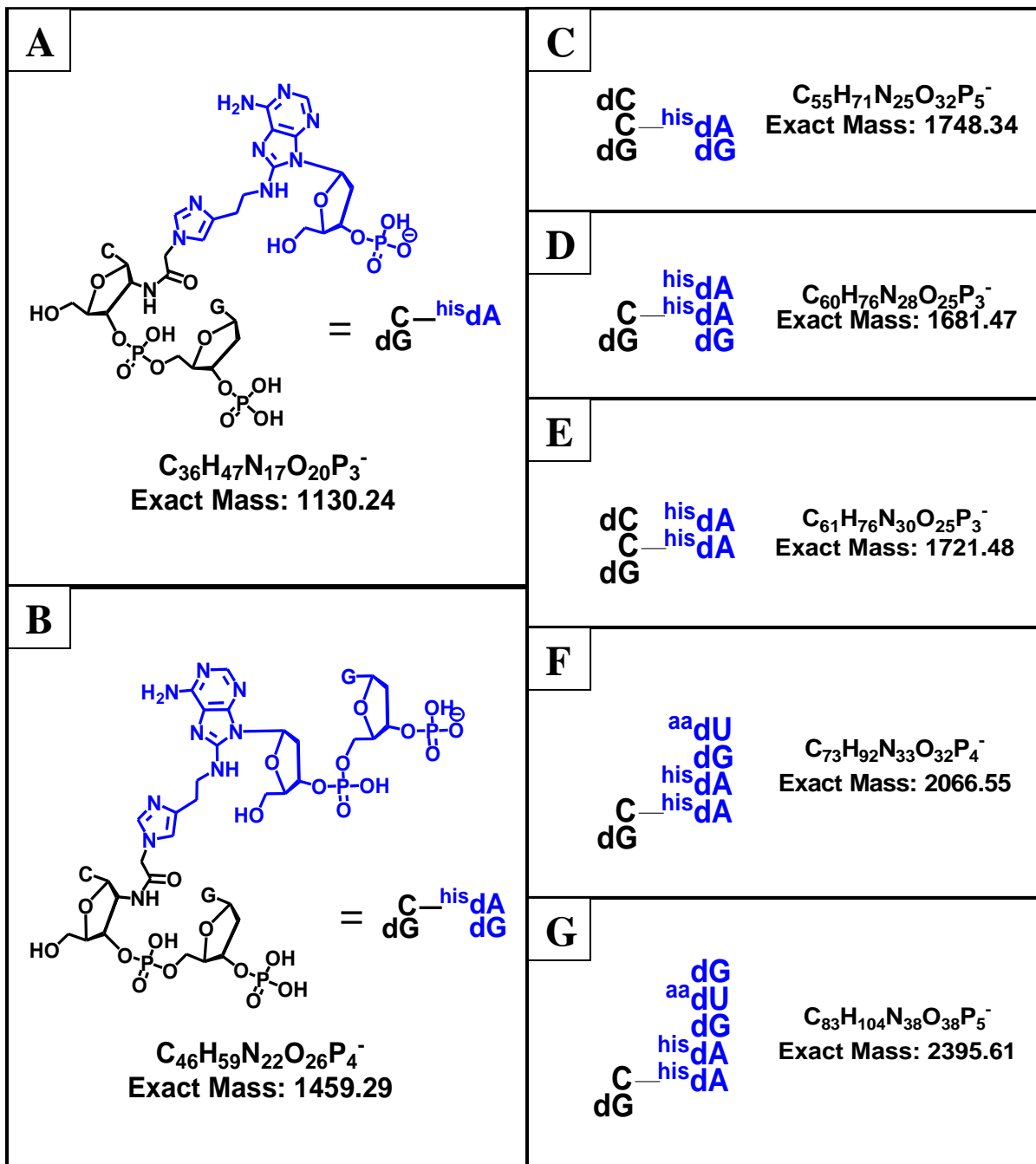


**Table 3.4:** Assignments and predicted and observed m/z values for the peaks observed in the MALDI-TOF spectra shown in Figures 3.15 and 3.16. Residues which originate from the DNAzyme and substrate analogue strands are coloured blue and black, respectively.

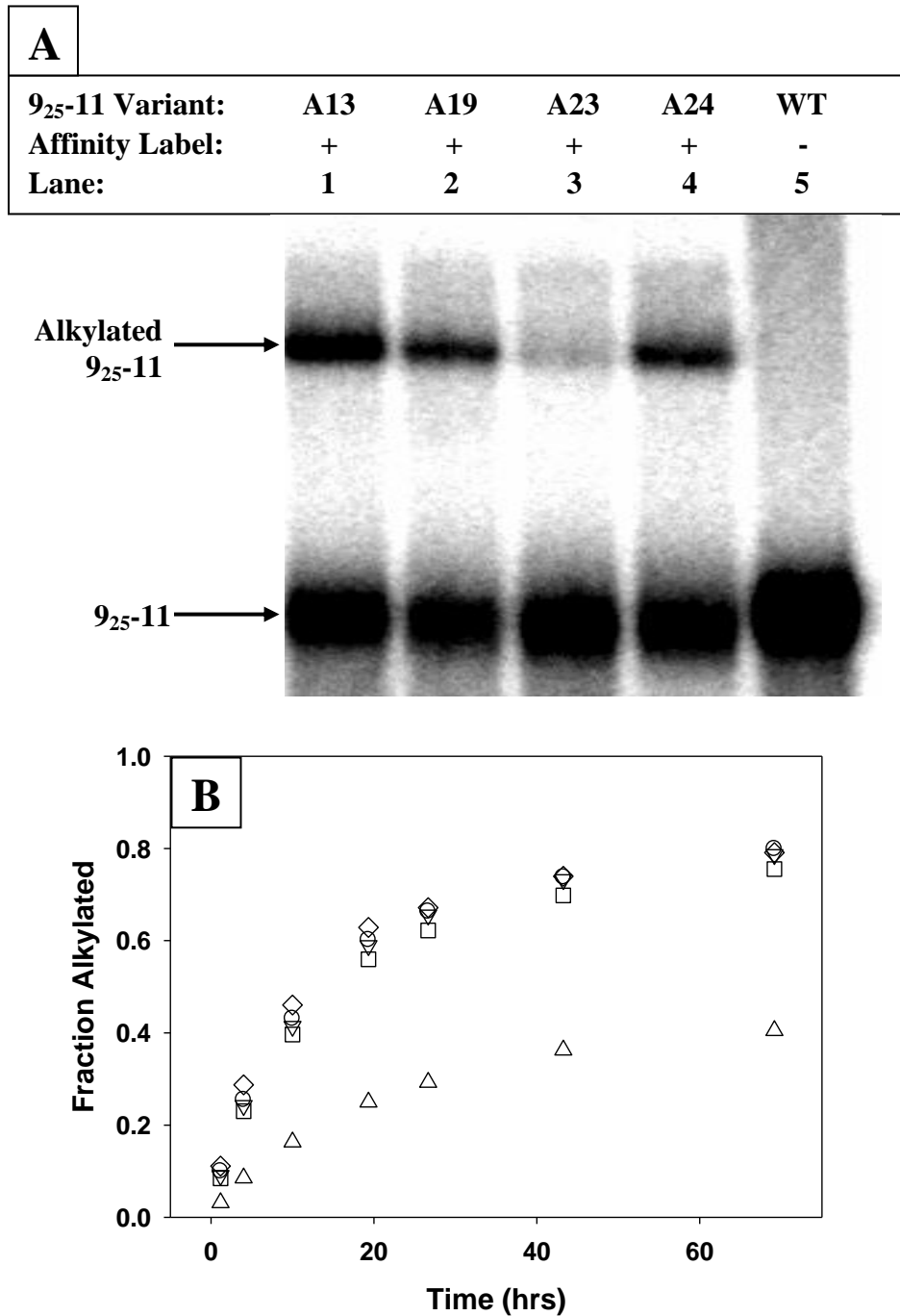
Assignment	[M-H] <sup>-</sup> Predicted m/z	[M-H] <sup>-</sup> Observed m/z
d(TpGpG)	898.2	898.3
See Figure 3.17A	1130.2	1130.2
d(ApCpGpC)	1157.2	1156.7
d( <sup>aa</sup> UpCp <sup>his</sup> Ap <sup>aa</sup> Up)	1418.3	1418.5
Figure 3.17B	1459.3	1458.4
d( <sup>his</sup> Ap <sup>aa</sup> UpCpCpG)	1611.4	1611.2
d( <sup>aa</sup> UpCp <sup>aa</sup> UpCp <sup>his</sup> A)	1627.4	1627.2
Figure 3.17C	1681.5	1681.3
Figure 3.17D	1721.5	1721.4
Figure 3.17E	1748.3	1747.2
Figure 3.17F	2066.6	2066.4
Figure 3.17G	2395.6	2396.0

**Figure 3.17:** Structures assigned to digestion fragments that contain the alkylation linkage (based on MALDI-TOF spectra in Figures 3.15 and 3.16). Residues which originate from the DNAzyme and substrate analogue strands are coloured blue and black, respectively.



In order to determine which of <sup>his</sup>dA23 and <sup>his</sup>dA24 had been alkylated, and whether the alkylation linkage involved an imidazole side chain, affinity labeling was performed for all 9<sub>25-11</sub> imidazole deletion variants. 9<sub>25-11</sub> alkylation was significantly diminished only when the imidazole side chain of <sup>his</sup>dA23 was absent, in the A23 variant (Figure 3.18). This finding suggests that alkylation occurs, at least primarily, on the imidazole moiety of <sup>his</sup>dA23 in wildtype 9<sub>25-11</sub>. Therefore, this functional group appears to be positioned similarly to the His12 general base in RNaseA, which was likewise identified by alkylation.<sup>94-96</sup> The remaining alkylation activity observed for the A23 variant could result from promiscuous alkylation of the adjacent, catalytically dispensable imidazole side chain of the <sup>his</sup>dA24 residue. The alkylation product of the A23 variant showed no significant difference in d-PAGE mobility relative to alkylation products of other 9<sub>25-11</sub> variants (Figure 3.18A), (such a difference would certainly indicate the existence of an alternative alkylation linkage in the A23 variant). It is not surprising, however, that the products resulting from alkylation of adjacent DNAzyme nucleotides (like <sup>his</sup>dA23 and <sup>his</sup>dA24) would be electrophoretically indistinguishable, considering that the products of the alkylation of four consecutive residues in the hammerhead ribozyme were inseparable by high resolution d-PAGE (*vide infra*).

**Figure 3.18:** Alkylation of 9<sub>25-11</sub> imidazole deletion variants in standard buffer at pH 7.5. (A) Autoradiogram showing d-PAGE separated products resulting from the alkylation of the indicated 9<sub>25-11</sub> variants. (B) The fraction of DNazyme alkylated is plotted as a function of time for wildtype 9<sub>25-11</sub> (◇) and the A13 (○), A19 (▽), A23 (△), and A24 (□) imidazole deletion variants.



The data from the digestion/mass spectrometry and imidazole deletion experiments, along with the noted stability of the alkylation lesion to hot piperidine treatment, strongly support the assignment of the imidazole side chain of the <sup>his</sup>dA23 residue as the 9<sub>25</sub>-11 alkylation site. The correlation of the properties of the alkylation and catalytic reactions provides strong evidence that this functional group acts as a general base in the 9<sub>25</sub>-11 catalytic mechanism. Overall, the 9<sub>25</sub>-11 affinity labeling results directly parallel the results of analogous experiments with RNaseA, where the general base catalyst (His12) was alkylated by 2'-bromoacetamido-mononucleotides. This notable parallel suggests that 9<sub>25</sub>-11 and RNaseA share a similar imidazole mediated general base catalysis mechanism.

### 3.3.4 Probing General Acid Catalysis

As described in Section 2.1.2, bridging phosphorothioate (S-link) substrates (Figure 3.3) have proven useful for identifying active site functional groups involved in general acid catalysis in both protein<sup>107, 113</sup> and ribozyme<sup>68</sup> catalyzed phosphodiester transfer reactions. In S-link substrate cleavage, the more labile departure of the lower p*K*<sub>a</sub> sulphur leaving group is known to proceed without benefit from general acid catalysis. Catalyst functional groups that contribute specifically to general acid catalysis can therefore be identified based on which mutations or chemical modifications lead to a conspicuously large ratio of rate constants for S-link and O-link substrate cleavage (*k*<sub>S</sub>/*k*<sub>O</sub>) relative to that for wildtype catalyst.

The rate constants for single turnover cleavage of O-link and S-link substrates, along with the corresponding *k*<sub>S</sub>/*k*<sub>O</sub> values, for wildtype and variant 9<sub>25</sub>-11 DNAzymes

are compared in Table 3.5. The largest value of  $k_S/k_O$  was observed upon removal of the imidazole side chain of <sup>his</sup>dA19, which suggests that this imidazole group is involved in general acid catalysis. This result directly parallels the findings of Thompson and Raines, who showed that the mutation of the His119 general acid in RNaseA significantly impairs cleavage of native RNA substrates, but has relatively little effect on cleavage of substrate with a *para*-nitrophenolate leaving group (see Section 2.1.2).<sup>35</sup> Specifically, for the H119A mutant, the ratio of rate constants ( $k_{cat}$ ) for nitrophenolate to native substrate cleavage (the analogue of  $k_S/k_O$ ) was nearly 1000-fold greater than the same ratio for wildtype RNaseA. In the case of 9<sub>25-11</sub>, the value of  $k_S/k_O$  for the A19 9<sub>25-11</sub> variant is only 87 times that for wildtype 9<sub>25-11</sub>. Furthermore, the degree to which the H119A mutation impaired native substrate cleavage (~2000-fold) is more severe than the degree to which the A19 variant is impaired (~280-fold). These differences suggest that His119 is better optimized for general acid catalysis in RNaseA and makes a greater contribution to transition state stabilization than the A19 imidazole in 9<sub>25-11</sub>; this is consistent with the fact that RNaseA is a much more efficient catalyst than 9<sub>25-11</sub>. Similarly, Das and Piccirilli have reported much larger  $k_S/k_O$  values for general acid mutation in the HDV ribozyme (see Section 2.1.2); in that case, C76 mutation led to  $k_S/k_O$  values of up to ~60,000-fold greater than for wildtype.<sup>68</sup> More akin to the results for 9<sub>25-11</sub>, Tsai and coworkers observed  $k_S/k_O$  values ~100-fold greater than wildtype upon general acid mutation in a phospholipase enzyme (see Section 2.1.2).<sup>107, 113</sup> Apparently general acid catalysis provides a more comparable contribution of transition state stabilization in these two catalysts, as opposed to the HDV ribozyme or RNaseA.

**Figure 3.19:** Representative data for S-link substrate cleavage catalyzed by 9<sub>25-11</sub>. (A) Autoradiogram showing time dependent S-link cleavage for wildtype 9<sub>25-11</sub> (time points taken from 0.17 to 28 minutes for wild type, longer time points were taken for other mutants). (B) Plots of showing the progress of S-link substrate cleavage for wildtype (◇), A24 (○), A19 (△), and A23 (□).

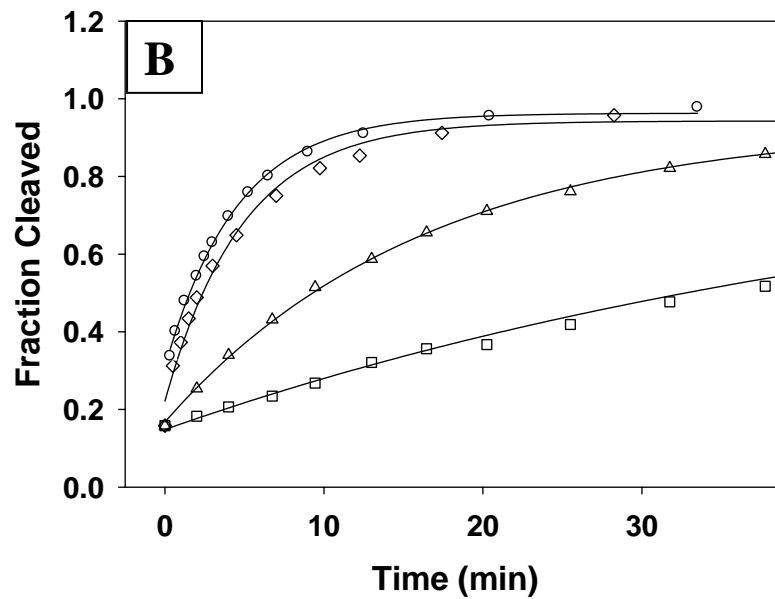
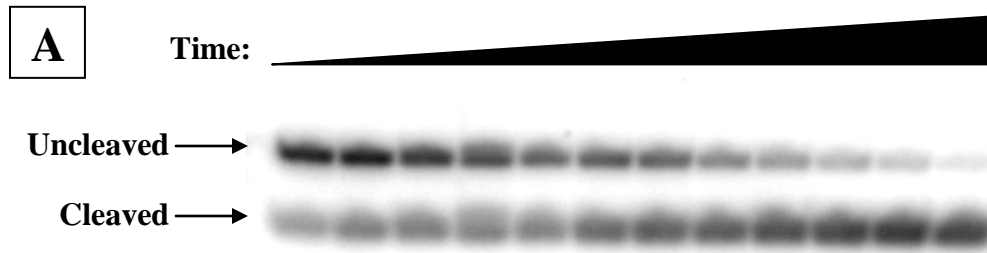


**Table 3.5:** The effects of individual synthetic functional group deletion on the observed rate constants for 9<sub>25-11</sub> catalyzed cleavage of the bridging 5'-phosphorothioate (S-link) substrate in standard buffer (pH 7.5). The data for native substrate cleavage from Table 3.3 are included for comparison.

DNAzyme <sup>a</sup>	$k_O$ (min <sup>-1</sup> )	$k_{O\text{ rel}}$ <sup>b</sup>	$k_S$ (min <sup>-1</sup> )	$k_{S\text{ rel}}$ <sup>b</sup>	$k_S/k_O$
WT	0.020	1	0.20	1	10
A13	0.00005	0.0025	0.019	0.095	380
A19	0.00007	0.0035	0.061	0.31	871
A23	<0.00001	<0.00005	0.0017	0.0085	>170
A24	0.045	2.3	0.22	1.1	4.9
T8	0.0074	0.37	0.067	0.34	9.0
T9	0.0068	0.34	0.052	0.26	7.6
T11	0.0025	0.13	0.048	0.24	19
T14	0.0097	0.49	0.086	0.43	8.9
T18	0.012	0.60	0.097	0.49	8.1
T21	0.0004	0.020	0.011	0.055	28
none <sup>c</sup>	n.d. <sup>d</sup>	n.d. <sup>d</sup>	0.00069	0.0035	n.d. <sup>d</sup>

<sup>a</sup> 9<sub>25-11</sub> variants named as in Table 3.3

<sup>b</sup>  $k_{\text{rel}}$  is the ratio  $k(\text{variant})/k(\text{wildtype})$  for either native (O-link) or S-link substrate cleavage.

<sup>c</sup> background cleavage rate constant in standard buffer (pH 7.5).

<sup>d</sup> n.d. = not determined

Although not as large as that for the A19 variant, the  $k_S/k_O$  value observed for the A13 variant is still conspicuously greater than that for wildtype 9<sub>25-11</sub>. This indicates that the <sup>his</sup>dA13 imidazole may also be important for efficient general acid catalysis, although less so than the <sup>his</sup>dA19 imidazole. Restoration of activity against S-link substrates where active site residues other than the putative general acid are mutated has

been observed before in a phospholipase enzyme. In that case, the additionally identified residue is hypothesized to engage in hydrogen bonding interactions that are important for the proper alignment of the general acid for proton transfer to the substrate.<sup>107, 113</sup> A similar interaction has also been identified in RNaseA based on crystallographic and biochemical data, where the carboxylate side chain of Asp121 forms a hydrogen bond with His119 so as to optimize orientation of the latter for general acid catalysis.<sup>215, 221</sup> It is possible that the <sup>his</sup>dA13 imidazole may contribute similarly to proper positioning of the <sup>his</sup>dA19 imidazole for proton transfer to the leaving group, although in the absence of structural data its role remains unclear.

The A23 9<sub>25-11</sub> variant also exhibited a rather large  $k_S/k_O$  value relative to wildtype 9<sub>25-11</sub>, which was not expected given that the <sup>his</sup>dA23 imidazole is implicated in general *base* catalysis (Section 3.3.3). The rate constant for S-link substrate cleavage by the A23 variant, however, is just three fold greater than the background cleavage rate constant (Table 3.5). It is certainly plausible that such a minor degree of rate enhancement could result from structural constraints in the substrate-DNAzyme complex that might favour the in-line nucleophilic attack geometry required in RNA cleavage.<sup>222</sup> Overall, the S-link substrate cleavage data suggest that the imidazole side chain of <sup>his</sup>dA19 mediates general acid catalysis in 9<sub>25-11</sub>, with direct analogy to the mechanistic role of His119 in RNaseA. The imidazole side chain of <sup>his</sup>dA13 may also play a less direct role in facilitating general acid catalysis.

### 3.3.5 Probing DNAzyme-Scissile Phosphate Interactions

In RNaseA, the cationic amine functionality of Lys41 is believed to provide hydrogen bond stabilization of the negative charge that accumulates on the nonbridging oxygens in the phosphorane transition state.<sup>31, 36</sup> To probe for similar interactions in 9<sub>25</sub>-11 catalysis, we examined the cleavage of a nonbridging phosphorothioate substrate analogue (Figure 3.3) in the context of DNAzyme functional group deletion. The nonbridging sulphur substitution alters the electronic and hydrogen-bonding properties of the scissile phosphate; therefore, we hypothesized that this substitution should significantly affect catalysis by altering any DNAzyme-transition state interaction(s) involving the scissile phosphate nonbridging oxygen(s). Furthermore, in 9<sub>25</sub>-11 variants in which such interactions are absent or disrupted, we expected that: (1) cleavage of the native substrate should be significantly impaired, and (2) cleavage of the nonbridging phosphorothioate and native substrates should be very similar, as observed for base catalyzed phosphorothioate cleavage (*vide infra*). In contrast, for 9<sub>25</sub>-11 variants in which the DNAzyme-scissile phosphate interaction remains intact, the disruptive effects of nonbridging phosphorothioate substitution on catalytic activity should be similar to those observed for wildtype 9<sub>25</sub>-11 catalysis.

In our experiments, we used the (~1:1) mixture of cleavage site phosphorothioate diastereomers which results from the standard sulphurization reaction in solid phase synthesis.<sup>223</sup> Kinetic data for carbonate-induced cleavage of the phosphorothioate substrate mixture fit very well to a monophasic model with  $R^2 = 0.9982$  (Figure 3.20). This result indicates that non-enzymatic, base catalyzed cleavage of the two diastereomers proceeds through transition states which are nearly energetically

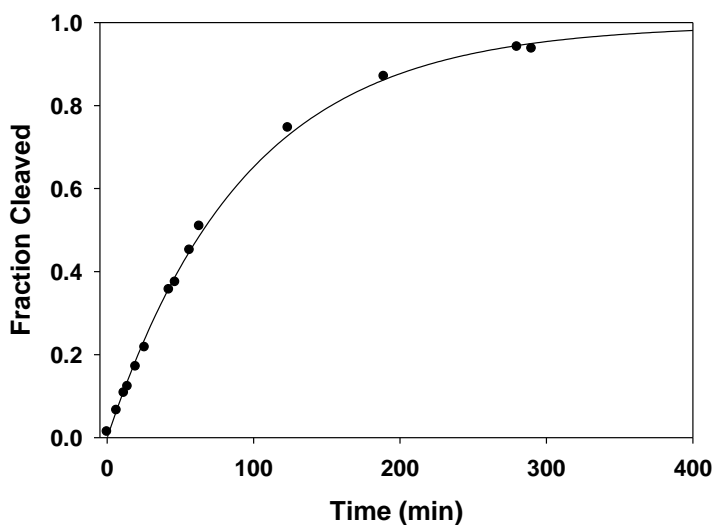
indistinguishable (this has been demonstrated previously for different RNA sequences<sup>224-226</sup> and has also been predicted theoretically<sup>109, 110</sup>). In contrast, cleavage of this diastereomeric substrate mixture catalyzed by wildtype 9<sub>25</sub>-11, and all but one of the variants tested (*vide infra*), was clearly biphasic (Figure 3.21). Clearly, the biphasic nature of 9<sub>25</sub>-11-catalyzed phosphorothioate cleavage must result from diastereoselective DNAzyme-scissile phosphate interaction(s), and not from intrinsic transition state energy differences inherent in the cleavage of the two substrate diastereomers (at least where nonbridging oxygen negative charge is not stabilized by protonation, as is the case in the specific base catalyzed mechanism).<sup>12</sup>

As expected for the biphasic cleavage of a 1:1 substrate mixture, the faster phosphorothioate cleavage phases for all 9<sub>25</sub>-11 variants exhibited endpoints close to half the size of those for native substrate cleavage. Similarly, the slow phosphorothioate cleavage phases all exhibited endpoints less than half the size of those for native substrate cleavage. The T21 variant is a notable exception (Figure 3.21) in that it exhibited monophasic cleavage of the phosphorothioate mixture (as shown in Table 3.6, the biphasic fit returned an improved  $R^2$  value relative to the monophasic fits for all variants except T21). Furthermore, the T21 variant cleaved *more than half* of the phosphorothioate substrate mixture monophasically, and to nearly the same endpoint as observed for native substrate cleavage by the T21 variant (Table 3.7). Thus, it seems clear that the single phosphorothioate cleavage phase observed for the T21 variant comprises the cleavage of both substrate diastereomers at indistinguishable rates.

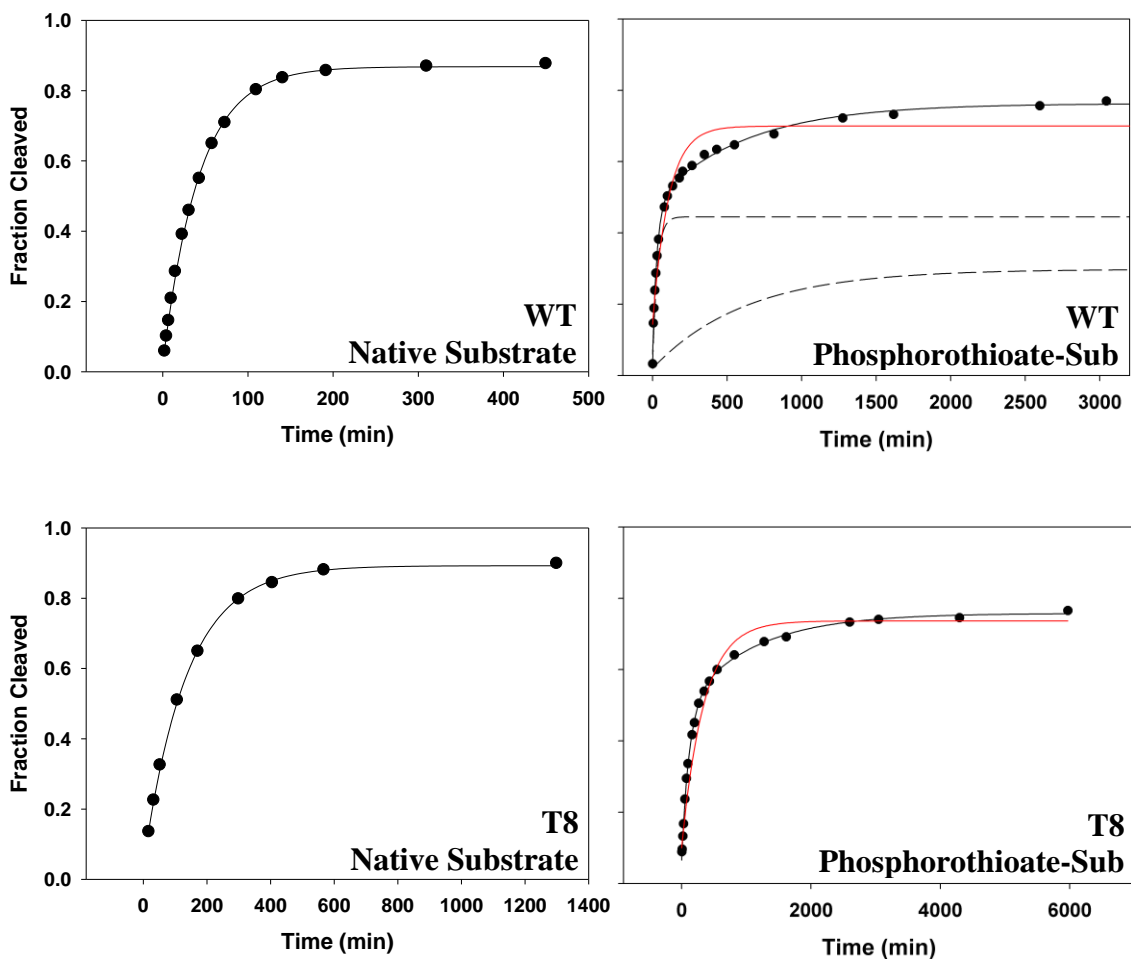
In 9<sub>25</sub>-11 catalyzed nonbridging phosphorothioate cleavage, the rate of the faster cleaving phase is not significantly affected relative to native substrate cleavage for

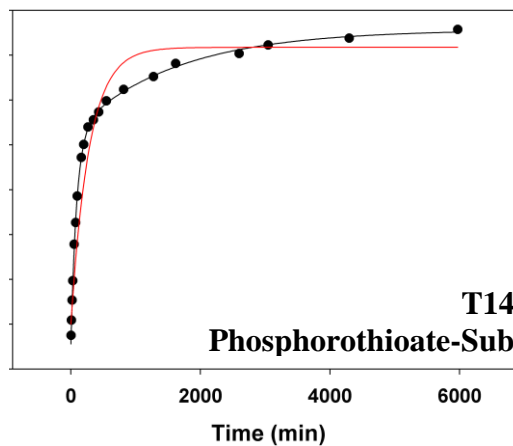
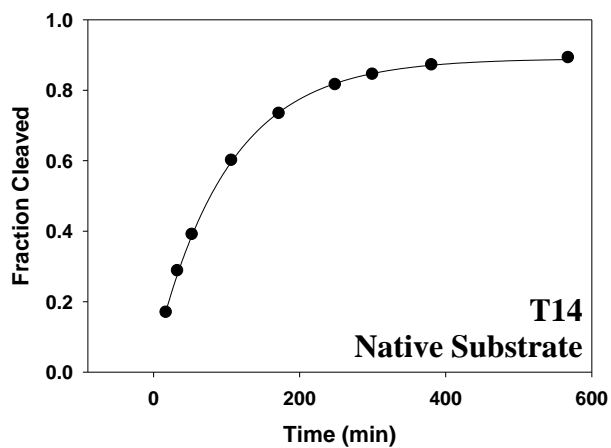
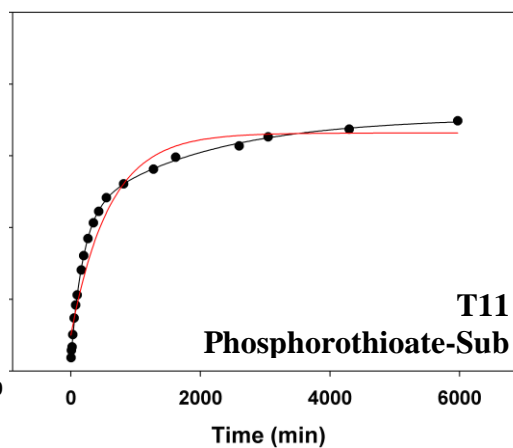
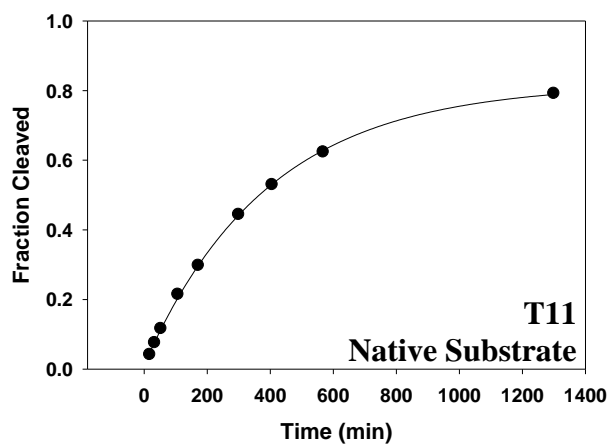
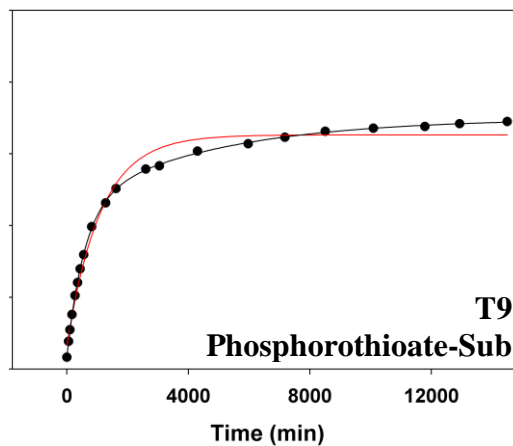
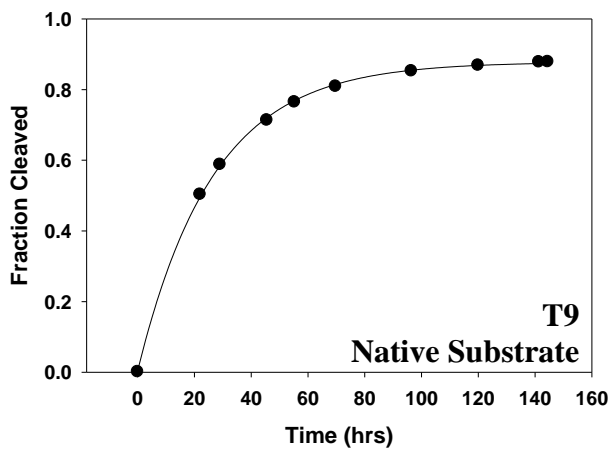
wildtype 9<sub>25</sub>-11 and all variants tested (Table 3.7). Thus, with a similar rate constant to native substrate cleavage, the fast phase likely reflects cleavage of the substrate diastereomer in which sulphur replaces the nonbridging oxygen that is not involved in the scissile phosphate-DNAzyme interaction(s). The slower phosphorothioate cleavage phase proceeds roughly 10-fold more slowly than native substrate cleavage for all of the 9<sub>25</sub>-11 variants for which a slow cleaving phase was detected. Thus the slower cleaving phase represents cleavage of the phosphorothioate diastereomer where the nonbridging sulphur atom disrupts interactions between the scissile phosphate and 9<sub>25</sub>-11.

**Figure 3.20:** Monophasic cleavage of the nonbridging phosphorothioate substrate in 0.5% K<sub>2</sub>CO<sub>3</sub> at 92 °C under mineral oil. The data were fit to the single exponential Equation 3.8, yielding the following parameters:  $P_0 = 9.4 \times 10^{-11}$ ,  $P_\infty = 0.995$ ,  $k_{\text{obs}} = 0.0107 \text{ min}^{-1}$ ,  $R^2 = 0.9983$ .



**Figure 3.21:** Comparison of native substrate and phosphorothioate substrate (diastereomeric mixture) cleavage kinetics for wildtype 9<sub>25-11</sub> and variants in which individual <sup>aa</sup>dU residues are replaced with dT. All native substrate cleavage data were fit to monophasic Equation 3.8; nonbridging phosphorothioate substrate cleavage data were fit to both Equation 3.8 (red), and biphasic Equation 3.9 (black). The constituent cleavage phases are shown as dashed lines for wildtype cleavage of the nonbridging phosphorothioate substrate mixture.  $R^2$  values for all fits are given in Table 3.6, and kinetic parameters are given in Table 3.7. All reactions were performed in standard buffer at pH 7.5.





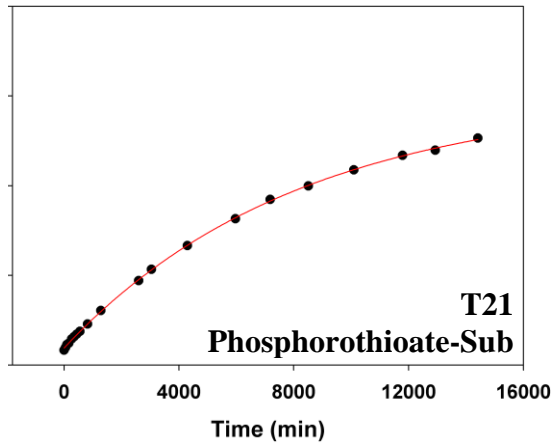
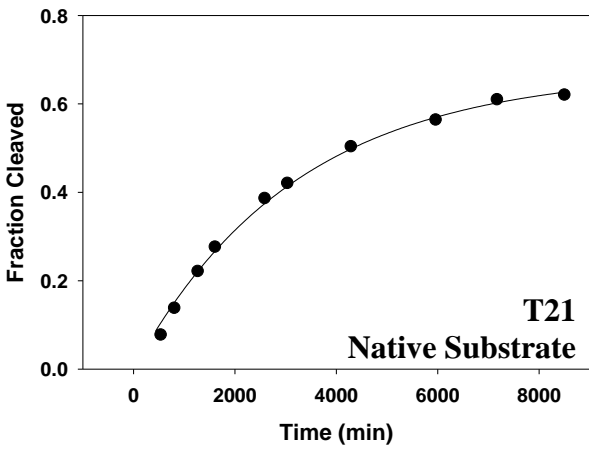
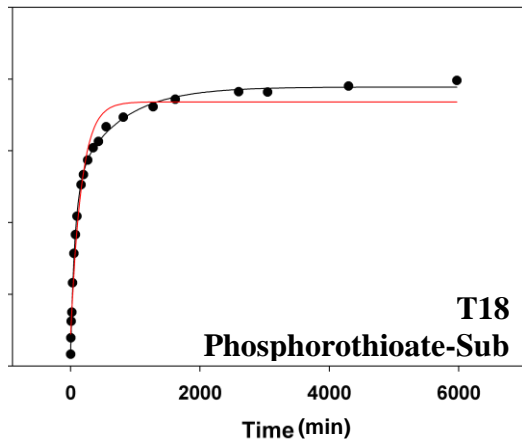
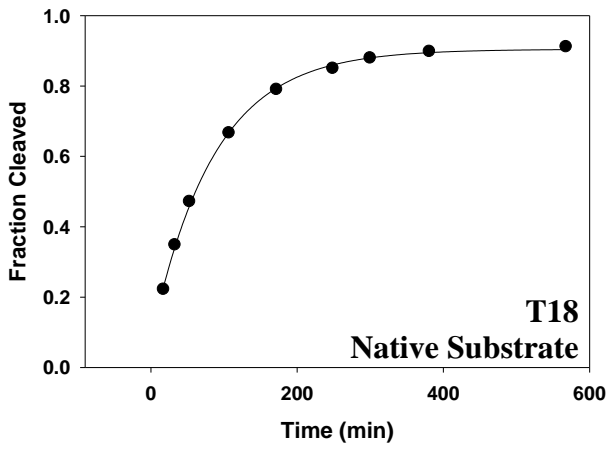


**Table 3.6:**  $R^2$  values for the fits of the kinetic data in Figure 3.21. Clearly, native substrate cleavage fits very well to a monophasic model for wildtype and all mutants tested. Cleavage of the nonbridging phosphorothioate mixture fits well to a monophasic model only for the T21 mutant; notably, this is the only case in which the biphasic fit offers no improvement in the  $R^2$  value. In all other cases, the biphasic fits returned much improved  $R^2$  values relative to the monophasic fits.

DNAzyme	Native Substrate	Nonbridging Phosphorothioate Substrate	
	Monophasic $R^2$	Monophasic $R^2$	Biphasic $R^2$
WT	0.9993	0.9445	0.9975
T8	0.9996	0.9241	0.9995
T9	0.9997	0.9879	0.9998
T11	0.9997	0.9354	0.9996
T14	0.9997	0.8350	0.9995
T18	0.9992	0.9779	0.9985
T21	0.9996	0.9998	0.9998

**Table 3.7:** First order rate constants for nonbridging phosphorothioate cleavage by 9<sub>25</sub>-11 and variants (determined by fitting the data in Figure 3.21).  $k_{S \text{ fast}}$  and  $k_{S \text{ slow}}$  describe the fast and slow phases, respectively, for biphasic cleavage of the nonbridging phosphorothioate substrate mixture.

<b>DNazyme</b>	$k_{S \text{ fast}}^a$ ( <b>min<sup>-1</sup></b> )	$k_{S \text{ slow}}^a$ ( <b>min<sup>-1</sup></b> )
WT	0.034 ±0.003	0.0018 ±0.0002
T8	0.0079 ±0.0004	0.0009 ±0.0002
T9	0.00173 ±0.00006	0.00022 ±0.00002
T11	0.0047 ±0.0002	0.0005 ±0.0001
T14	0.0121 ±0.0006	0.0007 ±0.0001
T18	0.014 ±0.001	0.0016 ±0.0003
T21	0.000119 ±0.000003	n.d. <sup>b</sup>

<sup>a</sup> errors reported are the standard deviations returned for each parameter by the fits.

<sup>b</sup> n.d.= a slow cleavage phase was not detected in this reaction

**Table 3.8:** Comparison of the kinetic parameters determined for native and nonbridging phosphorothioate substrate cleavage by 9<sub>25</sub>-11 and variants.  $k_O$  is the observed rate constant for native substrate cleavage (see Table 3.3) and  $k_{S \text{ fast}}$  and  $k_{S \text{ slow}}$  are the observed rate constants for the fast and slow phases, respectively, of nonbridging phosphorothioate substrate cleavage (see Table 3.7). The endpoints ( $P_\infty$ ) for each of the phosphorothioate cleavage phases and those for native substrate are also compared.

<b>DNAzyme</b>	$k_{S \text{ fast}}/k_O$	$k_{S \text{ slow}}/k_O$	$P_\infty \text{ S fast}^a$	$P_\infty \text{ S slow}^a$	$P_\infty \text{ O}^a$
WT	1.7	0.1	0.41 ±0.01	0.28 ±0.01	0.86 ±0.01
T8	0.89	0.1	0.46 ±0.02	0.23 ±0.02	0.848 ±0.009
T9	1.7	0.2	0.41 ±0.01	0.24 ±0.01	0.872 ±0.007
T11	0.77	0.07	0.41 ±0.02	0.27 ±0.01	0.798 ±0.009
T14	1.3	0.08	0.463 ±0.009	0.232 ±0.008	0.856 ±0.006
T18	0.81	0.1	0.44 ±0.03	0.30 ±0.03	0.83 ±0.01
T21	0.60	n.d. <sup>b</sup>	0.567 ±0.003	n.d. <sup>b</sup>	0.62 ±0.01

<sup>a</sup> errors reported are the standard deviations returned for each parameter by the fits.

<sup>b</sup> n.d.= a slow cleavage phase was not detected in this reaction

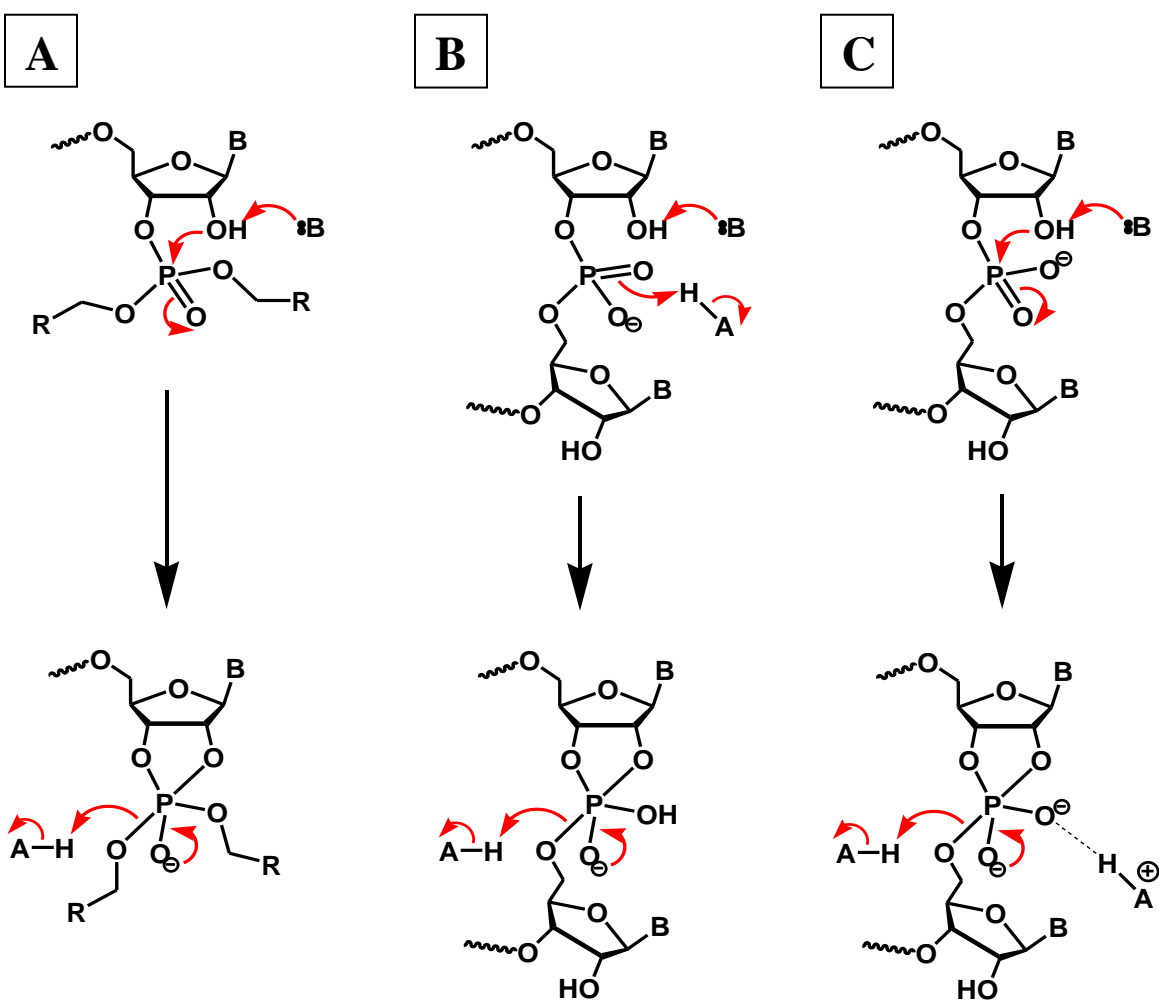
In the case of the T21 variant, the fact that the two diastereomers of the nonbridging phosphorothioate substrate are cleaved at indistinguishable rates, which are also similar to the rate of native substrate cleavage, indicates the distinct absence of DNAzyme-scissile phosphate interactions in the T21 variant. This finding suggests that the cationic amine side chain of the <sup>aa</sup>dU21 residue is responsible for the diastereoselective interaction with a nonbridging scissile phosphate oxygen. In the case of a phospholipase enzyme, similar reasoning has been used, in light of crystal structure data, to verify the diastereoselective interaction of an arginine side chain with a substrate nonbridging phosphate oxygen. In that case, arginine mutation completely abolished a

7600-fold rate difference for the cleavage of the two nonbridging phosphorothioate diastereomers that had been observed for the wildtype enzyme.<sup>227</sup>

The magnitude of nonbridging thio-effects has also been used to distinguish between transition state stabilization by full protonation of a nonbridging oxygen in a “triest-er-like” mechanism<sup>228</sup> (Figure 3.22B), or by electrostatic and hydrogen bond type interactions in a “classical” mechanism (Figure 3.22C).<sup>229</sup> At low pH, full protonation of nonbridging oxygens via specific acid catalysis is well characterized in the cleavage of RNA model systems;<sup>9, 10, 12</sup> under these conditions, nonbridging phosphorothioate substitution is known to diminish cleavage rate by factors of 100 or more.<sup>230, 231</sup> In contrast, nonbridging phosphorothioate substitution has very little effect on specific base catalyzed RNA cleavage,<sup>224-226, 230, 231</sup> where nonbridging oxygens remain deprotonated.<sup>12</sup> Therefore, large nonbridging thio-effects in enzyme catalyzed phosphoryl transfer reactions have been suggested to indicate a triester mechanism where a nonbridging oxygen atom is fully protonated by an acidic active site residue.<sup>229</sup> For example, phospholipase (wildtype) catalysis was diminished by factors of  $10^5$  and 3 for the two diastereomeric phosphorothioate substrates relative to the native substrate, which was taken to indicate a triester mechanism in which the *pro-S* oxygen, specifically, is protonated.<sup>113</sup> In contrast, RNaseA catalysis is diminished by factors of only 70 and 2 for the two phosphorothioate isomers.<sup>224</sup> This smaller nonbridging thio-effect argues against a triester mechanism in the case of RNaseA;<sup>229</sup> instead, Lys41 is thought to stabilize the anionic transition state via Coulombic interaction with, or hydrogen bond donation to, a nonbridging scissile phosphate oxygen.<sup>36, 232</sup> Similarly, negligible nonbridging thio-effects have been observed for model systems that involve intramolecular hydrogen bond

stabilization (by a hydroxyl group) of negative charge on nonbridging oxygens.<sup>233</sup> Nonbridging phosphorothioate substitution has a minor effect on 9<sub>25</sub>-11 catalysis (<10-fold), which is consistent with the involvement of the cationic amine side chain of <sup>aa</sup>dU21 in a hydrogen bonding and/or Coulombic interaction with the scissile phosphate (Figure 3.22C), rather in full protonation of a nonbridging oxygen (Figure 3.22B).

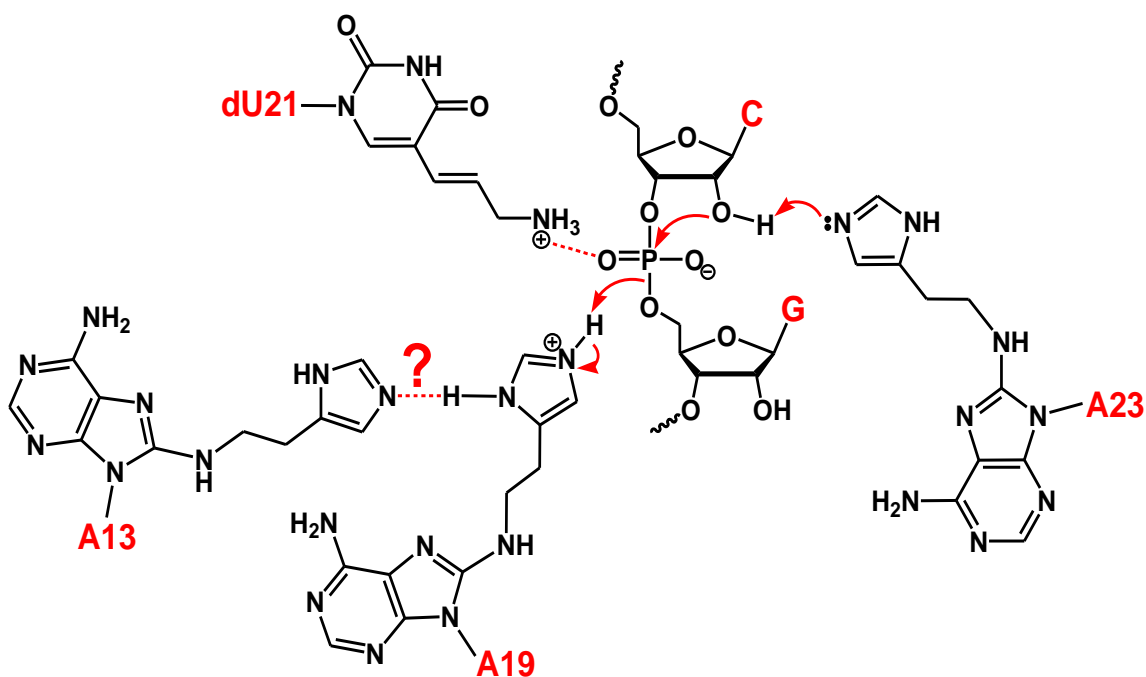
**Figure 3.22:** Possible enzymatic mechanisms for acid/base catalyzed cleavage of phosphoester linkages by 2'-transphosphorylation. (A) Phosphotriester cleavage, (B) phosphodiester cleavage via a “triest-er-like” mechanism,<sup>228</sup> and (C) phosphodiester cleavage via a “classical” dianionic mechanism.<sup>229</sup>



### 3.4 CONCLUSIONS

In this study, we have applied a broad range of chemical probing and enzymological experiments to investigate the catalytic mechanism of the 9<sub>25</sub>-11 DNAzyme. The methods used were inspired by analogous experiments used previously to characterize the catalytic mechanisms of RNaseA and RNA cleaving ribozymes. In particular, the results of our affinity labeling and bridging phosphorothioate substrate experiments highlight remarkable parallels between the characteristics of RNaseA and 9<sub>25</sub>-11 catalysis. That is, in both cases specific imidazole groups are implicated in general acid and base catalysis. We have also found strong evidence that a particular cationic amine of 9<sub>25</sub>-11 interacts diastereoselectively with a nonbridging scissile phosphate oxygen, reminiscent of the role of Lys41 in RNaseA catalysis. This work provides compelling evidence that certain 9<sub>25</sub>-11 side chains mimic the mechanistic roles of their counterparts in the active site of RNaseA (Figure 3.23); however, the organization of these catalytic functional groups in 9<sub>25</sub>-11 is not optimized to the degree to which evolution has optimized the active site structure of RNaseA. Note that in the absence of structural data, we cannot rule out other mechanistic possibilities including more complex proton transfer processes (such as those considered in specific acid/base and buffer catalyzed mechanisms)<sup>12, 234, 235</sup> or the involvement of active site water molecules in catalysis (as has been considered for some ribozymes).<sup>236-240</sup>

**Figure 3.23:** Catalytic mechanism for 9<sub>25</sub>-11 proposed based upon the data presented in this chapter. The role depicted for A13 is highly speculative.



Our findings appear to confirm that 9<sub>25</sub>-11 is the first synthetic, sequence specific RNaseA mimic capable of moderately efficient multiple catalytic turnover ( $k_{cat}/K_m \sim 5 \cdot 10^5 \text{ M}^{-1} \text{ min}^{-1}$ ). The capability for multiple turnover catalysis distinguishes 9<sub>25</sub>-11 from other sequence specific synthetic catalysts that have been generated by rational design. In 9<sub>25</sub>-11, synthetically added, protein-like functionalities are incorporated into a familiar 2D-anatomy resembling the minimal hammerhead ribozyme and 10-23 DNAzyme; therefore, 9<sub>25</sub>-11 serves as a prototypical hybrid of natural nucleic acid catalysts and synthetic ribonuclease mimics.

The use of an “RNaseA-like” mechanism by 9<sub>25</sub>-11 provides a significant catalytic advantage (1-2 orders of magnitude) compared to unmodified nucleic acid catalysts in the absence of a  $\text{M}^{2+}$  cofactor,<sup>90, 91</sup> at physiological pH and ionic strength.<sup>87</sup>

However, the catalytic power of 9<sub>25</sub>-11 still falls far short of that of RNaseA (the value of  $k_{\text{cat}}$  for RNaseA<sup>3</sup> is some 10<sup>4</sup>-10<sup>5</sup> fold greater than  $k_{\text{cat}}$  for 9<sub>25</sub>-11). The *in vitro* evolution of an active site that is optimized to fully exploit the power of an RNaseA-like mechanism is likely to come from optimization of the *in vitro* selection methodology as well as the inclusion of different and/or additional modified nucleotides.

Our findings demonstrate that supplying appropriate chemical functionality in the context of a combinatorial DNAzyme selection experiment can result in biomimetic catalysts that functionally differ from unmodified nucleic acid catalysts selected to catalyze similar reactions. In this case, it appears that the evolutionary demand for RNA cleavage in the absence of a M<sup>2+</sup> has been met by deploying active site functional groups that mimic those found at the active site of RNaseA. Thus the addition of synthetic, protein-like functionality has, at least in the case of 9<sub>25</sub>-11, expanded the diversity of mechanistic strategies available to a nucleic acid based catalyst.

# CHAPTER 4: PROBING GENERAL ACID/BASE CATALYSIS IN THE HAMMERHEAD RIBOZYME

## 4.1 INTRODUCTION

### 4.1.1 “Minimal” Hammerheads: A Structure and Function Dilemma

As discussed in Section 1.5.1, the hammerhead ribozyme was first discovered in viral satellite RNAs, where it undergoes sequence specific self-cleavage via 2'-transphosphorylation.<sup>53, 54</sup> Amongst the known small ribonucleolytic ribozymes, the hammerhead motif appears to be the most wide spread in Nature. Aside from numerous viral satellites and viroids, hammerhead ribozymes have now been identified in a wide variety of species; for example, in the transcripts of satellite DNA in newts<sup>241</sup> and parasitic *Schistoma* flukes,<sup>242</sup> and in mRNA 3'-UTR sequences in mouse, horse, and platypus, to name a few.<sup>243</sup> Based on early biochemical data and sequence homology between species, the catalytic core of the ribozyme was identified as the eleven almost universally conserved nucleotides (those numbered in Figure 4.1) that surround the substrate cleavage site, at the junction of three base paired helices.<sup>55, 244-246</sup> Sequence conservation was not apparent in the based paired helices, where sequence variation appeared to have little effect on catalytic activity.<sup>247</sup>

Extensive structure-function studies were undertaken using “minimal hammerhead” constructs, such as the HH16 variant<sup>211</sup> (Figure 4.1A), which comprise only the highly conserved sequence and secondary structure elements. The importance for activity of nearly every functional group in the catalytic core was probed in

mutation/chemical modification experiments, and a number of critical residues were identified, although their actual functions remained unclear.<sup>248</sup> Unfortunately, the crystal structures of minimal hammerhead ribozymes<sup>249-251</sup> (Figures 4.2B & D) provided little mechanistic insight, and for the most part, could not be reconciled with most of the vast body of structure-function data. In light of these inconsistencies, it is now widely accepted that the minimal hammerhead crystal structures represent an inactive conformation of the ribozyme/substrate complex<sup>248, 252, 253</sup> (either a ground-state or an entirely inconsequential structure, as has been observed in an attempt to crystallize the 10-23 DNAzyme<sup>254</sup>). Indeed, several studies of minimal hammerhead ribozyme folding have provided evidence that multiple ribozyme conformations might exist,<sup>255-257</sup> and furthermore, that a conformational change may be the rate limiting step in catalysis.<sup>258</sup>

The mechanistic role of a  $M^{2+}$  cofactor has been perhaps the most heavily scrutinized aspect of hammerhead catalysis in earlier biochemical and spectroscopic experiments.  $M^{2+}$ -independent catalytic activity, albeit somewhat diminished, has been observed in the presence of exchange inert  $Co(NH_3)_6^{3+}$  or high concentrations of monovalent cations (usually  $Li^+$  or  $NH_4^+$ ).<sup>160-162</sup> These findings demonstrated that a  $M^{2+}$  cofactor is not strictly required in the chemical step. Nevertheless,  $M^{2+}$  cations provided far superior stimulation of activity, and thus appeared to serve a specific role in hammerhead catalysis and/or structure, rather than a non-specific role in screening charge repulsion between phosphates. Indeed, specific  $M^{2+}$  interactions with both ribozyme and substrate functional groups have been implicated in active site chemistry, based on data from nonbridging phosphorothioate substitution<sup>206, 207, 259, 260</sup>, as well as NMR<sup>261</sup> and ESR<sup>262, 263</sup> experiments. Specifically, a  $M^{2+}$  cofactor, chelated by the N7 of G10.1 and

the *pro*-R oxygen of the A9 5'-phosphate, was proposed to stabilize the negative charge build up in transition state on the *pro*-R oxygen of the scissile phosphate.<sup>207, 259</sup> However, these conclusions were called into question by Taira and coworkers, based on their data and alternative interpretations of the previous data.<sup>264-267</sup> It was also difficult to imagine how a  $M^{2+}$  cofactor bound at the A9/G10.1 site could interact with the scissile phosphate, given that these sites are separated by  $>20 \text{ \AA}$  in the minimal hammerhead crystal structures.<sup>252</sup>

**Figure 4.1:** Secondary structure diagrams of the *trans*-cleaving (A) HH16 (minimal)<sup>211</sup> and (B) *S. mansoni* (extended)<sup>268</sup> hammerhead ribozymes that were used in this study. The nucleotides in the conserved catalytic core are numbered according to convention.<sup>269</sup> The substrate cleavage sites are indicated with red arrows. The unpaired loops involved in tertiary interactions (unique to extended hammerheads) are indicated by the red box.

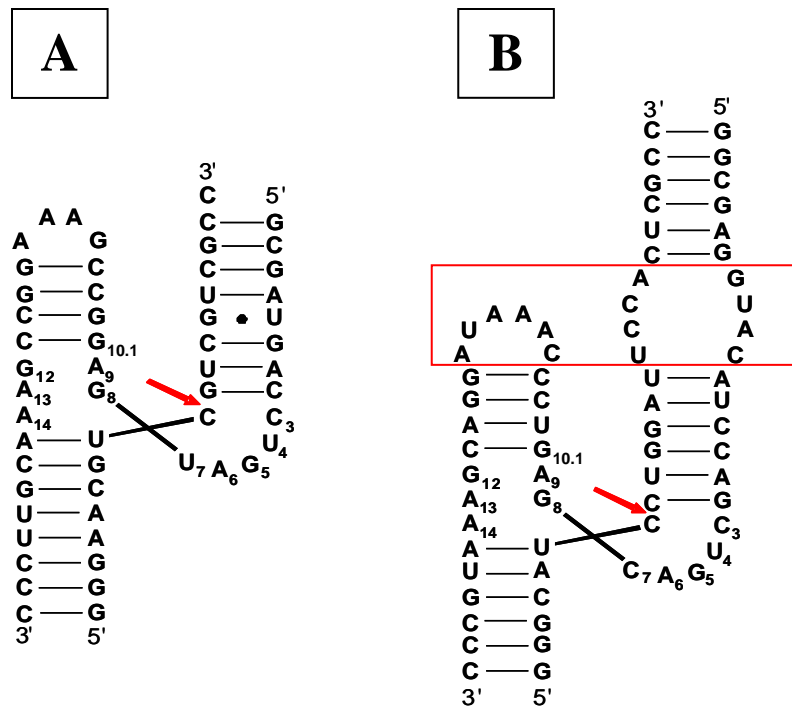
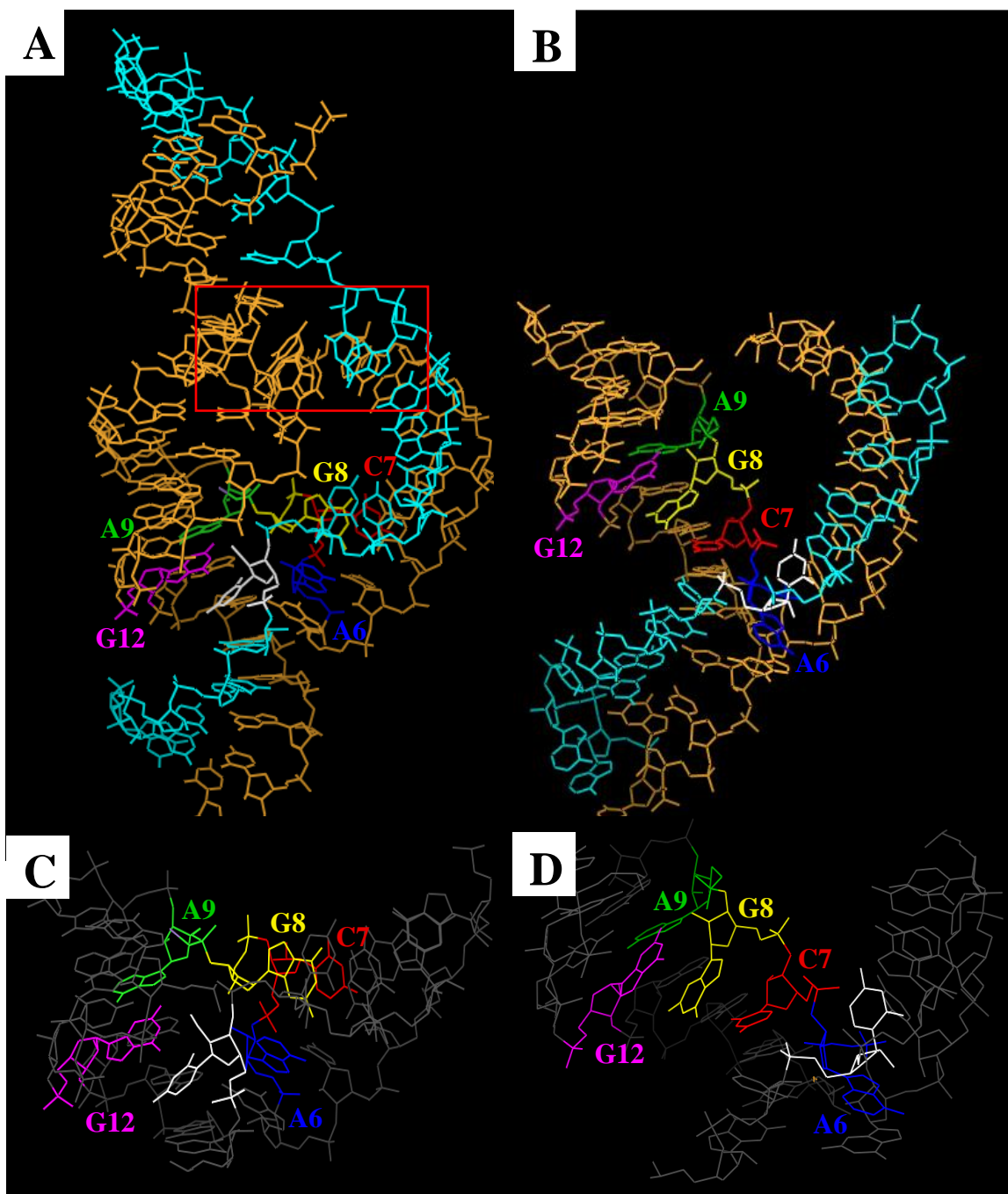


**Figure 4.2:** Crystal structures of (A) the *S. mansoni* (extended)<sup>270</sup> and (B) a minimal hammerhead<sup>249</sup> ribozyme. The ribozyme and substrate strands are coloured orange and teal respectively; the nucleotides of interest in this study are colour coded as indicated; the scissile substrate nucleotide is coloured white. Close up images are focused on the nucleotides of interest in this study for (C) the *S. mansoni* and (D) the minimal hammerheads ribozymes. Images were generated using PyMol.<sup>67</sup>



With regard to general acid/base catalyzed 2'-hydroxyl deprotonation or leaving group protonation, the minimal hammerhead structures provided no indication that ribozyme functional groups might be involved in these functions. The catalytic rate constant was observed to increase log-linearly with pH, consistent with general or specific base catalysis. However, the interpretation of such kinetic data for minimal hammerheads is problematic given that rate limiting conformational changes might mask the properties of the chemical step.<sup>258</sup> Nevertheless, several hypotheses were forwarded which generally involved metal-hydroxide-mediated base catalysis<sup>271</sup> and/or Lewis-acid catalysis, within a one-metal ion<sup>101, 251, 272</sup> or two-metal ion mechanism (see Figure 4.23 and discussion thereof – *vide infra*).<sup>30, 99, 273-276</sup> It was not until much more recently that Han and Burke provided  $pK_a$  perturbation evidence that implicated the G8 and G12 nucleobases in general acid/base catalysis, although kinetic ambiguity prevented the assignment of their respective functions.<sup>277</sup> Burke and coworkers also provided notable photocrosslinking data which detected a radically different active site from that represented in the minimal hammerhead crystal structures.<sup>278</sup> Overall, despite extensive study for nearly two decades, and the solution of three similar crystal structures, much controversy has persisted regarding the nature of the active structure and catalytic mechanism of the hammerhead ribozyme.<sup>248, 253</sup> At long last, in 2006 Martick and Scott provided a resolution to this conundrum by solving the crystal structure of an extended hammerhead ribozyme (*vide infra*).<sup>270</sup>

### 4.1.2 “Extended” Hammerheads: Resolution of the Structure-Function Dilemma?

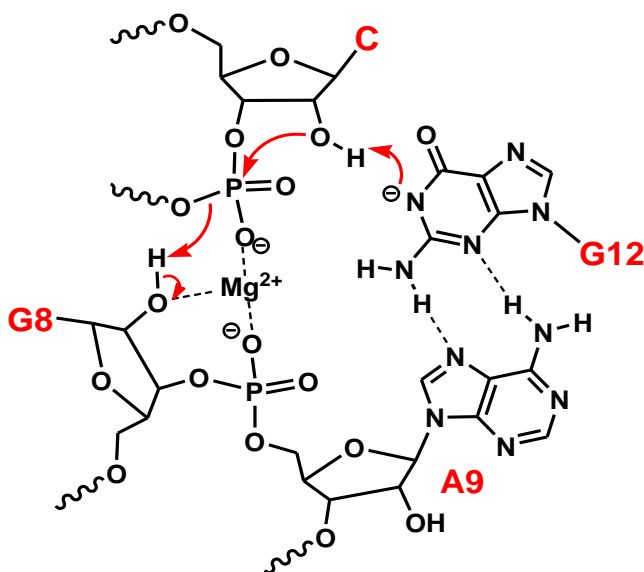
Since ~2004, the focus of hammerhead research has shifted to “extended” ribozyme constructs, which include more of their naturally occurring peripheral sequence regions than the minimal ribozyme constructs (compare Figure 4.1A & B). Unlike the sequence of the catalytic core, these peripheral sequences are not strongly conserved across different species, and are not absolutely required for activity. As a result, these peripheral sequences were overlooked in the initial design of minimal hammerhead ribozyme constructs for mechanistic studies.

In the extended hammerhead ribozymes, such as that derived from the as the *S. mansoni* sequence (Figure 4.1B), the added peripheral sequences provide additional tertiary stabilization of the active conformation.<sup>279, 280, 281</sup> As a result, extended hammerheads exhibit greatly enhanced catalysis at lower  $M^{2+}$  concentrations.<sup>282, 283</sup> Recent extended hammerhead crystal structures<sup>270, 284, 285</sup> have provided ground-breaking insight by revealing an active site that differs radically from that in the minimal hammerhead structures (Figure 4.2A & C). Notably, many of the predictions derived from the data of Burke and coworkers<sup>277, 278</sup>, which departed so radically from the minimal hammerhead structures, are consistent with the extended hammerhead structures (namely, the proximity of G5, G8, and G12 to the cleavage site). Much of the other earlier structure-function data can also now be reconciled with the extended hammerhead crystal structures;<sup>248</sup> therefore, these structures are believed to closely represent the catalytically active ribozyme conformation. The crystallization of a structure that is apparently relevant to catalysis, along with the increased cleavage rates compared to

minimal hammerheads, suggests that in the extended hammerheads it is unlikely that a conformational change is rate limiting. Thus, the extended hammerheads should be a more ideal choice for structure-activity studies aimed at understanding the chemical step in catalysis.

In light of the extended hammerhead crystal structures, a novel mechanistic hypothesis has been proposed involving ribozyme mediated general acid and base catalysis by G8 and G12 respectively (Figure 4.3).<sup>270, 284, 286, 287</sup> The extended hammerhead crystal structures also confirm that the A9 phosphate binds an  $M^{2+}$  cofactor close to the active site, although no bonding interaction with the scissile phosphate or the putative general acid (the G8 2'-hydroxyl) could be identified.<sup>284, 285</sup> Based on the extended hammerhead crystal structures, significant computational effort has also been devoted to predicting the role of an  $M^{2+}$  cofactor in transition state stabilization. York and co-workers suggest that an  $M^{2+}$  cofactor, bound to the A9 phosphate, could stabilize negative charge on the nonbridging oxygens of the scissile phosphate (as predicted based on the phosphorothioate substrate cleavage data).<sup>286, 287</sup> These authors further suggest that the same metal ion could coordinate the G8 2'-hydroxyl to lower its  $pK_a$  and facilitate general acid catalysis (Figure 4.3). Experimentally, Burke and co-workers have demonstrated that substitution of  $Cd^{2+}$  for  $Mg^{2+}$  leads to a drastic change in the pH-rate profile, at least in an artificially selected extended hammerhead (RzB).<sup>288</sup> This effect could be consistent with general acid catalysis by either an  $M^{2+}$ -bound water molecule or an  $M^{2+}$ -bound ribozyme functional group (such as the G8 2'-hydroxyl); that is,  $M^{2+}$  substitution would be expected to cause  $pK_a$  perturbation in either case.

**Figure 4.3:** Catalytic mechanism for hammerhead ribozymes that has been proposed based on the *S. mansoni* crystal structure and subsequent computational studies.<sup>270, 284-287</sup>



Aside from kinetically ambiguous evidence that G12, G8, and a  $M^{2+}$  cofactor might play roles in general acid/base catalysis, there have been relatively few studies that have directly interrogated the mechanism proposed in Figure 4.3. Given the lack of detailed functional evidence for general acid/base catalysis in the hammerhead ribozyme, I have applied the same probes used in the study of the 9<sub>25-11</sub> DNAzyme, namely 2'-bromoacetamide affinity labeling and bridging phosphorothioate substrate substitution, each in conjunction with active site mutation. The results of these experiments provide the first direct functional evidence that the anionic N1 of G12 acts as the general base, while the  $M^{2+}$ -bound 2'-hydroxyl of G8 acts as the general acid. I have also demonstrated general acid  $pK_a$  perturbation in response to  $M^{2+}$  substitution as well as G8 2'-hydroxyl modification, in which case  $M^{2+}$ -bound water appears to assume the role of general acid. Overall my data strongly support the mechanism depicted in Figure 4.3, and confirm that

the extended hammerhead crystal structure indeed represents the catalytically active ribozyme conformation.

## 4.2 MATERIALS AND METHODS

### 4.2.1 Chemicals and Biochemicals

All chemicals and buffers salts were purchased from Sigma-Aldrich (molecular biology or reagent grade purity) and were used as received. DNA and RNA oligonucleotides were synthesized by the University of Calgary DNA Services Lab. RNA was also synthesized by *in vitro* run-off transcription from synthetic DNA templates<sup>289</sup> using the T7 Mega Short Script kit (Ambion).  $\gamma$ -<sup>32</sup>P-ATP and 5'-<sup>32</sup>P-pCp were purchased from Perkin-Elmer. T4 polynucleotide kinase and terminal transferase were purchased from Invitrogen, RNase A, RNase T1, and shrimp alkaline phosphatase from Fermentas, RNA ligase from New England Biolabs, and Super-ase-in RNase inhibitor from Ambion.

### 4.2.2 Oligonucleotide Sequences

The *trans*-cleaving *S. mansoni* hammerhead ribozyme and substrate sequences were taken from Canny *et al.*<sup>268</sup> Wildtype (WT) ribozyme sequence: 5'-GGCGAGGUA CAUCCAGCUGACGAGUCCCAAUAGGACGAAAUGCCC (the mutations made to this sequence are described in the text and figures); 5'-product: 5'-d(GGGCAT)**X** where **X** is ribo-cytidine; 3'-product: 5'-d(CTGGATTCCACTCGCC); S-link substrate: d(GGGCAT-**X**-**Y**<sub>2</sub>-TGGATTCCACT CGCC) where **Y**<sub>2</sub> is 2',5'-dideoxy-5'-mercapto-

cytidine; O-link substrate: d(GGGCAT-**X**-CTGGATTCCACTCGCC); ligation template: 5'-d(AATCCAGGATGCCC)-3'-biotin; 2'-amino DNA substrate analogue: d(GGGCAT-**Z**-CTGGATTCCACTCGCC) where **Z** is 2'-deoxy-2'-amino-cytidine; 2'-amino RNA substrate analogue: GGGCAU-**Z**-CUGGAUUCCACUCGCC.

The *trans*-cleaving HH16 hammerhead ribozyme and substrate sequences were taken from Hertel *et al.*<sup>211</sup> Wildtype ribozyme: 5'-GCGAUGACCUGAUGAGGCCGA AAGGCCGAAACGUUCCC; 2'-amino DNA substrate analogue: 5'-d(GGGAACGT-**Z**-GTCGTCGCC); 2'-amino RNA substrate analogue: 5'-GGGAACGU-**Z**-GUCGUCGCC.

### 4.2.3 Oligonucleotide Preparation

All ribozymes used in footprinting experiments were synthesized by automated solid phase phosphoramidite chemistry because runoff transcription commonly produces sequence inhomogeneity at the 3'-termini, and in some cases at the 5'-termini of transcripts.<sup>289</sup> (Sequence inhomogeneity causes complex, ambiguous footprinting and sequencing patterns by d-PAGE analysis.) All sequences that include a single noncanonical nucleotide substitution also required the use of solid phase phosphoramidite chemistry. Oligonucleotides bearing N7-deaza-purine modifications required the use of <sup>t</sup>butyl-hydroperoxide in the oxidation cycles instead of the standard aqueous iodine treatment.<sup>290</sup> Other hammerhead ribozymes that were not used in footprinting experiments, and which contained only canonical RNA nucleotides, were prepared by *in vitro* run-off transcription from single stranded synthetic DNA templates bearing a double stranded T7 promoter.<sup>289</sup>

All ribozyme sequences were purified by 10% TBE d-PAGE, and then eluted into 1% LiClO<sub>4</sub>/10 mM Tris-HCl (pH 8) by freeze/thaw followed by heating for 30 minutes at 65 ° C. The eluates were concentrated by butanol extraction, ethanol precipitated, resuspended in H<sub>2</sub>O, and desalted by G-25 spin column. The substrate and product oligonucleotides, with the exception of the S-link substrate, were purified similarly by 20% denaturing TBE d-PAGE, and desalted by G-10 spin column.

#### **4.2.4 Affinity Labeling Reactions**

The 2'-bromoacetamide substrate analogues were prepared as described in Section 2.2.3. The standard conditions for hammerhead ribozyme alkylation reactions were: 50 mM MgCl<sub>2</sub>, 100 mM NaCl, and 50 mM buffer (Na-PIPES pH 6.5 and 7, Tris-HCl pH 7.5-8.5, Na-borate pH 9) at room temperature (21-22 °C). Variations on these conditions are described in the figures and text. The ribozyme concentration was 2.5 μM (including a trace of 5'-<sup>32</sup>P-labeled ribozyme) and the substrate analogue concentration was 3 μM. Reaction time points were quenched with three to five volumes of 90% formamide/50 mM EDTA/0.01% xylene cyanol/0.01% bromophenol blue. Reaction products were resolved by 10% d-PAGE and quantified by phosphorimagery (Molecular Dynamics Imagequant v5.2). In order to minimize the effects of pH-dependent bromoacetamide solvolysis over the long reaction times needed for alkylation reactions to reach completion (up to ~50 hours), initial rates were analyzed using early time points (<10-15% of reaction completed). The fraction of alkylated ribozyme was plotted versus time and initial rate constants (hr<sup>-1</sup>) were determined from the slope of a linear regression

using Sigma Plot. The  $[\text{Mg}^{2+}]$  dependence of G12 alkylation was fit to the Hill-type binding equation:

$$k_{\text{obs}} = \frac{k_{\text{max}} [\text{Mg}^{2+}]^n}{K_d + [\text{Mg}^{2+}]^n} + k_0 \quad (4.1)$$

where  $k_{\text{max}}$  is the rate constant at saturating  $[\text{Mg}^{2+}]$  for the  $\text{Mg}^{2+}$  dependent reaction channel,  $n$  is the Hill-type coefficient, and  $K_d$  is the apparent dissociation constant for  $\text{Mg}^{2+}$  binding. The rate constant  $k_0$  was included in order to account for significant hammerhead alkylation through a  $\text{Mg}^{2+}$ -independent reaction channel. The  $[\text{Mg}^{2+}]$  required for half-maximal alkylation rate is defined by  $[\text{Mg}^{2+}]_{1/2} = K_d^{(1/n)}$ .

#### 4.2.5 Alkaline Footprinting of the Alkylation Sites

For experiments with 5'-labeled ribozyme, the 2'-amino substrate analogue was 5'-phosphorylated using unlabeled ATP and T4 polynucleotide kinase prior to bromoacetylation. The samples were extracted twice with phenol/chloroform, ethanol precipitated, and desalted over a G-25 spin column. Alkylation reactions were carried out as described above at pH 7.5, but on a larger scale with ~1-2 nmol of synthetic ribozyme (5'-hydroxy terminated). The reactions were quenched after 48 hrs by addition of a quantity of EDTA, stoichiometric with respect to the  $\text{Mg}^{2+}$  in the sample. The samples were then concentrated by butanol extraction, ethanol precipitated, and resuspended in 90% formamide/50 mM EDTA/0.01% xylene cyanol/0.01% bromophenol blue. Cross-linked alkylation products were separated from unreacted ribozyme by 10% d-PAGE. Bands of interest were identified by UV-shadowing and excised from the gel.

Elution and desalting was performed as above for ribozymes, with the exception that elution was carried out by freeze/thaw followed by soaking at 37 °C for ~2 hours. The purified alkylated ribozyme was then 5'-radiolabeled using  $\gamma$ -<sup>32</sup>P-ATP and T4 polynucleotide kinase. Only the ribozyme strand is 5'-radiolabeled as labeling of the 5'-terminus of the substrate analogue strand was blocked by prior phosphorylation with unlabeled ATP.

For experiments with 3'-labeled ribozyme, the 3'-terminus of the 2'-amino substrate analogue was extended by one nucleotide by treatment with unlabeled 2',3'-dideoxy-ATP and terminal transferase, prior to bromoacetylation. The samples were extracted twice with phenol/chloroform, ethanol precipitated, and desalted on a G-25 spin column. Alkylation reactions were performed and the products purified as described above for the 5'-labeled samples. The purified, alkylated ribozymes were then 3'-radiolabeled using 5'-<sup>32</sup>P-pCp and RNA ligase. Only the ribozyme strand is 3'-radiolabeled as the labeling reaction is blocked by the 2',3'-dideoxy terminus of the substrate analogue strand.

Following radiolabeling, both the 5'- and 3'-labeled alkylation products were repurified by 10% d-PAGE and desalted prior to footprinting analysis. To generate the alkaline hydrolysis ladders, samples were treated with 0.5% K<sub>2</sub>CO<sub>3</sub> (pH 10.3, measured at 22 ° C) at 95 ° C for 4 min. To generate the G-specific cleavage ladders, samples were combined with 5 nmol of carrier RNA (unlabeled ribozyme RNA) in 10  $\mu$ L of 10 mM Tris-HCl (pH 7.5) and treated with 1 unit of RNase T1 at 37 ° C for 4 min. Reactions were terminated by adding 2 volumes of 90% formamide/50 mM EDTA/0.01% xylene cyanol/0.01% bromophenol blue and placing the samples on ice.

The digestions were immediately analyzed on 10% or 12% d-PAGE sequencing gels as indicated in the figure legends. A secondary structure compression interfered with routine d-PAGE analysis of the 3'-labeled samples; it was necessary to run these gels at higher temperature by applying power of 100 W instead of the standard 40 W.

#### **4.2.6 Aniline Footprinting of the Alkylation Sites**

Purified 3'-labeled alkylated ribozyme samples were treated with 0.5 M anilinium-acetate (pH 4.5) at 37 °C for 20 min (10 µL reactions). The samples were then lyophilized, and twice resuspended in 50 µL water and re-lyophilized to thoroughly remove the volatile anilinium-acetate buffer. Alkaline and RNase T1 digestions were performed as above, with the exception that the reactions were not stopped by addition of formamide/EDTA. The alkaline digestions were terminated by placing the samples on ice and immediately neutralizing them with 10 mM HCl; the RNase T1 digestions were terminated by adding 5 units RNase inhibitor (Ambion). In order to harmonize the phosphorylation states of the digestion products resulting from each of the alkaline, RNase T1, and aniline digestions, all samples were treated with T4 polynucleotide kinase: digestion samples were diluted into 10 volumes of polynucleotide kinase buffer (containing 1 mM unlabeled ATP) and treated with 20 units of the enzyme for 2 hours at 37 °C. Samples were analyzed on 12% d-PAGE sequencing gels run at 100 W.

#### **4.2.7 Ribozyme Kinetic Experiments**

Reactions were conducted under single turnover conditions with a saturating excess of ribozyme (10 to 12.5 µM) and a trace of 5'-<sup>32</sup>P-labeled substrate (<10 nM). The

standard conditions were 2 mM MgCl<sub>2</sub>, 100 mM NaCl, 50 mM Na-PIPES (pH 7) at room temperature (21-22 °C). pH-rate profiles were conducted using Na-MES (pH 5.5 & 6), Na-PIPES (pH 6.5 & 7), Tris-HCl (pH 7.5-8.5), Na-Borate (pH 9). Ribozymes were diluted first in buffer alone and heated to 95 °C for 2 min, then allowed to cool to room temp for ~10 min. At this point substrate was added to ribozyme. The mixture was allowed to stand at room temp for 1 min, at which point an aliquot was removed and quenched for a zero time point. The reaction was started immediately by adding MgCl<sub>2</sub> and NaCl, or other metal salts as indicated in the text. Time point aliquots were quenched in 4 volumes of either 90% formamide/50 mM Na-PIPES (pH 6.4)/25 mM EDTA/0.01% xylene cyanol/0.01% bromophenol blue for S-link reactions, or 90% formamide/50 mM EDTA/0.01% xylene cyanol/0.01% bromophenol blue for O-link reactions. Immediately following the addition of the quench solution, the aliquots were placed on powdered dry ice. The products were resolved by 20% TBE d-PAGE for O-link and 20% TAE<sup>118</sup> d-PAGE for S-link experiments. S-link samples were loaded onto running gels, with care taken to minimize the time the aliquots were thawed before gel loading. Autoradiographic data was processed using Imagequant v5.2. Non-linear least squares fits were generated using Sigma Plot. Substrate cleavage data were fit to:

$$P = P_o + P_\infty \left(1 - e^{-k_{obs}t}\right) \quad (4.2)$$

where  $P$  is the fraction substrate cleaved,  $P_o$  is the initial fraction cleaved,  $P_\infty$  is the final fraction cleaved,  $k_{obs}$  is the observed first order rate constant, and  $t$  is time. All experiments were repeated 3 to 5 times and the results averaged. Error bars for plotted data points represent standard deviations.

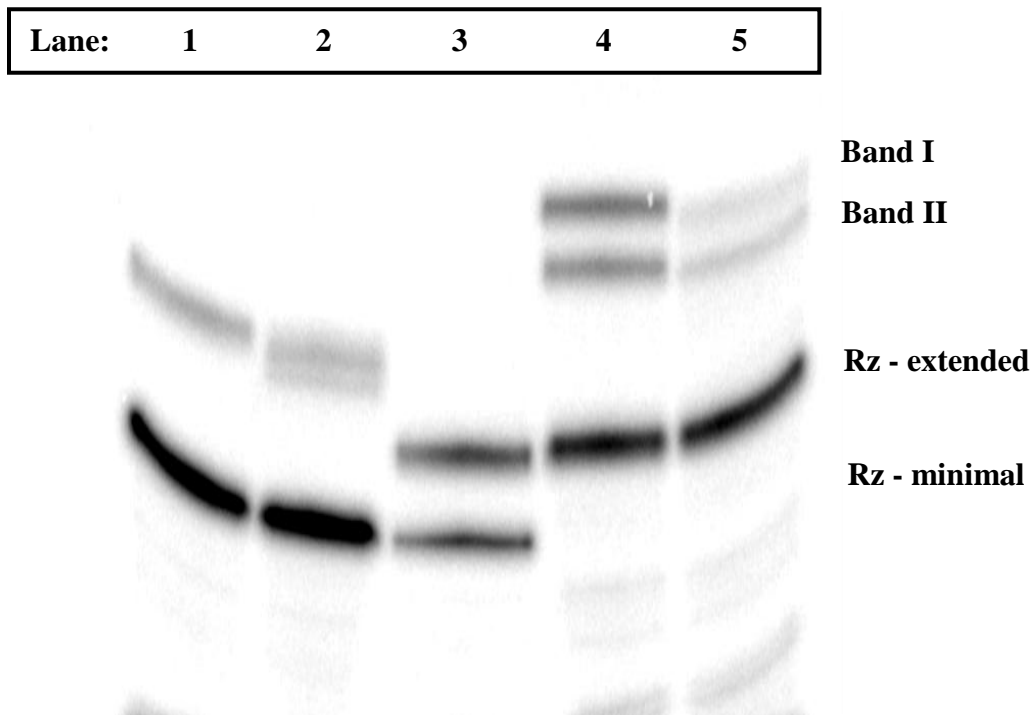
## 4.3 PROBING GENERAL BASE CATALYSIS IN THE HAMMERHEAD RIBOZYME

### 4.3.1 Results

#### 4.3.1.1 Hammerhead Ribozyme Affinity Labeling

Both RNA and DNA substrate analogues bearing an electrophilic 2'-bromoacetamide in place of the cleavage site 2'-hydroxyl were reacted in *trans* with the HH16 and *S. mansoni* hammerhead ribozymes. The standard reaction conditions were 2.5  $\mu$ M ribozyme, 3  $\mu$ M substrate analogue, 50 mM MgCl<sub>2</sub>, 100 mM NaCl, 50 mM Tris-HCl (pH 8) at room temperature in the dark. In the case of the HH16 minimal hammerhead ribozyme, yields of alkylated ribozyme were low, and the separation and analysis of what appeared to be two or more alkylation products proved to be intractable (Figure 4.4, Lanes 1 & 2). In keeping with the trend of increased cleavage activity from minimal to extended hammerheads,<sup>279, 280</sup> the alkylation reaction was more fruitful for the *S. mansoni* extended hammerhead than for the HH16 minimal hammerhead. Two alkylation products (Band I and II) for the *S. mansoni* ribozyme appeared in greater yield and were much better resolved by d-PAGE than those of the HH16 ribozyme (Figure 4.4, Lanes 4 & 5).

**Figure 4.4:** Alkylation of the HH16 (minimal) and the *S. mansoni* (extended) hammerhead ribozymes (5'-<sup>32</sup>P-labeled) with both RNA and DNA 2'-bromoacetamide substrate analogues in 50 mM MgCl<sub>2</sub>, 100 mM NaCl, 50 mM Tris-HCl pH 7.5 for 24 hrs. The alkylation bands characterized in this study (Bands I and II) are indicated. Lane 1: HH16 ribozyme + DNA substrate analogue. Lane 2: HH16 ribozyme + RNA substrate analogue. Lane 3: Co-spot of unreacted HH16 and *S. mansoni* ribozymes. Lane 4: *S. mansoni* ribozyme + DNA substrate analogue. Lane 5: *S. mansoni* ribozyme + RNA substrate analogue. Samples were analyzed by 10% d-PAGE. Rz = ribozyme.



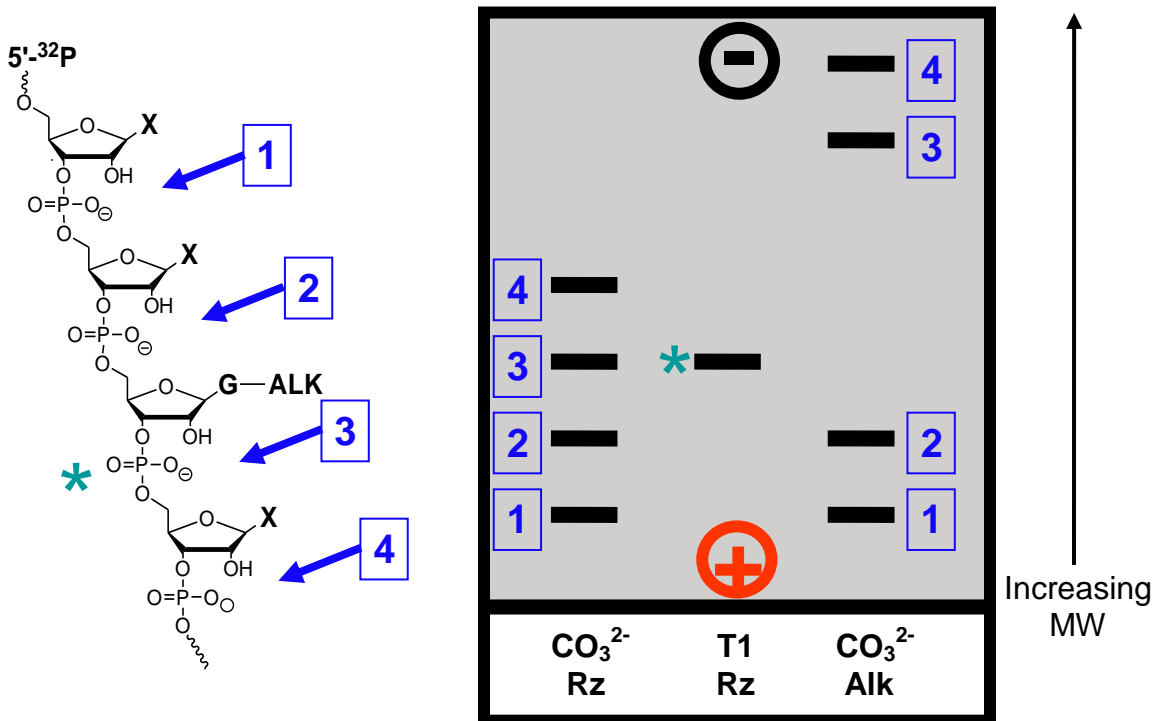
#### 4.3.1.2 Footprinting the Alkylation Site: 5'-Labeled Ribozyme

Using footprinting analysis, I sought to determine the sites of ribozyme alkylation for both alkylation products of the *S. mansoni* hammerhead (*vide infra*). Thus, Bands I and II were excised from the gel, radiolabeled specifically at the 5'-end of the ribozyme strand, repurified by d-PAGE, and subjected to limited alkaline digestion. The alkylation products resulting from the reaction of an all-RNA substrate analogue proved to be

refractory to clear alkaline footprint analysis (data not shown). The failure of this experiment is likely due to alkaline cleavage of the substrate strand, which produces  $^{32}\text{P}$ -labeled cleavage products that complicate the footprinting pattern. In order to circumvent this problem, I applied a DNA substrate analogue with a 2'-bromoacetamido-C at the native cleavage site. This substitution is justified given that the corresponding DNA substrates with a single embedded ribose at the cleavage site are efficiently cleaved by both minimal<sup>102, 291</sup> and extended hammerheads.<sup>292</sup> Not only were the yields of Bands I and II unexpectedly enhanced using the DNA-based affinity label (Figure 4.4), but both bands generated much clearer alkaline footprint patterns (Figure 4.6 - *vide infra*) because only the labeled ribozyme strand is susceptible to alkaline cleavage in this case.

As illustrated in Figure 4.5, alkaline cleavage of the ribozyme produces a rather uniform ladder of cleavage products, where cleavage at each ribophosphodiester linkage produces a unique labeled fragment (the molecular weight of the labeled fragments increases with the distance of the cleavage site from the label). The sequence of the fragments is referenced to a G-specific cleavage ladder produced by limited RNase T1 digestion of unmodified ribozyme. Because RNase T1 cleaves ribophosphodiesterases at the 3'-side of G residues, the assigned fragment sequences reflect the last nucleotide left attached to the 5'-label. If additional molecular weight is appended to a particular nucleotide, cleavage at its 3'-side will produce a labeled fragment with higher molecular weight and reduced electrophoretic mobility relative to the corresponding fragment of the unmodified ribozyme. The alkylated residue of a 5'-labeled ribozyme is therefore identified in the alkaline footprinting pattern by locating the first cleavage band with retarded electrophoretic mobility relative to the ribozyme cleavage ladder.

**Figure 4.5:** Illustration explaining the interpretation of alkaline footprinting patterns with 5'-<sup>32</sup>P-labeled ribozyme alkylated at the indicated G residue. RNA cleavage sites and the corresponding bands they produce in d-PAGE analysis are numbered as indicated. X = A, C, or U.



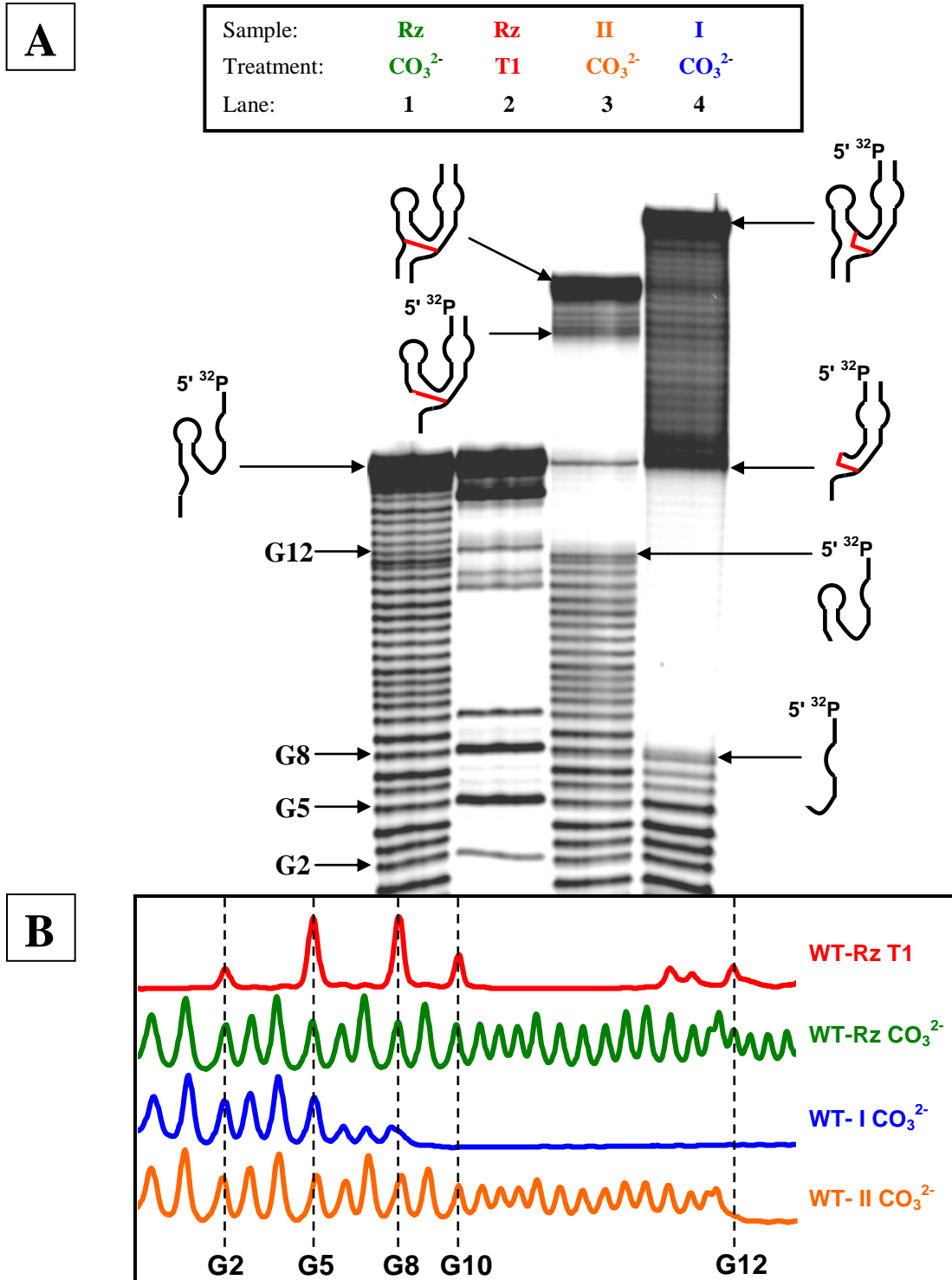
\* = T1 cleavage

• First shifted band locates alkylated nucleotide

Footprinting analysis with 5'-labeled, alkylated ribozyme clearly identifies G12 as the site of ribozyme alkylation for Band II (Figure 4.6, Lane 3) based on comparison to the RNase T1 (G specific) sequencing ladder (Figure 4.6, Lane 2). In contrast to Band II, the footprinting pattern for Band I (Figure 4.6, Lane 4) appears to be more complex. Clearly, the band corresponding to cleavage at A9 is completely shifted to higher molecular weight, which demonstrates unequivocally that some alkylation has occurred at A9. However, the cleavage band intensity also drops markedly at A6 relative to the

more uniform band intensities observed for alkaline cleavage of the ribozyme (Figure 4.6, Lane 1). This observation suggests that Band I represents a mixture of alkylations of both A6 and A9. Mutation of A6 to U restored the uniform band intensity up to the completely shifted A9 band (Figure 4.16, Lane 4), which demonstrates that the anomalous intensity pattern for the wildtype sample was indeed the result of A6 alkylation.

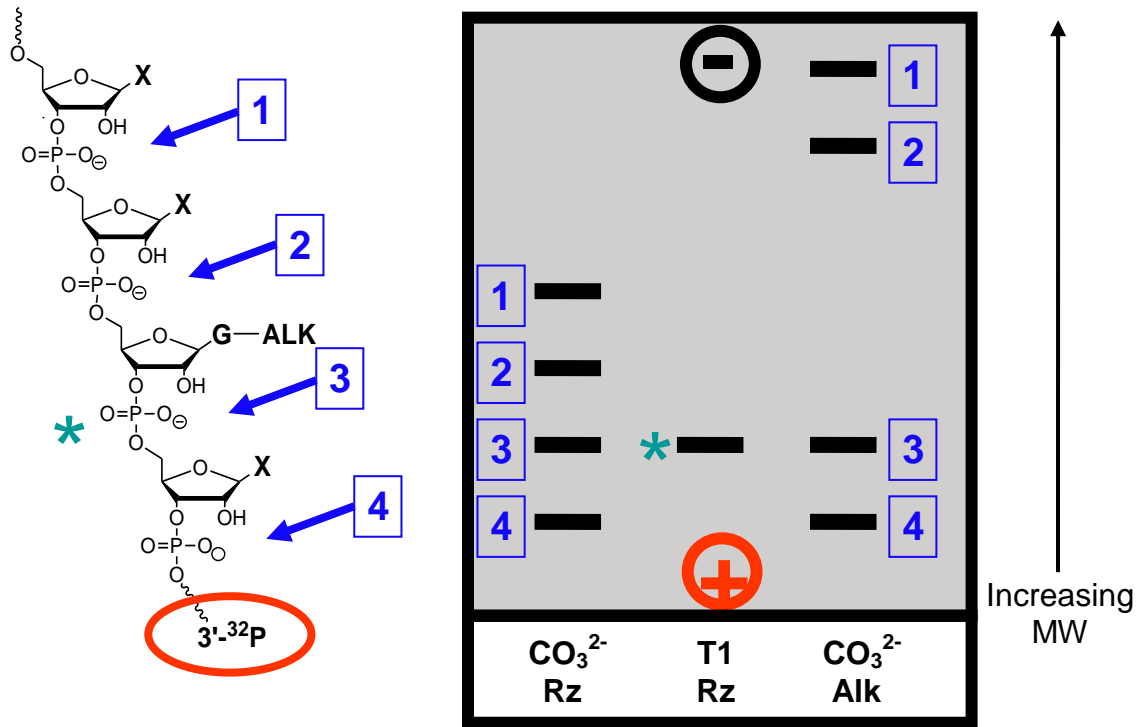
**Figure 4.6:** (A) Alkaline footprinting analysis with 5'-<sup>32</sup>P-labeled *S. mansoni* hammerhead ribozyme. Lane 1: Ribozyme treated with 0.5% K<sub>2</sub>CO<sub>3</sub>; Lane 2: Ribozyme treated with RNase T1; Lane 3: Band II treated with 0.5% K<sub>2</sub>CO<sub>3</sub>; Lane 4: Band I treated with 0.5% K<sub>2</sub>CO<sub>3</sub>. (B) Quantitative analysis of autoradiography data in panel (A).



### 4.3.1.3 Footprinting the Alkylation Site: 3'-Labeled Ribozyme

In order to further investigate the nature of Band I, and to confirm that Band II represents alkylation of G12 alone, I carried out complementary footprinting experiments with Band I and II samples that were produced using 3'-labeled ribozyme. As illustrated in Figure 4.7, the interpretation of footprinting patterns for 3'-labeled ribozyme differs from the 5'-labeled case. Regardless of the label position, the fragment sequences are referenced to RNase T1 cleavage sites, which occur at the 3'-side of G residues; therefore, all labeled fragments are named to reflect the nucleotide to the 5'-side of the scissile phosphate. Consequently, the nucleotide for which a cleavage fragment is named remains attached to a 5'-label, but is detached from a 3'-label by the same cleavage event. Similarly, cleavage at the 3'-side of an alkylation lesion ensures that the added molecular weight remains linked to a 5'-<sup>32</sup>P-label, whereas cleavage at the same site severs the link between the lesion and a 3'-<sup>32</sup>P-label. The alkylated nucleotide of a 3'-labeled ribozyme is therefore identified in the alkaline footprinting pattern by the nucleotide assignment of the last cleavage band with *unaltered* electrophoretic mobility (relative to the ribozyme cleavage ladder).

**Figure 4.7:** Illustration explaining the interpretation of alkaline footprinting patterns with 3'-<sup>32</sup>P-labeled ribozyme alkylated at the indicated G residue. RNA cleavage sites and the corresponding bands they produce in d-PAGE analysis are numbered as indicated. X = A, C, or U.



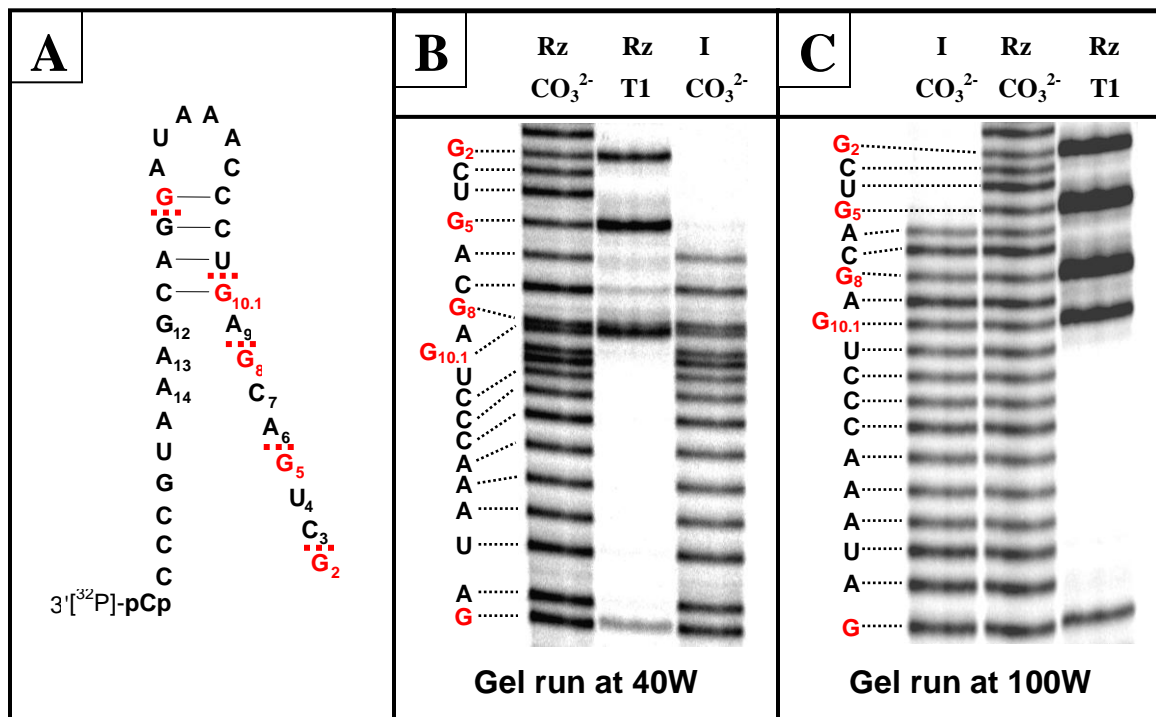
\* = T1 cleavage

• last *unshifted* band locates alkylated nucleotide

The interpretation of Band I footprinting data for 3'-labeled samples was hampered by the anomalous electrophoretic mobilities exhibited by certain cleavage fragments (Figure 4.8B). This effect is attributed to incomplete denaturation (even in 7M urea/TBE buffer) of especially stable secondary structures, the formation of which alters a fragment's effective size to charge ratio, and thus its electrophoretic mobility (this effect is referred to as "secondary structure compression"). Considering the positions of G-specific RNase T1 cleavage, the compressed fragments appear to be those that result

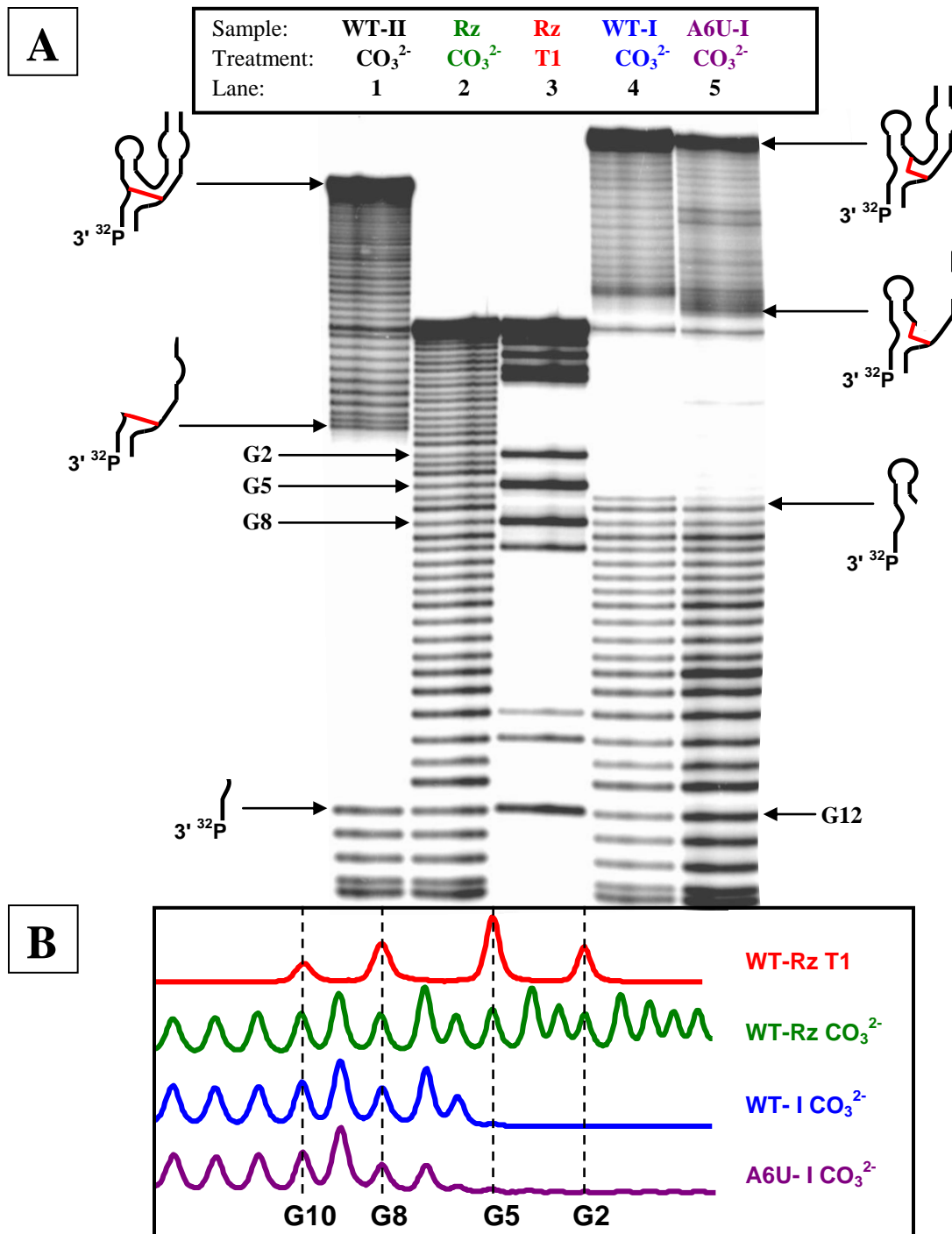
from cleavage at or near G10.1. The 3'-termini of these fragments form the hairpin loop shown in Figure 4.8A. In order to abrogate the effects of secondary structure compression, so that Band I footprinting pattern could be unambiguously interpreted, sequencing gels were preheated and electrophoresed at 100 W (instead of the standard 40 W). Evidently the high temperature in the gel adequately denatures the stable hairpin loop, so that the predicted sequencing pattern was observed (Figure 4.8C). Such high electrophoresis temperatures are problematic, given the risk of damage to the glass plates into which the gels are cast.

**Figure 4.8:** Secondary structure compression near G10 prevents clear sequence assignment in standard d-PAGE analysis of footprinting experiments with 3'-<sup>32</sup>P-labeled ribozyme (B). The application of higher power (100 W) during electrophoresis (C) prevents formation of the hairpin loop responsible for the compression observed in panel B. The sequence region of interest is shown in panel (A) where the RNase T1 cleavage sites are indicated by dashed red lines.



The alkaline footprinting pattern for 3'-labeled Band II (Figure 4.9, Lane 1) clearly shows a shift in molecular weight after G12. This finding is in agreement with that for 5'-labeled ribozyme, and unequivocally demonstrates that Band II represents a single structure, in which only G12 is alkylated. For 3'-labeled Band I, the alkaline footprinting pattern clearly shifts after A6 (Figure 4.9, Lane 4), which unambiguously demonstrates that Band I consists of a mixture of A6 and A9 alkylation linkages. Nevertheless, it is still possible that other alkylation linkages exist in the intervening sequence (C7 or G8). Indeed, when A6 alkylation is suppressed by the A6U mutation, the resulting footprinting pattern for 3'-labeled Band I indicates alkylation of C7 (Figure 4.9, Lane 5).

**Figure 4.9:** (A) Alkaline footprinting analysis with 3'-<sup>32</sup>P-labeled *S. mansoni* hammerhead ribozyme. Lane 1: Band II treated with 0.5% K<sub>2</sub>CO<sub>3</sub>; Lane 2: Ribozyme treated with 0.5% K<sub>2</sub>CO<sub>3</sub>; Lane 3: Ribozyme treated with RNase T1; Lane 4: Band I (wildtype ribozyme) treated with 0.5% K<sub>2</sub>CO<sub>3</sub>; Lane 5: Band I (A6U ribozyme) treated with 0.5% K<sub>2</sub>CO<sub>3</sub>. (B) Quantitative analysis of autoradiography data in panel (A).



To more directly probe for alkylation lesions at C7 and G8 in the wildtype ribozyme, which would not be readily identified in alkaline footprinting experiments, the 3'-labeled samples were treated with anilinium-acetate (pH 4.5). This treatment reveals, by strand cleavage, any abasic sites that result from depurination/depyrimidination of alkylated residues.<sup>293, 294</sup> Aniline-catalyzed strand cleavage proceeds via  $\beta$ -elimination to afford 3'-<sup>32</sup>P-labeled fragments with 5'-phosphorylated termini; due to their added negative charge, these fragments exhibit altered d-PAGE mobility compared to the 5'-hydroxy-terminated fragments generated by RNase T1 or alkaline cleavage (Figure 4.10). In order to facilitate direct comparison with the alkaline footprint and RNase T1 sequencing patterns, all samples were treated with polynucleotide kinase and ATP to synchronize the 3'- and 5'-phosphorylation states. Aniline treatment of Band I (Figure 4.11A, Lane 6) revealed cleavage at all of A6, C7, G8, and A9, suggesting that Band I consists of a mixture of ribozymes alkylated at any one of these positions. Quantification of the components of the mixture based on this data is problematic due to variation of the rate of abasic site formation with nucleobase and alkylation site.<sup>220</sup> Mutation of A6 and C7 to U, as well as mutation of A9 to 7-deaza-A diminished aniline cleavage at these residues, which provides confirmation of the sequence assignment of the aniline cleavage sites (Figure 4.12, Lanes 2, 3, and 5, respectively).

I then attempted to ascertain which atom had been alkylated on each of G8, A9, and G12, as these residues were present in the active site observed in the *S. mansoni* crystal structure. To this end, I first tested whether the N7 atom of these purines had been alkylated, as the N7 position of guanine in particular is generally amongst the most nucleophilic positions in nucleic acids (under neutral conditions). The guanine N7

position is a very weak base ( $pK_a \sim 3.2^{237}$ ); therefore, N7 alkylation is not likely to be indicative of general base catalysis, but rather fortuitous positioning of the nucleophile near the bromoacetamide electrophile. The G12 alkylation rate was not significantly affected relative to wildtype for the 7-deaza-G12 mutant (Table 4.1 - *vide infra*), which demonstrates that N7 of G12 is not alkylated in the wildtype ribozyme. Furthermore, Band II is not significantly cleaved by aniline treatment (Figure 4.11, Lane 1), which suggests that alkylation occurred at N1 of G12 (N7 or N3 alkylation accelerate depurination, whereas N1 alkylation does not<sup>220</sup>). With respect to Band I, the 7-deaza-A9 substitution (“A9c<sup>7</sup>”) nearly eliminated the aniline induced cleavage at A9 (Figure 4.12, Lane 5); these results provide strong evidence that the N7 position of A9 is alkylated. The strong aniline cleavage at G8 was retained for Band I of the 7-deaza-G8 substituted (“G8c<sup>7</sup>”) ribozyme (Figure 4.12, Lane 4), which rules out N7 alkylation of G8. Therefore, process of elimination dictates that G8 alkylation most likely occurs at N3 (N1 alkylation is not suspected as this should not lead to significant depurination and subsequent aniline cleavage<sup>220</sup>).

**Figure 4.10:** Aniline catalyzed cleavage at abasic sites produces 5'-phosphorylated-3'-<sup>32</sup>P-labeled fragments, whereas RNase T1 or alkaline cleavage produces 5'-hydroxy-3'-<sup>32</sup>P-labeled fragments. Subsequent treatment of both samples with polynucleotide kinase and unlabeled ATP synchronizes both the 5'- and 3'-phosphorylation states of all fragments (polynucleotide kinase is both a 5'-kinase and a 3'-phosphatase).

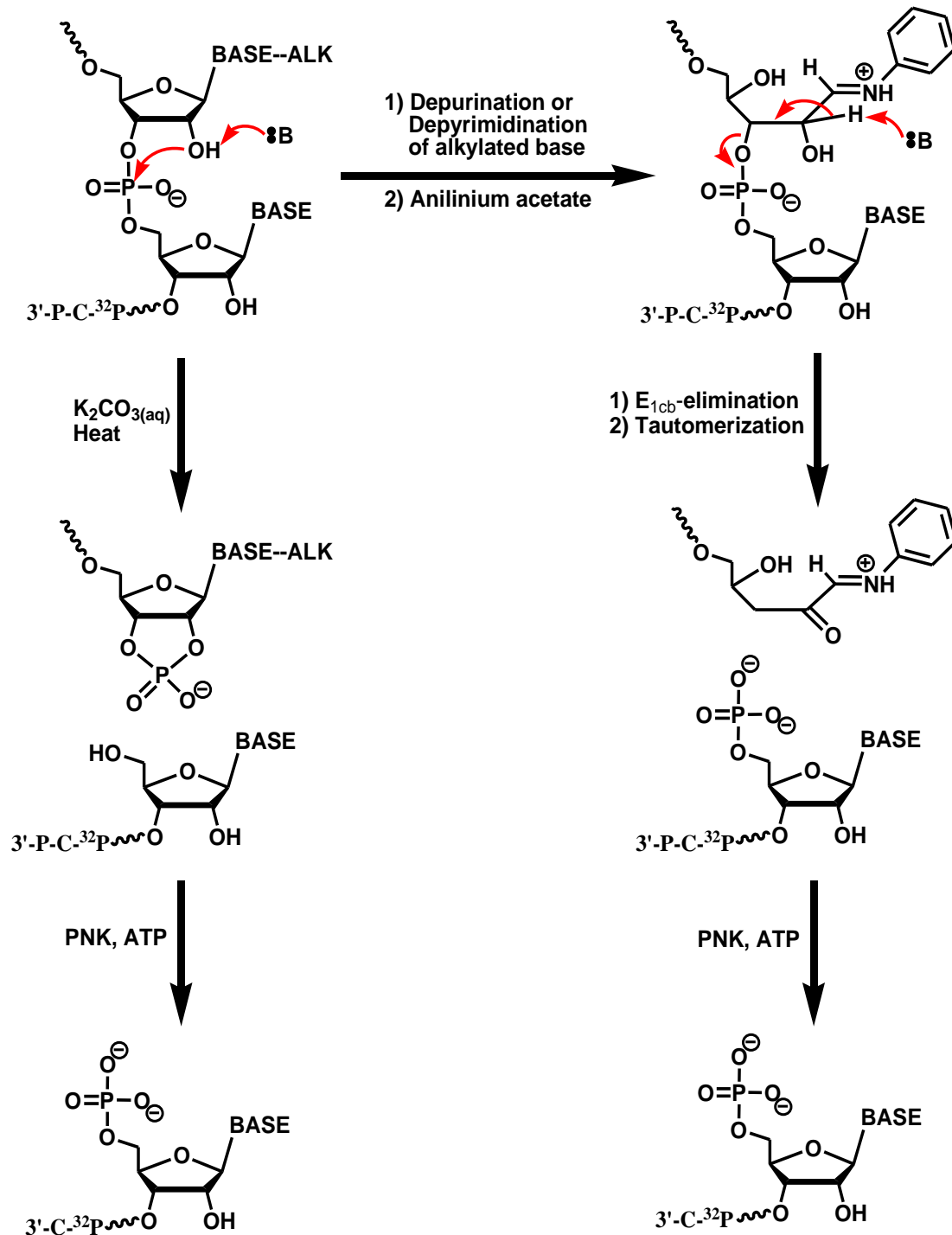


**Figure 4.11:** Comparison of aniline and alkaline footprinting patterns for Bands I and II ( $3'$ - $^{32}$ P-labeled wildtype ribozyme). Lane 1: Band II treated with 0.5 M anilinium acetate; Lane 2: Band II treated with 0.5%  $K_2CO_3$ ; Lane 3: Ribozyme treated with RNase T1; Lane 4: Ribozyme treated with  $K_2CO_3$ ; Lane 5: Band I treated with  $K_2CO_3$ ; Lane 6: Band I treated with 0.5 M anilinium acetate. To facilitate direct comparison of electrophoretic mobilities, all samples were treated with polynucleotide kinase and ATP to synchronize the  $3'$ - and  $5'$ -phosphorylation states before d-PAGE analysis.

Sample:	WT-II	WT-II	Rz	Rz	WT-I	WT-I
Treatment:	AnAc	$CO_3^{2-}$	T1	$CO_3^{2-}$	$CO_3^{2-}$	AnAc
Lane:	1	2	3	4	5	6

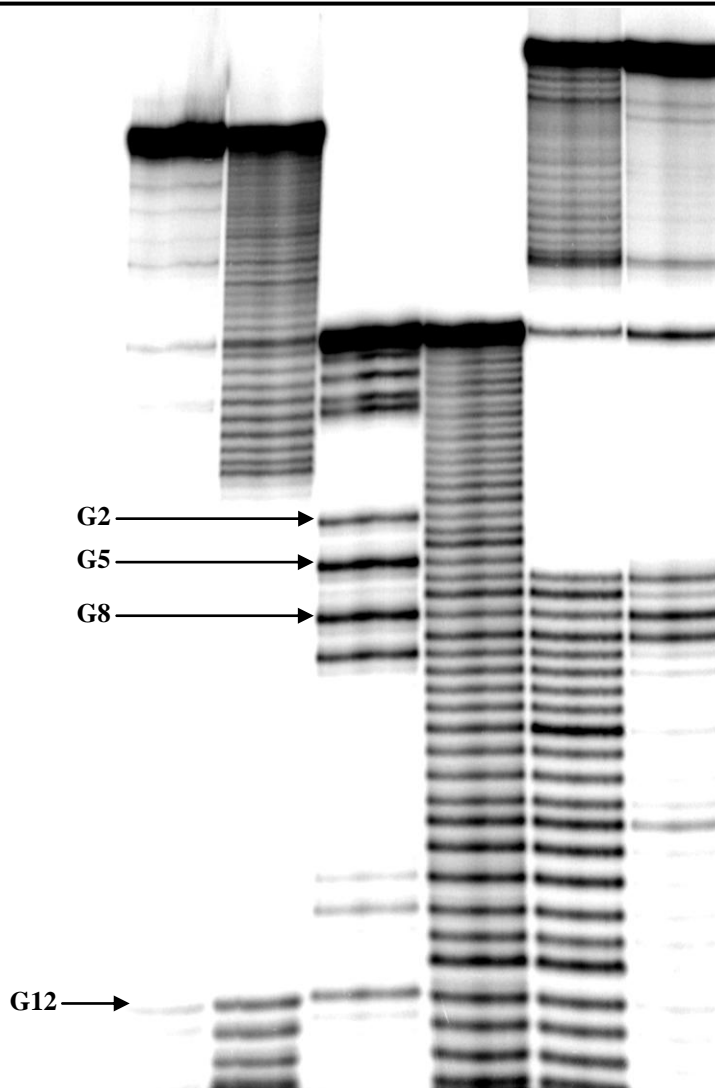
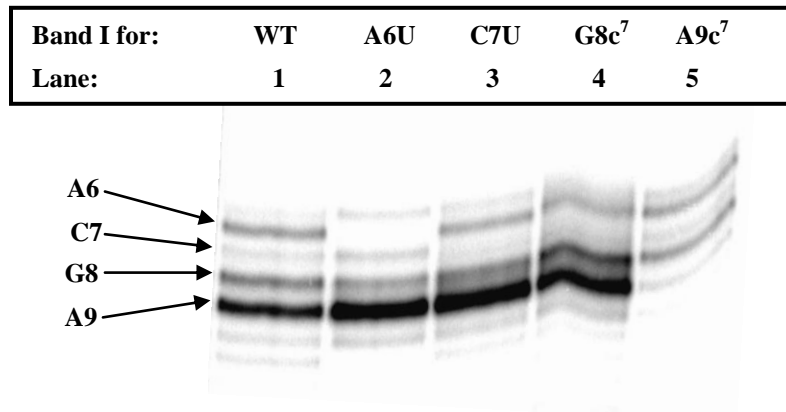


**Figure 4.12:** Close up view of anilinium acetate footprinting patterns of Band I for the indicated 3'-<sup>32</sup>P-labeled mutant *S. mansoni* hammerhead ribozymes.



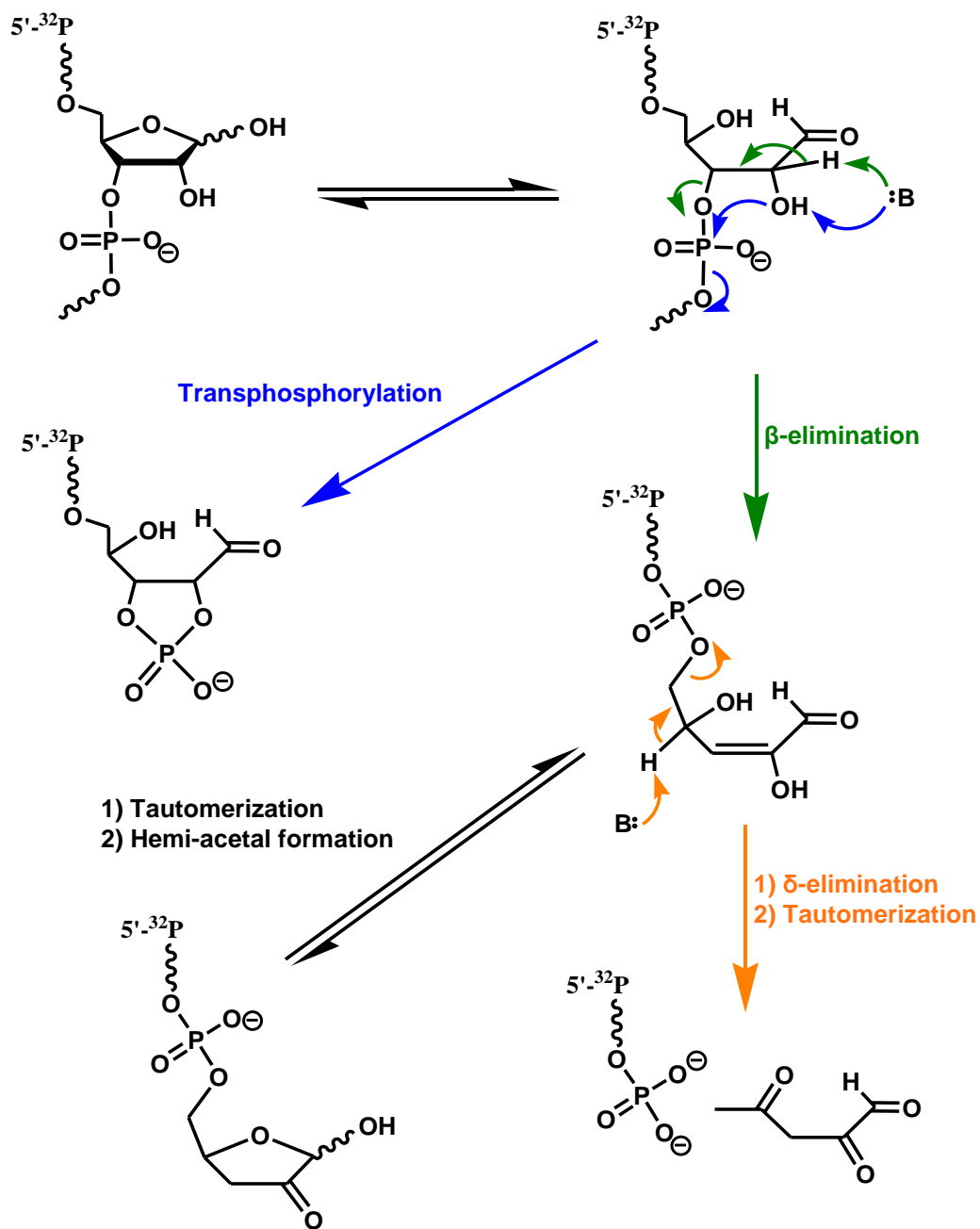
#### 4.3.1.4 Assignment of an Unidentified 5'-Labeled Cleavage Fragment

Closer inspection of the 5'-labeled footprinting pattern for Band I (Figure 4.6, Lane 4) reveals that the band for A9 cleavage does not perfectly mirror the appearance of the corresponding band in the ribozyme digestion sample. Higher resolution d-PAGE analysis uncovered an unidentified cleavage band in the Band I footprinting pattern that migrates between the C7 and G8 bands. This band is completely absent from the alkaline cleavage pattern of the ribozyme (the unidentified band is marked by a red asterisk in Figure 4.14, Lanes 3 & 4, and Figure 4.16, Lanes 1-5, 10 & 11 – *vide infra*). I felt that the origin of this band should not be overlooked as it undoubtedly results from alkylation of the ribozyme, and might suggest yet another alkylation site that might have eluded detection in the characterization of Band I presented thus far.

Given that the unidentified band arises as a result of alkylation, I hypothesized that it was a product of alkaline cleavage of an abasic site formed upon depurination or depyrimidination of an alkylated nucleobase. Küpfer and Leumann have characterized

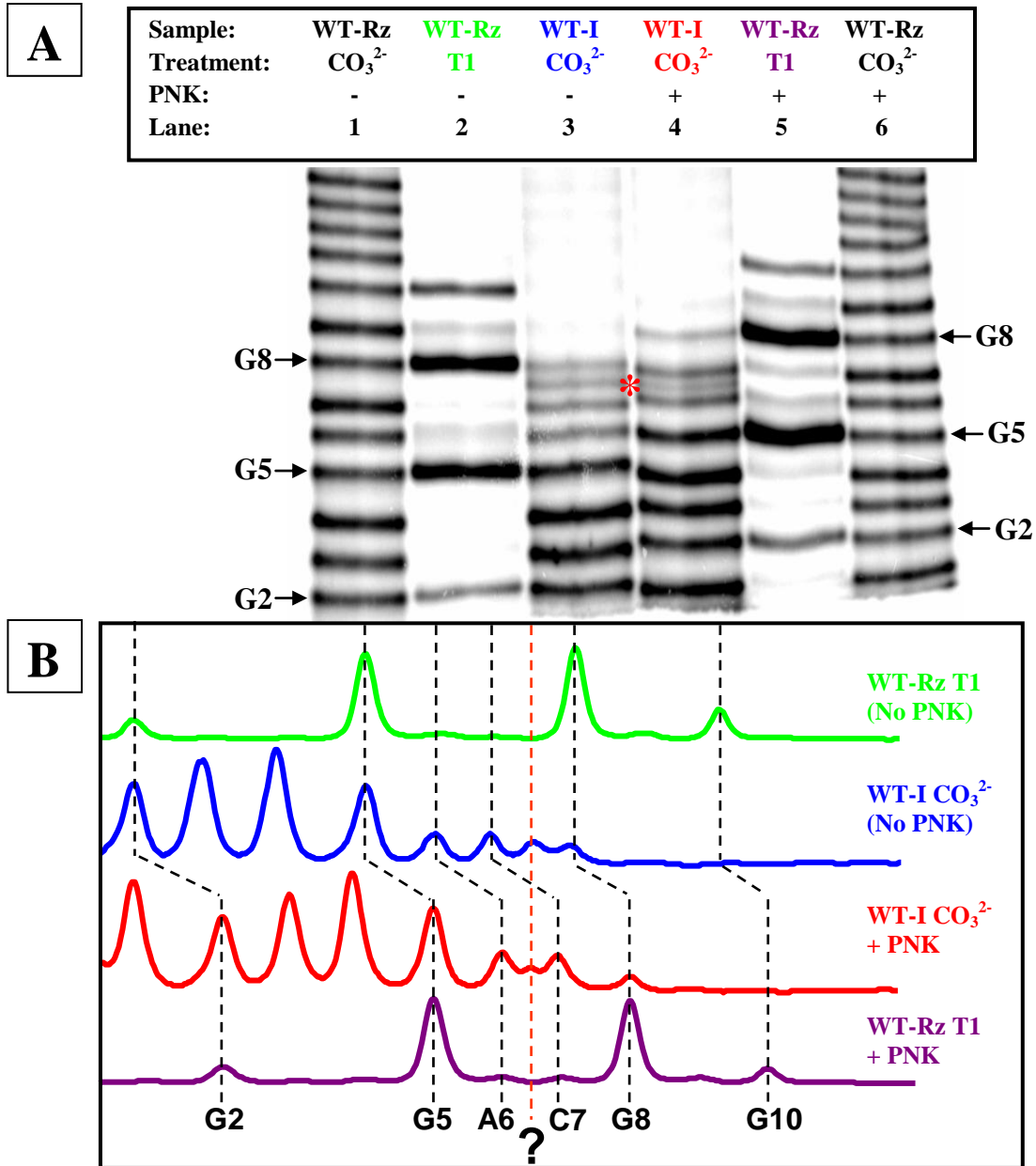
the products that result from alkaline cleavage of abasic sites in RNA;<sup>295</sup> the products observed, and their mechanisms of formation, are summarized in Figure 4.13.

**Figure 4.13:** Reactions observed by Küpfer and Leumann upon alkaline treatment of abasic sites in RNA.<sup>295</sup>



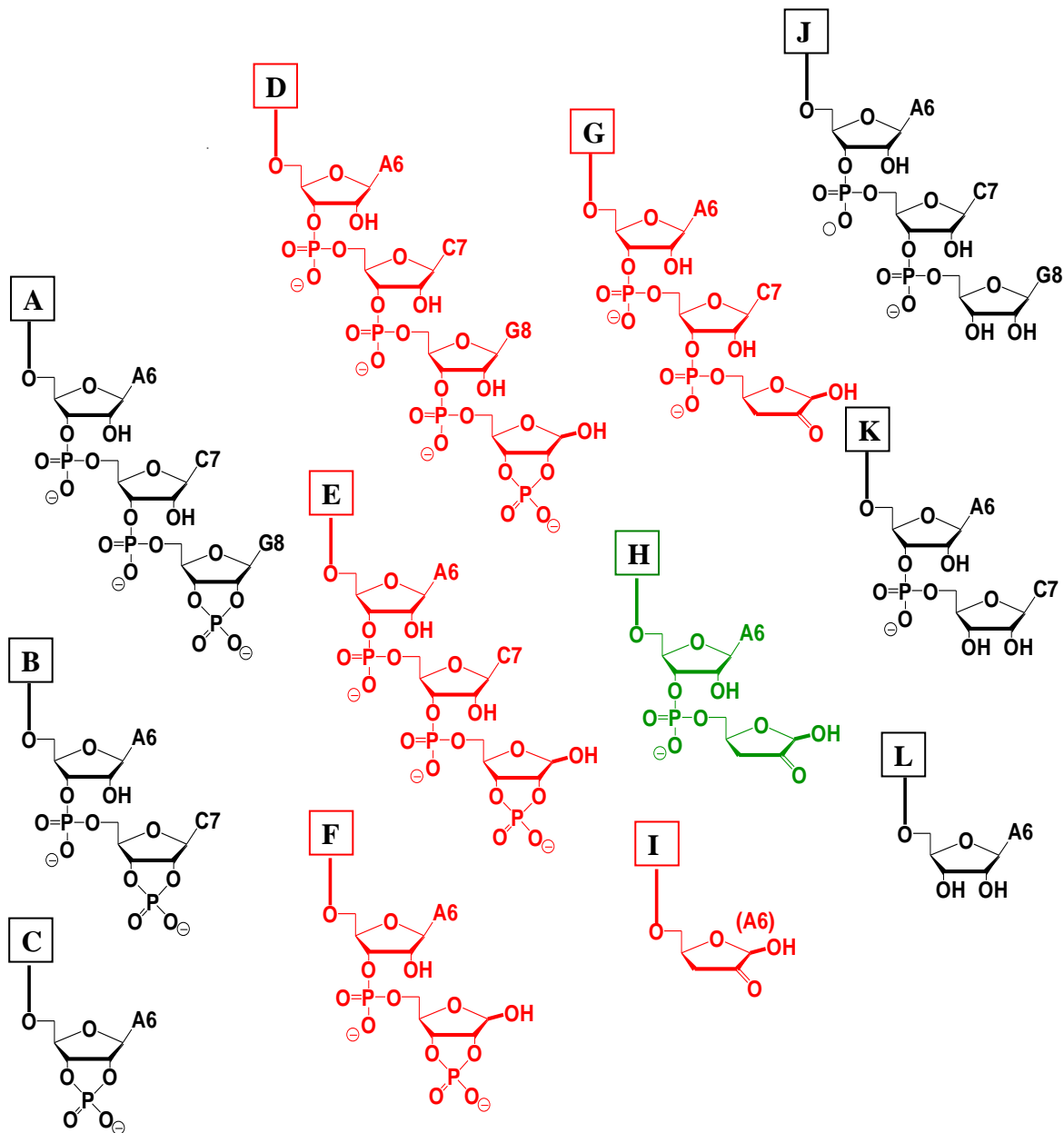
I first entertained the possibility that the unidentified band represents an (open) 3'-phosphate that could result from successive  $\beta$ - and  $\delta$ -elimination reactions at an abasic site (Figure 4.13) formed as a result of depurination or depyrimidination of an alkylated nucleobase. In principle, 3'-phosphate terminated fragments can be separated from their 2',3'-cyclic phosphate counterparts, which are the predominant products of limited alkaline RNA cleavage (the latter have one less negative charge and thus slightly retarded electrophoretic mobility). In practice, however, this separation is usually observed only for shorter fragments ( $< \sim 7$ -mer). Nevertheless, I eliminated the possibility that the unidentified band represented a 3'-phosphate terminated fragment by showing that its mobility was unchanged after 3'-dephosphorylation by polynucleotide kinase treatment (Figure 4.14, compare Lanes 3 & 4). In contrast, all of the other labeled fragments, which bear 2',3'-cyclic phosphates, showed significantly retarded mobility as a result of 3'-dephosphorylation.

**Figure 4.14:** (A) Alkaline footprinting analysis of Band I (5'-<sup>32</sup>P-labeled wildtype ribozyme) with and without subsequent polynucleotide kinase catalyzed 3'-dephosphorylation of all fragments. The red asterisk marks the anomalous cleavage band. (B) Quantitative analysis of autoradiography data in panel (A).



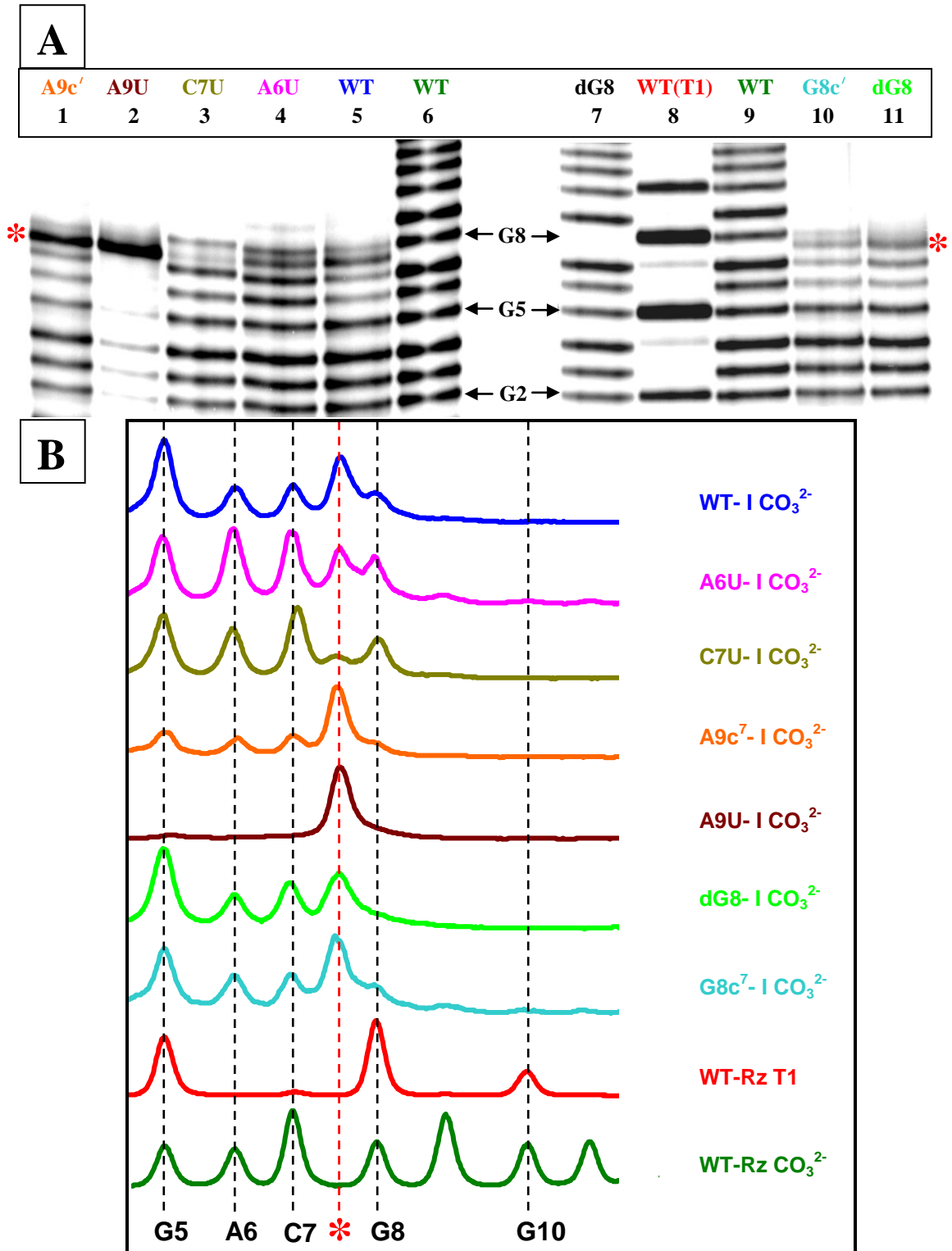
The remaining structures that are predicted to have electrophoretic mobilities that could be consistent with the unidentified band are shown in Figure 4.15. In order to assign the correct structure, I tested the effects of mutating each residue that had been identified as an alkylation site in Band I. Only the C7U mutation significantly diminished the production of the unidentified band (Figure 4.16, Lane 3). This observation suggests that alkylation of the deprotonated N3 of C7 (conjugate acid  $pK_a = 4.2^{125}$ ) leads to the production of the unidentified band. The C7U mutation suppresses this alkylation as uridine is largely protonated at N3 ( $pK_a = 9.4^{125}$ ). Of the two possible fragments that could stem from depyrimidination of alkylated C7, only the 2'-keto  $\beta$ -elimination product (Figure 4.15, structure H) is expected to have an electrophoretic mobility consistent with the unidentified band (specifically, structure H is predicted to have an electrophoretic mobility intermediate between structures B & K). The electrophoretic mobility of the other fragment that could result from C7 depyrimidination, the C7-abasic 2',3'-cyclic phosphate terminated fragment (Figure 4.15, structure F), is inconsistent with of the unidentified band, as this fragment should migrate faster than the intact (non-abasic) C7 cleavage fragment (Figure 4.15, structure B).

**Figure 4.15:** Candidate structures considered for the unidentified cleavage band in footprinting patterns of Band I. Black coloured structures are those which result from alkaline cleavage of the ribozyme (at right with PNK treatment, at left without PNK treatment). The red structures are ruled out based on their predicted electrophoretic mobility and/or the results of mutation experiments (see text). The green structure is assigned to the unidentified cleavage band. Fragment structures are arranged according to their predicted electrophoretic mobilities.



The data for the other ribozyme mutants also support the assignment of C7 alkylation as the source of the unidentified band. First of all, the A6 and A9 mutations that have been shown to strongly diminished alkylation of these residues (Figure 4.12, Lanes 2 & 5) did not diminish the production of the unidentified band (Figure 4.16, Lanes 1, 2, and 4); therefore, structures D & I in Figure 4.15 are eliminated. In fact, A9 mutations strongly enhanced the intensity of the unidentified band. The origin of this effect is unclear, but evidently these mutations favour, to some extent, the ribozyme conformation in which C7 alkylation occurs. The G8-abasic, 2',3'-cyclic phosphate terminated fragment (Figure 4.15, structure E) can also be definitively ruled out because the unidentified band is not affected by the 2'-deoxy-G8 (dG8) mutation, which prevents 2',3'-cyclic phosphate formation (Figure 4.16, Lane 11). Lastly, the 2'-keto  $\beta$ -elimination product of the G8-abasic site (Figure 4.15, structure G) can be ruled out as this fragment has one less negative charge, and is therefore expected to migrate more slowly than the intact G8 cleavage fragment (Figure 4.15, structure A). Having ruled out all other reasonable assignments, the unidentified band is tentatively assigned to the 2'-keto  $\beta$ -elimination product that follows from C7 depyrimidination (Figure 4.15, structure H).

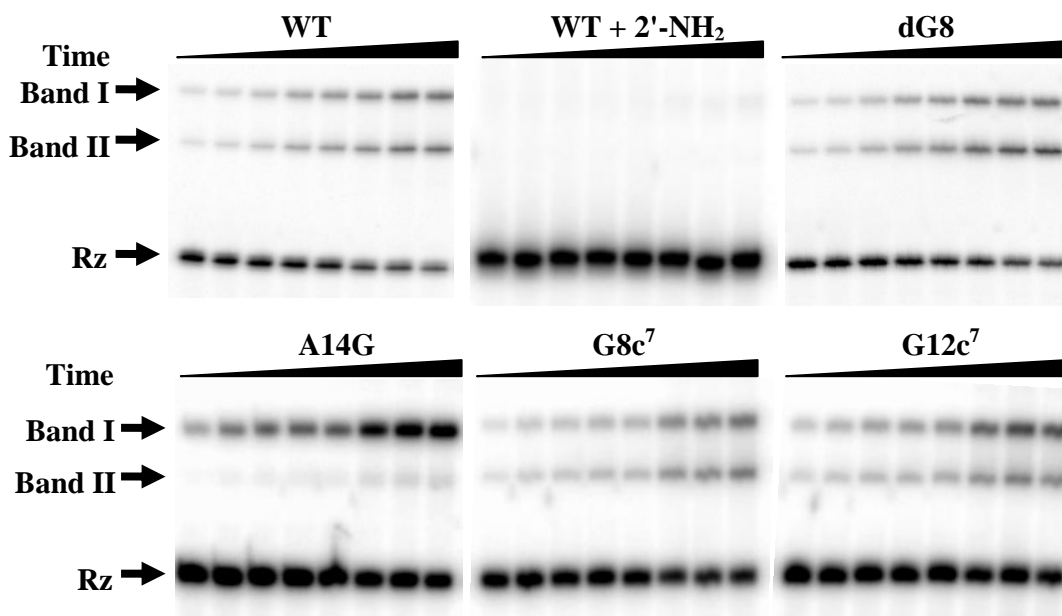
**Figure 4.16:** (A) Close-up view of the alkaline footprinting pattern of Band I for the indicated mutant ribozymes ( $5'$ - $^{32}$ P-labeled). The red asterisk marks the unidentified cleavage band. (B) Quantitative analysis of autoradiography data in panel (A).



#### 4.3.1.5 Properties of the Affinity Labeling Reactions

Next I compared the properties of the alkylation reaction with those of the catalytic reaction in an effort to gauge whether one or both of the G12 or A6-A9 alkylation events reflect the catalytic mechanism (Table 4.1 and Figure 4.17). The formation of both Bands I and II was completely inhibited by the addition of (non-bromoacetylated) 2'-amino-substrate analogue, which demonstrates that all of the alkylation events depend upon normal binding of the affinity label to the ribozyme in place of the native substrate. Various residues in the vicinity of the active site observed in the *S. mansoni* crystal structure<sup>270, 284, 285</sup> were mutated and the effects on the initial rates of alkylation were measured. Only two of the mutations tested had notable effect: A14G significantly diminished, whereas G12A enhanced the formation of Band II (G12 alkylation); both of these mutations had little effect on Band I formation. All other mutations had only modest effects on alkylation rate, contrary to the substantial inhibition (orders of magnitude) of native catalysis observed for most of the mutations tested.<sup>248</sup>

**Figure 4.17:** Alkylation reaction time courses for the indicated 5'-<sup>32</sup>P-labeled *S. mansoni* hammerhead ribozymes in 50 mM Tris-HCl pH 8, 100 mM NaCl, 50 mM MgCl<sub>2</sub>. “WT + 2'-NH<sub>2</sub>” indicates that the reaction contained 10 μM 2'-amino substrate analogue, in addition to the 2'-bromoacetamide affinity label. Time points were taken to 43 hours in each case.



The influence of metal cations on the alkylation reaction was also investigated. The  $[\text{Mg}^{2+}]$ -dependence of the initial rates of Band I and II formation is characterized in Figures 4.18. The data for Band II (G12 alkylation) fit quite well ( $R^2 = 0.98$ ) to a two-state  $\text{Mg}^{2+}$  binding model (Equation 4.1), which yielded a  $[\text{Mg}^{2+}]_{1/2}$  value of 47 mM and a Hill-type coefficient value of  $\sim 1.05$ . These parameters are in close agreement with those determined for the  $[\text{Mg}^{2+}]$ -dependence of the catalytic reaction. In notable contrast to the catalytic activity, which is nearly undetectable in the absence of  $\text{Mg}^{2+}$ , significant formation of Bands I and II is observed in (buffered) 100 mM NaCl alone. However, the observed rate constant for G12 alkylation in the absence of  $\text{Mg}^{2+}$  is diminished by almost

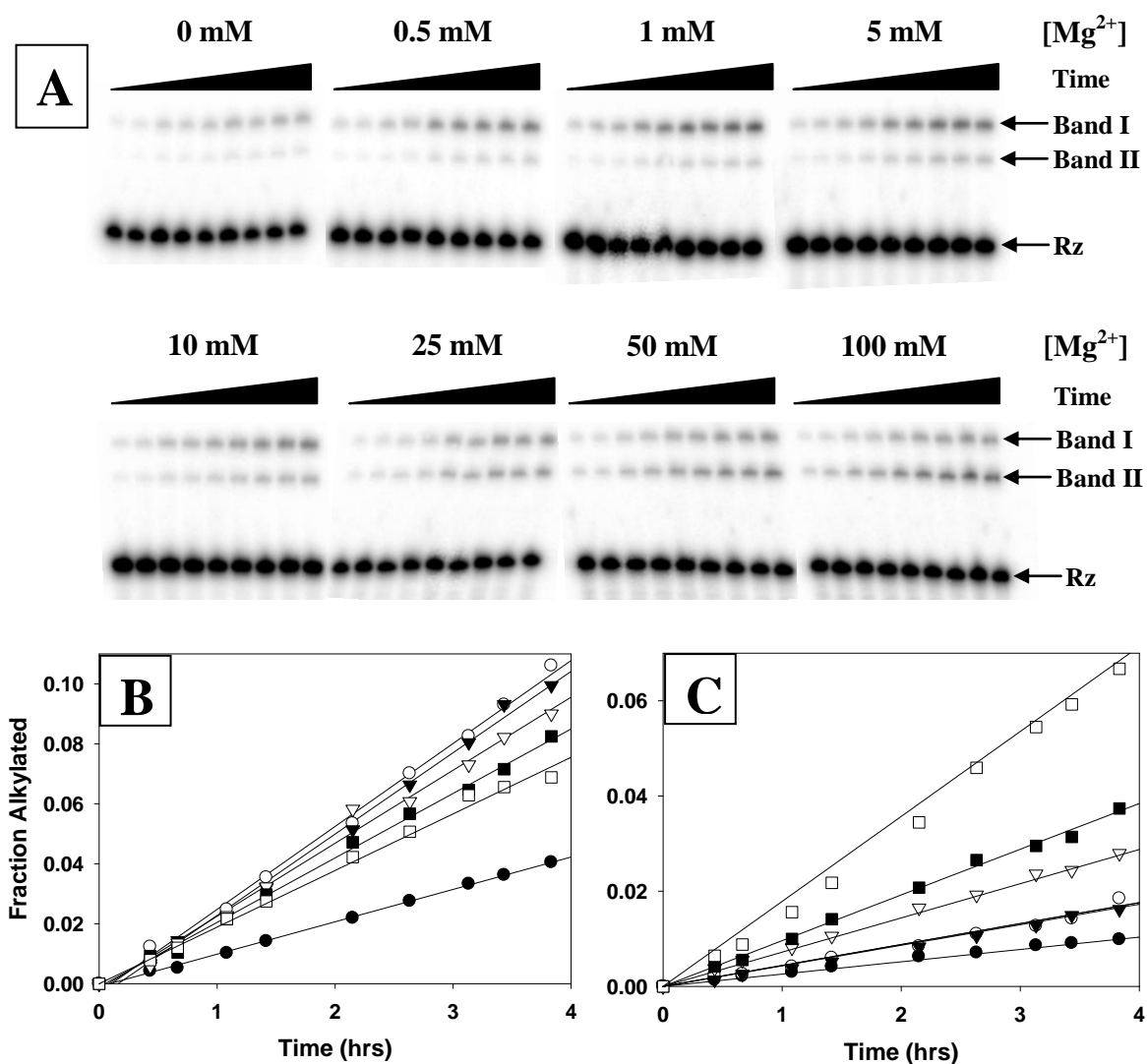
two orders of magnitude relative to  $k_{max}$  at saturating  $[Mg^{2+}]$ . The rate constant for A6-A9 alkylation displays a more complex  $[Mg^{2+}]$ -dependence, which is discussed qualitatively in Section 4.3.2.2.

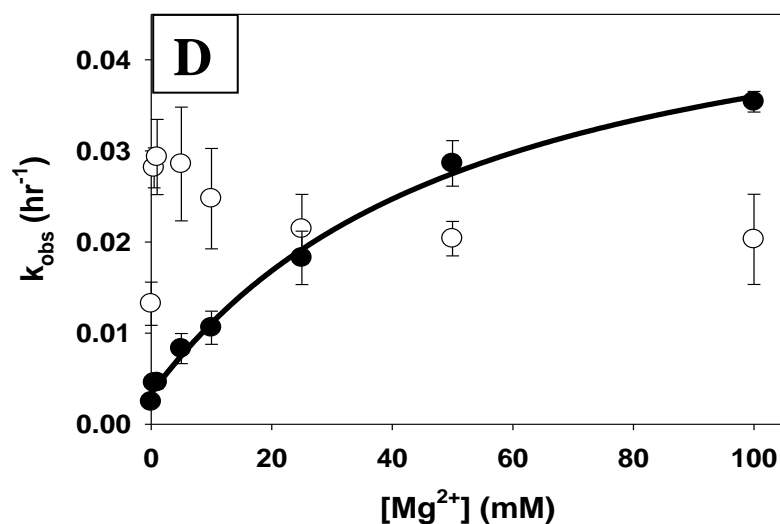
**Table 4.1:** Initial rate constants determined for the formation of Bands I and II for the wild type and various mutant *S. mansoni* hammerhead ribozymes. All reactions contained 50 mM MgCl<sub>2</sub>, 100 mM NaCl, 50 mM Tris-HCl pH 8, except for the reaction which lacked Mg<sup>2+</sup>, which contained 50 mM Tris-HCl pH 8, 100 mM NaCl, 5 mM EDTA.

Conditions (WT)	Band I: $k_{obs}$ (hr <sup>-1</sup> )	Band II: $k_{obs}$ (hr <sup>-1</sup> )
50 mM MgCl <sub>2</sub> , 100 mM NaCl	0.020	0.021
10 μM 2'-NH <sub>2</sub>	n.d. <sup>a</sup>	n.d. <sup>a</sup>
100 mM NaCl	0.013	0.0025
Ribozyme	Band I: $k_{obs}$ (hr <sup>-1</sup> )	Band II: $k_{obs}$ (hr <sup>-1</sup> )
WT	0.020	0.021
A14G	0.035	0.0017
G12A	0.018	0.073
G12c <sup>7</sup>	0.022	0.015
A9U	0.0070	0.030
A9c <sup>7</sup>	0.017	0.024
G8c <sup>7</sup>	0.014	0.013
dG8	0.015	0.017
G8A	0.017	0.010
A6U	0.0091	0.0068

<sup>a</sup> n.d. = not detected

**Figure 4.18:** (A) Autoradiograms showing time dependent hammerhead alkylation in 50 mM Tris-HCl pH 8.2, 100 mM NaCl, at various  $[Mg^{2+}]$ . The same time points were taken in each reaction to 3.8 hours. Plots of time dependent alkylation for (B) Band I and (C) Band II at  $[Mg^{2+}] = 0$  mM (●), 0.5 mM (○), 1 mM (▼), 5 mM (▽), 10 mM (■), and 25 mM (□). (D) Plot of the  $[Mg^{2+}]$ -dependence of the initial rate constants for (○) Band I and (●) Band II formation in the wildtype hammerhead. The 0 mM  $Mg^{2+}$  reaction contained 5 mM EDTA, and all reactions contained. The data for Band II (G12 alkylation) were fit to Equation 4.1, which returned  $k_{max} = 0.049$  hr<sup>-1</sup>,  $[Mg^{2+}]_{1/2} = 47$  mM, and a Hill-type coefficient  $n = 1.05$ .

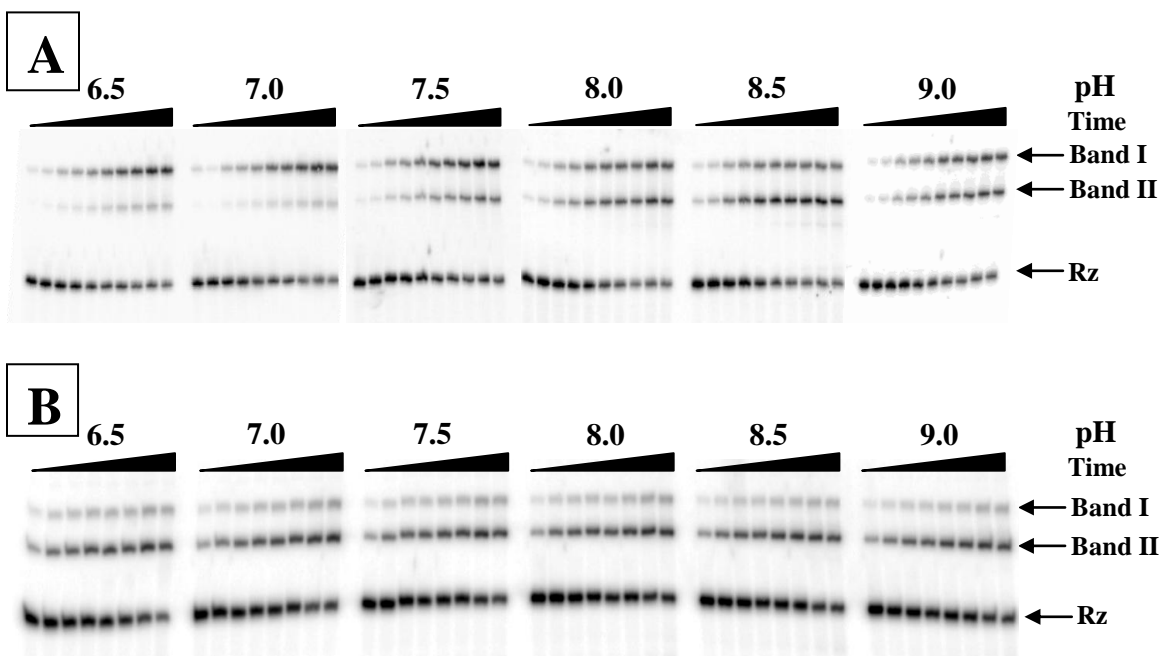


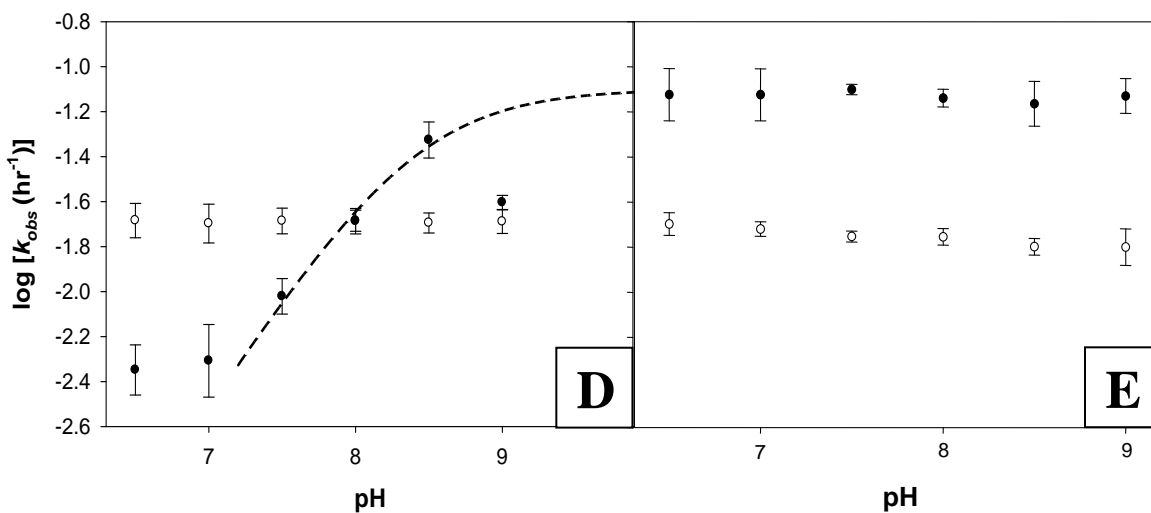
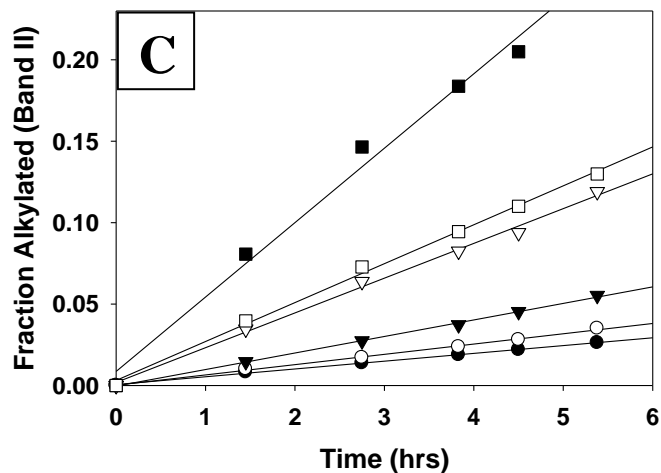


The pH-rate profiles for the formation of Band I and II formation were also determined for both the wildtype and G12A substituted ribozymes. The initial rate of G12 alkylation (Band II) in the wild type was strongly pH-dependent (Figure 4.19A, C, & D). The G12 alkylation rate constant shows a log-linear increase (slope of  $\sim 1$ ) from pH 7 to 8.5, as does the rate constant for the native cleavage reaction.<sup>268</sup> When G12 was mutated to A, the pH-dependence of Band II formation was completely abolished (Figure 4.19B & E). It is also striking that the maximum rate of G12 alkylation at pH 8.5, where N1 of G12 is presumably fully deprotonated, approaches the rate of A12 alkylation in the G12A mutant (compare Figure 4.19 D & E). These observations appear to reflect the titration of N1 of G12, whereas the G12A mutant presents the fully deprotonated N1 position at all pH's studied; this is illustrated by simulation of the G12 alkylation pH-rate-profile where  $pK_a = 8.4$  was assumed for N1 of G12, and  $k_{\max \text{ WT}}$  was set at the value of  $k_{\max \text{ G12A}}$ . In contrast to the simulation and to the cleavage reaction pH-rate profile, the G12 alkylation rate diminishes abruptly above  $\sim$ pH 8.5 and is pH-independent below pH

~7. The rate of formation of Band I is not dependent upon pH for either of the wildtype or G12A mutant ribozymes (Figures 4.19A, B, D & E), which suggests the alkylations of A6, C7, G8, or A9 occur at a non-titratable positions ( $pK_a < 7$ ).

**Figure 4.19:** Autoradiograms showing time dependent alkylation of the (A) wildtype, and (B) G12A hammerhead ribozymes in 50 mM buffer (at the indicated pH values), 100 mM NaCl, 50 mM MgCl<sub>2</sub>. For each ribozyme the same time points were taken for all reactions (out to 50 hours for wildtype and 43 hours for G12A). (C) Plots of time dependent wildtype alkylation for Band II at pH = 6.5 (●), 7 (○), 7.5 (▼), 8 (▽), 8.5 (■), and 9 (□). The pH-rate profiles are shown for alkylation of the (D) wildtype and (E) G12A hammerhead ribozymes. The logarithm of the initial rate constants (hr<sup>-1</sup>) for the formation of (○) Band I and (●) Band II are plotted as a function of pH. The idealized pH-rate profile (---) for alkylation of anionic N1 of G12 is simulated according to  $k_{obs} = k_{max}/(1+10^{pK_a-pH})$ , where  $\log(k_{max} WT) = \log(k_{max} G12A) = -1.1$  and  $pK_a = 8.4$  for N1 of G12.





## 4.3.2 Discussion

### 4.3.2.1 Structural Implications of the Affinity Labeling Data

Alkylation of five ribozyme residues was detected following the reaction of a 2'-bromoacetamide substrate analogue with the *S. mansoni* hammerhead. Based upon mutation and footprinting experiments, the identities of the alkylated nucleophiles were deduced to be N1 of G12, N7 of A9, N3 of G8, C7 (most likely at N3), and A6 (either N3 or N7 could be consistent with the aniline footprinting data). Only the alkylations of N1

of G12 and N7 of A9 are consistent with the active site observed in the *S. mansoni* crystal structure (Figure 4.2A & C), in that these potential nucleophiles are in close proximity to the scissile 2'-hydroxyl. The alkylation of A6 does not appear to be consistent with the *S. mansoni* crystal structure because, although A6 is present near the active site, neither N3 nor N7 is apposed to the scissile 2'-hydroxyl. Alkylation of A6 is, however, consistent with the minimal hammerhead ribozyme crystal structure, (Figure 4.2B & D) where N3 and particularly N7 of A6 are the only nucleophiles in close proximity to the scissile 2'-hydroxyl. Alkylation of A6 therefore confirms that the inactive conformation represented by the minimal hammerhead crystal structures<sup>250, 253</sup> is populated to a significant extent in the extended hammerhead ribozymes.

Notably, neither crystal structure can account for the alkylation of C7 nor G8, as these nucleobases are distant from the scissile 2'-hydroxyl in both structures. These alkylations could result from (1) fortuitous proximity of these residues to the 2'-bromoacetamide in previously unobserved folding intermediates, (2) the trajectory of these residues relative to the cleavage site during the transition from the inactive to the active fold, or possibly (3) a non-native conformation induced by the presence of the unnatural 2'-bromoacetamide structure. Overall, the identification of multiple alkylation sites that reflect multiple distinct conformations underscores the conformational plasticity of the hammerhead-substrate complex within the global Y-shaped fold (common to both the minimal and extended hammerhead crystal structures). In contrast, only one conformation could be detected by the alkylation of a single catalyst residue in RNaseA,<sup>94, 96</sup> the 9<sub>25-11</sub> DNAzyme (*vide supra*), and the hairpin ribozyme (*vide infra*).

### 4.3.2.2 Mechanistic Implications of the Affinity Labeling Data

Alkylation reaction pH-rate profiles were examined in order to establish whether any of the alkylated residues could be titrated in a manner consistent with titration observed in the catalytic pH-rate profile. The sum of the alkylation rates of A6, C7, G8, and A9 (the rate of Band I formation) is completely pH-independent. This implies that the observation of these alkylation reactions offers only structural insight and reflects fortuitous alkylation of non-titratable nucleophiles that are not likely to be involved in general base catalysis. In contrast, the rate of G12 alkylation (Band II formation) in the wild type ribozyme was strongly pH-dependent. As observed in the pH-rate profile for the catalytic reaction, the G12 alkylation rate showed a log-linear increase with increasing pH, at least from ~7 to ~8.5.<sup>268,288</sup> The G12A substitution abolished this pH-dependence, and further increased the rate of Band II formation. These results reflect the effect of substituting the fully deprotonated N1 of A12 for N1 of G12 (the  $pK_a$  of N1-protonated adenosine is just 3.5<sup>125</sup>, whereas the  $pK_a$  of free guanosine is 9.4). Thus, it is clear that the wildtype alkylation pH-dependence reflects titration of N1 of G12. Strikingly, at pH 8.5, where N1 of G12 appears to be largely deprotonated, the rate of wildtype alkylation approaches the rate of G12A alkylation where N1 of the A12 is completely deprotonated. This is illustrated by simulation in Figure 4.19D where it is assumed that deprotonated A12 and G12 are alkylated at the same rate ( $k_{\max \text{ WT}} = k_{\max \text{ G12A}}$ ), and that  $pK_a = 8.4$  for N1 of G12. Note that the simulation suggests a slightly higher  $pK_a$  value for G12 than that determined for the catalytic reaction ( $pK_a \sim 8$  – *vide infra*); this difference may reflect changes in active site structure caused by the presence of the bromoacetamide probe. Nevertheless, my data suggest that of  $pK_a$  of G12 (in the

catalytically active hammerhead conformation) is perturbed downward relative to free guanosine. Overall, the pH-rate analysis demonstrates that titration of N1 of G12 in the context of alkylation closely matches the general base titration which controls the catalytic reaction rate.

The pH-rate profile for wildtype G12 alkylation levels off below pH ~7, contrary to the continued titration of N1 observed for the native cleavage reaction.<sup>268</sup> This effect may stem from a pH-independent alkylation of protonated G12, followed by rapid loss of the N1-proton. The decrease in G12 alkylation rate at pH 9 is also unexpected. The fact that this effect is not observed for G12A alkylation suggests that denaturation at high pH is not the cause. This effect may be peculiar to the G12 alkylation reaction and not relevant to catalysis.

The  $[\text{Mg}^{2+}]$  dependence of the G12 alkylation is very similar to that of the native *S. mansoni* cleavage reaction ( $[\text{Mg}^{2+}]_{1/2} = 40$  mM for cleavage<sup>268</sup> and 47 mM for G12 alkylation, both with a Hill coefficient  $n = \sim 1$ ). This further supports the conclusion that G12 alkylation reflects the catalytically active conformation, and supports assignment of the recent *S. mansoni* crystal structure as the active fold.<sup>248, 253, 270</sup> Although my data confirm that  $\text{Mg}^{2+}$  binding strongly stabilizes the active fold, significant G12 alkylation in the absence of  $\text{Mg}^{2+}$  shows that the active fold is still populated, although to a lesser extent, in the absence of  $\text{Mg}^{2+}$  (in the presence of minimal NaCl and buffer). In contrast, *S. mansoni* hammerhead catalysis is nearly undetectable in 100 mM NaCl (*vide infra*). The comparatively strict  $\text{Mg}^{2+}$  requirement for catalysis (at low ionic strength) suggests that  $\text{Mg}^{2+}$  cofactor(s) serve both a structural role in stabilizing the active fold as well as a catalytic role other than general base catalysis.

The collective alkylations of A6, C7, G8, and A9 displayed a  $[\text{Mg}^{2+}]$ -dependence completely different from G12 alkylation and the native reaction.<sup>268</sup> At higher  $\text{Mg}^{2+}$  concentrations ( $[\text{Mg}^{2+}] > 1 \text{ mM}$ ), the decrease in A6-A9 alkylation likely partially reflects depopulation of the inactive fold at higher  $[\text{Mg}^{2+}]$ , in favour of the active fold in which G12 is alkylated. At  $[\text{Mg}^{2+}] < 1 \text{ mM}$ , the rise in A6-A9 alkylation likely reflects  $\text{Mg}^{2+}$ -assisted formation of the global, Y-shaped fold common to both the active and inactive conformations. Indeed, based upon FRET-based measurements of ribozyme folding, Lilley and coworkers observed  $\text{Mg}^{2+}$ -dependent formation of this global fold;<sup>280</sup> they determined that half the population was folded at  $[\text{Mg}^{2+}] = 160 \text{ }\mu\text{M}$ , qualitatively consistent with the sharp increase in A6-A9 alkylation at  $[\text{Mg}^{2+}] < 1 \text{ mM}$ . Substantial alkylation of A6-A9 was observed in NaCl alone, which indicates formation of the global fold in the absence of  $\text{Mg}^{2+}$ . This finding is in agreement with the results of a recent FRET study by Boots *et al.*, which demonstrated efficient formation of the global fold of the *S. mansoni* hammerhead in NaCl-containing buffers.<sup>281</sup>

### 4.3.3 Conclusions

In summary, affinity labeling has revealed the presence of two or more distinct conformations of the (substrate-bound) *S. mansoni* hammerhead ribozyme. Specifically, it appears that conformations corresponding to both the minimal<sup>249, 250</sup> and extended<sup>270, 284, 285</sup> hammerhead crystal structures are populated. My data also demonstrate that the G12 alkylation reaction expresses very similar pH- and  $[\text{Mg}^{2+}]$ -dependence to the native cleavage reaction, which suggests that the anionic N1 of G12 is alkylated in the catalytically active ribozyme conformation. Previous  $\text{p}K_{\text{a}}$  perturbation experiments

suggested a role for G12 in one of general acid or base catalysis,<sup>277</sup> but the ambiguity inherent in the interpretation of cleavage pH-rate profiles prevented the discrimination of these possibilities.<sup>23</sup> Although my results pertain to a different chemical reaction than the native RNA cleavage reaction, they do not suffer from the same kinetic ambiguity. The log-linear increase in the rate of G12 alkylation in the hammerhead ribozyme provides particularly compelling evidence that N1 of G12 functions as a *bona fide* general base in the hammerhead ribozyme. Moreover, the direct analogy with the pH-dependent alkylations of His12 in RNaseA<sup>94-96</sup> and the A23 imidazole in 9<sub>25-11</sub> (both putative general bases) provides strong precedent for this interpretation.

## **4.4 PROBING GENERAL ACID CATALYSIS IN THE HAMMERHEAD RIBOZYME**

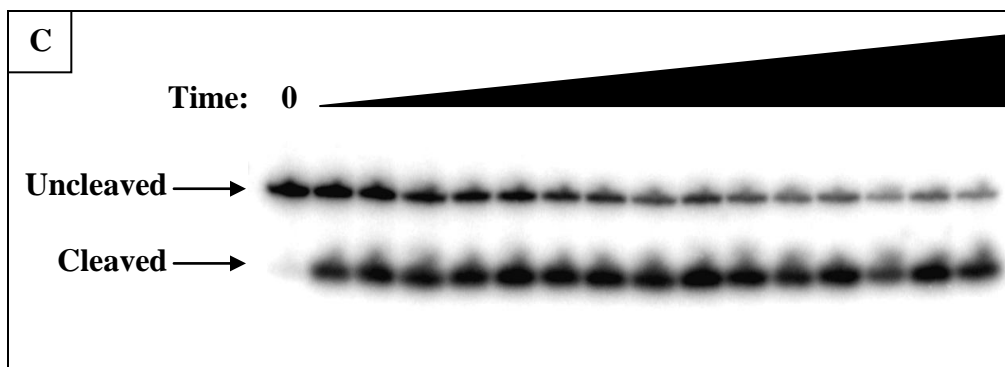
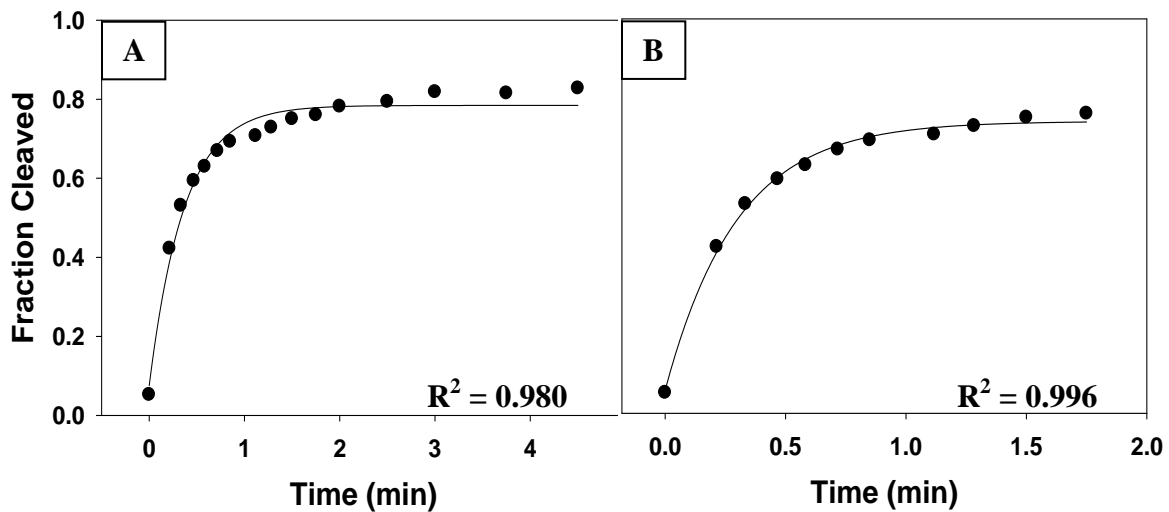
### **4.4.1 Results**

#### **4.4.1.1 S-link Substrate Cleavage and Ribozyme Mutation**

In an effort to locate ribozyme functional groups that are crucial for general acid catalysis, the cleavage of the S-link and O-link substrates was examined in the context of a wide variety of both sequence mutations and non-canonical chemical modifications. The standard reaction conditions (2 mM MgCl<sub>2</sub>, 100 mM NaCl, 50 mM Na-PIPES pH 7) were chosen such that all cleavage rates did not exceed that which could be monitored by manually quenched kinetics experiments. In several cases, biphasic S-link cleavage kinetics were observed (Figure 4.20A, for example), especially when longer time points were included. The reported rate constants represent the faster cleaving phase, and were obtained by fitting earlier time points (Figure 4.20B). In all cases, the majority of the

substrate was cleaved in the faster phase. Such biphasic kinetics have been reported by other investigators for extended hammerhead ribozymes, including the *S.mansoni*.<sup>262, 282,</sup>  
<sup>296</sup> Note also that a value of  $k_{obs}$  reported as  $<0.00001 \text{ min}^{-1}$  (for the only cleavage phase observed) indicates that amount of substrate cleaved over the monitored reaction time (up to 100 hours) was too small to reliably quantify rate constants.

**Figure 4.20:** An example of biphasic kinetics encountered for S-link cleavage by the *S. mansoni* hammerhead ribozyme and mutants. Data for single turnover cleavage of the S-link substrate by wildtype ribozyme are shown (reaction conditions: 2 mM MgCl<sub>2</sub>, 100 mM NaCl, 50 mM Na-PIPES pH 7). (A) The full data set clearly does not fit well ( $R^2 = 0.980$ ) to a monophasic model (Equation 4.2). (B) A truncated data set fit adequately to a monophasic model ( $R^2 = 0.996$ ) (the longest time points are removed while still preserving enough data to accurately fit the parameters). (C) The autoradiography data used to generate the plots in (A) and (B). Time points (in minutes) analyzed were: 0, 0.22, 0.33, 0.47, 0.58, 0.71, 0.85, 1.12, 1.28, 1.50, 1.75, 2.00, 2.50, 3.00, 3.75, 4.50.



Most of the ribozyme mutations chosen have been characterized kinetically for minimal hammerheads in the context of O-link substrates, but in most cases, not for extended hammerheads. Not unexpectedly, the effects of ribozyme mutations on O-link substrate cleavage reported here for the *S. mansoni* hammerhead generally parallel those for the minimal hammerheads.<sup>248</sup> I also find that a chimeric embedded ribose/DNA substrate is cleaved efficiently by the *S. mansoni* hammerhead as it is by minimal hammerheads;<sup>102, 291</sup> this was important to establish given that our S-link substrate synthesis is currently limited to such embedded ribose/DNA substrates.

The effect of hammerhead mutations has not previously been examined in the context of an S-link substrate. Table 4.2 presents the observed rate constants for single turnover cleavage of the S-link and O-link substrates by the *S. mansoni* hammerhead and various point mutants, as well as for background substrate cleavage. Cleavage of S-link and O-link substrates was also compared in the presence of various metal cations at pH 7 (Table 4.3). Considering that  $k_S/k_O$  values indicate that the mutation or reaction conditions impair general acid catalysis in particular,<sup>68, 104, 105, 107, 113, 297, 298</sup> the data suggest that both a divalent metal cation and the G8 2'-hydroxyl play crucial roles in general acid catalysis, although several other residues also appear to play important roles in facilitating general acid catalysis (see discussion in Section 4.4.2.1). I also tested an *S. mansoni* hammerhead that had been mutated so as to eliminate the tertiary interaction which is absent in the minimal hammerheads (compare Figures 4.21 and 4.1B). Modest diminution of both S-link and O-link cleavage was observed for this mutant, relative to the wildtype.

**Table 4.2:** First order rate constants determined for single turnover cleavage of O-link and S-link substrates by the wildtype and mutant *S. mansoni* hammerhead ribozymes. All reactions were carried out in 2 mM MgCl<sub>2</sub>, 100 mM NaCl, 50 mM Na-PIPES pH 7.

Ribozyme	$k_O$ (min <sup>-1</sup> )	$k_S$ (min <sup>-1</sup> )	$k_S/k_O$	$k_S/k_{\text{uncat S}}$	$k_O/k_{\text{uncat O}}$
WT	0.86	3.2	3.7	$1.1 \cdot 10^4$	$8.6 \cdot 10^7$
2'-OMe-G8 <sup>a</sup>	0.00013	1.9	14600	$6.6 \cdot 10^3$	$1.3 \cdot 10^4$
dG8 <sup>b</sup>	0.0025	4.6	1840	$1.6 \cdot 10^4$	$2.5 \cdot 10^5$
dA6 <sup>b</sup>	0.81	3.3	4.1	$1.1 \cdot 10^4$	$8.1 \cdot 10^7$
dG5 <sup>b</sup>	0.00079	0.33	417	$1.1 \cdot 10^3$	$7.9 \cdot 10^4$
A14G	<0.00001	0.02	>2000	$6.9 \cdot 10^1$	< $1.0 \cdot 10^3$
G12c <sup>7c</sup>	0.014	0.50	35	$1.7 \cdot 10^3$	$1.4 \cdot 10^6$
G12A	<0.00001	0.094	>9400	$3.2 \cdot 10^2$	< $1.0 \cdot 10^3$
G12U	<0.00001	0.058	>5800	$2.0 \cdot 10^2$	< $1.0 \cdot 10^3$
A9U	0.0076	4.0	526	$1.4 \cdot 10^4$	$7.6 \cdot 10^5$
A9c <sup>7d</sup>	0.0017	3.4	2000	$1.2 \cdot 10^4$	$1.7 \cdot 10^5$
G8A	0.00008	0.14	1750	$4.8 \cdot 10^2$	$8.0 \cdot 10^3$
A6U	0.00005	0.16	3200	$5.5 \cdot 10^2$	$5.0 \cdot 10^3$
BP <sup>e</sup>	0.030	1.1	36	$3.8 \cdot 10^3$	$3.0 \cdot 10^6$
Background	$\sim 1 \cdot 10^{-8}$ <sup>f</sup>	0.00029	$\sim 29000$	1	1

<sup>a</sup> 2'-O-methyl.

<sup>b</sup> 2'-deoxy-ribo.

<sup>c</sup> 7-deaza-guanosine.

<sup>d</sup> 7-deaza-adenosine.

<sup>e</sup> “Base Paired” meaning the ribozyme sequence was altered so that the tertiary interaction highlighted in Fig 1 is disrupted by forming a base paired helix with the substrate strand (see Figure 4.21).

<sup>f</sup> background (non-enzymatic) cleavage rate constant is estimated based on data in reference 222.

**Figure 4.21:** The “base paired” (BP) hammerhead ribozyme referred to in Table 4.2. The altered sequence is highlighted by the red box, and permits continuous base pairing with the substrate (more like a minimal hammerhead), and serves to prevent formation of the native tertiary contacts (see Figures 4.1B & 4.2A).

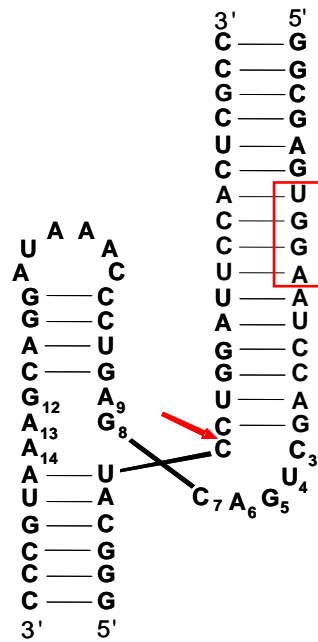


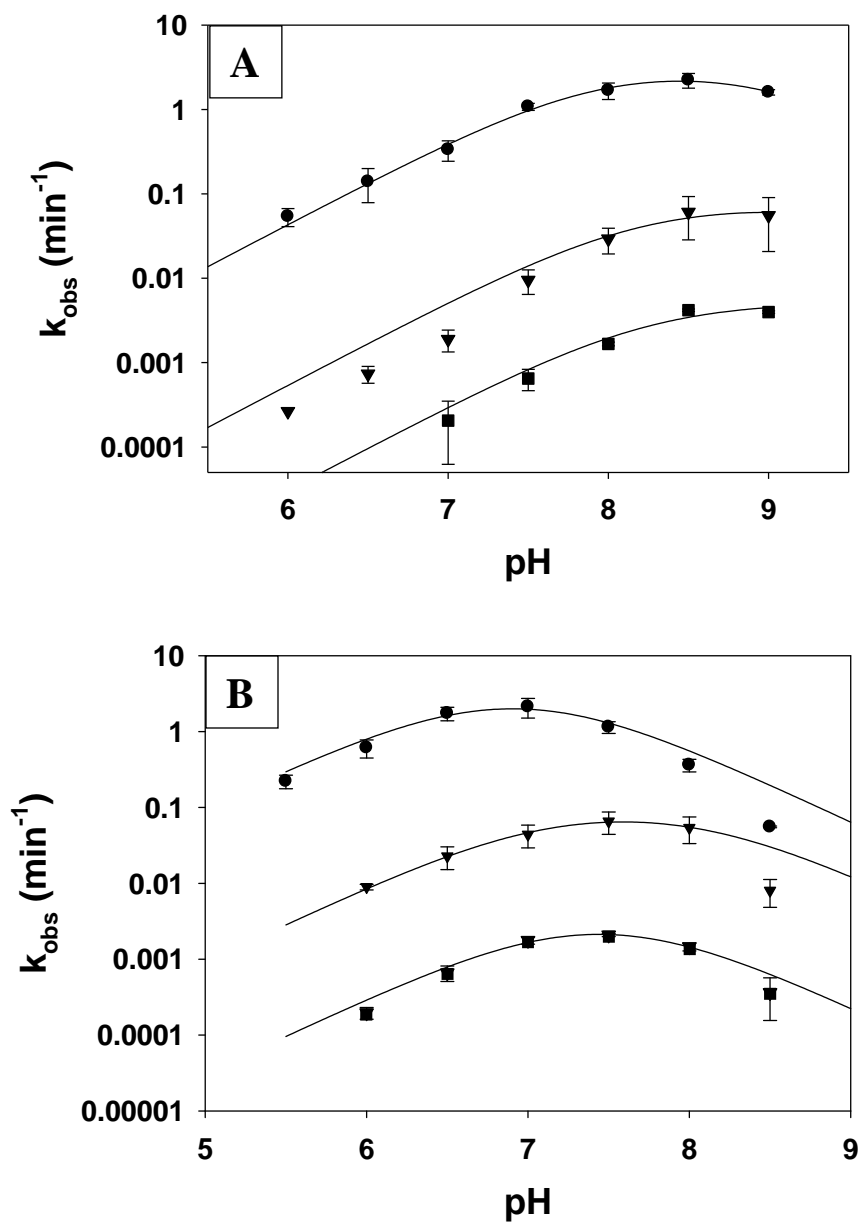
**Table 4.3:** First order rate constants determined for single turnover cleavage of O-link and S-link substrates by the wildtype, 2'-deoxy-G8, and 2'-O-methyl-G8 *S. mansoni* hammerhead ribozymes in the presence of various metal cations. All reactions were carried out in 50 mM Na-PIPES pH 7.

Conditions	Ribozyme	$k_O$ (min <sup>-1</sup> )	$k_S$ (min <sup>-1</sup> )	$k_S/k_O$
2 mM Mg <sup>2+</sup> + 100 mM NaCl	WT	0.86	3.2	3.7
	dG8	0.0025	4.6	1840
	2'-OMe-G8	0.00013	1.9	14600
0.2 mM Mn <sup>2+</sup> + 100 mM NaCl	WT	1.2	2.5	2.1
	dG8	0.0070	2.9	414
	2'-OMe-G8	0.0028	0.35	125
1 mM Cd <sup>2+</sup> + 100 mM NaCl	WT	2.2	2.7	1.2
	dG8	0.057	2.6	46
	2'-OMe-G8	0.0018	3.3	1830
100 mM NaCl + 5 mM EDTA	WT	<0.00001	2.7	>270000
	dG8	<0.00001	1.0	>100000
	2'-OMe-G8	<0.00001	0.17	>17000
100 mM LiCl + 5 mM EDTA	WT	0.00017	2.5	14700
	dG8	<0.00001	2.3	>230000
	2'-OMe-G8	<0.00001	0.70	>70000

#### 4.4.1.2 pH-Rate Profiles

Perturbation of the general acid  $pK_a$  was investigated to confirm the role of both the G8 2'-hydroxyl and a  $Mg^{2+}$  cofactor in general acid catalysis, and to help elucidate the mechanism in more detail. Perturbation of the general acid  $pK_a$  was brought about by: 1) by substitution of the more acidic  $Cd^{2+}$  cation for  $Mg^{2+}$  (the  $pK_a$  of  $Cd(H_2O)_6^{2+}$  is 8 whereas the  $pK_a$  of  $Mg(H_2O)_6^{2+}$  is 11.4)<sup>288</sup>, and/or 2) by alteration of the G8 2'-hydroxyl in the dG8 and 2'-OMe-G8 mutants. These effects were expressed in the pH-rate profiles for O-link substrate cleavage by the wildtype, dG8, and 2'-OMe-G8 hammerheads, in both  $Mg^{2+}$  and  $Cd^{2+}$  containing solutions (Figure 4.22). All pH-rate data were fit to a general acid/base catalysis model,<sup>23</sup> and the kinetic  $pK_a$ 's so generated are presented in Table 4.4. Given that general base catalysis by G12 (with  $pK_a \sim 8$ ), is suggested convincingly by the sum of crystallographic,<sup>270, 284, 285</sup> computational,<sup>286, 287</sup> and functional evidence,<sup>277, 299</sup> the kinetic  $pK_a$  closest to 8 was assigned to the general base, and the other to the general acid. In all cases except for the wildtype ribozyme in the presence of  $Cd^{2+}$ , one of the titrations clearly demonstrated a  $pK_a$  near 8 within the standard error limits. Note that the rate constants determined in the presence of  $Cd^{2+}$  at  $pH > 8$  are likely unreliable due to  $Cd(OH)_2$  precipitation; therefore, these data were not included in the fits.<sup>288</sup> (The  $K_{sp}$  for  $Cd(OH)_2$  is  $4.5 \cdot 10^{-15}$ , thus for solutions with  $[Cd^{2+}] = 1$  mM,  $K_{sp}$  is exceeded at  $pH = 8.3$ . Note, however, that this estimate is based on a  $K_{sp}$  value reported for solutions with zero ionic strength<sup>14</sup>).

**Figure 4.22:** pH-rate profiles for O-link substrate cleavage by the (●) wildtype, 2'-deoxy-G8 (▼), and (■) 2'-OMe-G8 *S. mansoni* hammerhead ribozymes in the presence of (A) 1 mM Mg<sup>2+</sup> or (B) 1 mM Cd<sup>2+</sup>. All reactions contained 100 mM NaCl and 50 mM Buffer. Data were fit to a general acid/base catalysis model according to  $k_{\text{obs}} = k_{\text{max}} / (1 + 10^{\text{p}K_{\text{a}1} - \text{pH}} + 10^{\text{pH} - \text{p}K_{\text{a}2}} + 10^{\text{p}K_{\text{a}1} - \text{p}K_{\text{a}2}})$ .<sup>23</sup> For Cd<sup>2+</sup> containing reactions, data for pH > 8 were omitted from the fits as 1 mM Cd<sup>2+</sup> is prone to precipitation above pH ~8. Error bars indicated standard deviations of the data points.



In the presence of  $\text{Cd}^{2+}$ , the general acid  $\text{p}K_a$  appears to increase slightly when proton transfer from the G8 2'-hydroxyl is abolished in both the dG8 and 2'-OMe-G8 variants (Table 4.4 and Figure 4.22B). The general acid titrations for the dG8 and 2'-OMe-G8 hammerheads in the presence of  $\text{Mg}^{2+}$  fell outside the observable pH range, so these  $\text{p}K_a$  values, which exceed 9, could not be determined with high precision. Nevertheless it is clear, qualitatively, that the general acid  $\text{p}K_a$  is perturbed slightly higher for the dG8 and 2'-OMe-G8 variants in the presence of  $\text{Mg}^{2+}$  (Figure 4.22A), as observed in the presence of  $\text{Cd}^{2+}$  (of course caution must be exercised in interpreting data so close to the onset of general alkaline RNA denaturation near pH ~9).

**Table 4.4:** The  $\text{p}K_a$  values determined from the pH-rate profile data (Figure 4.22) for O-link substrate cleavage by the wildtype, 2'-deoxy-G8, and 2'-O-methyl-G8 *S. mansoni* hammerhead ribozymes. All reactions contained 1 mM  $\text{M}^{2+}$ , 100 mM NaCl, 50 mM Buffer. Standard error limits generated by fitting the pH-rate profile data are given. The  $\text{p}K_a$  values reported as “ >9 ” could not be fit reliably because the titrations occur outside the observable pH range.

Ribozyme	$\text{M}^{2+}$	$\text{p}K_a$ closest to 8	Other $\text{p}K_a$
WT	$\text{Mg}^{2+}$	$7.9 \pm 0.2$	$9.0 \pm 0.2$
dG8	$\text{Mg}^{2+}$	$8.2 \pm 0.8$	>9
2'-OMe-G8	$\text{Mg}^{2+}$	$8.2 \pm 0.2$	>9
WT	$\text{Cd}^{2+}$	$7.0 \pm 0.6$	$6.7 \pm 0.4$
dG8	$\text{Cd}^{2+}$	$8.1 \pm 0.5$	$7.1 \pm 0.4$
2'-OMe-G8	$\text{Cd}^{2+}$	$7.5 \pm 0.6$	$7.4 \pm 0.5$

## 4.4.2 Discussion

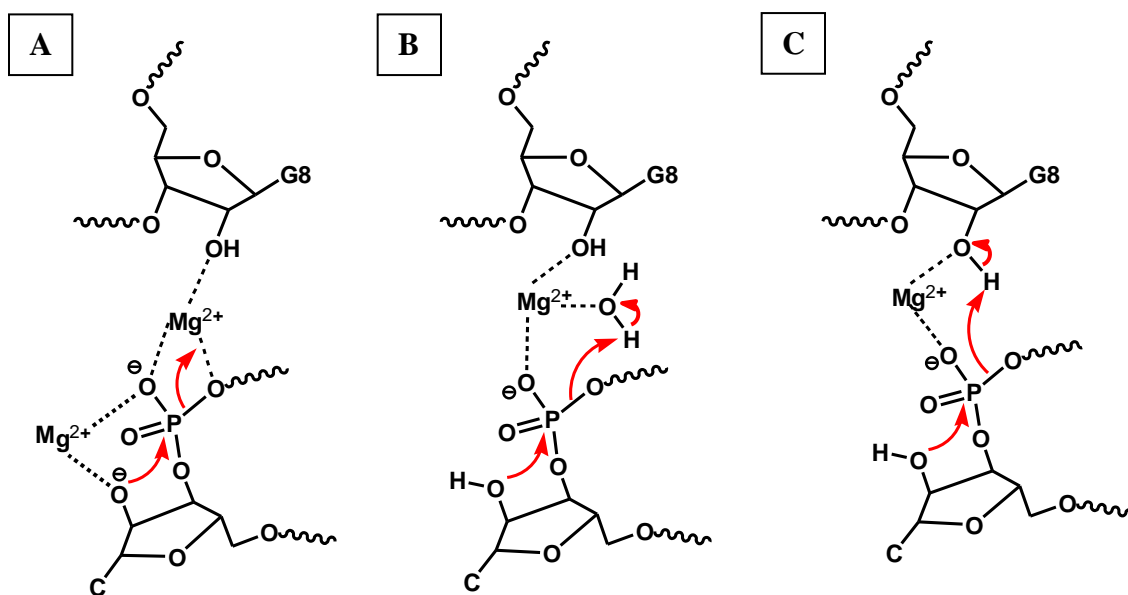
### 4.4.2.1 S-link Substrate Cleavage and Ribozyme Mutation

Although the bridging phosphorothioate linkage has previously been used to study minimal hammerhead ribozyme catalysis,<sup>98-102</sup> the role of ribozyme functional groups in general acid catalysis has not been investigated. These earlier studies offered differing conclusions regarding the identity of the rate limiting catalytic step, but agreed that, unlike non-enzymatic cleavage, hammerhead cleavage of S-link substrates was not significantly enhanced in the presence of soft metal cations. This latter observation has been taken as evidence that the 5'-leaving group is not stabilized by direct coordination to a Lewis-acidic metal cation<sup>102</sup> (compare with the data for S-link cleavage by the *Tetrahymena* ribozyme<sup>103</sup> described in Section 2.1.2). Nevertheless, two groups have cautioned that these S-link cleavage data could still be consistent with a mechanism in which two Mg<sup>2+</sup> cations provide Lewis-acid catalysis to both stabilize the leaving group and lower the pK<sub>a</sub> of the scissile 2'-hydroxyl (Figure 4.23A).<sup>99, 274</sup> My results confirm that soft metal cations (Mn<sup>2+</sup> and Cd<sup>2+</sup>) do not significantly enhance cleavage of the S-link substrate by the *S. mansoni* hammerhead relative to Mg<sup>2+</sup> or even monovalent cations alone (Table 4.3). It now appears likely that a two metal ion mechanism invoking double M<sup>2+</sup>-mediated Lewis-acid catalysis can be ruled out (Figure 4.23A) because: (1) recent biochemical, structural, and computational data convincingly implicate the G12 nucleobase in general base catalysis, and (2) S-link cleavage, which presumably benefits from general base catalysis, is largely unaffected by the absence of a M<sup>2+</sup> cofactor. It is also worth noting that *S. mansoni* hammerhead catalysis is not likely to be limited by a

slow conformational change that might mask  $Mn^{2+}$  or  $Cd^{2+}$  activation of S-link cleavage, as could be the case in minimal hammerheads.<sup>255, 256, 258</sup>

The largest  $k_S/k_O$  values observed for hammerhead catalysis are manifested in the absence of divalent metal cations (Table 4.3). Even though a  $M^{2+}$  cofactor does not appear to act directly as a Lewis acid to stabilize the leaving group, its omission specifically disrupts general acid catalysis in O-link substrate cleavage. Moreover, the fact that S-link cleavage is not significantly affected by the absence of  $M^{2+}$  (in 100 mM NaCl or LiCl), suggests that a divalent metal ion does not play any crucial role in catalytic chemistry beyond facilitating general acid catalysis. Notably, cleavage of an S-link substrate by a minimal hammerhead in 0.5 M NaCl was reported to be undetectable.<sup>102</sup> This discrepancy suggests that divalent metal ions are more crucial for stabilizing the active ribozyme conformation in the minimal hammerhead, whereas in the *S. mansoni* hammerhead, the active conformation forms to a greater extent in the absence of  $M^{2+}$  cations.

**Figure 4.23:** Possible mechanisms of general acid catalysis in the wildtype *S. mansoni* hammerhead ribozyme that involve both the G8 2'-hydroxyl and a  $Mg^{2+}$  cofactor (the G12 general base has been omitted for clarity).



Consistent with its proximity to the leaving group in the *S. mansoni* crystal structure, the G8 2'-hydroxyl also appears to be crucial for general acid catalysis based on the large  $k_S/k_O$  values (Table 4.2) observed upon mutation of this functional group (in the 2'-dG8 and 2'-OMe-G8 mutants). In the clear-cut results reported for the HDV ribozyme,<sup>68</sup> large  $k_S/k_O$  values were observed uniquely for mutation of the N3 position of C75 (at least among the mutations tested). In contrast, large  $k_S/k_O$  values were observed for mutation of several hammerhead ribozyme residues in addition to the G8 2'-hydroxyl. Similar S-link rescue of multiple active site mutations has been observed by Tsai and coworkers for the phospholipase enzyme.<sup>107, 113</sup> Based on previous crystal structure data, the authors concluded that S-link rescue of mutations to residues other than the putative general acid resulted from disruption of hydrogen bond networks necessary for proper

general acid placement (see Section 2.1.2). In the hammerhead ribozyme, the crystallographically observed<sup>270</sup> G8:C3 canonical base pair is crucial for efficient activity, and has been predicted computationally<sup>287</sup> to be crucial for proper positioning of the G8 2'-hydroxyl to engage in proton transfer to the oxygen leaving group. The significant S-link rescue for the G8A mutation is consistent with this hypothesis. The significant S-link rescue of the A9U, and A9-7deaza (A9c<sup>7</sup>) mutations also shows that the G12:A9 sheared pair, observed in the *S. mansoni* crystal structure,<sup>270</sup> is important for proper placement of the adjacent general acid residue (G8). It is worth noting that most of the mutations examined in this study, with the exception of A14G, did not significantly affect placement of the putative general base (G12), as judged by affinity labeling data (see Table 4.1); productive structural positioning of the general acid appears to be much more sensitive to mutations in the hammerhead catalytic core.

Large  $k_S/k_O$  values were also observed upon mutation of the putative hammerhead general base (G12). Again, it is not surprising that disruption of the G12:A9 interaction, by G12 mutation this time, should affect proper placement of the G8 2'-hydroxyl and/or a divalent metal cation bound to the A9-phosphate. However, Scott and coworkers have recently shown that the G12A mutation does not significantly perturb the structure of the pre-reactive state,<sup>285</sup> although perturbation of the transition state structure cannot be ruled out.

It should also be noted that while the activities of the A6U, G12A, G12U, and A14G mutants appear to be rescued for the S-link substrate based on large  $k_S/k_O$  ratios, both S-link and O-link cleavage is enhanced by a factor of less than  $10^3$  relative to background cleavage for these mutants. Soukup and Breaker have reported such

enhancement of uncatalyzed RNA cleavage due to geometrical constraints imposed by secondary and tertiary structures.<sup>222</sup> Similarly, Kuimelis and McLaughlin observed that background S-link cleavage was sensitive to structural context.<sup>118</sup> It is certainly possible that the relatively small enhancements of both S-link and O-link cleavage in the aforementioned mutants results largely from structural constraints which favour the in-line attack geometry when substrate is bound to ribozyme.

#### 4.4.2.2 pH-Rate Profiles

The S-link cleavage data are consistent with the proposed role of a divalent metal cation in acidifying the G8 2'-hydroxyl, which, in the context of the *S. mansoni* crystal structure, is properly positioned to transfer a proton to the 5'-oxygen leaving group (Figure 4.23C). A purely structural role for the G8 2'-hydroxyl should also be considered, where it serves as a ligand to ensure proper placement of a hydrated divalent metal ion near the leaving group. In this case, a  $M^{2+}$ -bound water ligand could act directly as the general acid (Figure 4.23B). In order to discriminate between these two closely related mechanisms, and to validate the S-link cleavage data, I examined the effects on the pH-rate profile of  $M^{2+}$  substitution and mutation of the G8 2'-hydroxyl.

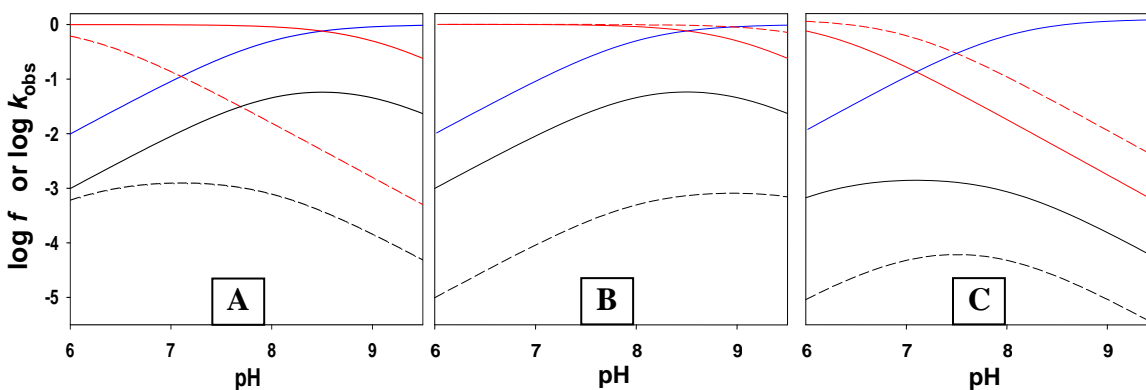
In general, the assignment of kinetic  $pK_a$ 's to the general acid or general base is inherently ambiguous (Section 2.1.3); however, this ambiguity can be overcome with the benefit of S-link cleavage data and guidance from crystal structures.<sup>23</sup> Das and Piccirilli provide a superb example of such reasoning in their study of general acid catalysis in the HDV ribozyme. Not only did these authors convincingly implicate the N3 of C75 in

general acid catalysis by specific S-link rescue of mutations to this residue, but they also demonstrated general acid  $pK_a$  perturbation using a C75(6-azaC) mutant ribozyme.

Considering that my S-link cleavage findings and the *S. mansoni* crystal structure<sup>270</sup> implicate both the G8 2'-hydroxyl and a  $M^{2+}$  cofactor in general acid catalysis, the pH-rate profile changes due to  $M^{2+}$  or G8 2'-hydroxyl modification are attributed to general acid  $pK_a$  perturbation. Consistent with this interpretation, a kinetic  $pK_a$  close to 8 was determined in almost all cases, which was taken to reflect invariant general base catalysis by G12.<sup>288</sup> Unexpectedly, the general base  $pK_a$  determined for the wildtype ribozyme in the presence of  $Cd^{2+}$  was slightly lower, although  $Cd(OH)_2$  precipitation above pH ~8 likely contributes to significant error in fitting the general base  $pK_a$  in all cases.

For each of the wild type, dG8, and 2'-OMe-G8 hammerheads, substitution of  $Cd^{2+}$  for  $Mg^{2+}$  lowers the general acid  $pK_a$ . This effect is illustrated by simulation in Figure 4.24. These findings confirm  $M^{2+}$ -involvement in general acid catalysis, as suggested by the S-link cleavage data, and agree well with previous data for cleavage of a natural all-RNA substrate by a different extended hammerhead (RzB).<sup>288</sup> However, these data do not resolve whether a  $Mg^{2+}$ -coordinated water molecule (Figure 4.23B) or the G8 2'-hydroxyl (Figure 4.23C) transfers a proton to the 5'-oxygen leaving group.

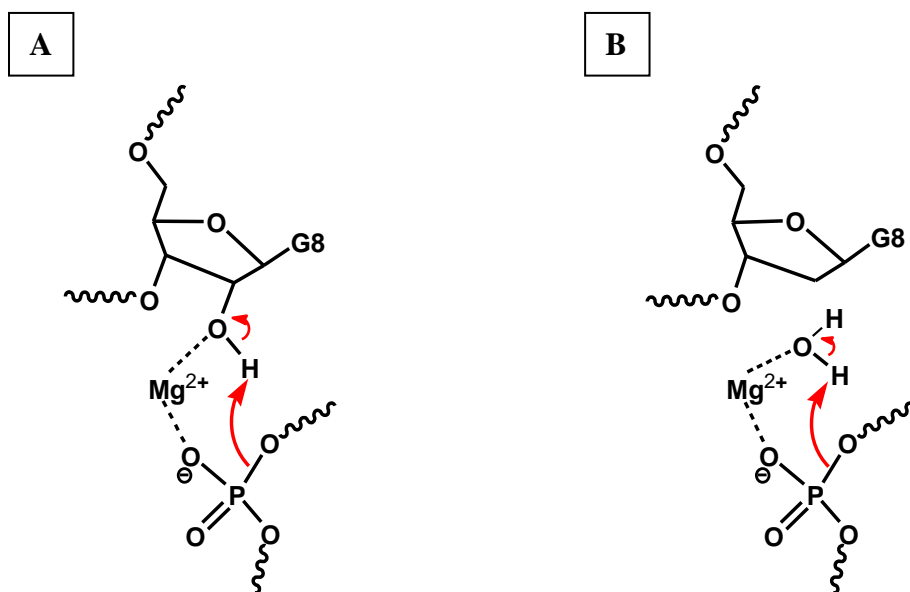
**Figure 4.24:** Simulation of the effects of general acid  $pK_a$  perturbation on the pH-rate profile for O-link substrate cleavage catalyzed by the *S. mansoni* hammerhead ribozyme. The general base titrations are coloured blue, the general acid titrations are coloured red, and the pH-rate profiles are coloured black. (A) Substitution of  $Cd^{2+}$  (---) for  $Mg^{2+}$  (—) dramatically lowers the  $pK_a$  of the general acid. (B) Presumed substitution of a  $Mg^{2+}$ -bound water ligand for the G8 2'-hydroxyl slightly increases the  $pK_a$  of the general acid in the dG8 mutant (---) relative to wildtype (—). (C) The dG8 mutation (---) similarly raises the general acid  $pK_a$  relative to wildtype (—) in the presence of  $Cd^{2+}$ . The general base titration is invariant in all cases ( $pK_a$  set to 8). For clarity,  $k_{max}$  was set to 0.1 for wildtype and 0.001 for dG8. Simulations were generated as described in Section 2.2.1.



In order to discriminate between the mechanisms in Figures 4.23B & C, the pH-rate profiles for native substrate cleavage by the wild type, dG8, and 2'-OMe-G8 hammerheads were compared in the presence of both  $Mg^{2+}$  and  $Cd^{2+}$  (Figure 4.22). Regardless of  $M^{2+}$ , the general acid  $pK_a$  appears to be shifted higher for both the dG8 and 2'-OMe-G8 mutants relative to wild type. This effect is particularly clear in the presence of  $Cd^{2+}$ , and appears to hold true in the presence of  $Mg^{2+}$ , although one must be cautious in drawing conclusions from pH effects so close to the onset of general alkaline denaturation of RNA (at pH ~9). I propose that the upward shift in general acid  $pK_a$  signals that a  $M^{2+}$ -bound water ligand assumes the duty of transferring a proton to the

leaving group in cases where the G8 2'-hydroxyl is modified to prevent such proton transfer (Figure 4.24B). This interpretation is qualitatively consistent with the  $pK_a$  difference between free water ( $pK_a = 15.7$ ) and a 2'-hydroxyl in RNA (experimentally determined 2'-hydroxyl  $pK_a$  values in model compounds range from  $\sim 12.5$  to  $13.7$ ,<sup>4, 300, 301</sup> although theoretical predictions range as high as  $14.9$ <sup>302</sup>). It is thus reasonable that this  $pK_a$  difference should be reflected, qualitatively at least,<sup>99</sup> in the general acid  $pK_a$  expressed by  $M^{2+}$ -bound water versus G8 2'-hydroxyl (Figure 4.25A & B). This hypothesis is also consistent with the more severely impaired activity and greater S-link rescue for the 2'-OMe-G8 versus the dG8 mutant; the added methyl group in the former presents a structural impediment to proton transfer from a  $M^{2+}$ -bound water ligand to the 5'-oxygen leaving group.

**Figure 4.25:** General acid catalysis mechanisms hypothesized based on the data presented in this chapter for (A) wildtype and (B) dG8 *S. mansoni* hammerhead ribozymes.



### 4.4.3 Conclusions

In summary, I have reported the first experimental investigation focused on evaluating the synergistic involvement of the G8 2'-hydroxyl and a divalent metal cation in general acid catalysis in the hammerhead ribozyme. The rescue of activity for G8 2'-hydroxyl mutations with this S-link substrate, coupled with general acid  $pK_a$  perturbation by both  $M^{2+}$  substitution and replacement of the G8 2'-hydroxyl by water, provides compelling evidence that supports the general acid catalysis mechanism depicted in Figure 4.23C. The S-link data also reveal the importance for general acid catalysis specifically of new structural interactions uncovered in the *S. mansoni* crystal structure (namely the G8:C3 base pair and the G12:A9 sheared pair).<sup>270</sup> My findings help to clarify the unique mechanism of general acid catalysis in the hammerhead ribozyme, and confirm the role of a divalent metal cation therein. More generally, this study demonstrates that  $M^{2+}$ -mediated  $pK_a$  perturbation can be exploited by ribozymes/DNAzymes to help overcome their intrinsic lack of functionality well-suited for general acid/base catalysis at physiological pH.<sup>40, 303, 304</sup>

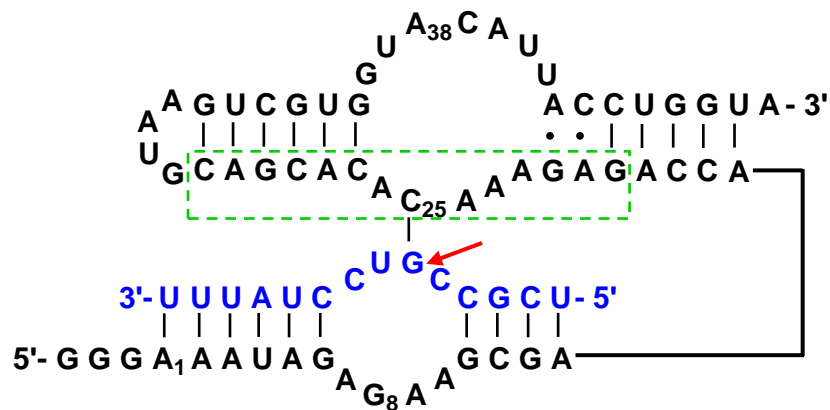
# CHAPTER 5: PROBING GENERAL BASE CATALYSIS IN THE HAIRPIN RIBOZYME

## 5.1 INTRODUCTION

### 5.1.1 Hairpin Ribozyme Structure and Function

The hairpin ribozyme constructs used in mechanistic studies comprise the naturally occurring structural elements that are minimally required for activity.<sup>305-307</sup> As illustrated in the secondary structure of the *trans*-cleaving EH4 construct used in this study (Figure 5.1), a hairpin ribozyme consists of two domains linked at a hinge point (in the natural context the hinge point occurs at a four-way helical junction).<sup>307</sup> Each of these two domains consists of two base paired helices, separated by an unpaired loop region. Sequence variation is well tolerated in the base paired regions, but the loop sequences are largely conserved between species and are important for efficient activity. Early structural insights furnished by photocrosslinking<sup>308</sup> and FRET<sup>309, 310</sup> studies, as well as mutational and kinetic studies<sup>311, 312</sup> have established that the two domains are arranged parallel to each other in the catalytically active conformation. Furthermore, specific tertiary contacts between the two unpaired loops were identified such as a C25:G(-1) base pair,<sup>311</sup> and a “ribose zipper” interaction based on hydrogen bonds formed amongst the 2'-hydroxyl groups and nucleobases of several residues.<sup>313, 314</sup>

**Figure 5.1:** Secondary structure representation of the *trans*-cleaving EH4 hairpin ribozyme in complex with substrate.<sup>315</sup> The ribozyme strand (black) is numbered from 5' to 3' starting from A<sub>1</sub>; ribozyme residues particularly crucial for catalytic activity are numbered. In the substrate strand (blue), the cleavage site is indicated by the red arrow. Canonical Watson-Crick base pairs are indicated by the black bars; non-canonical base pairs are indicated by black dots. The reverse transcription primer binding site corresponds to the ribozyme sequence inside the dashed green box (see Section 5.2.4).



Although folding and activity of the hairpin ribozyme are strongly enhanced at higher  $Mg^{2+}$  concentrations,<sup>316</sup> there is ample evidence that  $Mg^{2+}$  plays an entirely passive role in catalysis. First of all, the contribution of  $Mg^{2+}$  to catalysis can be replaced quite efficiently by any of a chemically diverse variety of positively charged cofactors; for example, reasonably efficient  $M^{2+}$ -independent hairpin activity has been observed in the presence of monovalent cations ( $Li^+$  or  $NH_4^+$ )<sup>160</sup> or the exchange-inert  $[Co(NH_3)_6]^{3+}$  complex,<sup>159</sup> as well as cationic peptides, aminoglycoside antibiotics, or spermine.<sup>317</sup> Second, metal cation coordination of the scissile phosphate, as proposed in the hammerhead ribozyme, has been clearly ruled out by the fact that hairpin cleavage of nonbridging phosphorothioate substrates is not sensitive to either soft metal cation substitution or the absence of  $M^{2+}$  cations altogether.<sup>158, 238</sup> Overall, these findings

suggested the involvement of ribozyme functional groups and/or specific acid and/or base catalysts in active site chemistry.

The solution of hairpin ribozyme crystal structures by Ferré D'Amaré and coworkers confirmed the predicted tertiary structure and clarified the nature of the interdomain contacts.<sup>318</sup> With regard to active site mechanism, the crystal structure of a vanadate inhibited hairpin ribozyme-substrate complex pinpointed several potential transition state stabilizing hydrogen bond interactions, which involve the base pairing faces of G8 and A38 and scissile substrate residue (Figures 5.2 & 5.3).<sup>319</sup> The position of G8 is similar to that of G12 in the hammerhead structure,<sup>270, 285</sup> in that N1 of each of these residues is within hydrogen bonding distance of the scissile 2'-hydroxyl. A38 appears poised to deliver a proton to the 5'-alkoxide leaving group, in analogy to the role of C75/76 in the HDV ribozymes.<sup>68</sup> There is also strong functional evidence based upon abasic rescue<sup>320</sup> and A38 mutation studies<sup>321, 322</sup> which indicate that the positively charged, N1 protonated form of A38 is required for catalysis (either in general acid catalysis<sup>23</sup> or electrostatic stabilization of the transition state<sup>323</sup>). The role of G8 in catalysis, which is the focus of this work, has been much more controversial, and requires more detailed consideration.

**Figure 5.2:** Crystal structure of a hairpin ribozyme bound to a vanadate-triester transition state analogue.<sup>319</sup> The ribozyme and substrate strands are coloured teal and orange, respectively; the U1A RNA binding protein is coloured green; the scissile substrate nucleotide is coloured white; and the G8 and A38 ribozyme residues are colour coded as indicated. The full structure (A) is depicted along with a cartoon stick and ribbon model (B). A close up view of the active site is also shown (C). Images were generated from protein data bank (pdb) files using PyMol.<sup>67</sup>

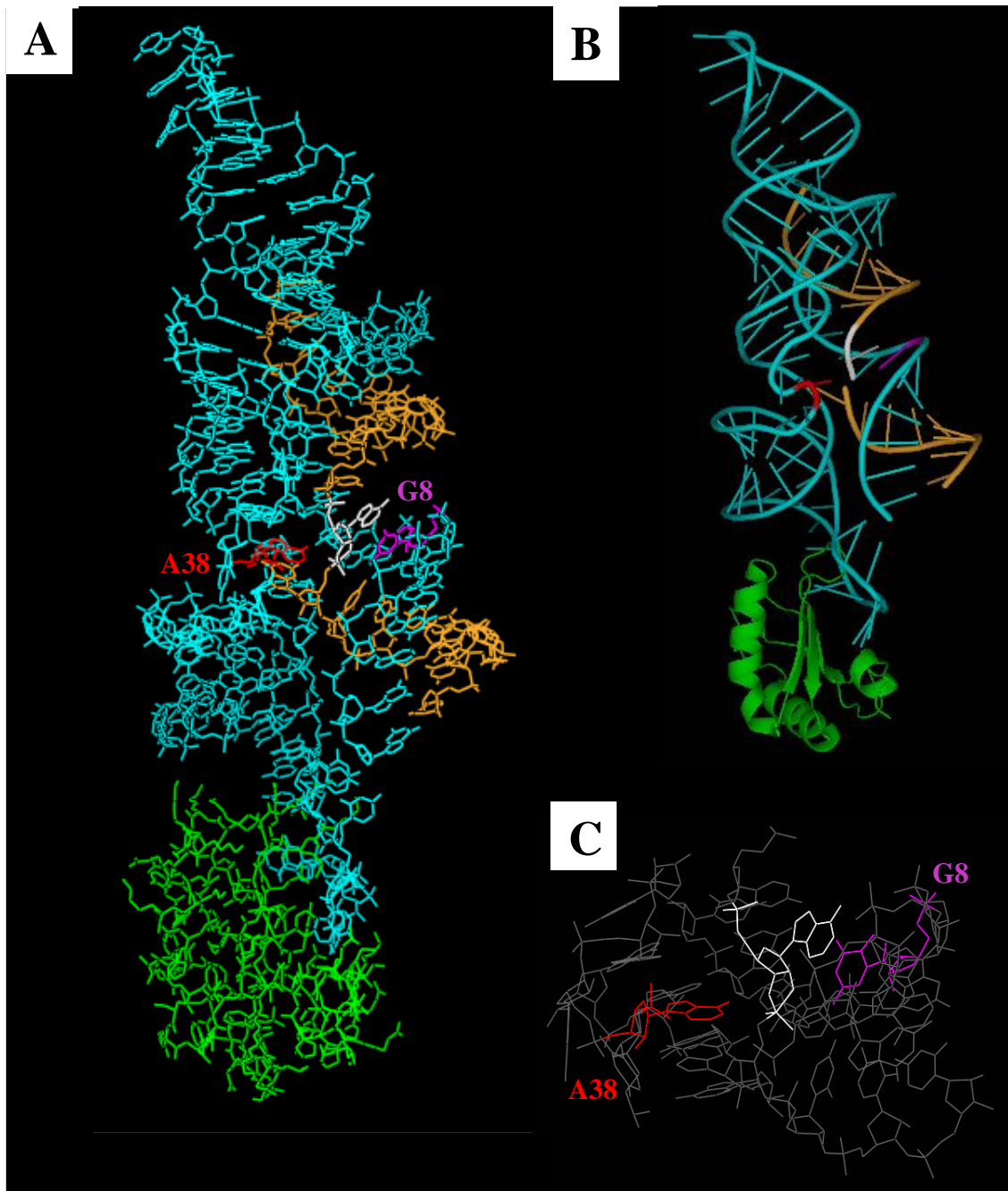
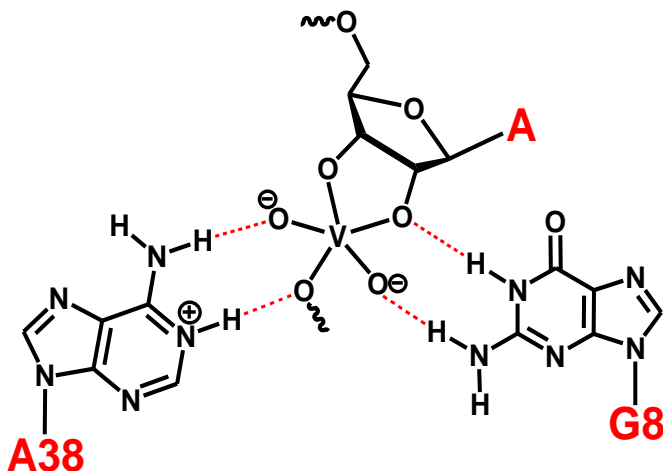


**Figure 5.3:** Hydrogen bond interactions (dashed red lines) involving G8 and A38, which were identified in the crystal structure of the hairpin ribozyme bound to a vanadate transition state analogue.<sup>319</sup>

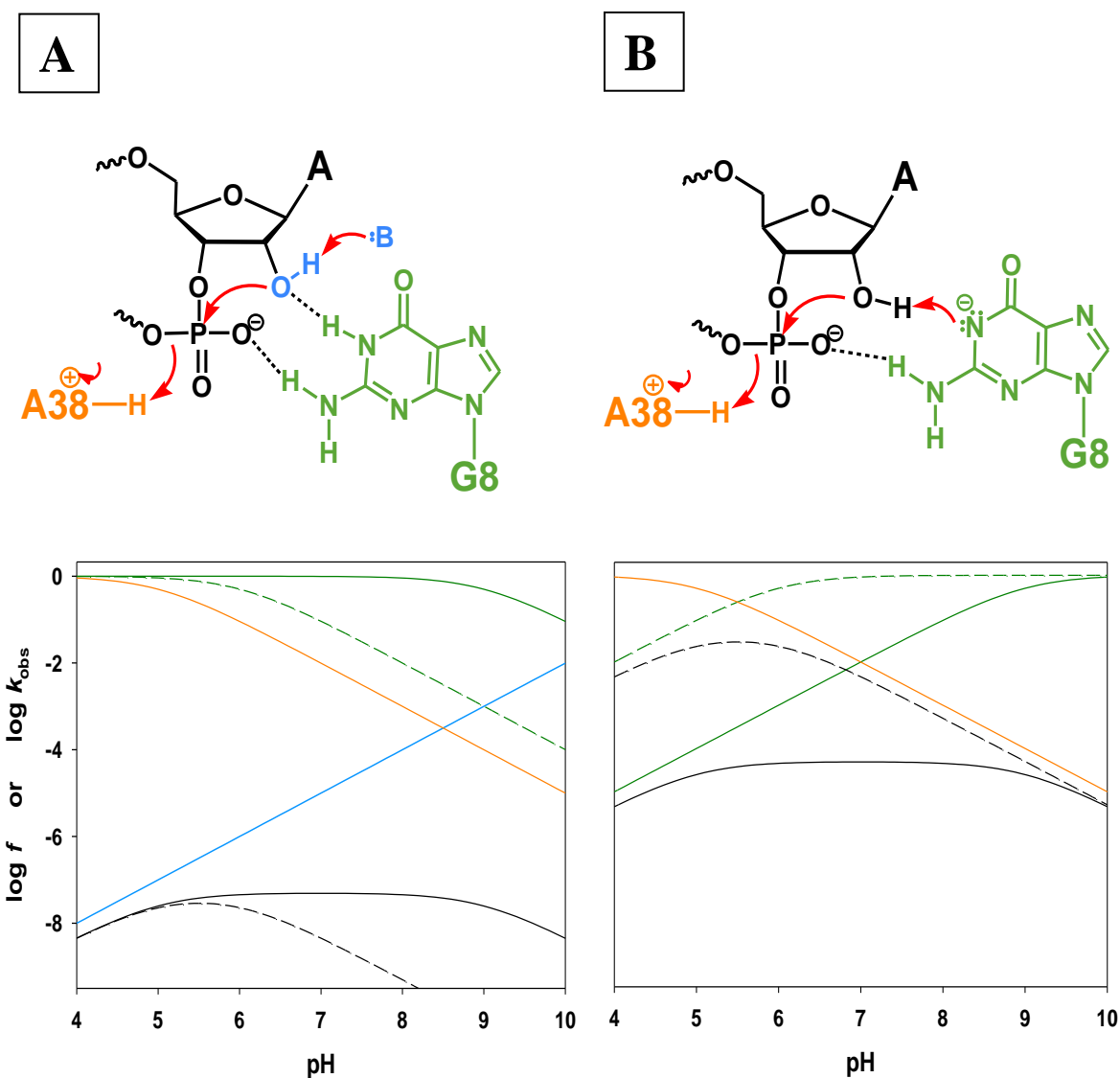


### 5.1.2 The Role of G8 in Hairpin Catalysis

In light of the hairpin crystal structures,<sup>318, 319</sup> as well as detailed structure-function data, there exists ample evidence that the N1 position of G8 is directly involved in transition state stabilization.<sup>23, 320-322, 324-328</sup> pH-rate and  $pK_a$  perturbation experiments have provided insightful functional data regarding the role of G8 in catalysis. For the wildtype hairpin ribozyme, the pH-rate profile is rather flat throughout the physiological range, which could reflect two titratable catalytic residues with well separated  $pK_a$  values (Figure 5.4B). The higher  $pK_a$  titration in the pH-rate profile (the  $pK_a$  value varies slightly with ribozyme construct, but is always  $>9$ ) has been attributed to deprotonation of N1 of G8, based on the observation that the  $pK_a$  of this titration shifts predictably in response to replacing G8 with lower N1  $pK_a$  isosteres such as 2,6-diaminopurine and inosine.<sup>324</sup> Very similar  $pK_a$  perturbation effects have also been observed for the

chemical rescue of G8-abasic hairpin ribozymes using lower  $pK_a$  guanine analogues.<sup>326</sup> Since the work described herein, Fedor and coworkers have also studied the titration of G8 by exploiting the protonation state-dependent fluorescence of 8-aza-guanosine.<sup>329</sup> Fluorescence titration experiments using the G8(8-aza-G) mutant ribozyme demonstrated that the  $pK_a$  value for G8 closely matches that observed for the higher  $pK_a$  titration in the pH-rate profile for the same mutant ribozyme.<sup>330</sup>

**Figure 5.4:** Either of two kinetically ambiguous mechanisms can account for the change in pH-rate profile caused substitution of 2,6-diaminopurine for G8 in the hairpin ribozyme. (A) Mechanism requiring protonated G8 and A38, and specific base catalysis.<sup>324-326</sup> (B) Mechanism requiring deprotonated G8 and protonated A38.<sup>23</sup> pH-rate profiles are shown in black; solid lines correspond to wildtype and dashed lines to the G8(2,6-diaminopurine) mutant. Titrations are colour green for G8 and diaminopurine, orange for A38, and blue for the 2'-hydroxyl. The following  $pK_a$  values were used: 9 for G8, 6 for 2,6-diaminopurine, 5 for A38, and 13 for the substrate 2'-hydroxyl. For clarity,  $k_{max}$  was arbitrarily set to  $0.5 \text{ min}^{-1}$  in all cases. Simulations were generated as described in Section 2.2.1.



In light of the available data, a mechanism has been proposed in which protonated N1 of G8 acts like an “oxy-anion hole” in donating a hydrogen bond to stabilize negative charge build up on the 2'-oxygen as it is activated for nucleophilic attack by deprotonation (Figure 5.4A).<sup>158, 324</sup> In this proposed mechanism, N1 of G8 must be protonated for activity; therefore, in simulating the effects of G8 mutation on the pH-rate profile (Figure 5.4A), an acidic titration must be assigned to G8. In this analysis, I have also assumed that A38 must be protonated for activity, which dictates that the lower  $pK_a$  titration is also acidic as it reflects inhibition of activity caused by deprotonation of A38. Clearly, in order to maintain the experimentally observed pH-rate profile shape, a third titration (for a general or specific base) must be introduced.

The issue of base catalysis within the current mechanistic model remains very much unresolved. For the purposes of this discussion, I have invoked a basic titration with a  $pK_a$  of 13.5 that reflects specific base catalyzed 2'-hydroxyl deprotonation (Figure 5.4A). This model reproduces the experimental pH-rate profile, and is reasonable because no other ribozyme-based general base candidate is obvious in the crystal structure. The results of a recent computational study suggest another possible general base catalysis mechanism in which the scissile 2'-hydroxyl proton is transferred to a nonbridging scissile phosphate oxygen.<sup>331</sup> However, the fact that nonbridging phosphorothioate substitution of the scissile phosphate has little effect on hairpin activity appears to be inconsistent with this hypothesis.<sup>229</sup> It is also unclear to me how this hypothesis could be reconciled with the pH-rate data, given the very low  $pK_a$  ( $\sim 1$ )<sup>12</sup> for a nonbridging oxygen.

As pointed out by Bevilacqua,<sup>23</sup> the principle of kinetic ambiguity dictates that the pH-rate profile and  $pK_a$ -perturbation data can be equally well explained by a simple general acid/base catalysis model (Figure 5.4B). That is, because the  $k_{max}$  value cannot be predicted *a priori* for mutant ribozymes containing G8 isosteres, none of the data presented to date can distinguish between the kinetically equivalent models in Figures 5.4A & B. In Bevilacqua's model, the single acidic titration can be assigned to A38 deprotonation (as was done in Figure 5.4A), while the assignment of the higher  $pK_a$  titration is changed to a basic titration, which reflects the fact that G8 must be deprotonated in order to act as a general base catalyst.<sup>23</sup>

In light of my findings that suggest general base catalysis by N1-deprotonated G12 in the hammerhead ribozyme, which occupies a conspicuously similar structural position to G8 in the hairpin ribozyme, Bevilacqua's model<sup>23</sup> for hairpin catalysis seems especially attractive. To provide a direct comparison of the functional properties of hammerhead G12 and hairpin G8, I have applied the 2'-bromoacetamide affinity labeling experiment to the hairpin ribozyme. Not surprisingly, my data clearly confirm that N1 of G8 is positioned proximal to the scissile 2'-hydroxyl, in direct analogy to the results for G12 in the hammerhead ribozyme. However, in contrast to the data for alkylation of the hammerhead G12 residue, G8 alkylation in the hairpin ribozyme shows very little pH dependence. The implications for ribozyme mechanism are discussed in light of this difference.

## 5.2 MATERIALS AND METHODS

### 5.2.1 Chemicals and Biochemicals

All chemicals and buffers were from Sigma-Aldrich (molecular biology or reagent grade purity) and were used as received. DNA oligonucleotides were synthesized by the NAPS unit at UBC; RNA oligonucleotides were synthesized by Dharmacon and Trilink Biotech. The T7 Mega Short Script kit (Ambion) was used for *in vitro* transcription of ribozyme RNA. Reverse transcription reactions were carried out using the SuperScript II kit (Invitrogen). The  $\alpha$ - and  $\gamma$ - $^{32}\text{P}$ -ATP were purchased from Perkin-Elmer, polynucleotide kinase from New England Biolabs, and RNase T1 and RNase I from Fermentas.

### 5.2.2 Oligonucleotide Preparation

Body labeled hairpin ribozymes were prepared by run-off transcription<sup>289</sup> from synthetic DNA templates in the presence of  $\alpha$ - $^{32}\text{P}$ -ATP. The DNA transcription template encoded the wild type “EH4” ribozyme sequence:<sup>315</sup> 5'-pppGGGAAUAGAGAAGCG AACCAGAGAAACACACGACGUAAGUCGUGGUACAUAUACCUUGGUA (mutations to this sequence are described in the text). Ribozyme mutants containing only canonical nucleotides were also synthesized by run-off transcription from appropriately modified DNA templates. All ribozyme transcripts were purified by 10% denaturing PAGE, eluted with 1%  $\text{LiClO}_4$ /10 mM Tris-HCl (pH 8) for 30 minutes at 65 °C, concentrated by butanol extraction, precipitated with ethanol, resuspended in  $\text{H}_2\text{O}$ , and desalted on a G-25 spin column prior to use.

The mutant ribozyme in which 2'-deoxy-7-deaza-guanosine replaces the natural G8 residue was prepared by ligation of a short oligonucleotide containing the synthetic modification to a truncated, 5'-phosphorylated ribozyme transcript that comprised the remainder of the ribozyme sequence. The two RNAs to be joined were annealed to a splint DNA and treated with T4 DNA ligase at 16 °C overnight.<sup>332</sup> The resulting full-length hairpin RNA was then d-PAGE purified as above for the other ribozyme sequences, and 5'-<sup>32</sup>P labeled using T4 polynucleotide kinase and  $\gamma$ -<sup>32</sup>P-ATP.

The 2'-amino substrate analogue was synthesized by automated solid phase synthesis, purified by 20% d-PAGE, and eluted and desalted as described above for ribozyme sequences. The 2'-amino substrate analogue sequence was: 5'-UCGC-**Z**-GUCCUAUUU where **Z** is 2'-deoxy-2'-amino-cytidine. The affinity label was prepared by bromoacetylating this substrate analogue, as described in Section 2.2.3.

### 5.2.3 Ribozyme Affinity Labeling Reactions

Alkylation reactions were performed with 5'-<sup>32</sup>P-labeled ribozyme and unlabeled affinity label oligonucleotide in 50 mM sodium borate (for pH 8, 8.5, and 9) or sodium cacodylate (for pH 7.5) buffer with 50 mM MgCl<sub>2</sub>. Reactions were conducted in the dark at room temperature (21-22 °C). The ribozyme concentration was 5  $\mu$ M and the concentration of substrate analogue was 5.5  $\mu$ M. Reactions aliquots were quenched by mixing with two volumes of 90% formamide/50 mM EDTA/0.01% xylene cyanol/0.01% bromophenol blue. Reaction products were resolved by 10% d-PAGE and quantified by phosphorimager (Imagequant v5.2).

#### **5.2.4 Reverse Transcription Footprinting of the Alkylation Site**

Alkylated wildtype and G8A mutant hammerhead ribozyme were excised from the gel, eluted, and desalted as described above for ribozymes. A trace (< 1 pmol) of 5'-<sup>32</sup>P-labeled RT primer (5'-<sup>32</sup>P-GTCGTGTGTTTCTC) was then annealed to alkylated ribozyme template (~5 pmol, d-PAGE purified). Following the manufacturer's instructions, primer and template were combined in Superscript II buffer, heated to 65 °C for 2 minutes, and then cooled on ice briefly. The following components were then added to the reaction mixture: dATP, dCTP, dGTP, dTTP (each to 250 μM), DTT (to 10 mM), 200 units Superscript III reverse transcriptase, and 1 unit RNase inhibitor.

For dideoxy sequencing reactions unmodified ribozyme (10 pmol) was used as template RNA. The dideoxy nucleotide triphosphates (ddATP, ddCTP, ddGTP, or ddTTP) were added separately to each of four reactions to a concentration of 750 μM; in each case, the corresponding nucleotide triphosphate concentration was also lowered to 125 μM (the other three nucleotide triphosphates were maintained at 250 μM).

All reactions were incubated at 53 °C for 30 minutes, and were then terminated by adding two volumes of 90% formamide/50 mM EDTA/0.01% xylene cyanol/0.01% bromophenol blue. Prior to analysis by high resolution 10% d-PAGE, the samples were heated to 95 °C for 10 minutes and placed on ice to denature the RNA:DNA hetero-duplex that results from reverse transcription,

#### **5.2.5 Alkaline Footprinting of the Alkylation Site**

Prior to bromoacetylation, the 2'-amino substrate analogue was 5'-phosphorylated using unlabeled ATP and T4 polynucleotide kinase. The sample was extracted twice

with phenol/chloroform, precipitated with ethanol, and desalted on a G-25 spin column. Following transcription, the ribozyme was 5'-dephosphorylated by treatment with shrimp alkaline phosphatase; the reaction was terminated by heat inactivation of the enzyme (65° for 10 minutes), after which the sample was extracted twice with phenol/chloroform, precipitated with ethanol, and desalted by G-25 spin column. The ribozyme was reacted with the 5'-phosphorylated, bromoacetylated substrate analogue as described above (at pH 8 for ~48 hours), on larger scale (1-2 nmol ribozyme). The reactions were terminated by the addition of EDTA to 50 mM; the samples were then concentrated by butanol extraction, and precipitated with ethanol. Unlabeled, alkylated hairpin ribozyme was purified by 10% denaturing PAGE, visualized by UV shadowing, eluted, and desalted as described for the ribozyme transcripts. The alkylated ribozyme was then radiolabeled using  $\gamma$ -<sup>32</sup>P-ATP and T4 polynucleotide kinase, and repurified by 10% d-PAGE. Only the 5'-end of the ribozyme is radiolabeled, as the 5'-end of the substrate strand was previously phosphorylated using unlabeled ATP.

Alkaline footprinting was carried out by treating the 5'-end labeled ribozyme and alkylated ribozyme samples with 0.5% K<sub>2</sub>CO<sub>3</sub> at 95 °C for 3 minutes in a volume of 20  $\mu$ L. To generate the G specific cleavage pattern, the 5'-end labeled ribozyme was combined with 5 nmol of carrier RNA (a synthetic 16-mer oligonucleotide: 5'-GCGUGCCCGUCUGUdG) in 10  $\mu$ L of 1 mM Tris-HCl (pH 7.5) and treated with 1 unit of RNase T1 at 37°C for 4 min. Reactions were terminated by adding 40  $\mu$ L of 90% formamide/50 mM EDTA/0.01% xylene cyanol/0.01% bromophenol blue. The footprinting samples were analyzed immediately on 20% d-PAGE sequencing gels run at 40 W.

### **5.2.6 Nuclease Digestion/MALDI-TOF Mass Spectrometry**

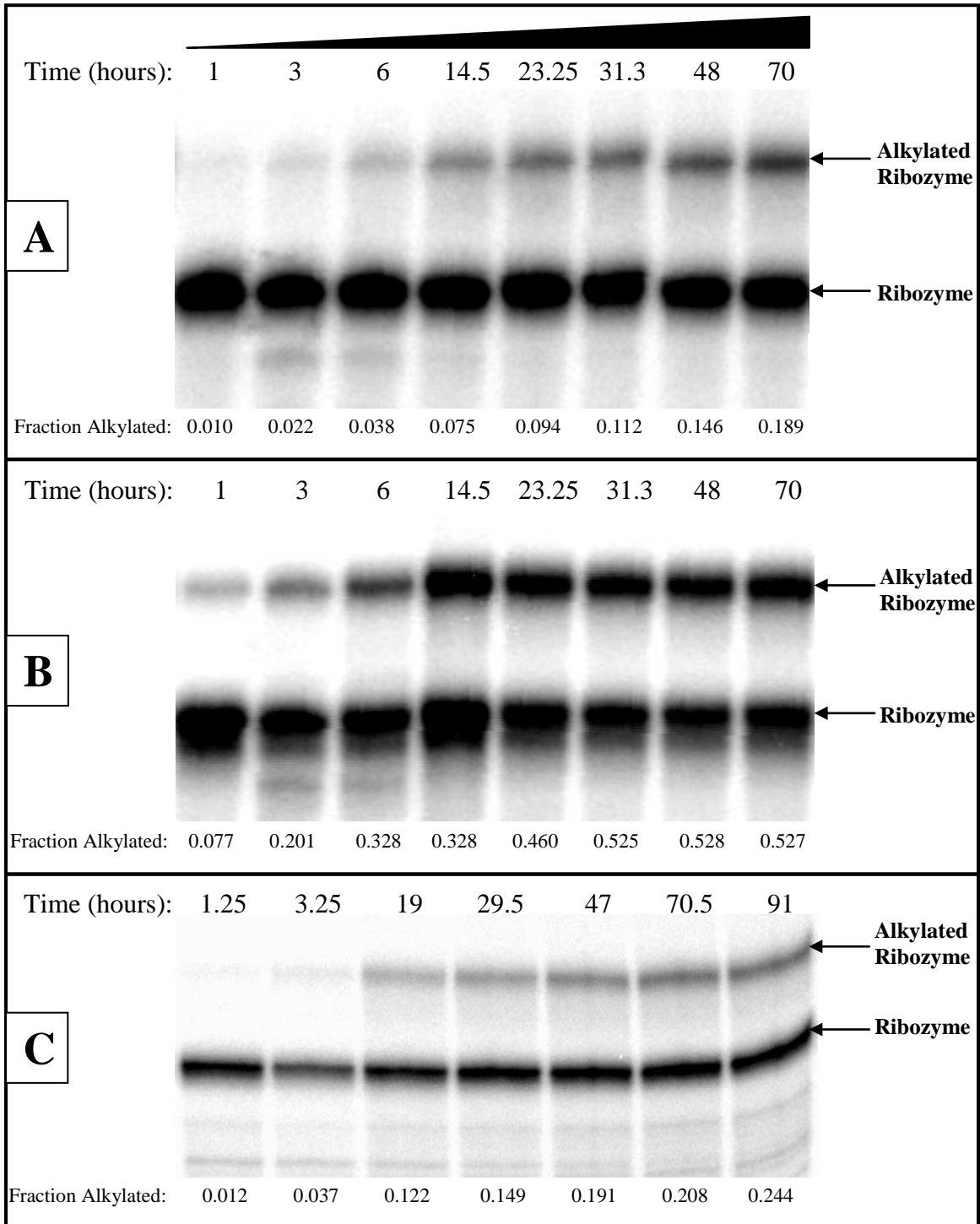
Approximately 2 nmol of alkylated hairpin ribozyme was prepared and purified as described in Section 5.2.3. Following elution from the gel, the sample was ethanol precipitated, resuspended in water, and G-25 desalted. Digestion of the alkylated ribozyme was then carried out by adding 200 units each of RNase T1 and RNase I, and incubating the mixture at 37 °C for 2 hours. The sample was then further desalted by incubating the sample at room temperature for one hour with a small portion of cation exchange beads (Bio-Rad AG50W-X8 resin, NH<sub>4</sub><sup>+</sup> form). The MALDI-TOF matrix used consisted of an 8:2 mixture of a 0.5 M solution of trihydroxyacetophenone in ethanol and a 2.4 % aqueous solution of ammonium citrate. The matrix was combined in a 1:1 ratio with the aqueous digestion sample on the MALDI-TOF target and allowed to air dry at room temperature. MALDI-TOF spectra were recorded on a Bruker Biflex II instrument in reflexive negative ion mode.

## 5.3 RESULTS

### 5.3.1 Hairpin Ribozyme Affinity Labeling

Reaction of the 2'-bromoacetamide substrate analogue with the *trans*-acting EH4 hairpin ribozyme<sup>315</sup> yielded a significant amount of a single crosslinked product of higher molecular weight than the ribozyme (Figure 5.5). As in the case of the hammerhead ribozyme, the yield of the ribozyme alkylation reaction was highest when a slight excess of substrate analogue over hairpin ribozyme was used. The rate and extent of wildtype hairpin ribozyme alkylation was significantly diminished relative to that observed for either of the two hammerhead ribozyme alkylation products under similar conditions. It should be noted that the less efficient alkylation of the hairpin ribozyme cannot be attributed to poor bromoacetylation yield in the preparation of the affinity label (the gel shift assay data in Section 2.3.1 clearly indicate a yield of ~85%). Affinity label inactivation via self-alkylation in the context of a folded structure unique to this substrate sequence is another potential explanation for poor alkylation activity. However, this possibility is ruled out by the fact that alkylation of the G8A hairpin mutant is observed to proceed at a greater rate and to a greater extent, more closely resembling the results of the hammerhead alkylation reaction.

**Figure 5.5:** Observation of higher molecular weight, crosslinked species upon reaction of 5'-<sup>32</sup>P-labeled hairpin ribozymes with the 2'-bromoacetamido affinity label. The fraction alkylated at each time point is indicated for alkylation of (A) wildtype, (B) G8A, and (C) 7-deaza-dG8 ribozymes, each in 50 mM MgCl<sub>2</sub>, 50 mM Na-cacodylate pH 7.5.



### 5.3.2 Reverse Transcription Footprinting of the Alkylation Site

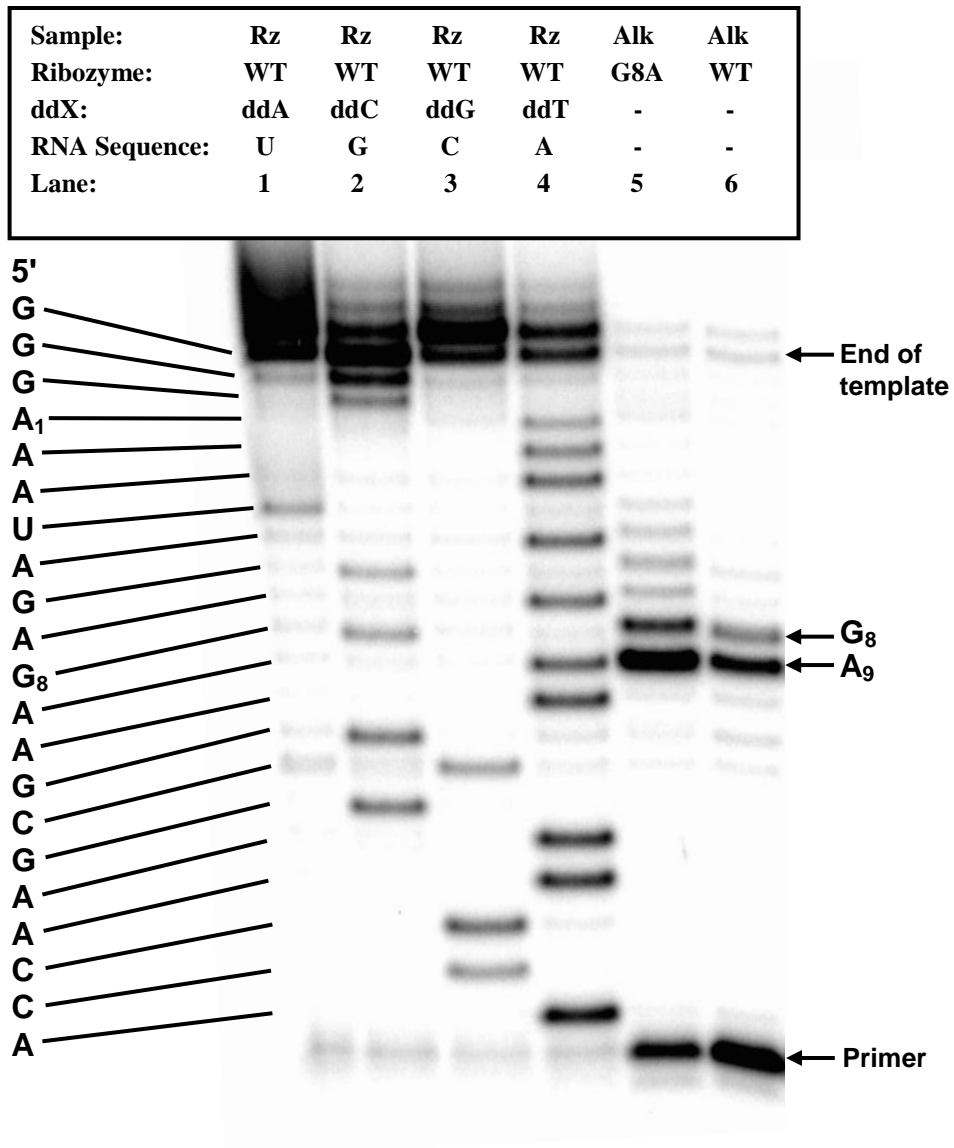
Initially, the site of hairpin ribozyme alkylation was probed using a reverse transcription (RT) footprinting assay (Figure 5.6). This technique relies on the premature termination of reverse transcription caused by chemically modified nucleotides in the RNA template. Most commonly, cDNA polymerization terminates at the template nucleotide immediately preceding the site of chemical modification; that is, the last efficiently incorporated cDNA nucleotide complements the template nucleotide immediately preceding the modified nucleotide (at its 3'-side). This termination pattern is observed for a wide variety of chemical modifications of RNA. Obviously, the modification of functional groups involved in Watson-Crick base pairing (such as alkylation of N3 of C or N1 of A by dimethyl-sulphate<sup>333, 334</sup>) very effectively disrupts the incorporation of a complementary cDNA nucleotide.<sup>335</sup> Although not directly disruptive to base pairing, purine N7 adducts (such as carboxyethylation of A<sup>333</sup> or platination of G<sup>336</sup>) lead to the same RT-termination pattern. The most comparable RNA lesions to the alkylation linkage in this work that have been probed by RT-footprinting are photo-induced interstrand crosslinks.<sup>337, 338</sup> Surprisingly, even in the case of such large oligonucleotide adduct structures, the same RT termination pattern is observed as for the aforementioned small molecule RNA modifications. The RT footprinting data for the alkylation linkage characterized here are therefore interpreted in this same way.

The 5'-<sup>32</sup>P-labeled primer used for RT-footprinting analysis of the alkylated hairpin ribozyme hybridizes to the ribozyme sequence such that the first nucleotide incorporated at the 3'-terminus of the primer (dT) is complementary A18 of the ribozyme sequence (the primer binding site is highlighted in Figure 5.1). Based on the crystal

structure, we hypothesized that alkylation was occurring at or near G8; therefore, the primer binding site was chosen such that cDNA products terminated near G8 could be readily separated by d-PAGE, with high resolution. It should be noted that this analysis cannot detect any alkylation lesions occurring in the sequence from A18 to the 3'-end of the ribozyme. Dideoxy-nucleotide terminated cDNA products served as electrophoretic mobility standards in d-PAGE analysis of cDNA resulting from footprinting experiments.

Reverse transcription of the alkylated hairpin ribozyme was most prominently terminated following incorporation of the cDNA nucleotide complementary to A9, with minor incorporation of a further nucleotide complementary to G8 in the wildtype or A8 in the G8A mutant (Figure 5.6, Lanes 5 & 6). These termination sites must be attributed to the presence of the alkylation linkage, because no natural arrest of reverse transcription was observed at these sites in the dideoxy sequencing lanes, in which unmodified hairpin ribozyme was used as the RT template. Surprisingly, very minor incorporation of several more nucleotides beyond G8, and even a small amount of cDNA polymerization to the end of the ribozyme template were observed. Clearly, A9 is the last ribozyme nucleotide for which a complementary nucleotide is efficiently incorporated by reverse transcriptase. This arrest at A9 is therefore consistent with alkylation of G8, assuming that reverse transcription is terminated by the novel alkylation linkage in the same way as for the other RNA crosslinks studied previously.

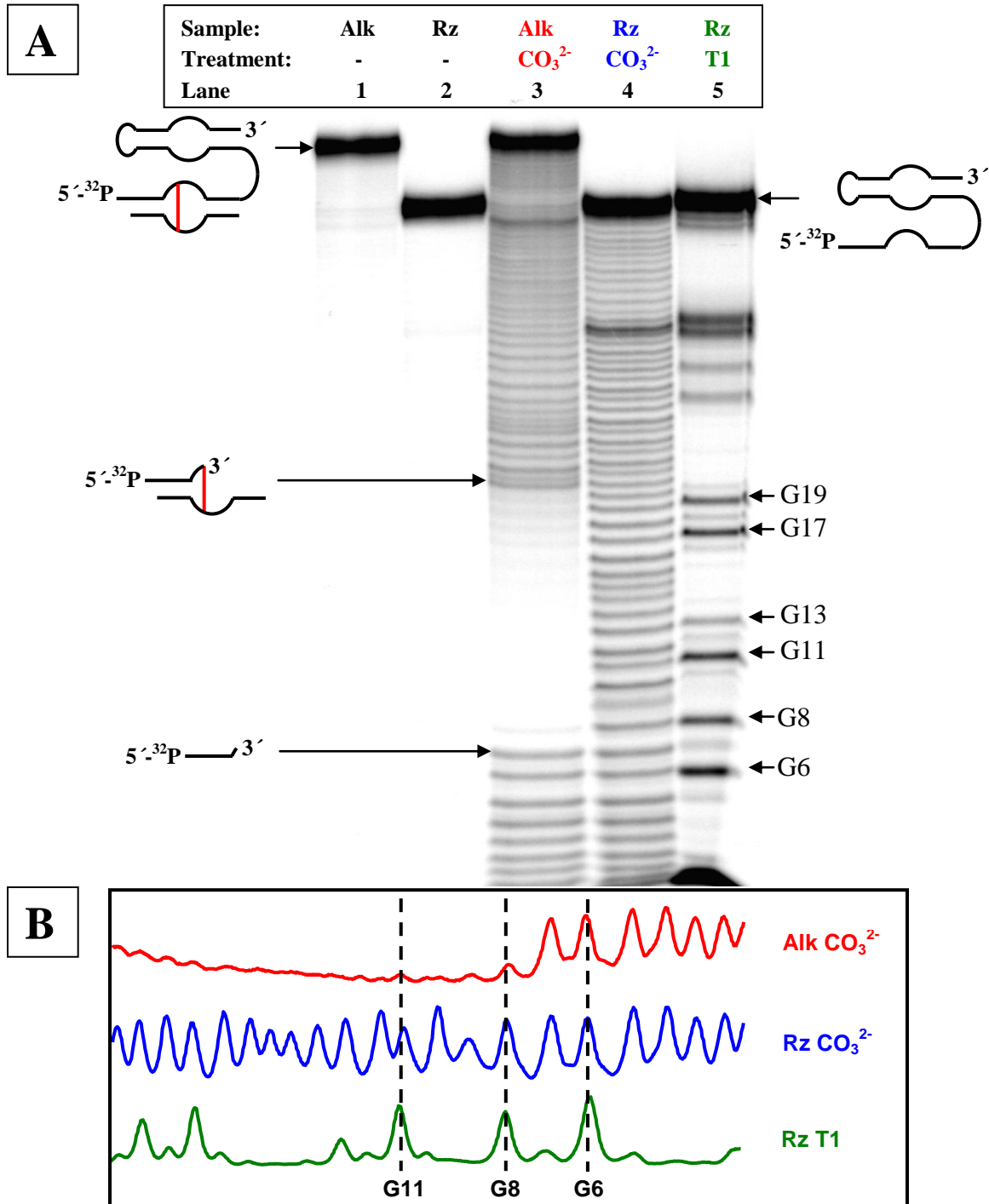
**Figure 5.6:** Reverse transcription footprinting assay (using a 5'-<sup>32</sup>P-labeled primer) to locate the alkylation linkage on the hairpin ribozyme (the primer binding site is indicated in Figure 5.1). Lanes 1-4: sequencing by dideoxy termination of (non-alkylated) hairpin ribozyme template. The dideoxy nucleotide (ddX) triphosphate included in each reaction is indicated, along with the complementary nucleotide in the RNA template sequence. Lanes 5 & 6: Reverse transcription of alkylated G8A and wildtype ribozymes respectively.



### 5.3.3 Alkaline Footprinting of the Alkylation Site

To locate the alkylation site with greater certainty, the d-PAGE purified, 5'-<sup>32</sup>P labeled alkylated ribozyme was subjected to alkaline footprinting analysis (see Figure 4.5 for explanation). The dramatic increase in molecular weight of the 5-<sup>32</sup>P-labeled cleavage fragments above A7 in the cleavage ladder for the alkylated ribozyme (Figure 5.7, Lane 3) indicates that G8 is the site of hairpin ribozyme alkylation. The abrupt disruption of the ribozyme cleavage ladder due to G8 alkylation is not as clean as that observed in footprinting the alkylated hammerhead ribozyme. The faint cleavage bands observed immediately above A7 are likely due to minor alkaline degradation of the RNA substrate strand (in the case of hammerhead alkylation, substrate strand degradation was suppressed by the use of DNA affinity labels). Also, a very small amount of alkylation linkage to A9 could be consistent with the footprinting data, although no such linkage was identified by enzymatic digestion/MALDI-TOF fragment analysis (*vide infra*).

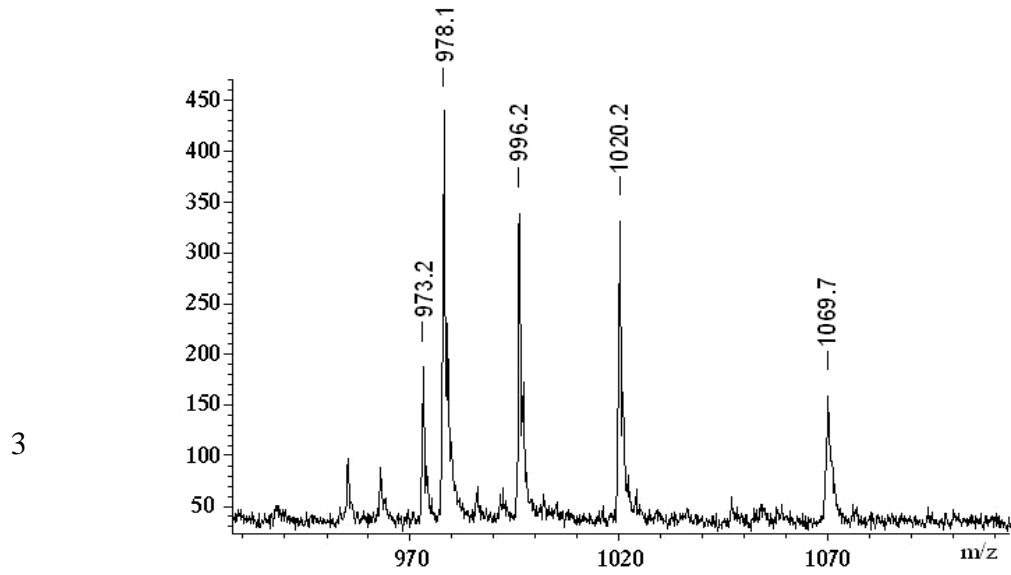
**Figure 5.7:** (A) Alkaline footprinting analysis with 5'-<sup>32</sup>P-labeled hairpin ribozyme. Lane 1: Untreated alkylated ribozyme; Lane 2: Untreated ribozyme; Lane 3: Alkylated ribozyme treated with 0.5% K<sub>2</sub>CO<sub>3</sub>; Lane 4: Ribozyme treated with 0.5% K<sub>2</sub>CO<sub>3</sub>; Lane 5: Ribozyme treated with RNase T1. (B) Quantitative analysis of autoradiography data in panel (A).



### 5.3.4 Enzymatic Digestion/MALDI-TOF Mass Spectrometric Analysis of the Alkylation Site

The alkylation of a G residue was also confirmed by MALDI-TOF mass spectrometric analysis of alkylated ribozyme fragments that were generated by non-specific nuclease digestion in the presence of RNase T1 and RNase I (Figures 5.8, Table 5.1). The digestion fragment that proves alkylation at a G residue is shown in Figure 5.9A (note that identification of this fragment does not identify *which* G in the hairpin sequence is alkylated). In both fragments that were assigned to contain the alkylation linkage, two nucleotides are necessarily derived from the substrate analogue strand because the G residue immediately to the 3'-side of the 2'-acetamide linkage cannot be removed by the nucleases (the presence of the 2'-acetamide linkage precludes 2'-transesterification, which prevents ribonuclease cleavage of the adjacent phosphodiester bond). One other digestion fragment assigned to contain the alkylation linkage was identified; this larger fragment does not indicate which nucleotide is alkylated, but the assigned sequence from the ribozyme strand is consistent with G8 alkylation (Figure 5.9B). Thus the MALDI-TOF data are in agreement with the footprinting data which indicate alkylation at G8. It should also be noted that no digestion fragments could be assigned that would indicate alkylation of any ribozyme residue other than G.

**Figure 5.8:** MALDI-TOF spectrum obtained for nuclease digested samples of alkylated hairpin ribozyme. The region of the spectrum from  $m/z = 930$  to  $1110$  is magnified in the inset.



9

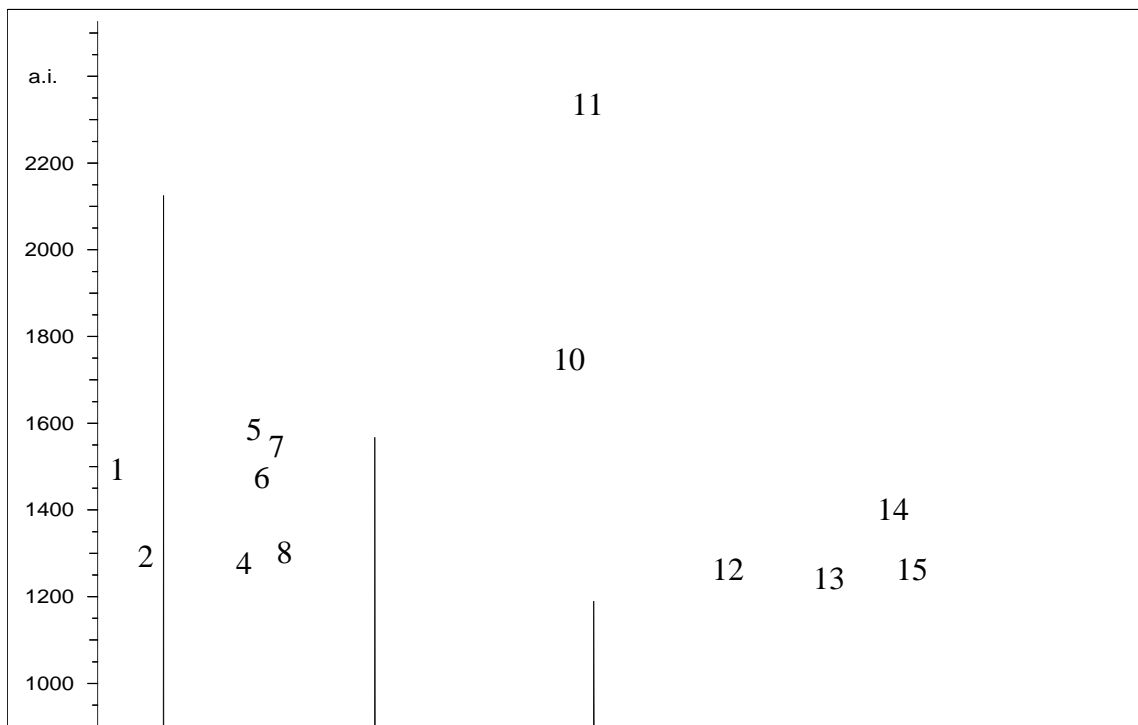


**Table 5.1:** Predicted and observed m/z values and sequence assignments for the digestion fragments observed in the MALDI-TOF spectra shown in Figure 5.8.

Peak Number	Observed m/z <sup>a</sup>	Predicted m/z <sup>a</sup>	Assignment
1	572.3	572.1	UpA <sup>b</sup>
2	667.3	667.1	CpGp
3	691.2	691.1	ApGp
4	973.2	973.1	CpUpGp
5	978.1	978.1	CpApG>p <sup>c</sup>
6	996.2	996.1	CpApGp
7	1020.2	1020.2	ApApGp
8	1067.7	1069.2	See Figure 5.9A below
9	1326.1	1326.2	UpApApGp
10	1959.5	1959.3	ApApCpCpApGp
11	1984.4	1984.3	ApApApUpApGp
12	2406.5	2406.3	UpCpCpUpApUpUpU <sup>d</sup>
13	2706.5	2706.4	See Figure 5.9B below
14	2905.0	2904.4	ApApApCpApCpApCpG>p <sup>c</sup>
15	2922.4	2922.4	ApApApCpApCpApCpGp

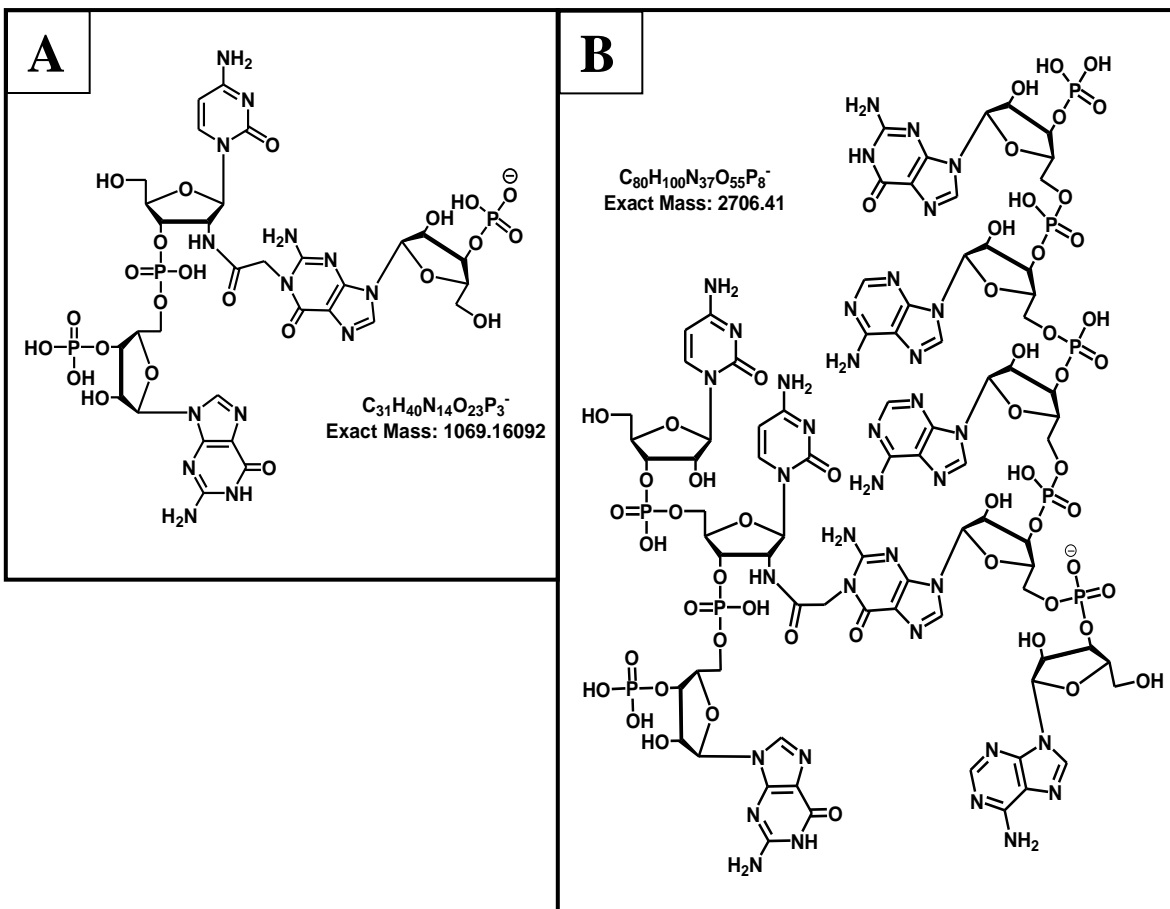
<sup>a</sup> m/z values reflect deprotonated, negatively charged molecular ions [M-H]<sup>-</sup>.

<sup>b</sup> This fragment represents the 3'-terminus of the ribozyme and therefore lacks a 3'-phosphate.

<sup>c</sup> >p denotes a 2',3'-cyclic phosphate terminated sequence.

<sup>d</sup> This fragment represents the 3'-terminus of the substrate analogue and therefore lacks a 3'-phosphate.

**Figure 5.9:** Structures assigned to the digestion fragments observed by MALDI-TOF analysis in Figure 5.8 whose  $m/z$  values are consistent with the presence of the alkylation linkage.



### 5.3.5 Properties of the Alkylation Reaction

The correlation of the properties of the hairpin alkylation and cleavage reactions was examined with regard to the effects of reaction conditions, ribozyme mutations, and a competitive inhibitor (Figure 5.10 and Table 5.2). First, prior addition of a stoichiometric quantity of unreactive 2'-amino substrate analogue was found to essentially inhibit alkylation of the ribozyme by the affinity label. This result demonstrates that the alkylation reaction depends upon normal binding to the ribozyme of

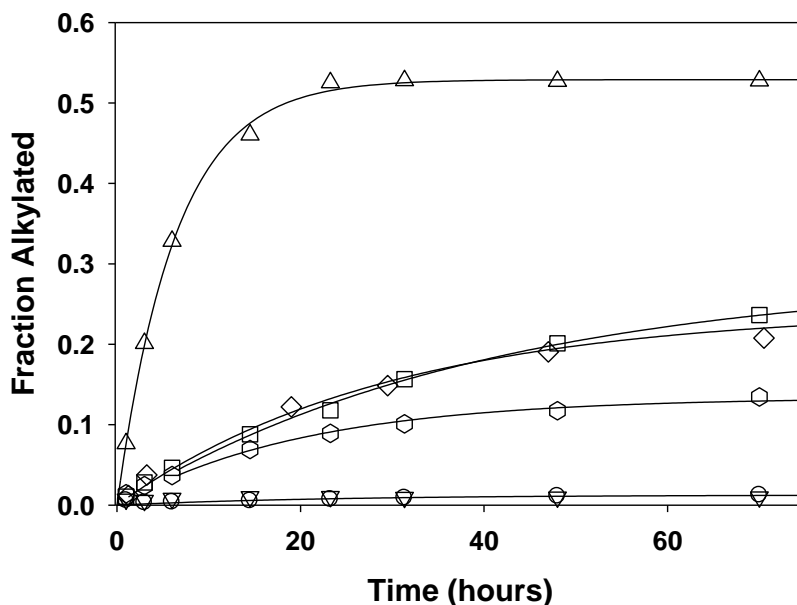
the affinity label (in place of the substrate). Like the catalytic reaction, alkylation was almost completely inhibited in low ionic strength buffer lacking  $Mg^{2+}$ , which is necessary for tertiary structure formation and catalysis. We also observed that the extent of alkylation was significantly diminished by the C25A mutation, which is known to inhibit tertiary structure formation (and catalysis) by disrupting the interdomain base pair formed between C25 and G(-1) residues of the ribozyme and substrate, respectively (see Figure 5.1).<sup>311</sup> While a lower extent of alkylation is consistent with the fact that a small proportion of C25A ribozyme forms the active (docked) conformation, this effect is not as dramatic as the reduction in the native catalytic activity.<sup>311, 324</sup> It is also perplexing that the first order and initial rate constants for C25A mutant alkylation appear to slightly exceed those of wildtype alkylation, despite the lowered endpoint. Perhaps by coincidence G8 is better positioned for alkylation, but not catalysis, in the small proportion of C25A ribozyme in which the two domains are docked. Overall, the properties of the G8 alkylation reaction appear to reflect the properties of the native cleavage reaction, for the most part. This suggests that alkylation occurs, at least primarily, when the ribozyme is folded in a catalytically competent conformation in the presence of  $Mg^{2+}$ .

Given that G8 was identified convincingly as the site of alkylation by footprinting analysis, we examined the effects of G8 mutation in an effort to assign the position of alkylation on this residue. Previous studies have established that the N7 position is generally the most reactive nucleophile of free guanosine with respect to simple alkylating agents (such as dimethyl-sulphate) under neutral conditions.<sup>220, 339, 340</sup> Of the other possible nucleophilic sites on guanosine, N3 is alkylated to a lesser extent, and N1

and the exocyclic N<sup>2</sup> are not alkylated appreciably under neutral conditions.<sup>220, 339, 340</sup> With a pK<sub>a</sub> of 9.4,<sup>237</sup> the alkylation of anionic N1 can be enhanced in alkaline solution,<sup>339</sup> or under neutral conditions when the N1 pK<sub>a</sub> is perturbed downward in the active site of a ribozyme, such as in the case of hammerhead G12 alkylation.

In light of the noted nucleophilicity of the N7 position of free guanine under neutral conditions, we first determined whether this was the site of G8 alkylation in the hairpin ribozyme. Alkylation of N7 of G8 would likely be entirely unrelated to general base catalysis because: 1) a 7-deaza-deoxyguanosine substitution has only a minor effect on catalysis,<sup>324</sup> and 2) the N7 position of G8 is not in close proximity to the scissile 2'-hydroxyl in the crystal structure, and is thus unlikely to participate directly in catalysis.<sup>319</sup> In order to determine whether N7 of G8 had been alkylated, an active mutant ribozyme was synthesized where 2'-deoxy-7-deaza-guanosine replaced G8 (referred to as “dG8c<sup>7</sup>”). This mutant showed very similar alkylation activity to the wildtype ribozyme (Figure 5.10), which demonstrates convincingly that N7 of G8 is not alkylated in the wildtype ribozyme. Note also that the 2'-deoxy substitution in this mutant is also inconsequential for alkylation, which rules out the unlikely possibility that the 2'-oxygen of G8 is alkylated.

**Figure 5.10:** Kinetic plots of hairpin ribozyme alkylation under various conditions and for ribozyme mutants. Unless otherwise stated, reactions were in 50 mM Na-Cacodylate pH 7.5, 50 mM MgCl<sub>2</sub>, for wildtype (◇), dG8c<sup>7</sup> (□), G8A (△), C25A (○), Wiltype in the presence of unreactive 2'-NH<sub>2</sub> substrate analogue (▽), and Wildtype in the absence of Mg<sup>2+</sup> (○).



Alkylation of a G8A ribozyme mutant was also examined (Figure 5.10) to further refine the assignment of the alkylation site. The G8A mutation is detrimental to catalytic activity,<sup>324</sup> but led to much enhanced alkylation activity relative to the wild type ribozymes, under the same conditions. This contrast appears to reflect the differing N1 protonation states of free adenosine and guanosine; the N1 position of free adenosine is fully deprotonated ( $pK_a$  of the conjugate acid of N1 is 3.5<sup>125</sup>) and is readily alkylated in neutral solution<sup>340, 341</sup>, whereas N1 of free guanosine is largely protonated (with an N1  $pK_a$  9.4<sup>125</sup>) and is therefore much less nucleophilic. Aside from N7, which is ruled out above, alkylation of N3 of either A8 or G8 is also plausible, as these positions are fully

deprotonated at neutral pH in both cases. However, N3 alkylation is inconsistent with the marked enhancement of alkylation for the G8A mutant.<sup>220</sup> Also, from a structural perspective, the crystallographic data of the hairpin ribozyme suggest that N1 is the site alkylation and not N3 (See Figures 5.2 and 5.3).<sup>319</sup> Finally, I note that the increase in hairpin alkylation rate in the G8A mutant is very similar to difference in alkylation rate of N1-protonated G12 (at pH <7) and N1-deprotonated A12 in the hammerhead ribozyme (G to A mutation increases the alkylation rate by slightly greater than one order of magnitude in both cases). Overall there is an abundant reason to assign the site of hairpin alkylation to N1 of G8.

The pH-dependence of the rate constant and the extent of reaction for G8 alkylation were also examined for signs of N1 titration (Figure 5.11 and Table 5.2). Hairpin alkylation activity, as gauged by any of first order rate constants, initial rates, or maximal extent of alkylation, increased only slightly with increasing pH from 7.5 to 9. These results clearly contrast with the log-linear increase (slope ~1) observed for hammerhead G12 alkylation over the same pH range (see Section 5.4 for discussion).

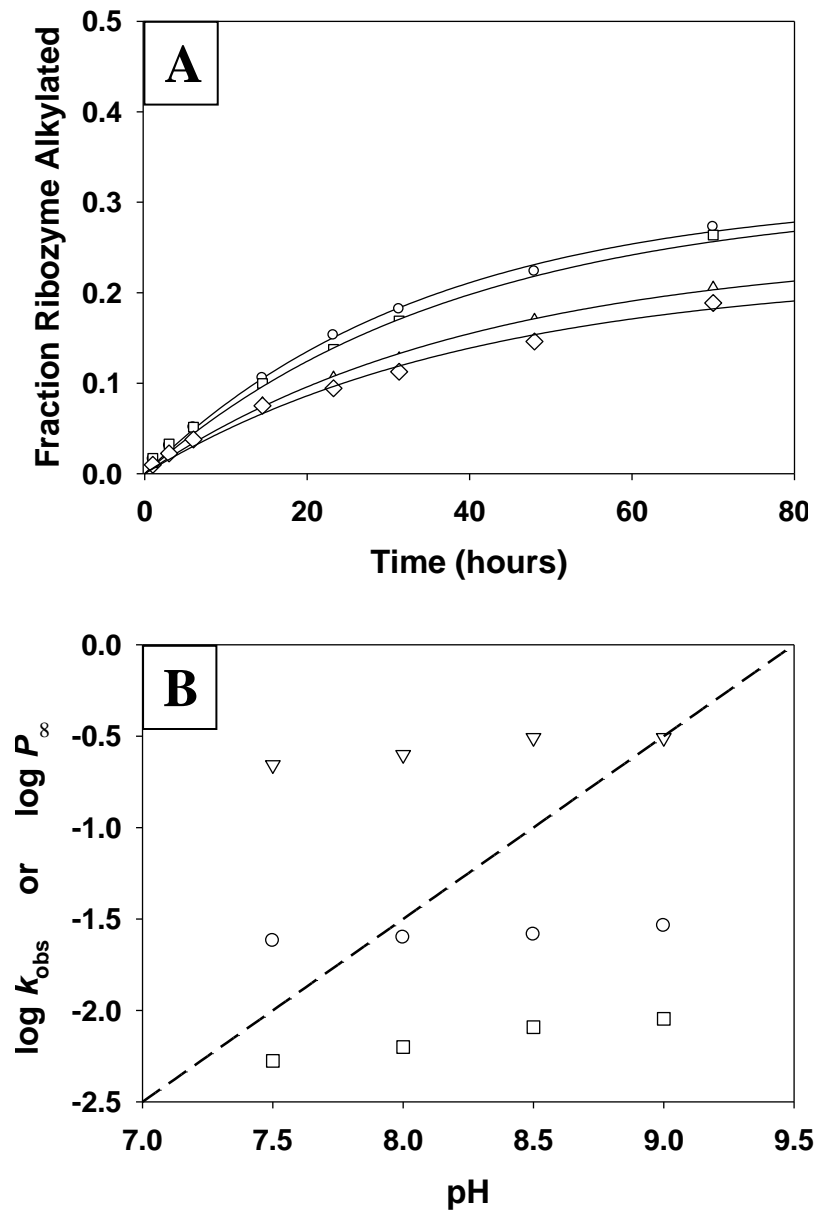
**Table 5.2:** Rate constants and extents of reaction for the hairpin ribozyme affinity labeling in 50 mM Na-Cacodylate pH 7.5, 50 mM MgCl<sub>2</sub>.

<b>Ribozyme/ Conditions</b>	<b>1<sup>st</sup> Order Rate Constant <sup>a</sup> (hr<sup>-1</sup>)</b>	<b>Maximum Fraction Alkylated (<math>P_{\infty}</math>)</b>	<b>Initial Rate Constant (hr<sup>-1</sup>) <sup>b</sup></b>
Wildtype:			
pH 7.5	0.024	0.22	0.0053
pH 8.0	0.025	0.25	0.0063
pH 8.5	0.026	0.31	0.0081
pH 9.0	0.029	0.31	0.0090
G8A pH 7.5	0.16	0.53	0.085
dG8c <sup>7</sup> pH 7.5	0.034	0.24	0.0082
C25A pH 7.5	0.049	0.13	0.0064

<sup>a</sup> 1<sup>st</sup> order rate constants,  $k_{\text{obs}}$ , determined by fitting the data in Figures 5.10 and 5.11 to  $P = P_{\infty}(1 - e^{-k_{\text{obs}}t})$ .

<sup>b</sup> Initial rate constants estimated using the fitted first order rate constants ( $k_{\text{obs}}$ ) and endpoints ( $P_{\infty}$ ) using  $dP/dt = P_{\infty}k_{\text{obs}}e^{-k_{\text{obs}}t} = k_{\text{initial}}$ , where  $t$  was set to zero, such that  $P = k_{\text{initial}}t$ , where  $k_{\text{initial}}$  would be the slope of a plot at early time points of product formed (note that  $P$  is expressed of a fraction of reactant converted to product).

**Figure 5.11:** (A) Plots of the progress of wildtype hairpin ribozyme alkylation in 50 mM  $\text{MgCl}_2$  and 50 mM buffer at pH 7.5 ( $\diamond$ ), pH 8.0 ( $\triangle$ ), pH 8.5 ( $\square$ ), and pH 9.0 ( $\circ$ ). (B) Logarithmic plot of the pH-dependence of the reaction endpoint ( $P_\infty$ ) ( $\triangle$ ), the first order alkylation rate constant determined by fitting the data in Panel A ( $\circ$ ), and the initial rate constant ( $\square$ ), estimated as described in the Table 5.1 footnotes. For comparison, a log-linear plot with slope of 1 is included (dashed line).



## 5.4 DISCUSSION AND CONCLUSIONS

The hairpin ribozyme affinity labeling reaction proceeds under the same conditions that support the normal hairpin ribozyme cleavage reaction. Like the cleavage reaction, alkylation is diminished when affinity label binding is inhibited by competition with a non-reactive substrate analogue, or when ribozyme tertiary structure formation is inhibited 1) in low ionic strength buffer that lacks  $Mg^{2+}$ , or 2) by the C25A mutation. Therefore, as concluded for alkylation of the hammerhead G12 residue, the hairpin alkylation reaction appears to proceed in the context of a catalytically active conformation.

Unlike the hammerhead ribozyme, only one alkylation product could be detected in the hairpin-substrate complex. G8 appears to be the sole hairpin ribozyme alkylation site, based on the results reverse transcription and alkaline footprinting analyses, as well as MALDI analysis of the ribonuclease digestion fragments of the alkylated ribozyme. The increased alkylation activity for the G8A mutant, as well as the indifference of alkylation activity toward N7-deaza-dG8 substitution implicate N1 of G8 as the alkylation site. Therefore, my results confirm that, in solution, N1 of G8 is in close proximity to the scissile 2'-hydroxyl, as observed in the crystal structures.<sup>238, 239, 318, 319</sup> These results, along with the biochemical data,<sup>23, 324-326, 330</sup> leave little doubt that N1 of G8 is an active participant in hairpin catalysis.

With regard to mechanistic implications, the most salient results reported here concern the lack of a strong pH-dependence for the hairpin alkylation reaction. This finding clearly contrasts with the log-linear increase in the rate of hammerhead G12 alkylation with increasing pH. Evidently, hairpin G8 alkylation is dominated by a pH-

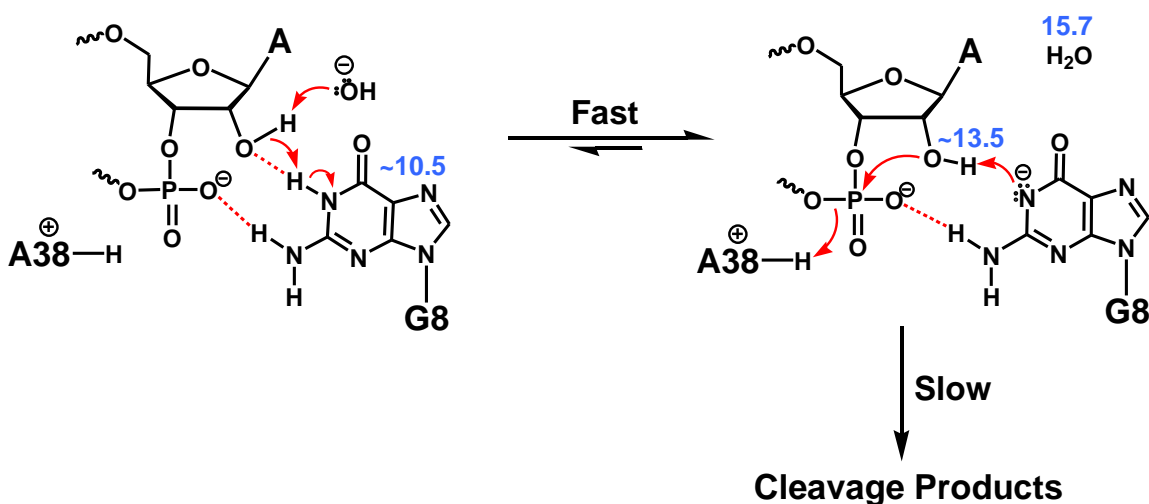
independent electrophilic aromatic substitution-like mechanism, as proposed to dominate below pH ~7 for hammerhead G12 alkylation. It is therefore clear that G8 exists in its N1 deprotonated form to just a very small extent, even up to pH 9, whereas the hammerhead G12 appears to become nearly fully deprotonated by pH 8.5. Given that the log-linear increase in hammerhead alkylation persisted for ~1.5 pH units below the estimated G12  $pK_a$ , it follows that the  $pK_a$  of G8 must be >10, if a similar titration is to be expected as G8 becomes deprotonated. Clearly the  $pK_a$  of the hairpin G8 is much higher than that of the hammerhead G12, at least in the context of the alkylation reaction. Note that it is certainly possible that the presence of the bromoacetamide probe could disrupt the hairpin active site structure in particular, so as to alter the  $pK_a$ 's of active site residues relative to those expressed in the context of catalysis.

Overall, my data strongly suggest that the higher  $pK_a$  (>9) titration in the catalytic pH-rate profile should be attributed to G8 deprotonation, a suggestion which has subsequently been confirmed by the 8-aza-G8 titration studies of Fedor and coworkers (*vide supra*).<sup>330</sup> Neither of these results, however, clarify whether G8 deprotonation activates catalysis (as in Figure 5.4B where G8 acts as general base) or deactivates catalysis (as in Figure 5.4A where G8 donates a hydrogen bond to the scissile 2'-oxygen). At the very least, the contrast between hammerhead and hairpin alkylation pH-rate profiles suggests that G12 in the hammerhead would seem to be much better adapted (in terms of N1  $pK_a$ ) for general base catalysis than G8 in the hairpin. In other words, it would seem surprising that, with such a high  $pK_a$ , G8 could function efficiently as a general base (with a  $pK_a$  >10, less than 0.01% of G8 would exist in the active, N1 deprotonated form at neutral pH);<sup>330</sup> however, Bevilacqua has cautioned that surprisingly

efficient catalysis is possible, even when the  $pK_a$ 's of catalytic residues would seem far from ideal.<sup>23</sup>

Considering the simulations shown in Figure 5.4, it appears that the pH-rate profile for hairpin catalysis must include a titration attributable to a specific or general base; whether this titration is attributable to G8 or another species is the point of contention. My data certainly help to correlate the high  $pK_a$  titration in the hairpin catalytic pH-rate profile with G8 deprotonation, but the role of G8 still cannot be definitively assigned. Indeed, the distinction between the two limiting cases for the catalytic role of G8 general base may be moot: it is possible that the two protonation states for G8 could rapidly equilibrate with the aid of a specific or general base catalyst prior to rate limiting nucleophilic attack of the 2'-oxygen on the scissile phosphate (Figure 5.12). If this were the case, considering the  $pK_a$  values for water, the 2'-OH, and the N1 of G8, the N1-deprotonated state for G8 should be thermodynamically favoured (Figure 5.12, at right). Therefore, despite its considerably higher  $pK_a$  and its different alkylation pH-rate profile, the hairpin G8 may indeed function as a general base in its anionic form to deprotonate the scissile 2'-OH, much like the hammerhead G12.

**Figure 5.12:** The two limiting cases proposed in the literature<sup>23, 158, 324</sup> for the role hairpin G8 (see Figure 5.4A & B) could be rapidly interconverting with the aid of a specific or general base prior to nucleophilic attack by the 2'-oxygen. The  $pK_a$ 's for the protonation sites of interest are indicated in blue text. The protonation state depicted at right is thermodynamically favoured.



Future studies should apply the 2'-bromoacetamide affinity label to other small nucleolytic ribozymes, as well as to RNA cleaving DNAzymes. The *GlmS* ribozyme is of particular interest in this regard, as recent biochemical<sup>342</sup> and crystal structure<sup>343, 344</sup> data suggest that the N1 position of an active site guanine residue is positioned near the scissile 2'-hydroxyl, as in the hammerhead and hairpin ribozymes. As in the case of the hairpin ribozyme, it is unclear whether this guanine acts directly as a general base, or whether it provides transition state stabilization in its N1-protonated form. Also, although no crystal structure yet exists, biophysical evidence has been presented that again implicates a particular active site guanine N1 position in general acid or base chemistry in the VS ribozyme.<sup>345</sup> Overall, the participation of guanine in 2'-hydroxyl activation appears to be emerging as a recurring theme in natural ribozyme mechanisms,

and 2'-bromoacetamide affinity labeling should be useful in characterizing this phenomenon further.

## REFERENCES

1. In some cases, such as in RNA-containing viruses and viroids, genetic information is stored in the form of RNA.
2. Dennis, E. A.; Westheimer, F. H., The Geometry of the Transition State in the Hydrolysis of Phosphate Esters. *Journal of the American Chemical Society* **1966**, *88*, 3431-3432.
3. Westheimer, F. H., Pseudo-rotation in the Hydrolysis of Phosphate Esters. *Accounts of Chemical Research* **1968**, *1*, 70-78.
4. Li, Y. F.; Breaker, R. R., Kinetics of RNA Degradation by Specific Base Catalysis of Transesterification Involving the 2'-Hydroxyl Group. *Journal of the American Chemical Society* **1999**, *121*, 5364-5372.
5. Radzicka, A.; Wolfenden, R., A Proficient Enzyme. *Science* **1995**, *267*, 90-93.
6. Gerlt, J. A.; Westheimer, F. H.; Sturtevant, J. M., Enthalpies of Hydrolysis of Acyclic, Monocyclic, and Glycoside Cyclic Phosphate Diesters. *Journal of Biological Chemistry* **1975**, *250*, 5059-5067.
7. Nesbitt, S. M.; Erlacher, H. A.; Fedor, M. J., The Internal Equilibrium of the Hairpin Ribozyme: Temperature, Ion, and pH Effects. *Journal of Molecular Biology* **1999**, *286*, 1009-1024.
8. Taira, K.; Fanni, T.; Gorenstein, D. G., Stereoelectronic Effects in the Hydrolysis of Methyl Ethylene Phosphate. *Journal of the American Chemical Society* **1984**, *106*, 1521-1523.
9. Oivanen, M.; Schnell, R.; Pfeleiderer, W.; Lonnberg, H., Interconversion and Hydrolysis of Monomethyl and Monoisopropyl Esters of Adenosine 2'-Monophosphates and 3'-Monophosphates - Kinetics and Mechanisms. *Journal of Organic Chemistry* **1991**, *56*, 3623-3628.
10. Jarvinen, P.; Oivanen, M.; Lonnberg, H., Interconversion and Phosphoester Hydrolysis of 2',5'-Dinucleoside and 3',5'-Dinucleoside Monophosphates - Kinetics and Mechanisms. *Journal of Organic Chemistry* **1991**, *56*, 5396-5401.
11. Note that the specific acid/base catalyzed pH-rate profile is constructed using rate constants that are obtained by extrapolation to zero buffer concentration.
12. Emilsson, G. M.; Nakamura, S.; Roth, A.; Breaker, R. R., Ribozyme Speed Limits. *RNA* **2003**, *9*, 907-918.
13. Oivanen, M.; Kuusela, S.; Lonnberg, H., Kinetics and Mechanisms for the Cleavage and Isomerization of the Phosphodiester Bonds of RNA by Bronsted Acids and Bases. *Chemical Reviews* **1998**, *98*, 961-990.
14. Harris, D. C., *Quantitative Chemical Analysis*. Freeman and Co.: New York, 1995.
15. Lonnberg, H.; Stromberg, R.; Williams, A., Compelling Evidence for a Stepwise Mechanism of the Alkaline Cyclisation of Uridine 3'-Phosphate Esters. *Organic & Biomolecular Chemistry* **2004**, *2*, 2165-2167.
16. Breslow, R., How Do Imidazole Groups Catalyze the Cleavage of RNA in Enzyme Models and in Enzymes - Evidence from Negative Catalysis. *Accounts of Chemical Research* **1991**, *24*, 317-324.

17. Breslow, R.; Labelle, M., Sequential General Base Acid Catalysis in the Hydrolysis of RNA by Imidazole. *Journal of the American Chemical Society* **1986**, 108, 2655-2659.
18. Menger, F. M., The Negative Rate Constants of Breslow and Huang. *Journal of Organic Chemistry* **1991**, 56, 6251-6252.
19. Perrin, C. L., On the Mechanism of Buffer-Catalyzed Hydrolysis of RNA Models. *Journal of Organic Chemistry* **1995**, 60, 239-1243.
20. Haim, A., Imidazole Buffer-Catalyzed Cleavage and Isomerization-Reactions of Dinucleotides - The Proposed Mechanism is Incompatible with the Kinetic Measurements. *Journal of the American Chemical Society* **1992**, 114, 8384-8388.
21. Kirby, A. J.; Marriott, R. E., Mechanism Of RNA Cleavage by Imidazole - Catalysis vs. Medium Effects. *Journal of the American Chemical Society* **1995**, 117, 833-834.
22. Breslow, R.; Dong, S. D.; Webb, Y.; Xu, R., Further Studies on the Buffer-catalyzed Cleavage and Isomerization of Uridyluridine. Medium and Ionic Strength Effects on Catalysis by Morpholine, Imidazole, and Acetate Buffers Help Clarify the Mechanisms Involved and their Relationship to the Mechanism used by the Enzyme Ribonuclease and by a Ribonuclease Mimic. *Journal of the American Chemical Society* **1996**, 118, 6588-6600.
23. Bevilacqua, P. C., Mechanistic Considerations for General Acid/Base Catalysis by RNA: Revisiting the Mechanism of the Hairpin Ribozyme. *Biochemistry* **2003**, 42, 2259-2265.
24. Eichhorn, G. L.; Tarien, E.; Butzow, J. J., Interaction of Metal Ions with Nucleic Acids and Related Compounds 16: Specific Cleavage Effects in Depolymerization of Ribonucleic Acids by Zinc(II) Ions. *Biochemistry* **1971**, 10, 2014-2018.
25. Breslow, R.; Huang, D. L., Effects of Metal-Ions, Including  $Mg^{2+}$  and Lanthanides, on the Cleavage of Ribonucleotides and RNA Model Compounds. *Proceedings of the National Academy of Sciences* **1991**, 88, 4080-4083.
26. Kuusela, S.; Lonnberg, H., Metal-Ion-Promoted Hydrolysis of Polyuridylic Acid. *Journal of the Chemical Society-Perkin Transactions 2* **1994**, 2301-2306.
27. Ikenaga, H.; Inoue, Y., Metal Ion Catalyzed Transphosphorylation of 4 Homodinucleotides and 5 Pairs of Dinucleotide Sequence Isomers. *Biochemistry* **1974**, 13, 577-582.
28. Thomson, J. B.; Patel, B. K.; Jimenez, V.; Eckart, K.; Eckstein, F., Synthesis and Properties of Di-uridine Phosphate Analogues Containing Thio and Amino Modifications. *Journal of Organic Chemistry* **1996**, 61, 6273-6281.
29. Kuimelis, R. G.; McLaughlin, L. W., Mechanisms of Ribozyme-mediated RNA Cleavage. *Chemical Reviews* **1998**, 98, 1027-1044.
30. Steitz, T. A.; Steitz, J. A., A General Two Metal Ion Mechanism for Catalytic RNA. *Proceedings of the National Academy of Sciences* **1993**, 90, 6498-6502.
31. Raines, R. T., Ribonuclease A. *Chemical Reviews* **1998**, 98, 1045-1065.
32. An enzyme is defined as catalytically perfect in cases where the rate of the catalytic step equals or exceeds that of diffusion controlled substrate association. In such cases, theoretically, every substrate binding event leads to products, rather than dissociation of the Michaelis complex.
33. Bugg, T., *An Introduction to Enzyme and Coenzyme Chemistry*. Blackwell Science Ltd.: Oxford, U.K., 1997.

34. Park, C.; Raines, R. T., Quantitative Analysis of the Effect of Salt Concentration on Enzymatic Catalysis. *Journal of the American Chemical Society* **2001**, 123, 11472-11479.
35. Thompson, J. E.; Raines, R. T., Value of General Acid/Base Catalysis to Ribonuclease A. *Journal of the American Chemical Society* **1994**, 116, 5467-5468.
36. Messmore, J. M.; Fuchs, D. N.; Raines, R. T., Ribonuclease A - Revealing Structure Function Relationships with Semisynthesis. *Journal of the American Chemical Society* **1995**, 117, 8057-8060.
37. Trawick, B. N.; Daniher, A. T.; Bashkin, J. K., Inorganic Mimics of Ribonucleases and Ribozymes: From Random Cleavage to Sequence-Specific Chemistry to Catalytic Antisense Drugs. *Chemical Reviews* **1998**, 98, 939-960.
38. Liu, C. T.; Neverov, A. A.; Brown, R. S., Biomimetic Cleavage of RNA Models Promoted by a Dinuclear Zn(II) Complex in Ethanol. Greater than 30 kcal/mol Stabilization of the Transition State for Cleavage of a Phosphate Diester. *Journal of the American Chemical Society* **2008**, 130, 16711-16720.
39. Bunn, S. E.; Liu, C. T.; Lu, Z. L.; Neverov, A. A.; Brown, R. S., The Dinuclear Zn(II) Complex Catalyzed Cyclization of a Series of 2'-Hydroxypropyl-aryl-phosphate RNA Models: Progressive Change in Mechanism from Rate-limiting P-O Bond Cleavage to Substrate Binding. *Journal of the American Chemical Society* **2007**, 129, 16238-16248.
40. Sigel, R. K. O.; Pyle, A. M., Alternative Roles for Metal Ions in Enzyme Catalysis and the Implications for Ribozyme Chemistry. *Chemical Reviews* **2007**, 107, 97-113.
41. Pyle, A. M.; Sigel, R., Metal Ions for Folding and Catalysis by a Group II Intron Ribozyme. *Journal of Inorganic Biochemistry* **2001**, 86, (1), 7-17.
42. Fedor, M. J., The Role of Metal Ions in RNA Catalysis. *Current Opinion in Structural Biology* **2002**, 12, 289-295.
43. De Vivo, M.; Dal Peraro, M.; Klein, M. L., Phosphodiester Cleavage in Ribonuclease H Occurs via an Associative Two-metal-aided Catalytic Mechanism. *Journal of the American Chemical Society* **2008**, 130, 10955-10962.
44. Note that the discovery of reverse transcription, where RNA serves as a template for DNA polymerization, deviates slightly from the original dogma; normally RNA is transcribed from a DNA template.
45. Guerriertakada, C.; Gardiner, K.; Marsh, T.; Pace, N.; Altman, S., The RNA Moiety of Ribonuclease-P is the Catalytic Subunit of the Enzyme. *Cell* **1983**, 35, 849-857.
46. Kruger, K.; Grabowski, P. J.; Zaug, A. J.; Sands, J.; Gottschling, D. E.; Cech, T. R., Self-Splicing RNA - Auto-Excision and Auto-Cyclization of the Ribosomal-RNA Intervening Sequence of Tetrahymena. *Cell* **1982**, 31, 147-157.
47. North, G., Back to the RNA World and Beyond. *Nature* **1987**, 328, 18-19.
48. Gilbert, W., Origin of Life - The RNA World. *Nature* **1986**, 319, 618-618.
49. Johnston, W. K.; Unrau, P. J.; Lawrence, M. S.; Glasner, M. E.; Bartel, D. P., RNA-catalyzed RNA Polymerization: Accurate and General RNA-templated Primer Extension. *Science* **2001**, 292, 1319-1325.
50. Lilley, D. M. J., The Ribosome Functions as a Ribozyme. *ChemBioChem* **2001**, 2, 31-35.
51. Cech, T. R., Structural biology - The Ribosome is a Ribozyme. *Science* **2000**, 289, 878-879.

52. Gesteland, R. F.; Cech, T. R.; Atkins, J. F., *The RNA World*. 3rd ed.; Cold Spring Harbour Laboratory Press: 2006.
53. Prody, G. A.; Bakos, J. T.; Buzayan, J. M.; Schneider, I. R.; Bruening, G., Autolytic Processing of Dimeric Plant-Virus Satellite RNA. *Science* **1986**, 231, 1577-1580.
54. Symons, R. H., Plant Pathogenic RNAs and RNA Catalysis. *Nucleic Acids Research* **1997**, 25, 2683-2689.
55. Buzayan, J. M.; Gerlach, W. L.; Bruening, G., Satellite Tobacco Ringspot Virus RNA a Subset of the RNA Sequence is Sufficient for Autolytic Processing. *Proceedings of the National Academy of Sciences* **1986**, 83, (23), 8859-8862.
56. Buzayan, J. M.; Gerlach, W. L.; Bruening, G., Nonenzymatic Cleavage and Ligation of RNAs Complementary to a Plant-Virus Satellite RNA. *Nature* **1986**, 323, 349-353.
57. Wu, H. N.; Lin, Y. J.; Lin, F. P.; Makino, S.; Chang, M. F.; Lai, M. M. C., Human Hepatitis-Delta Virus-RNA Subfragments Contain an Autocleavage Activity. *Proceedings of the National Academy of Sciences* **1989**, 86, 1831-1835.
58. Kuo, M. Y. P.; Sharmeen, L.; Dintergottlieb, G.; Taylor, J., Characterization of Self-Cleaving RNA Sequences on the Genome and Antigenome of Human Hepatitis Delta-Virus. *Journal of Virology* **1988**, 62, 4439-4444.
59. Sharmeen, L.; Kuo, M. Y. P.; Dintergottlieb, G.; Taylor, J., Antigenomic RNA of Human Hepatitis Delta-Virus Can Undergo Self-Cleavage. *Journal of Virology* **1988**, 62, 2674-2679.
60. Salehi-Ashtiani, K.; Luptak, A.; Litovchick, A.; Szostak, J. W., A Genomewide Search for Ribozymes Reveals an HDV-like Sequence in the Human CPEB3 Gene. *Science* **2006**, 313, 1788-1792.
61. Saville, B. J.; Collins, R. A., A Site-Specific Self-Cleavage Reaction Performed by a Novel RNA in Neurospora Mitochondria. *Cell* **1990**, 61, 685-696.
62. Winkler, W. C.; Nahvi, A.; Roth, A.; Collins, J. A.; Breaker, R. R., Control of Gene Expression by a Natural Metabolite-responsive Ribozyme. *Nature* **2004**, 428, 281-286.
63. Chay, C. A.; Guan, X.; Bruening, G., Formation of Circular Satellite Tobacco Ringspot Virus RNA in Protoplasts Transiently Expressing the Linear RNA. *Virology* **1997**, 239, 413-425.
64. Nakano, S.; Chadalavada, D. M.; Bevilacqua, P. C., General Acid-base Catalysis in the Mechanism of a Hepatitis Delta Virus Ribozyme. *Science* **2000**, 287, 1493-1497.
65. Ferre-D'Amare, A. R.; Zhou, K. H.; Doudna, J. A., Crystal Structure of a Hepatitis Delta Virus Ribozyme. *Nature* **1998**, 395, 567-574.
66. Ferre-D'Amare, A. R.; Doudna, J. A., Crystallization and Structure Determination of a Hepatitis Delta Virus Ribozyme: Use of the RNA-binding Protein U1A as a Crystallization Module. *Journal of Molecular Biology* **2000**, 295, 541-556.
67. LLC, D. S. *PyMOL*, DeLano Scientific LLC: San Carlos, California, U.S.A., 2009.
68. Das, S. R.; Piccirilli, J. A., General Acid Catalysis by the Hepatitis Delta Virus Ribozyme. *Nature Chemical Biology* **2005**, 1, 45-52.
69. Tuerk, C.; Gold, L., Systematic Evolution of Ligands by Exponential Enrichment - RNA Ligands to Bacteriophage-T4 DNA Polymerase. *Science* **1990**, 249, 505-510.
70. Ellington, A. D.; Szostak, J. W., *In Vitro* Selection of RNA Molecules that Bind Specific Ligands. *Nature* **1990**, 346, 818-822.

71. Breaker, R. R.; Joyce, G. F., A DNA Enzyme with Mg<sup>2+</sup>-Dependent RNA Phosphoesterase Activity. *Chemistry & Biology* **1995**, 2, 655-660.
72. Santoro, S. W.; Joyce, G. F., A General Purpose RNA-cleaving DNA Enzyme. *Proceedings of the National Academy of Sciences* **1997**, 94, 4262-4266.
73. Dass, C. R.; Choong, P. F. M.; Khachigian, L. M., DNzyme technology and cancer therapy: cleave and let die. *Molecular Cancer Therapeutics* **2008**, 7, (2), 243-251.
74. Santiago, F. S.; Lowe, H. C.; Kavurma, M. M.; Chesterman, C. N.; Baker, A.; Atkins, D. G.; Khachigian, L. M., New DNA Enzyme Targeting Egr-1 mRNA Inhibits Vascular Smooth Muscle Proliferation and Regrowth after Injury. *Nature Medicine* **1999**, 5, 1264-1269.
75. Dass, C. R., Deoxyribozymes: Cleaving a Path to Clinical Trials. *Trends in Pharmacological Sciences* **2004**, 25, 395-397.
76. Isaka, Y., DNzymes as Potential Therapeutic Molecules. *Current Opinion in Molecular Therapeutics* **2007**, 9, 132-136.
77. Sioud, M.; Iversen, P. O., Ribozymes, DNzymes and Small Interfering RNAs as Therapeutics. *Current Drug Targets* **2005**, 6, 647-653.
78. Schubert, S.; Kurreck, J., Ribozyme- and Deoxyribozyme-strategies for Medical Applications. *Current Drug Targets* **2004**, 5, 667-681.
79. Hou, W.; Ni, Q.; Wo, J. N.; Li, M. W.; Liu, K. Z.; Chen, L. W.; Hu, Z. R.; Liu, R. H.; Hu, M. J., Inhibition of Hepatitis B Virus X Gene Expression by 10-23 DNzymes. *Antiviral Research* **2006**, 72, 190-196.
80. Toyoda, T.; Imamura, Y.; Takaku, H.; Kashiwagi, T.; Hara, K.; Iwahashi, J.; Ohtsu, Y.; Tsumura, N.; Kato, H.; Hamada, N., Inhibition of Influenza Virus Replication in Cultured Cells by an RNA-cleaving DNA Enzyme. *FEBS Letters* **2000**, 481, 113-116.
81. Zhang, L.; Gasper, W. J.; Stass, S. A.; Ioffe, O. B.; Davis, M. A.; Mixson, A. J., Angiogenic Inhibition Mediated by a DNzyme that Targets Vascular Endothelial Growth Factor Receptor 2. *Cancer Research* **2002**, 62, 5463-5469.
82. Sun, L. Q.; Cairns, M. J.; Gerlach, W. L.; Witherington, C.; Wang, L.; King, A., Suppression of Smooth Muscle Cell Proliferation by a c-Myc RNA-cleaving Deoxyribozyme. *Journal of Biological Chemistry* **1999**, 274, 17236-17241.
83. Yu, S. H.; Wang, T. H.; Au, L. C., Specific Repression of Mutant K-RAS by 10-23 DNzyme: Sensitizing Cancer Cells to Anti-cancer Therapies. *Biochemical and Biophysical Research Communications* **2009**, 378, 230-234.
84. Mitchell, A.; Dass, C. R.; Sun, L. Q.; Khachigian, L. M., Inhibition of Human Breast Carcinoma Proliferation, Migration, Chemoinvasion and Solid Tumour Growth by DNzymes Targeting the Zinc Finger Transcription Factor EGR-1. *Nucleic Acids Research* **2004**, 32, 3065-3069.
85. Schubert, S.; Furste, J. P.; Werk, D.; Grunert, H. P.; Zeichhardt, H.; Erdmann, V. A.; Kurreck, J., Gaining Target Access for Deoxyribozymes. *Journal of Molecular Biology* **2004**, 339, 355-363.
86. Chaudhury, I.; Raghav, S. K.; Gautam, H. K.; Das, H. R.; Das, R. H., Suppression of Inducible Nitric Oxide Synthase by 10-23 DNzymes in Murine Macrophage. *FEBS Letters* **2006**, 580, 2046-2052.
87. Perrin, D. M.; Garestier, T.; Helene, C., Bridging the Gap between Proteins and Nucleic Acids: A Metal-independent RNaseA Mimic with Two Protein-like Functionalities. *Journal of the American Chemical Society* **2001**, 123, 1556-1563.

88. Ting, R.; Thomas, J. M.; Lermer, L.; Perrin, D. M., Substrate Specificity and Kinetic Framework of a DNAzyme with an Expanded Chemical Repertoire: a Putative RNaseA Mimic that Catalyzes RNA Hydrolysis Independent of a Divalent Metal Cation. *Nucleic Acids Research* **2004**, *32*, 6660-6672.
89. Santoro, S. W.; Joyce, G. F., Mechanism and Utility of an RNA-cleaving DNA Enzyme. *Biochemistry* **1998**, *37*, 13330-13342.
90. Geyer, C. R.; Sen, D., Evidence for the Metal Cofactor Independence of an RNA Phosphodiester-cleaving DNA Enzyme. *Chemistry & Biology* **1997**, *4*, 579-593.
91. Faulhammer, D.; Famulok, M., Characterization and Divalent Metal-ion Dependence of *In Vitro* Selected Deoxyribozymes which Cleave DNA/RNA Chimeric Oligonucleotides. *Journal of Molecular Biology* **1997**, *269*, 188-202.
92. Sidorov, A. V.; Grasby, J. A.; Williams, D. M., Sequence-specific Cleavage of RNA in the Absence of Divalent Metal Ions by a DNAzyme Incorporating Imidazolyl and Amino Functionalities. *Nucleic Acids Research* **2004**, *32*, 1591-1601.
93. Lermer, L.; Roupioz, Y.; Ting, R.; Perrin, D. M., Toward an RNaseA Mimic: a DNAzyme with Imidazoles and Cationic Amines. *Journal of the American Chemical Society* **2002**, *124*, 9960-9961.
94. Hummel, C. F.; Pincus, M. R.; Brandtrauf, P. W.; Frei, G. M.; Carty, R. P., Reaction of Bromoacetamido-nucleoside Affinity Labels with Ribonuclease A - Evidence for Steric Control of Reaction Specificity and Alkylation Rate. *Biochemistry* **1987**, *26*, 135-146.
95. Nachman, J.; Miller, M.; Gilliland, G. L.; Carty, R.; Pincus, M.; Wlodawer, A., Crystal Structure of Two Covalent Nucleoside Derivatives of Ribonuclease A. *Biochemistry* **1990**, *29*, 928-937.
96. Lan, L. T.; Carty, R. P., Synthesis of 2'-Bromoacetamido-2'-deoxyuridine and its Reaction with Ribonuclease A. *Biochemical and Biophysical Research Communications* **1972**, *48*, 585-591.
97. Lennette, E. P.; Plapp, B. V., Transition State Analysis of the Facilitated Alkylation of Ribonuclease A by Bromoacetate. *Biochemistry* **1979**, *18*, 3938-3946.
98. Zhou, D. M.; Usman, N.; Wincott, F. E.; MatulicAdamic, J.; Orita, M.; Zhang, L. H.; Komiyama, M.; Kumar, P. K. R.; Taira, K., Evidence for the Rate-limiting Departure of the 5'-Oxygen in Non-enzymatic and Hammerhead Ribozyme-catalyzed Reactions. *Journal of the American Chemical Society* **1996**, *118*, 5862-5866.
99. Zhou, D. M.; Zhang, L. H.; Taira, K., Explanation by the Double-metal-ion Mechanism of Catalysis for the Differential Metal Ion Effects on the Cleavage Rates of 5'-Oxy and 5'-Thio Substrates by a Hammerhead Ribozyme. *Proceedings of the National Academy of Sciences* **1997**, *94*, 14343-14348.
100. Kuimelis, R. G.; McLaughlin, L. W., Application of a 5'-Bridging Phosphorothioate to Probe Divalent Metal and Hammerhead Ribozyme Mediated RNA Cleavage. *Bioorganic & Medicinal Chemistry* **1997**, *5*, 1051-1061.
101. Kuimelis, R. G.; McLaughlin, L. W., Ribozyme-mediated Cleavage of a Substrate Analogue Containing an Internucleotide-bridging 5'-Phosphorothioate: Evidence for the Single Metal Model. *Biochemistry* **1996**, *35*, 5308-5317.
102. Kuimelis, R. G.; McLaughlin, L. W., Hammerhead Ribozyme-Mediated Cleavage of a Substrate Analog Containing an Internucleotidic Bridging 5'-Phosphorothioate -

- Implications for the Cleavage Mechanism and the Catalytic Role of the Metal Cofactor. *Journal of the American Chemical Society* **1995**, 117, 11019-11020.
103. Piccirilli, J. A.; Vyle, J. S.; Caruthers, M. H.; Cech, T. R., Metal-Ion Catalysis in the Tetrahymena Ribozyme Reaction. *Nature* **1993**, 361, 85-88.
104. Krogh, B. O.; Shuman, S., Catalytic Mechanism of DNA Topoisomerase IB. *Molecular Cell* **2000**, 5, 1035-1041.
105. Burgin, A. B.; Huizenga, B. N.; Nash, H. A., A Novel Suicide Substrate for DNA Topoisomerases and Site-Specific Recombinases. *Nucleic Acids Research* **1995**, 23, 2973-2979.
106. Curley, J. F.; Joyce, C. M.; Piccirilli, J. A., Functional Evidence that the 3'-5' Exonuclease Domain of *Escherichia coli* DNA Polymerase I Employs a Divalent Metal Ion in Leaving Group Stabilization. *Journal of the American Chemical Society* **1997**, 119, 12691-12692.
107. Hondal, R. J.; Bruzik, K. S.; Zhao, Z.; Tsai, M. D., Mechanism of Phosphatidylinositol-phospholipase C 2: Reversal of a Thio Effect by Site-directed Mutagenesis. *Journal of the American Chemical Society* **1997**, 119, 5477-5478.
108. Bonvicini, P.; Levi, A.; Lucchini, V.; Scorrano, G., The Acid-Base Behaviour of Sulphides. *Journal of the Chemical Society - Perkin Transactions 2* **1972**, 2267-2269.
109. Gregersen, B. A.; Lopez, X.; York, D. M., Hybrid QM/MM Study of Thio Effects in Transphosphorylation Reactions. *Journal of the American Chemical Society* **2003**, 125, 7178-7179.
110. Gregersen, B. A.; Lopez, X.; York, D. M., Hybrid QM/MM Study of Thio Effects in Transphosphorylation Reactions: the Role of Solvation. *Journal of the American Chemical Society* **2004**, 126, 7504-7513.
111. Hammond, G. S., A Correlation of Reaction Rates. *Journal of the American Chemical Society* **1955**, 77, 334-338.
112. Ye, J. D.; Barth, C. D.; Anjaneyulu, P. S. R.; Tuschl, T.; Piccirilli, J. A., Reactions of Phosphate and Phosphorothiolate Diesters with Nucleophiles: Comparison of Transition State Structures. *Organic & Biomolecular Chemistry* **2007**, 5, 2491-2497.
113. Hondal, R. J.; Zhao, Z.; Riddle, S. R.; Kravchuk, A. V.; Liao, H.; Bruzik, K. S.; Tsai, M. D., Phosphatidylinositol-specific Phospholipase C .3. Elucidation of the Catalytic Mechanism and Comparison with Ribonuclease A. *Journal of the American Chemical Society* **1997**, 119, 9933-9934.
114. Hondal, R. J.; Zhao, Z.; Kravchuk, A. V.; Liao, H.; Riddle, S. R.; Yue, X.; Bruzik, K. S.; Tsai, M. D., Mechanism of phosphatidylinositol-specific Phospholipase C: a Unified View of the Mechanism of Catalysis. *Biochemistry* **1998**, 37, 4568-4580.
115. Heinz, D. W.; Ryan, M.; Bullock, T. L.; Griffith, O. H., Crystal-Structure of the Phosphatidylinositol-Specific Phospholipase-C from *Bacillus-Cereus* in Complex with Myoinositol. *EMBO Journal* **1995**, 14, 3855-3863.
116. Sigel, R. K. O.; Song, B.; Sigel, H., Stabilities and Structures of Metal Ion Complexes of Adenosine 5'-O-Thiomonophosphate in Comparison with those of its Parent Nucleotide in Aqueous Solution. *Journal of the American Chemical Society* **1997**, 119, 744-755.
117. Pecoraro, V. L.; Hermes, J. D.; Cleland, W. W., Stability Constants of Mg<sup>2+</sup> and Cd<sup>2+</sup> Complexes of Adenine Nucleotides and Thionucleotides and Rate Constants for

- Formation and Dissociation of MgATP and MgADP. *Biochemistry* **1984**, 23, 5262-5271.
118. Kuimelis, R. G.; McLaughlin, L. W., Cleavage Properties of an Oligonucleotide Containing a Bridged Internucleotide 5'-Phosphorothioate RNA Linkage. *Nucleic Acids Research* **1995**, 23, 4753-4760.
  119. Harris, T. K.; Turner, G. J., Structural Basis of Perturbed  $pK_a$  Values of Catalytic Groups in Enzyme Active Sites. *IUBMB Life* **2002**, 53, 85-98.
  120. Jencks, W. P., *Catalysis in Chemistry and Enzymology*. Dover Publications, Inc.: New York, 1969.
  121. Jackson, D. Y.; Burnier, J.; Quan, C.; Stanley, M.; Tom, J.; Wells, J. A., A Designed Peptide Ligase for Total Synthesis of Ribonuclease A with Unnatural Catalytic Residues. *Science* **1994**, 266, 243-247.
  122. Kirk, K. L.; Cohen, L. A., Photochemistry of Diazonium Salts 1: Synthesis of 4-Fluoroimidazoles, 4-Fluorohistamine, and 4-Fluorohistidine. *Journal of the American Chemical Society* **1973**, 95, 4619-4624.
  123. Cerrone-Szakal, A. L.; Siegfried, N. A.; Bevilacqua, P. C., Mechanistic Characterization of the HDV Genomic Ribozyme: Solvent Isotope Effects and Proton Inventories in the Absence of Divalent Metal Ions Support C75 as the General Acid. *Journal of the American Chemical Society* **2008**, 130, 14504-14520.
  124. Searls, T.; McLaughlin, L. W., Synthesis of the Analogue Nucleoside 3-Deaza-2'-deoxycytidine and its Template Activity with DNA Polymerase. *Tetrahedron* **1999**, 55, 11985-11996.
  125. Saenger, W., *Principles of Nucleic Acid Structure*. Springer-Verlag: New York, 1984.
  126. Perrotta, A. T.; Shih, I. H.; Been, M. D., Imidazole Rescue of a Cytosine Mutation in a Self-cleaving Ribozyme. *Science* **1999**, 286, 123-126.
  127. Perrotta, A. T.; Wadkins, T. S.; Been, M. D., Chemical Rescue, Multiple Ionizable Groups, and General Acid-base Catalysis in the HDV Genomic Ribozyme. *RNA* **2006**, 12, 1282-1291.
  128. Wadkins, T. S.; Shih, I. H.; Perrotta, A. T.; Been, M. D., A pH-sensitive RNA Tertiary Interaction Affects Self-cleavage Activity of the HDV Ribozymes in the Absence of Added Divalent Metal Ion. *Journal of Molecular Biology* **2001**, 305, 1045-1055.
  129. Povsic, T. J.; Dervan, P. B., Sequence-Specific Alkylation of Double-Helical DNA by Oligonucleotide-directed Triple-helix Formation. *Journal of the American Chemical Society* **1990**, 112, 9428-9430.
  130. Miller, G. P.; Kool, E. T., A Simple Method for Electrophilic Functionalization of DNA. *Organic Letters* **2002**, 4, 3599-3601.
  131. Zhang, B. L.; Cui, Z. Y.; Sun, L. L., Synthesis of 5'-Deoxy-5'-thioguanosine-5'-monophosphorothioate and its Incorporation into RNA 5'-Termini. *Organic Letters* **2001**, 3, 275-278.
  132. Chamberlin, S. I.; Weeks, K. M., Mapping Local Nucleotide Flexibility by Selective Acylation of 2'-Amine Substituted RNA. *Journal of the American Chemical Society* **2000**, 122, 216-224.

133. Gherghe, C. M.; Krahn, J. M.; Weeks, K. M., Crystal Structures, Reactivity and Inferred Acylation Transition States for 2'-Amine A substituted RNA. *Journal of the American Chemical Society* **2005**, 127, 13622-13628.
134. Povsic, T. J.; Strobel, S. A.; Dervan, P. B., Sequence-Specific Double-Strand Alkylation and Cleavage Of DNA Mediated by Triple-helix Formation. *Journal of the American Chemical Society* **1992**, 114, 5934-5941.
135. Dai, Q.; Lea, C. R.; Lu, J.; Piccirilli, J. A., Syntheses of (2')3'-<sup>15</sup>N-Amino-(2')3'-deoxy-guanosine and Determination of their pK<sub>a</sub> Values by <sup>15</sup>N-NMR Spectroscopy. *Organic Letters* **2007**, 9, 3057-3060.
136. Dittmer, D. C. R., O. B.; Spalding, R. E., Reactivity of Thiophosphates II: Hydrolysis of S-*n*-Butylphosphorothioate and S-(2-Aminoethyl)phosphorothioate. *Journal of Organic Chemistry* **1963**, 28, 1273-1278.
137. Verheyden, J. P. H.; Moffatt, J. G., Synthesis of Some 4',5'-Unsaturated Pyrimidine Nucleosides. *Journal of Organic Chemistry* **1974**, 39, 3573-3579.
138. Verheyden, J. P. H.; Moffatt, J. G., Halo Sugar Nucleosides I: Iodination of the Primary Hydroxyl Groups of Nucleosides with Methyltriphenoxyposphonium Iodide. *Journal of Organic Chemistry* **1970**, 35, 2319-2326.
139. Dimitrijevič, S. D.; Verheyden, J. P. H.; Moffatt, J. G., Halo Sugar Nucleosides 6: Synthesis of Some 5'-Deoxy-5'-iodo and 4',5'-Unsaturated Purine Nucleosides. *Journal of Organic Chemistry* **1979**, 44, 400-406.
140. Breslow, R., Biomimetic Chemistry and Artificial Enzymes - Catalysis by Design. *Accounts of Chemical Research* **1995**, 28, 146-153.
141. Orth, E. S.; Brandao, T. A. S.; Milagre, H. M. S.; Eberlin, M. N.; Nome, F., Intramolecular Acid-base Catalysis of a Phosphate Diester: Modeling the Ribonuclease Mechanism. *Journal of the American Chemical Society* **2008**, 130, 2436-2437.
142. Lorente, A.; Espinosa, J. F.; FernandezSaiz, M.; Lehn, J. M.; Wilson, W. D.; Zhong, Y. Y., Syntheses of Imidazole-Acridine Conjugates as Ribonuclease A Mimics. *Tetrahedron Letters* **1996**, 37, 4417-4420.
143. Vlassov, V. V.; Zuber, G.; Felden, B.; Behr, J. P.; Giege, R., Cleavage of Transfer-RNA with Imidazole and Spermine Imidazole Constructs - a New Approach for Probing RNA Structure. *Nucleic Acids Research* **1995**, 23, 3161-3167.
144. Scheffer, U.; Strick, A.; Ludwig, V.; Peter, S.; Kalden, E.; Gobel, M. W., Metal-free Catalysts for the Hydrolysis of RNA Derived from Guanidines, 2-Aminopyridines, and 2-Aminobenzimidazoles. *Journal of the American Chemical Society* **2005**, 127, 2211-2217.
145. Breslow, R.; Doherty, J. B.; Guillot, G.; Lipsey, C., Beta-Cyclodextrinyl-bis-imidazole, a Model for Ribonuclease. *Journal of the American Chemical Society* **1978**, 100, 3227-3229.
146. Razkin, J.; Nilsson, H.; Baltzer, L., Catalysis of the cleavage of uridine 3'-2,2,2-trichloroethylphosphate by a designed Helix-Loop-Helix motif peptide. *Journal of the American Chemical Society* **2007**, 129, 14752-14758.
147. Gnaccarini, C.; Peter, S.; Scheffer, U.; Vonhoff, S.; Klussmann, S.; Gobel, M. W., Site-specific Cleavage of RNA by a Metal-free Artificial Nuclease Attached to Antisense Oligonucleotides. *Journal of the American Chemical Society* **2006**, 128, 8063-8067.

148. Beloglazova, N. G.; Fabani, M. M.; Zenkova, M. A.; Bichenkova, E. V.; Polushin, N. N.; Sil'nikov, V. V.; Douglas, K. T.; Vlassov, V. V., Sequence-specific Artificial Ribonucleases. I. Bis-imidazole-containing Oligonucleotide Conjugates Prepared Using Precursor-based Strategy. *Nucleic Acids Research* **2004**, *32*, 3887-3897.
149. Beloglazova, N. G.; Sil'nikov, V. N.; Zenkova, M. A.; Vlassov, V. V., Cleavage of Yeast tRNA(Phe) with Complementary Oligonucleotide Conjugated to a Small Ribonuclease Mimic. *FEBS Letters* **2000**, *481*, 277-280.
150. Petersen, L.; de Koning, M. C.; van Kuik-Romeijn, P.; Weterings, J.; Pol, C. J.; Platenburg, G.; Overhand, M.; van der Marel, G. A.; van Boom, J. H., Synthesis and *In Vitro* Evaluation of PNA-peptide-DETA Conjugates as Potential Cell Penetrating Artificial Ribonucleases. *Bioconjugate Chemistry* **2004**, *15*, 576-582.
151. Verheijen, J. C.; Deiman, B.; Yeheskiely, E.; van der Marel, G. A.; van Boom, J. H., Efficient Hydrolysis of RNA by a PNA-diethylenetriamine Adduct. *Angewandte Chemie* **2000**, *39*, 369-373.
152. Verbeure, B.; Lacey, C. J.; Froeyen, M.; Rozenski, J.; Herdewijn, P., Synthesis and Cleavage Experiments of Oligonucleotide Conjugates with a Di-imidazole-derived Catalytic Center. *Bioconjugate Chemistry* **2002**, *13*, 333-350.
153. Beloglazova, N. G.; Fabani, M. M.; Zenkova, M. A.; Bichenkova, E. V.; Polushin, N. N.; Sil'nikov, V. V.; Douglas, K. T.; Vlassov, V. V., Sequence-specific Artificial Ribonucleases I: Bis-imidazole Containing Oligonucleotide Conjugates Prepared Using Precursor-based Strategy. *Nucleic Acids Research* **2004**, *32*, 3885-3895.
154. Mulquiney, P. J.; Kuchel, P. W., Free Magnesium-ion Concentration in Erythrocytes by  $^{31}\text{P}$ -NMR: the Effect of Metabolite-haemoglobin Interactions. *NMR in Biomedicine* **1997**, *10*, 129-137.
155. Murphy, E.; Steenbergen, C.; Levy, L. A.; Raju, B.; London, R. E., Cytosolic Free Magnesium Levels in Ischemic Rat Heart. *Journal of Biological Chemistry* **1989**, *264*, 5622-5627.
156. Suzuki, Y.; Komatsu, H.; Ikeda, T.; Saito, N.; Araki, S.; Citterio, D.; Hisamoto, H.; Kitamura, Y.; Kubota, T.; Nakagawa, J.; Oka, K.; Suzuki, K., Design and Synthesis of  $\text{Mg}^{2+}$ -selective Fluoroionophores Based on a Coumarin Derivative and Application for  $\text{Mg}^{2+}$  Measurement in a Living Cell. *Analytical Chemistry* **2002**, *74*, 1423-1428.
157. Hampel, A.; Cowan, J. A., A Unique Mechanism for RNA Catalysis: the Role of Metal Cofactors in Hairpin Ribozyme Cleavage. *Chemistry & Biology* **1997**, *4*, 513-517.
158. Nesbitt, S.; Hegg, L. A.; Fedor, M. J., An Unusual pH-independent and Metal-ion-independent Mechanism for Hairpin Ribozyme Catalysis. *Chemistry & Biology* **1997**, *4*, 619-630.
159. Young, K. J.; Gill, F.; Grasby, J. A., Metal Ions Play a Passive Role in the Hairpin Ribozyme Catalyzed Reaction. *Nucleic Acids Research* **1997**, *25*, 3760-3766.
160. Murray, J. B.; Seyhan, A. A.; Walter, N. G.; Burke, J. M.; Scott, W. G., The Hammerhead, Hairpin and VS ribozymes are Catalytically Proficient in Monovalent Cations Alone. *Chemistry & Biology* **1998**, *5*, 587-595.

161. O'Rear, J. L.; Wang, S. L.; Feig, A. L.; Beigelman, L.; Uhlenbeck, O. C.; Herschlag, D., Comparison of the Hammerhead Cleavage Reactions Stimulated by Monovalent and Divalent Cations. *RNA* **2001**, *7*, 537-545.
162. Curtis, E. A.; Bartel, D. P., The Hammerhead Cleavage Reaction in Monovalent Cations. *RNA* **2001**, *7*, 546-552.
163. Carrigan, M. A.; Ricardo, A.; Ang, D. N.; Benner, S. A., Quantitative Analysis of a RNA-cleaving DNA Catalyst Obtained via *In Vitro* Selection. *Biochemistry* **2004**, *43*, 11446-11459.
164. Gnaccarini, C. P., S.; Scheffer, U.; Vonhoff, S.; Klussmann, S.; Goebel, M. W., Site-Specific Cleavage of RNA by a Metal-Free Artificial Nuclease Attached to Antisense Oligonucleotides. *Journal of the American Chemical Society* **2006**, *128*, 8063-8067.
165. Bevilacqua, P. C.; Yajima, R., Nucleobase Catalysis in Ribozyme Mechanism. *Current Opinion in Chemical Biology* **2006**, *10*, 455-464.
166. Narlikar, G. J.; Herschlag, D., Mechanistic Aspects of Enzymatic Catalysis: Lessons from Comparison of RNA and Protein Enzymes. *Annual Review of Biochemistry* **1997**, *66*, 19-59.
167. Gugliotti, L. A.; Feldheim, D. L.; Eaton, B. E., RNA-Mediated Control of Metal Nanoparticle Shape. *Journal of the American Chemical Society* **2005**, *127*, 17814-17818.
168. Gugliotti, L. A.; Feldheim, D. L.; Eaton, B. E., RNA-mediated Metal-metal Bond Formation in the Synthesis of Hexagonal Palladium Nanoparticles. *Science* **2004**, *304*, 850-852.
169. Tarasow, T. M.; Tarasow, S. L.; Eaton, B. E., RNA-catalysed Carbon-carbon Bond Formation. *Nature* **1997**, *389*, 54-57.
170. Santoro, S. W.; Joyce, G. F.; Sakthivel, K.; Gramatikova, S.; Barbas, C. F., RNA Cleavage by a DNA Enzyme with Extended Chemical Functionality. *Journal of the American Chemical Society* **2000**, *122*, 2433-2439.
171. Teramoto, N.; Imanishi, Y.; Ito, Y., *In Vitro* Selection of a Ligase Ribozyme Carrying Alkylamino Groups in the Side Chains. *Bioconjugate Chemistry* **2000**, *11*, 744-748.
172. Hollenstein, M.; Hipolito, C.; Lam, C.; Dietrich, D.; Perrin, D. M., A Highly Selective DNAzyme Sensor for Mercuric ions. *Angewandte Chemie* **2008**, *47*, 4346-4350.
173. Lee, J. H.; Wang, Z. D.; Liu, J. W.; Lu, Y., Highly Sensitive and Selective Colorimetric Sensors for Uranyl (UO<sub>2</sub><sup>2+</sup>) : Development and Comparison of Labeled and Label-free DNAzyme-/Gold Nanoparticle Systems. *Journal of the American Chemical Society* **2008**, *130*, 14217-14226.
174. Li, J.; Lu, Y., A Highly Sensitive and Selective Catalytic DNA Biosensor for Lead Ions. *Journal of the American Chemical Society* **2000**, *122*, 10466-10467.
175. Liu, J.; Lu, Y., A DNAzyme Catalytic Beacon Sensor for Paramagnetic Cu<sup>2+</sup> Ions in Aqueous Solution with High Sensitivity and Selectivity. *Journal of the American Chemical Society* **2007**, *129*, 9838-+.
176. Liu, J.; Lu, Y., Rational design of "Turn-On" Allosteric DNAzyme Catalytic Beacons for Aqueous Mercury Ions with Ultrahigh Sensitivity and Selectivity. *Angewandte Chemie* **2007**, *46*, 7587-7590.

177. Liu, J. W.; Lu, Y., A Colorimetric Lead Biosensor Using DNAzyme-directed Assembly of Gold Nanoparticles. *Journal of the American Chemical Society* **2003**, 125, 6642-6643.
178. Lu, Y.; Liu, J. W.; Li, J.; Bruesehoff, P. J.; Pavot, C. M. B.; Brown, A. K., New Highly Sensitive and Selective Catalytic DNA Biosensors for Metal Ions. *Biosensors & Bioelectronics* **2003**, 18, 529-540.
179. Vannela, R.; Adriaens, P., DNAzymes in Environmental Sensing. *Critical Reviews in Environmental Science and Technology* **2006**, 36, 375-403.
180. Willner, I.; Shlyahovsky, B.; Zayats, M.; Willner, B., DNAzymes for Sensing, Nanobiotechnology and Logic Gate Applications. *Chemical Society Reviews* **2008**, 37, 1153-1165.
181. Xiao, Y.; Rowe, A. A.; Plaxco, K. W., Electrochemical Detection of Parts-per-billion Lead via an Electrode-bound DNAzyme Assembly. *Journal of the American Chemical Society* **2007**, 129, 262-263.
182. Liu, Z. J.; Mei, S. H. J.; Brennan, J. D.; Li, Y. F., Assemblage of Signaling DNA Enzymes with Intriguing Metal-ion Specificities and pH Dependences. *Journal of the American Chemical Society* **2003**, 125, 7539-7545.
183. Kapinos, L. E.; Song, B.; Sigel, H., Metal Ion-coordinating Properties of Imidazole and Derivatives in Aqueous Solution, Interrelation between Complex Stability and Ligand Basicity. *Inorganica Chimica Acta* **1998**, 280, 50-56.
184. Sigel, H.; Saha, A.; Saha, N.; Carloni, P.; Kapinos, L. E.; Griesser, R., Evaluation of Intramolecular Equilibria in Complexes Formed between Substituted Imidazole Ligands and Nickel(II), Copper(II) or Zinc(II). *Journal of Inorganic Biochemistry* **2000**, 78, 129-137.
185. Brooks, P.; Davidson, N., Mercury(II) Complexes of Imidazole and Histidine. *Journal of the American Chemical Society* **1960**, 82, 2118-2123.
186. Kuklenyik, Z.; Marzilli, L. G., Mercury(II) Site-selective Binding to a DNA Hairpin: Relationship of Sequence-dependent Intra- and Interstrand Cross-linking to the Hairpin-duplex Conformational Transition. *Inorganic Chemistry* **1996**, 35, 5654-5662.
187. Froystein, N. A.; Sletten, E., Interaction of Mercury(II) with the DNA Dodecamer CGCGAATTCGCG - A <sup>1</sup>H And <sup>15</sup>N NMR-Study. *Journal of the American Chemical Society* **1994**, 116, 3240-3250.
188. Sigel, H., Interactions Of Metal-Ions With Nucleotides and Nucleic-Acids and their Constituents. *Chemical Society Reviews* **1993**, 22, 255-267.
189. Knobloch, B.; Linert, W.; Sigel, H., Metal Ion-binding Properties of (N3)-deprotonated Uridine, Thymidine, and Related Pyrimidine Nucleosides in Aqueous Solution. *Proceedings of the National Academy of Sciences* **2005**, 102, 7459-7464.
190. Knobloch, B.; Da Costa, C. P.; Linert, W.; Sigel, H., Stability Constants of Metal Ion Complexes Formed with N3-deprotonated Uridine in Aqueous Solution. *Inorganic Chemistry Communications* **2003**, 6, 90-93.
191. Herschlag, D.; Jencks, W. P., The Effect of Divalent Metal-Ions on the Rate and Transition-state Structure of Phosphoryl-Transfer Reactions. *Journal of the American Chemical Society* **1987**, 109, 4665-4674.
192. Cowan, J. A., Metal Activation of Enzymes in Nucleic Acid Biochemistry. *Chemical Reviews* **1998**, 98, 1067-1087.

193. Song, B.; Sigel, H., Metal Ion-coordinating Properties of 2'-Deoxyguanosine 5'-Monophosphate (dGMP(2-)) in Aqueous Solution. Quantification of Macrochelate Formation. *Inorganic Chemistry* **1998**, *37*, 2066-2073.
194. Sigel, H.; Massoud, S. S.; Corfu, N. A., Comparison of the Extent of Macrochelate Formation in Complexes of Divalent Metal-ions with Guanosine (GMP(2-)), Inosine (IMP(2-)), and Adenosine 5'-Monophosphate (AMP(2-)) - the Crucial Role of N7 Basicity in Metal-ion-nucleic Base Recognition. *Journal of the American Chemical Society* **1994**, *116*, 2958-2971.
195. Mantri, Y.; Lippard, S. J.; Baik, M. H., Bifunctional Binding of Cis-platin to DNA: Why does Cis-platin form 1,2-Intrastrand Cross-links with AG but not with GA? *Journal of the American Chemical Society* **2007**, *129*, 5023-5030.
196. Spingler, B.; Whittington, D. A.; Lippard, S. J., 2.4 Angstrom Crystal Structure of an Oxali-platin 1,2-d(GpG) Intrastrand Cross-link in a DNA Dodecamer Duplex. *Inorganic Chemistry* **2001**, *40*, 5596-5602.
197. Jamieson, E. R.; Lippard, S. J., Structure, Recognition, and Processing of Cis-platin-DNA Adducts. *Chemical Reviews* **1999**, *99*, 2467-2498.
198. Miyake, Y.; Togashi, H.; Tashiro, M.; Yamaguchi, H.; Oda, S.; Kudo, M.; Tanaka, Y.; Kondo, Y.; Sawa, R.; Fujimoto, T.; Machinami, T.; Ono, A., Mercury(II)-mediated Formation of Thymine-Hg-II-thymine Base Pairs in DNA Duplexes. *Journal of the American Chemical Society* **2006**, *128*, 2172-2173.
199. Ono, A.; Togashi, H., Highly Selective Oligonucleotide-based Sensor for Mercury(II) in Aqueous Solutions. *Angewandte Chemie* **2004**, *43*, 4300-4302.
200. Zimmermann, N.; Meggers, E.; Schultz, P. G., A Novel Silver(I)-mediated DNA Base Pair. *Journal of the American Chemical Society* **2002**, *124*, 13684-13685.
201. Tanaka, K.; Yamada, Y.; Shionoya, M., Formation of Silver(I)-mediated DNA Duplex and Triplex through an Alternative Base Pair of Pyridine Nucleobases. *Journal of the American Chemical Society* **2002**, *124*, 8802-8803.
202. Zhang, L. L.; Meggers, E., An Extremely Stable and Orthogonal DNA Base Pair with a Simplified Three-carbon Backbone. *Journal of the American Chemical Society* **2005**, *127*, 74-75.
203. Atwell, S.; Meggers, E.; Spraggon, G.; Schultz, P. G., Structure of a Copper-mediated Base Pair in DNA. *Journal of the American Chemical Society* **2001**, *123*, 12364-12367.
204. Meggers, E.; Holland, P. L.; Tolman, W. B.; Romesberg, F. E.; Schultz, P. G., A Novel Copper-mediated DNA Base Pair. *Journal of the American Chemical Society* **2000**, *122*, 10714-10715.
205. Tanaka, K.; Tengeiji, A.; Kato, T.; Toyama, N.; Shiro, M.; Shionoya, M., Efficient Incorporation of a Copper Hydroxypyridone Base Pair in DNA. *Journal of the American Chemical Society* **2002**, *124*, 12494-12498.
206. Cunningham, L. A.; Li, J.; Lu, Y., Spectroscopic Evidence for Inner-sphere Coordination of Metal Ions to the Active Site of a Hammerhead Ribozyme. *Journal of the American Chemical Society* **1998**, *120*, 4518-4519.
207. Wang, S. L.; Karbstein, K.; Peracchi, A.; Beigelman, L.; Herschlag, D., Identification of the Hammerhead Ribozyme Metal Ion Binding Site Responsible for Rescue of the Deleterious Effect of a Cleavage Site Phosphorothioate. *Biochemistry* **1999**, *38*, 14363-14378.

208. Lermer, L.; Hobbs, J.; Perrin, D. M., Incorporation of 8-Histaminyl-deoxyadenosine into Oligodeoxyribonucleotides by Solid Phase Phosphoramidite Coupling. *Nucleosides Nucleotides & Nucleic Acids* **2002**, 21, 651-664.
209. May, J. P.; Ting, R.; Lermer, L.; Thomas, J. M.; Roupioz, Y.; Perrin, D. M., Covalent Schiff Base Catalysis and Turnover by a DNAzyme: A  $M^{2+}$  Independent AP-endonuclease Mimic. *Journal of the American Chemical Society* **2004**, 126, 4145-4156.
210. Schowen, K. B.; Schowen, R. L., Solvent Isotope Effects in Enzyme Systems. *Methods in Enzymology* **1982**, 87, 551-606.
211. Hertel, K. J.; Herschlag, D.; Uhlenbeck, O. C., A Kinetic and Thermodynamic Framework for the Hammerhead Ribozyme Reaction. *Biochemistry* **1994**, 33, 3374-3385.
212. Glasner, M. E.; Bergman, N. H.; Bartel, D. P., Metal Ion Requirements for Structure and Catalysis of an RNA Ligase Ribozyme. *Biochemistry* **2002**, 41, 8103-8112.
213. Dale, R. M. K.; Martin, E.; Livingston, D. C.; Ward, D. C., Direct Covalent Mercuration of Nucleotides and Polynucleotides. *Biochemistry* **1975**, 14, 2447-2457.
214. Fox, M. A.; Whitesell, J. K., *Organic Chemistry*. Jones and Bartlett: Sudbury, Massachusetts, 1997.
215. Schultz, L. W.; Quirk, D. J.; Raines, R. T., His - Asp Catalytic Dyad of Ribonuclease A: Structure and Function of the Wild-type, D121N, and D121A Enzymes. *Biochemistry* **1998**, 37, 8886-8898.
216. Del Rosario, E. J.; Hammes, G. G., Kinetic and Equilibrium Studies of the Bovine RNase Catalyzed Hydrolysis of 2',3-Cyclic UMP *Biochemistry* **1969**, 8, 1884-1889.
217. Markley, J. L., Observation of Histidine Residues in Proteins by Means of Nuclear Magnetic Resonance Spectroscopy. *Accounts of Chemical Research* **1975**, 8, 70-80.
218. Bruice, T. C.; Schmir, G. L., Imidazole Catalysis 2: the Reaction of Substituted Imidazoles with Phenyl Acetates in Aqueous Solution. *Journal of the American Chemical Society* **1958**, 80, 148-156.
219. Messmore, J. M.; Raines, R. T., Decavanadate Inhibits Catalysis by Ribonuclease A. *Archives of Biochemistry and Biophysics* **2000**, 381, 25-30.
220. Gates, K. S., *Reviews of Reactive Intermediate Chemistry*. John Wiley and Sons, Inc.: New York, 2007.
221. Quirk, D. J.; Park, C.; Thompson, J. E.; Raines, R. T., His - Asp Catalytic Dyad of Ribonuclease A: Conformational Stability of the Wild-type, D121N, D121A, and H119A Enzymes. *Biochemistry* **1998**, 37, 17958-17964.
222. Soukup, G. A.; Breaker, R. R., Relationship between Internucleotide Linkage Geometry and the Stability of RNA. *RNA* **1999**, 5, 1308-1325.
223. Wilk, A.; Stec, W. J., Analysis of Oligo Deoxynucleoside Phosphorothioates and their Diastereomeric Composition. *Nucleic Acids Research* **1995**, 23, 530-534.
224. Burgers, P. M. J.; Eckstein, F., Diastereomers of 5'-O-adenosyl 3'-O-uridyl Phosphorothioate - Chemical Synthesis and Enzymatic Properties. *Biochemistry* **1979**, 18, 592-596.
225. Almer, H.; Stromberg, R., Intramolecular Transesterification in Thiophosphate Analogs of an RNA Dimer. *Tetrahedron Letters* **1991**, 32, 3723-3726.

226. Herschlag, D.; Piccirilli, J. A.; Cech, T. R., Ribozyme-Catalyzed and Nonenzymatic Reactions of Phosphate Diesters - Rate Effects upon Substitution of Sulfur for a Nonbridging Phosphoryl Oxygen Atom. *Biochemistry* **1991**, 30, 4844-4854.
227. Hondal, R. J.; Riddle, S. R.; Kravchuk, A. V.; Zhao, Z.; Liao, H.; Bruzik, K. S.; Tsai, M. D., Phosphatidylinositol-specific Phospholipase C: Kinetic and Stereochemical Evidence for an Interaction between Arginine-69 and the Phosphate Group of Phosphatidylinositol. *Biochemistry* **1997**, 36, 6633-6642.
228. Breslow, R.; Xu, R., Recognition and Catalysis in Nucleic Acid Chemistry. *Proceedings of the National Academy of Sciences* **1993**, 90, 1201-1207.
229. Herschlag, D., Ribonuclease Revisited: Catalysis via the Classical General Acid-base Mechanism or a Triester-like Mechanism? *Journal of the American Chemical Society* **1994**, 116, 11632-11635.
230. Oivanen, M.; Ora, M.; Almer, H.; Stromberg, R.; Lonnberg, H., Hydrolytic Reactions of the Diastereomeric Phosphoromonothioate Analogs of Uridyl(3',5') Uridine - Kinetics and Mechanisms for Desulfurization, Phosphoester Hydrolysis, and Transesterification to the 2',5'-Isomers. *Journal of Organic Chemistry* **1995**, 60, 5620-5627.
231. Ora, M.; Oivanen, M.; Lonnberg, H., Phosphoester Hydrolysis and Intramolecular Transesterification of Ribonucleoside 2'- and 3'-Phosphoromonothioate Triesters: Kinetics and Mechanisms for the Reactions of 5'-O-methyluridine 2'- and 3'-Dimethylphosphoromonothioates. *Journal of Organic Chemistry* **1997**, 62, 3246-3253.
232. Gerlt, J. A.; Gassman, P. G., Understanding the Rates of Certain Enzyme-catalyzed Reactions - Proton Abstraction from Carbon Acids, Acyl-transfer Reactions, and Displacement-Reactions of Phosphodiester. *Biochemistry* **1993**, 32, 11943-11952.
233. Lonnberg, T.; Ora, M.; Virtanen, S.; Lonnberg, H., Thio Effects on the Departure of the 3'-linked Ribonucleoside from Diribonucleoside 3',3'-Phosphorodithioate Diesters and Triribonucleoside 3',3',5'-Phosphoromonothioate Triesters: Implications for Ribozyme Catalysis. *Chemistry-A European Journal* **2007**, 13, 4614-4627.
234. Lonnberg, T.; Lonnberg, H., Chemical Models for Ribozyme Action. *Current Opinion in Chemical Biology* **2005**, 9, 665-673.
235. Perreault, D. M.; Anslyn, E. V., Unifying the Current Data on the Mechanism of Cleavage - Transesterification of RNA. *Angewandte Chemie* **1997**, 36, 432-450.
236. Rhodes, M. M.; Reblova, K.; Sponer, J.; Walter, N. G., Trapped Water Molecules are Essential to Structural Dynamics and Function of a Ribozyme. *Proceedings Of The National Academy Of Sciences* **2006**, 103, 13380-13385.
237. Jang, Y. H.; Goddard, W. A.; Noyes, K. T.; Sowers, L. C.; Hwang, S.; Chung, D. S.,  $pK_a$  Values of Guanine in Water: Density Functional Theory Calculations Combined with Poisson-Boltzmann Continuum-solvation Model. *Journal of Physical Chemistry B* **2003**, 107, 344-357.
238. Salter, J.; Krucinska, J.; Alam, S.; Grum-Tokars, V.; Wedekind, J. E., Water in the Active Site of an All-RNA Hairpin Ribozyme and Effects of G8 Base Variants on the Geometry of Phosphoryl Transfer. *Biochemistry* **2006**, 45, 686-700.

239. Torelli, A. T.; Krucinska, J.; Wedekind, J. E., A Comparison of Vanadate to a 2'-5' Linkage at the Active Site of a Small Ribozyme Suggests a Role for Water in Transition State Stabilization. *RNA* **2007**, 13, 1052-1070.
240. Walter, N. G., Ribozyme Catalysis Revisited: Is Water Involved? *Molecular Cell* **2007**, 28, 923-929.
241. Epstein, L. M.; Gall, J. G., Self-Cleaving Transcripts of Satellite DNA from the Newt. *Cell* **1987**, 48, 535-543.
242. Ferbeyre, G.; Smith, J. M.; Cedergren, R., Schistosome Satellite DNA Encodes Active Hammerhead Ribozymes. *Molecular and Cellular Biology* **1998**, 18, 3880-3888.
243. Martick, M.; Horan, L. H.; Noller, H. F.; Scott, W. G., A Discontinuous Hammerhead Ribozyme Embedded in a Mammalian messenger RNA. *Nature* **2008**, 454, 899-U57.
244. Forster, A. C.; Symons, R. H., Self-Cleavage of Plus and Minus RNAs of a Virusoid and a Structural Model for the Active Sites. *Cell* **1987**, 49, 211-220.
245. Forster, A. C.; Symons, R. H., Self-Cleavage of Virusoid RNA is Performed by the Proposed 55-Nucleotide Active Site. *Cell* **1987**, 50, 9-16.
246. Ruffner, D. E.; Stormo, G. D.; Uhlenbeck, O. C., Sequence Requirements of the Hammerhead RNA Self-Cleavage Reaction. *Biochemistry* **1990**, 29, 10695-10702.
247. Fedor, M. J.; Uhlenbeck, O. C., Substrate Sequence Effects on Hammerhead RNA Catalytic Efficiency. *Proceedings of the National Academy of Sciences* **1990**, 87, 1668-1672.
248. Nelson, J. A.; Uhlenbeck, O. C., Hammerhead Redux: Does the New Structure Fit the Old Biochemical Data? *RNA* **2008**, 14, 605-615.
249. Scott, W. G.; Murray, J. B.; Arnold, J. R. P.; Stoddard, B. L.; Klug, A., Capturing the Structure of a Catalytic RNA Intermediate: the Hammerhead Ribozyme. *Science* **1996**, 274, 2065-2069.
250. Pley, H. W.; Flaherty, K. M.; McKay, D. B., 3-Dimensional Structure of a Hammerhead Ribozyme. *Nature* **1994**, 372, 68-74.
251. Scott, W. G.; Finch, J. T.; Klug, A., The Crystal Structure of an All-RNA Hammerhead Ribozyme - A Proposed Mechanism for RNA Catalytic Cleavage. *Cell* **1995**, 81, 991-1002.
252. Murray, J. B.; Scott, W. G., Does a Single Metal Ion Bridge the A-9 and Scissile Phosphate Groups in the Catalytically Active Hammerhead Ribozyme Structure? *Journal of Molecular Biology* **2000**, 296, 33-41.
253. Nelson, J. A.; Uhlenbeck, O. C., When to Believe What You See. *Molecular Cell* **2006**, 23, 447-450.
254. Nowakowski, J.; Shim, P. J.; Prasad, G. S.; Stout, C. D.; Joyce, G. F., Crystal Structure of an 82-nucleotide RNA-DNA Complex Formed by the 10-23 DNA Enzyme. *Nature Structural Biology* **1999**, 6, 151-156.
255. Dunham, C. M.; Murray, J. B.; Scott, W. G., A Helical Twist-induced Conformational Switch Activates Cleavage in the Hammerhead Ribozyme. *Journal of Molecular Biology* **2003**, 332, 327-336.
256. Hampel, K. J.; Burke, J. M., Solvent Protection of the Hammerhead Ribozyme in the Ground State: Evidence for a Cation-assisted Conformational Change Leading to Catalysis. *Biochemistry* **2003**, 42, 4421-4429.

257. Woisard, A.; Fourrey, J. L.; Favre, A., Multiple Folded Conformations of a Hammerhead Ribozyme Domain under Cleavage Conditions. *Journal of Molecular Biology* **1994**, 239, 366-370.
258. Murray, J. B.; Dunham, C. M.; Scott, W. G., A pH-dependent Conformational Change, Rather than the Chemical Step, Appears to be Rate-limiting in the Hammerhead Ribozyme Cleavage Reaction. *Journal of Molecular Biology* **2002**, 315, 121-130.
259. Peracchi, A.; Beigelman, L.; Scott, E. C.; Uhlenbeck, O. C.; Herschlag, D., Involvement of a Specific Metal ion in the Transition of the Hammerhead Ribozyme to its Catalytic Conformation. *Journal of Biological Chemistry* **1997**, 272, 26822-26826.
260. Scott, E. C.; Uhlenbeck, O. C., A Re-investigation of the Thio Effect at the Hammerhead Cleavage Site. *Nucleic Acids Research* **1999**, 27, 479-484.
261. Maderia, M.; Hunsicker, L. M.; DeRose, V. J., Metal-phosphate Interactions in the Hammerhead Ribozyme Observed by P-31 NMR and Phosphorothioate Substitutions. *Biochemistry* **2000**, 39, 12113-12120.
262. Vogt, M.; Lahiri, S.; Hoogstraten, C. G.; Britt, R. D.; DeRose, V. J., Coordination Environment of a Site-bound Metal Ion in the Hammerhead Ribozyme Determined by N-15 and H-2 ESEEM Spectroscopy. *Journal of the American Chemical Society* **2006**, 128, 16764-16770.
263. Morrissey, S. R.; Horton, T. E.; Grant, C. V.; Hoogstraten, C. G.; Britt, R. D.; DeRose, V. J., Mn<sup>2+</sup>-nitrogen Interactions in RNA Probed by Electron Spin-echo Envelope Modulation Spectroscopy: Application to the Hammerhead Ribozyme. *Journal of the American Chemical Society* **1999**, 121, 9215-9218.
264. Suzumura, K.; Yoshinari, K.; Tanaka, Y.; Takagi, Y.; Kasai, Y.; Warashina, M.; Kuwabara, T.; Orita, M.; Taira, K., A Reappraisal, Based on P-31 NMR, of the Direct Coordination of a Metal Ion with the Phosphoryl Oxygen at the Cleavage Site of a Hammerhead Ribozyme. *Journal of the American Chemical Society* **2002**, 124, 8230-8236.
265. Zhou, D. M.; Kumar, P. K. R.; Zhang, L. H.; Taira, K., Ribozyme Mechanism Revisited: Evidence Against Direct Coordination of a Mg<sup>2+</sup> Ion with the pro-R Oxygen of the Scissile Phosphate in the Transition State of a Hammerhead Ribozyme-catalyzed Reaction. *Journal of the American Chemical Society* **1996**, 118, 8969-8970.
266. Tanaka, Y.; Kasai, Y.; Mochizuki, S.; Wakisaka, A.; Morita, E. H.; Kojima, C.; Toyozawa, A.; Kondo, Y.; Taki, M.; Takagi, Y.; Inoue, A.; Yamasaki, K.; Taira, K., Nature of the Chemical Bond Formed with the Structural Metal Ion at the A9/G10.1 Motif Derived from Hammerhead Ribozymes. *Journal of the American Chemical Society* **2004**, 126, 744-752.
267. Yoshinari, K.; Taira, K., A Further Investigation and Reappraisal of the Thio Effect in the Cleavage Reaction Catalyzed by a Hammerhead Ribozyme. *Nucleic Acids Research* **2000**, 28, 1730-1742.
268. Canny, M. D.; Jucker, F. M.; Kellogg, E.; Khvorova, A.; Jayasena, S. D.; Pardi, A., Fast Cleavage Kinetics of a Natural Hammerhead Ribozyme. *Journal of the American Chemical Society* **2004**, 126, 10848-10849.

269. Hertel, K. J.; Pardi, A.; Uhlenbeck, O. C.; Koizumi, M.; Ohtsuka, E.; Uesugi, S.; Cedergren, R.; Eckstein, F.; Gerlach, W. L.; Hodgson, R.; Symons, R. H., Numbering System for the Hammerhead Ribozyme. *Nucleic Acids Research* **1992**, *20*, 3252-3252.
270. Martick, M.; Scott, W. G., Tertiary Contacts Distant from the Active Site Prime a Ribozyme for Catalysis. *Cell* **2006**, *126*, 309-320.
271. Dahm, S. C.; Derrick, W. B.; Uhlenbeck, O. C., Evidence for the Role of Solvated Metal Hydroxide in the Hammerhead Cleavage Mechanism. *Biochemistry* **1993**, *32*, 13040-13045.
272. Torres, R. A.; Himo, F.; Bruice, T. C.; Noodleman, L.; Lovell, T., Theoretical Examination of Mg<sup>2+</sup>-mediated Hydrolysis of a Phosphodiester Linkage as Proposed for the Hammerhead Ribozyme. *Journal of the American Chemical Society* **2003**, *125*, 9861-9867.
273. Leclerc, F.; Karplus, M., Two-metal-ion Mechanism for Hammerhead-ribozyme Catalysis. *Journal of Physical Chemistry B* **2006**, *110*, 3395-3409.
274. Pontius, B. W.; Lott, W. B.; vonHippel, P. H., Observations on Catalysis by Hammerhead Ribozymes are Consistent with a Two-divalent-metal-ion Mechanism. *Proceedings of the National Academy of Sciences* **1997**, *94*, 2290-2294.
275. Lott, W. B.; Pontius, B. W.; von Hippel, P. H., A Two-metal Ion Mechanism Operates in the Hammerhead Ribozyme-mediated Cleavage of an RNA Substrate. *Proceedings of the National Academy of Sciences* **1998**, *95*, 542-547.
276. Sawata, S.; Komiyama, M.; Taira, K., Kinetic Evidence Based on Solvent Isotope Effects for the Nonexistence of a Proton Transfer Process in Reactions Catalyzed by a Hammerhead Ribozyme - Implication to the Double-metal-ion Mechanism of Catalysis. *Journal of the American Chemical Society* **1995**, *117*, 2357-2358.
277. Han, J.; Burke, J. M., Model for General Acid-base Catalysis by the Hammerhead Ribozyme: pH-activity Relationships of G8 and G12 Variants at the Putative Active Site. *Biochemistry* **2005**, *44*, 7864-7870.
278. Lambert, D.; Heckman, J. E.; Burke, J. M., Three Conserved Guanosines Approach the Reaction Site in Native and Minimal Hammerhead Ribozymes. *Biochemistry* **2006**, *45*, 7140-7147.
279. Khvorova, A.; Lescoute, A.; Westhof, E.; Jayasena, S.D., Sequence Elements outside the Hammerhead Ribozyme Catalytic Core Enable Intracellular Activity *Nat. Struct. Biol.* **2003**, *10*, 708-712.
280. Penedo, J. C.; Wilson, T. J.; Jayasena, S. D.; Khvorova, A.; Lilley, D. M. J., Folding of the Natural Hammerhead Ribozyme is Enhanced by Interaction of Auxiliary Elements. *RNA* **2004**, *10*, 880-888.
281. Boots, J. L.; Canny, M. D.; Azimi, E.; Pardi, A., Metal Ion Specificities for Folding and Cleavage Activity in the *Schistosoma* Hammerhead Ribozyme. *RNA* **2008**, *14*, 2212-2222.
282. Canny, M. D.; Jucker, F. M.; Pardi, A., Efficient Ligation of the *Schistosoma* Hammerhead Ribozyme. *Biochemistry* **2007**, *46*, 3826-3834.
283. Saksmerprome, V.; Roychowdhury-Saha, M.; Jayasena, S.; Khvorova, A.; Burke, D. H., Artificial Tertiary Motifs Stabilize *Trans*-cleaving Hammerhead Ribozymes under Conditions of Submillimolar Divalent Ions and High Temperatures. *RNA* **2004**, *10*, 1916-1924.

284. Martick, M.; Lee, T. S.; York, D. M.; Scott, W. G., Solvent Structure and Hammerhead Ribozyme Catalysis. *Chemistry & Biology* **2008**, *15*, 332-342.
285. Chi, Y. I.; Martick, M.; Lares, M.; Kim, R.; Scott, W. G.; Kim, S. H., Capturing Hammerhead Ribozyme Structures in Action by Modulating General Base Catalysis. *PLoS Biology* **2008**, *6*, 2060-2068.
286. Lee, T. S.; Silva-Lopez, C.; Martick, M.; Scott, W. G.; York, D. M., Insight into the Role of Mg<sup>2+</sup> in Hammerhead Ribozyme Catalysis from X-ray Crystallography and Molecular Dynamics Simulation. *Journal of Chemical Theory and Computation* **2007**, *3*, 325-327.
287. Lee, T. S.; Lopez, C. S.; Giambasu, G. M.; Martick, M.; Scott, W. G.; York, D. M., Role of Mg<sup>2+</sup> in Hammerhead Ribozyme Catalysis from Molecular Simulation. *Journal of the American Chemical Society* **2008**, *130*, 3053-3064.
288. Roychowdhury-Saha, M.; Burke, D. H., Extraordinary Rates of Transition Metal Ion-mediated Ribozyme Catalysis. *RNA* **2006**, *12*, 1846-1852.
289. Milligan, J. F.; Groebe, D. R.; Witherell, G. W.; Uhlenbeck, O. C., Oligoribonucleotide Synthesis Using T7 RNA-Polymerase and Synthetic DNA Templates. *Nucleic Acids Research* **1987**, *15*, 8783-8798.
290. Sproat, B.; Colonna, F.; Mullah, B.; Tsou, D.; Andrus, A.; Hampel, A.; Vinayak, R., An Efficient Method for the Isolation and Purification of Oligoribonucleotides. *Nucleosides & Nucleotides* **1995**, *14*, 255-273.
291. Yang, J. H.; Perreault, J. P.; Labuda, D.; Usman, N.; Cedergren, R., Mixed DNA RNA Polymers are Cleaved by the Hammerhead Ribozyme. *Biochemistry* **1990**, *29*, 11156-11160.
292. this work, section 4.4
293. Nishikawa, K.; Adams, B. L.; Hecht, S. M., Chemical Excision of Apurinic Acids from RNA - a Structurally Modified Yeast Transfer RNA(phe). *Journal of the American Chemical Society* **1982**, *104*, 326-328.
294. Peattie, D. A., Direct Chemical Method for Sequencing RNA. *Proceedings of the National Academy of Sciences* **1979**, *76*, 1760-1764.
295. Kupfer, P. A.; Leumann, C. J., The Chemical Stability of Abasic RNA Compared to Abasic DNA. *Nucleic Acids Research* **2007**, *35*, 58-68.
296. Kim, N. K.; Murali, A.; DeRose, V. J., Separate Metal Requirements for Loop Interactions and Catalysis in the Extended Hammerhead Ribozyme. *Journal of the American Chemical Society* **2005**, *127*, 14134-14135.
297. Kubiak, R. J.; Yue, X. J.; Hondal, R. J.; Mihai, C.; Tsai, M. D.; Bruzik, K. S., Involvement of the Arg-Asp-His Catalytic Triad in Enzymatic Cleavage of the Phosphodiester Bond. *Biochemistry* **2001**, *40*, 5422-5432.
298. Kubiak, R. J.; Hondal, R. J.; Yue, X. J.; Tsai, M. D.; Bruzik, K. S., Identification of a Novel Catalytic Triad with Dual Functions in Enzymatic Cleavage of the P-O Bond. *Journal of the American Chemical Society* **1999**, *121*, 488-489.
299. this work, Section 4.3
300. Acharya, S.; Foldesi, A.; Chattopadhyaya, J., The pK<sub>a</sub> of the Internucleotidic 2'-Hydroxyl Group in Diribonucleoside (3'→5') Monophosphates. *Journal of Organic Chemistry* **2003**, *68*, 1906-1910.

301. Velikyan, I.; Acharya, S.; Trifonova, A.; Foldesi, A.; Chattopadhyaya, J., The  $pK_a$ 's of 2'-Hydroxyl Group in Nucleosides and Nucleotides. *Journal of the American Chemical Society* **2001**, 123, 2893-2894.
302. Lyne, P. D.; Karplus, M., Determination of the  $pK_a$  of the 2'-Hydroxyl Group of a Phosphorylated Ribose: Implications for the Mechanism of Hammerhead Ribozyme Catalysis. *Journal of the American Chemical Society* **2000**, 122, 166-167.
303. Lippert, B.; Anorbe, M. G.; Roitzsch, M.; Luth, M. S.; Muller, J.; Lax, P.; Sigel, H., Remarkable  $pK_a$  Shifts of Adenine and Cytosine Nucleobases into the Physiological pH Range Following Metal Binding. *Journal of Inorganic Biochemistry* **2003**, 96, 82-82.
304. Song, B.; Zhao, J.; Griesser, R.; Meiser, C.; Sigel, H.; Lippert, B., Effects of (N7)-Coordinated Nickel(II), Copper(II), or Platinum(II) on the Acid-base Properties of Guanine Derivatives and Other Related Purines. *Chemistry-A European Journal* **1999**, 5, 2374-2387.
305. Chowira, B. M.; Burke, J. M., Binding and Cleavage of Nucleic Acids by the Hairpin Ribozyme. **1991**, 30, 8518-8522.
306. Berzal-Herranz, A.; Joseph, S.; Burke, J. M., Essential Nucleotide Sequences and Secondary Structure Elements of the Hairpin Ribozyme. *EMBO Journal* **1993**, 12, 2567-2574.
307. Fedor, M. J., Structure and Function of the Hairpin Ribozyme. *Journal of Molecular Biology* **2000**, 297, 269-291.
308. Butcher, S. E.; Burke, J. M., A Photo-crosslinkable Tertiary Structure Motif Found in Functionally Distinct RNA Molecules is Essential for Catalytic Function of the Hairpin Ribozyme. *Biochemistry* **1994**, 33, 992-999.
309. Murchie, A. I. H.; Thomson, J. B.; Walter, F.; Lilley, D. M. J., Folding of the Hairpin Ribozyme in its Natural Conformation Achieves Close Physical Proximity of the Loops. *Molecular Cell* **1998**, 1, 873-881.
310. Walter, F.; Murchie, A. I. H.; Thomson, J. B.; Lilley, D. M. J., Structure and Activity of the Hairpin Ribozyme in its Natural Junction Conformation: Effect of Metal Ions. *Biochemistry* **1998**, 37, 14195-14203.
311. Pinard, R.; Lambert, D.; Walter, N. G.; Heckman, J. E.; Major, F.; Burke, J. M., Structural Basis for the Guanosine Requirement of the Hairpin Ribozyme. *Biochemistry* **1999**, 38, 16035-16039.
312. Earnshaw, D. J.; Masquida, B.; Muller, S.; Sigurdsson, S. T.; Eckstein, F.; Westhof, E.; Gait, M. J., Inter-domain Cross-linking and Molecular Modelling of the Hairpin Ribozyme. *Journal of Molecular Biology* **1997**, 274, 197-212.
313. Klostermeier, D.; Millar, D. P., Tertiary Structure Stability of the Hairpin Ribozyme in its Natural and Minimal Forms: Different Energetic Contributions from a Ribose Zipper Motif. *Biochemistry* **2001**, 40, 11211-11218.
314. Earnshaw, D. J.; Hamm, M. L. H.; Piccirilli, J. A.; Karpeisky, A.; Beigelman, L.; Ross, B. S.; Manoharan, M.; Gait, M. J., Investigation of the Proposed Interdomain Ribose Zipper in Hairpin Ribozyme Cleavage Using 2'-Modified Nucleosides. *Biochemistry* **2000**, 39, 6410-6421.
315. Esteban, J. A.; Banerjee, A. R.; Burke, J. M., Kinetic Mechanism of the Hairpin Ribozyme - Identification and Characterization of Two Non-exchangeable Conformations. *Journal of Biological Chemistry* **1997**, 272, 13629-13639.

316. Wilson, T. J.; Lilley, D. M. J., Metal Ion Binding and the Folding of the Hairpin Ribozyme. *RNA* **2002**, 8, 587-600.
317. Earnshaw, D. J.; Gait, M. J., Hairpin Ribozyme Cleavage Catalyzed by Aminoglycoside Antibiotics and the Polyamine Spermine in the Absence of Metal Ions. *Nucleic Acids Research* **1998**, 26, 5551-5561.
318. Rupert, P. B.; Ferre-D'Amare, A. R., Crystal Structure of a Hairpin Ribozyme-inhibitor Complex with Implications for Catalysis. *Nature* **2001**, 410, 780-786.
319. Rupert, P. B.; Massey, A. P.; Sigurdsson, S. T.; Ferre-D'Amare, A. R., Transition State Stabilization by a Catalytic RNA. *Science* **2002**, 298, 1421-1424.
320. Kuzmin, Y. I.; Da Costa, C. P.; Cottrell, J. W.; Fedor, M. J., Role of an Active Site Adenine in Hairpin Ribozyme Catalysis. *Journal of Molecular Biology* **2005**, 349, 989-1010.
321. Ryder, S. P.; Oyelere, A. K.; Padilla, J. L.; Klostermeier, D.; Millar, D. P.; Strobel, S. A., Investigation of Adenosine Base Ionization in the Hairpin Ribozyme by Nucleotide Analog Interference Mapping. *RNA* **2001**, 7, 1454-1463.
322. Spitale, R. C.; Volpini, R.; Heller, M. G.; Krucinska, J.; Cristalli, G.; Wedekind, J. E., Identification of an Imino Group Indispensable for Cleavage by a Small Ribozyme. *Journal Of The American Chemical Society* **2009**, 131, 6093-6095.
323. Nam, K.; Gao, J. L.; York, D. M., Electrostatic Interactions in the Hairpin Ribozyme Account for the Majority of the Rate Acceleration without Chemical Participation by Nucleobases. *RNA* **2008**, 14, 1501-1507.
324. Pinard, R.; Hampel, K. J.; Heckman, J. E.; Lambert, D.; Chan, P. A.; Major, F.; Burke, J. M., Functional Involvement of G8 in the Hairpin Ribozyme Cleavage Mechanism. *EMBO Journal* **2001**, 20, 6434-6442.
325. Lebruska, L. L.; Kuzmine, II; Fedor, M. J., Rescue of an Abasic Hairpin Ribozyme by Cationic Nucleobases: Evidence for a Novel Mechanism of RNA Catalysis. *Chemistry & Biology* **2002**, 9, 465-473.
326. Kumin, Y. I.; Da Costa, C. P.; Fedor, M. J., Role of an Active Site Guanine in Hairpin Ribozyme Catalysis Probed by Exogenous Nucleobase Rescue. *Journal of Molecular Biology* **2004**, 340, 233-251.
327. Fedor, M. J., The Catalytic Mechanism of the Hairpin Ribozyme. *Biochemical Society Transactions* **2002**, 30, 1109-1115.
328. Wilson, T. J.; Ouellet, J.; Zhao, Z. Y.; Harusawa, S.; Araki, L.; Kurihara, T.; Lilley, D. M. J., Nucleobase Catalysis in the Hairpin Ribozyme. *RNA* **2006**, 12, 980-987.
329. Da Costa, C. P.; Fedor, M. J.; Scott, L. G., 8-Azaguanine Reporter of Purine Ionization States in Structured RNAs. *Journal of the American Chemical Society* **2007**, 129, 3426-3432.
330. Liu, L.; Cottrell, J. W.; Scott, L. G.; Fedor, M. J., Direct Measurement of the Ionization State of an Essential Guanine in the Hairpin Ribozyme. *Nature Chemical Biology* **2009**, 5, 351-357.
331. Nam, K. H.; Gaot, J. L.; York, D. M., Quantum Mechanical/Molecular Mechanical Simulation Study of the Mechanism of Hairpin Ribozyme Catalysis. *Journal of the American Chemical Society* **2008**, 130, 4680-4691.
332. Moore, M. J. Q., C.C., Joining of RNAs by Splinted Ligation. **2000**, 317, 109-123.

333. Inoue, T. C., T.R., Secondary Structure of the Circular Form of the Tetrahymena rRNA Intervening Sequence: a Technique for RNA Structure Determination Using Chemical Probes and Reverse Transcriptase. *Proceedings of the National Academy of Sciences* **1985**, 82, 648-652.
334. Moazed, D. S., S.; Noller, H.F., Rapid Chemical Probing of Conformation in 16S Ribosomal RNA and 30S Ribosomal Subunits Using Primer Extension. *Journal Of Molecular Biology* **1986**, 187, 399-416.
335. Youvan, D. C.; Hearst, J. E., Reverse Transcriptase Pauses at N2-Methylguanine During *in vitro* Transcription of *Escherichia Coli* 16S Ribosomal RNA. *Proceedings of the National Academy of Sciences* **1979**, 76, 3751-3754.
336. Suo, Z. L., S.J.; Johnson, A.J., Single d(GpG)/*cis*-Diammineplatinum(II) Adduct-induced Inhibition of DNA Polymerization. *Biochemistry* **1999**, 38, 715-726.
337. Ericson, E.; Wollenzien, P., Use of Reverse Transcription to Determine the Exact Locations of Psoralen Photochemical Crosslinks in RNA. *Analytical Biochemistry* **1988**, 174, 215-223.
338. Barta, A.; Steiner, G.; Brosius, J.; Noller, H. F.; Kuechler, E., Identification of a Site on 23S Ribosomal-RNA Located at the Peptidyl Transferase Center. *Proceedings of the National Academy of Sciences* **1984**, 81, 3607-3611.
339. Singer, B., Reaction of Guanosine with Ethylating Agents. *Biochemistry* **1972**, 11, 3939-3946.
340. Jones, J. W.; Robins, R. K., Purine Nucleosides 3: Methylation Studies of Certain Naturally Occurring Purine Nucleosides. *Journal of the American Chemical Society* **1963**, 85, 193-199.
341. Singer, B.; Sun, L.; Fraenkel, H., Reaction of Adenosine with Ethylating Agents. *Biochemistry* **1974**, 13, 1913-1920.
342. Klein, D. J.; Been, M. D.; Ferré-D'Amaré, A. R., Essential Role of an Active-Site Guanine in *GlmS* Ribozyme Catalysis. *Journal of the American Chemical Society* **2007**, 129, 14858-14859.
343. Klein, D. J.; Ferré-D'Amaré, A. R., Structural Basis of *GlmS* Ribozyme Activation by Glucosamine-6-Phosphate. *Science* **2006**, 313, 1752-1756.
344. Cochrane, J. C.; Lipchock, S. V.; Strobel, S. A. Structural Investigation of the *GlmS* Ribozyme Bound to its Catalytic Cofactor. *Chemistry & Biology* **2007**, 14, 97-105
345. Wilson T. J., McLeod A. C., Lilley D. M., A Guanine Nucleobase Important for Catalysis by the VS Ribozyme. *EMBO Journal* **2007**, 26, 2489-500.